University of Calgary

PRISM Repository **https://prism.ucalgary.ca**

The Vault Open Theses and Dissertations

2018-08-20

Membrane Interactions of Cobalt and Nickel

Umbsaar, Jenelle

Umbsaar, J. (2018). Membrane Interactions of Cobalt and Nickel (Master's thesis, University of Calgary, Calgary, Canada). Retrieved from https://prism.ucalgary.ca. doi:10.11575/PRISM/32831

http://hdl.handle.net/1880/107651

Downloaded from PRISM Repository, University of Calgary

UNIVERSITY OF CALGARY

Membrane Interactions of Cobalt and Nickel

by

Jenelle Umbsaar

A THESIS

SUBMITTED TO THE FACULTY OF GRADUATE STUDIES

IN PARTIAL FULFILMENT OF THE REQUIREMENTS FOR THE

DEGREE OF MASTER OF SCIENCE

GRADUATE PROGRAM IN BIOLOGICAL SCIENCES

CALGARY, ALBERTA

AUGUST, 2018

© Jenelle Umbsaar 2018

Abstract

The metals Cobalt (Co) and Nickel (Ni) are common industrial metals which are becoming increasingly prevalent in everyday life. Despite their ubiquity, disruption to homeostasis of trace metals can have severe consequences, as elevated levels of Co^{2+} and Ni^{2+} have been associated with various toxic effects. The mechanisms by which metals including Co^{2+} and Ni^{2+} exert these effects are not fully understood and may involve various biomolecules.

The primary focus of this thesis is on the interactions of Co^{2+} and Ni^{2+} with lipid membranes, as disruption to membrane properties may have consequences for transport, signalling, and overall cellular integrity. This study has shown that Co^{2+} and Ni^{2+} rigidify membranes containing negatively-charged lipids in both simple and complex model membranes. Additionally, Co^{2+} and Ni^{2+} were found to affect respiration and neutral lipid content in the model organism *S. cerevisiae*, suggesting that both direct and indirect effects on membrane properties may occur.

Acknowledgements

Thank you Dr. Elmar Prenner for supervising me in my graduate studies and for allowing me to explore many creative and interesting scientific ideas in the lab over the past years. I am so grateful for the many opportunities you have given me to expand my skills, including the project in New Zealand and CSC conference in Edmonton. My graduate school experience has been a very positive one thanks to your constant support, patience, and encouragement.

As well, thank you to my dear family: Maryanne, Don, Darren, and Jonathan Umbsaar who have supported me completely through these past years in so many ways. You have helped me to stay motivated and positive and I am so thankful for all of you.

I would also like to thank my committee members Dr. Vanina Zaremberg and Dr. Jürgen Gailer for their helpful advice and insights on various aspects of my project. I am very grateful to Dr. Zaremberg for her kindness in allowing me to collaborate with her lab and for teaching me many new techniques in microbiology. I am also very grateful to past and present members of the Zaremberg lab for their help in answering my many questions, notably Brittney Kozlowski and Suriakarthiga Ganesan for their technical contributions. Thank you as well to Dr. Sergei Noskov as the internal examiner, and Dr. Marie Fraser as the neutral chair for my thesis defense. Additionally, thank you to Dr. Lohmeier-Vogel and Dr. Edwards for their involvement in my TA experience.

I am also very thankful to fellow members of the Prenner lab who have been so supportive and such amazing friends. A special thanks to Robyn Mundle, Kevin Sule, and Evan Kerek for working alongside me and teaching me techniques in the metals project, and to Dr. Patrick Lai and Weiam Daear for help with lung surfactant experiment. Thank you as well to Dr. Mark Mahadeo for answering my many questions on various problems.

Table of Contents

List of Tables

List of Figures and Illustrations

List of Equations

List of Symbols, Abbreviations and Nomenclature

Symbol	Definition
Ag	Silver
Al	Aluminum
As	Arsenic
ATSDR	Agency for Toxic Substances and Disease Registry
Be	Beryllium
BLES	Bovine Lipid Extract Surfactant
BSA	Bovine serum albumin
C1-GFP	Green fluorescent protein with C1 domain
Ca	Calcium
Cd	Cadmium
Cera	Ceramide
Cere	Cerebroside
Chol	Cholesterol
CL	Cardiolipin
Co	Cobalt
Cr	Chromium
Cu	Copper
DAG	Diacylglycerol
DH-	Di-hexadecanoyl
DLS	Dynamic Light Scattering
DM-	Di-myristoyl
DMSO	Dimethyl sulfoxide
DO-	Di-oleyl
DP-	Di-palmitoyl
DPH	Diphenylhexatriene
DSC	Differential Scanning Calorimetry
DTT	Dithiothreitol
E. coli	*Escherichia coli*
EDTA	Ethylenediaminetetraacetic acid
EM	EDTA MOPS buffer
ER	Endoplasmic reticulum
Ergo	Ergosterol
FA	Fatty acids
Fe	Iron
GP	Generalized Polarization
GSH	Glutathione
Hb	Hemoglobin
HEPES	(4-(2-hydroxyethyl)-1-piperazineethanesulfonic acid)
Hg	Mercury
HIF-1	Hypoxia inducible factor 1
HPLC	High-performance liquid chromatography
HSA	Human serum albumin

IPC	Inositol phosphorylceramide
ITC	Isothermal Titration Calorimetry
K_d	Dissociation constant
LD	Lipid droplet
LS	Lung surfactant
LSM	Lung surfactant mimic
LUV	Large unilamellar vesicle
Mg	Magnesium
MIC	Minimum inhibitory concentration
MLV	Multi-lamellar vesicle
Mn	Manganese
MOPS	3-(N-morpholino)propanesulfonic acid
MP-	Myristoyl-palmitoyl
MPTP	Mitochondrial permeability transition pore
MSR	MitoSOX Red Mitochondrial Superoxide Indicator
mtDNA	Mitochondrial DNA
MTG-FM	MitoTracker Green FM
NBD	Nitrobenzoxadiole
Ni	Nickel
NL	Neutral lipid
NMR	Nuclear magnetic resonance
OD	Optical density
PA	Phosphatidic acid
Pb	Lead
PC	Phosphatidylcholine
PDI	Polydispersity index
PE	Phosphatidylethanolamine
PG	Phosphatidylglycerol
PI	Phosphatidylinostiol
PL	Polar lipids
PM	Plasma membrane
PO-	Palmitoyl-oleyl
PS	Phosphatidylserine
PSM	Palmitoyl sphingomyelin
Rb	Rubidium
RBC	Red blood cell
RD	Respiratory deficiency
ROS	Reactive oxygen species
S. cerevisiae	*Saccharomyces cerevisiae*
SA-	Stearoyl-arachidonoyl
SC	Synthetic complete
SC Glu	Synthetic complete with glutamate
SD-ura	Synthetic defined minus uracil
SE	Sterol esters
SEM	Sucrose EDTA MOPS buffer
SGD	Saccharomyces Genome Database

SM	Sphingomyelin
SO-	Stearoyl-oleyl
SP	Surfactant protein
TAG	Triacylglycerol
Tgl	Triacylglycerol lipase
Th	Thallium
TLC	Thin layer chromatography
T_m	Melting temperature
TM-	Tetra-myristoyl
TO-	Tetra-oleyl
TP-	Tetra-palmitoyl
YE	Yeast extract
YPD	Yeast extract peptone dextrose
YPE	Yeast polar lipid extract
YPG	Yeast extract peptone glycerol
YTE	Yeast total lipid extract
Zn	Zinc

Epigraph

Don’t adventures ever have an end? I suppose not.

Someone else always has to carry on the story.

–J.R.R Tolkien, The Lord of the Rings

Chapter One: Introduction

1.1 Essentiality and Uses of Cobalt and Nickel

The transition metals Cobalt (Co) and Nickel (Ni) reside adjacent to each other in the periodic table and are generally classified as essential trace elements for humans or microorganisms (1, 2). Co is a relatively rare earth metal at 0.0025% (*wt/wt*) of the Earth's crust (3), while Ni is present at a slightly greater abundance of 0.005% (2). The major oxidation state of both metals in nature is (II), though (III) and (I) states are also prevalent (1, 4–7). This thesis is focused on the divalent species, Co^{2+} and Ni^{2+}. Both metals are widely-used in industry due to their favourable properties which include being ferromagnetic, ductile, corrosion-resistant, and able to form alloys (1, 2, 4). Co compounds commonly find use as significant components (5–20%) of hard metal alloys, but compounds are also used in paints and pigments (1). Ni compounds are common in everyday life as well, found in objects such as utensils, appliances, and jewelry (2, 4). An application of Co and Ni alloys is in metal surgical implants, representing a unique internal source of exposure for these patients (4, 8).

Aside from their industrial applications, the main importance of Co^{2+} and Ni^{2+} to human life is in their biological relevance. The status of Co^{2+} as an essential element is due to its presence as a coordinating ion in the corrin ring of vitamin B_{12} and other cobalamins (3), important in several metabolic and synthesis pathways (1, 9). The oxidation state of Co in cobalamins cycles between (III), (II), and (I), thus dictating its function (6, 10). Humans cannot produce vitamin B_{12}, but it is synthesized by bacteria in the gut (11). Deficiencies of vitamin B_{12} are associated with severe health effects including anemia, bone marrow damage, and neurological disorders (12).

A direct biological function of Ni^{2+} in humans has not been identified, as studying Ni^{2+} deficiency in humans is nearly impossible (4), though it may play a role in regulating iron absorption (4, 13). However, Ni^{2+} is an essential cofactor in enzymes of many microorganisms including a form of superoxide dismutase (7), making it at least relevant for human life. Similarly to Co in vitamin B_{12}, the redox cycling of Ni through (III), (II), and (I) states is important to its function in various enzymes (7).

The pathways of natural exposure to Co^{2+} and Ni^{2+} include: ingestion, inhalation, and dermal absorption (1, 2), but the primary route through which humans obtain minor amounts of these essential metals is through food and water (1, 2). Co consumption in Canada averages 11 µg/day (14), while Ni consumption is much higher, at 200 µg/day (15). Once the metals have been ingested, they may be absorbed in the intestine depending on the solubility and speciation of the metal-containing compound, along with the presence of other ions (1, 2). Solubilized metal salts, which this thesis is focused on, are normally absorbed at levels of 5–20% Co^{2+} and 1–5% Ni^{2+} (1, 2, 4). The uptake of Co^{2+} and Ni^{2+} ions is thought to occur mainly through a broad-specificity ion channel, sharing a pathway with other essential and toxic metals (16).

1.2 Toxicity of Cobalt and Nickel

1.2.1 General aspects of toxicity

While Co^{2+} and Ni^{2+} are essential and tolerable at low levels, increased exposure has been associated with toxic effects (1, 2). This is of special concern regarding industrial exposure in which inhaled Co and Ni oxide or sulfide particulates and volatile metallic compounds represent a greater risk than under typical conditions (1, 2). Co^{2+} and Ni^{2+} are certainly not the most inherently toxic substances in the environment, but their prevalence may be higher than other such substances because of their wide usage. The Agency for Toxic Substances and Disease Registry (ATSDR) biennially compiles a list of the 275 most toxic substances based on their inherent toxicity, frequency, and potential of exposure (17). Co and Ni currently rank at #51 and 57, respectively, behind well-known toxic metals: As, Pb, Hg, Cd, Cr, and Be (17). While the ranking of Ni has declined slightly over the past 25+ years of study, the ranking of Co rose drastically in the late 90s (Figure 1), suggesting that industrial and commercial exposure, and the recognition of such, may have played a significant role in the hazard assessment of Co (17).

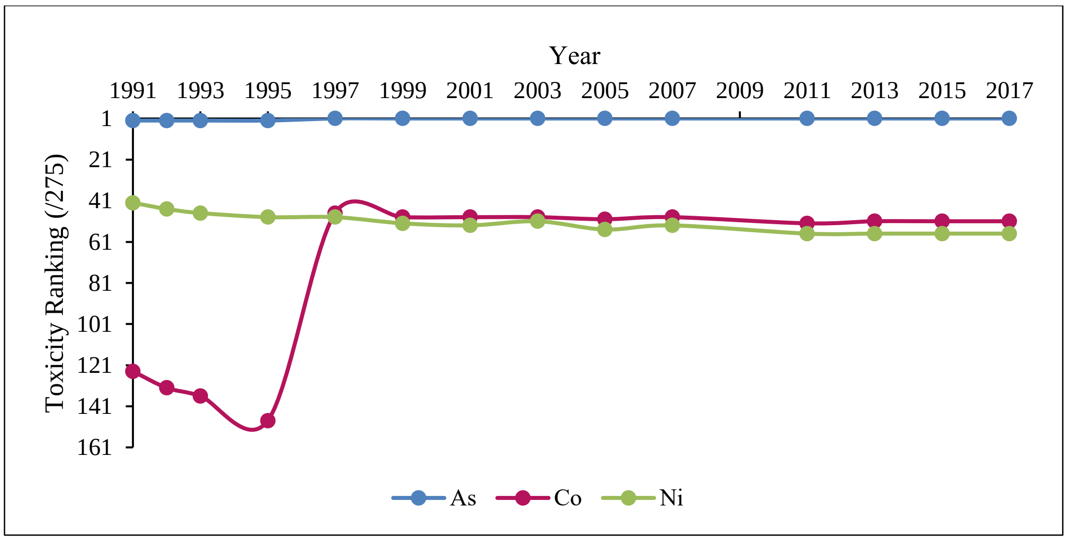

Figure 1. Toxicity rankings of Co, Ni, and As (the most toxic substance) from 1991–present according to the ATSDR substance priority report (17).

Some of the known effects of excessive exposure to Co^{2+} and Ni^{2+} compounds include: neurotoxicity (18–20), lung disease (2, 21), allergic reaction/contact dermatitis (22), and carcinogenesis (1, 2). Ni^{2+} is recognized as a potent human carcinogen (13), while Co^{2+} is classified as an animal carcinogen, but not yet a human carcinogen (1, 23). Other effects which are unique to Co^{2+} exposure include cardiomyopathy (1), ototoxicity (19, 24) and hard metal lung disease (21), characterized by a very specific pathology in the lungs (21). Co^{2+} species may accumulate in the liver, kidney, pancreas, heart, and skeletal muscle (23), while Ni^{2+} species appear to selectively accumulate in the lungs regardless of the route of uptake (4). $Ni(CO)_4$, formed during purification of metallic Ni by the Mond process, is considered to be one of the most toxic compounds in industry because of its high lipid solubility following inhalation, and rapid distribution of Ni^{2+} leading to acute poisoning (2, 4). In general, nanomolar concentrations of Co^{2+} and Ni^{2+} in the blood are normal (1, 2, 25, 26), but it has been found that concentrations in the low micromolar range are sufficient to induce toxic effects (8, 27).

As aforementioned, the release of Co^{2+} and Ni^{2+} from metal-based medical implants represents one of the main concerns for these patients, warranting further study (8, 28). Current treatments in cases of acute Co^{2+} or Ni^{2+} poisoning have seen some success with the use of chelators such as 2,3-dimercaptopropane-1-sulfonate for Co^{2+} (29) or Dithiocarb for Ni^{2+} (30), which contain electron-rich sulfur ligands which complex the metals, and mobilize them for excretion (31). Yet, a lack of detailed understanding of toxic mechanisms impedes specific treatment and prevention for cases of long-term exposure.

1.2.2 Biochemical considerations of toxicity

A key parameter that dictates direct binding interactions within the cell is metal speciation, as under physiological conditions of 100 mM NaCl pH 7.4, $CoCl_2$ and $NiCl_2$ speciate nearly entirely into positive divalent ions (Co^{2+} and Ni^{2+}), according to VMinteq chemical equilibrium software (32), which is essentially unchanged by pH (3.0–8.0) and NaCl (0.1–500 mM). This suggests that Co^{2+} and Ni^{2+} would have strong interactions with negatively-charged moieties, such as portions of proteins/peptides including: glutathione (33, 34), albumins (35), and hemoglobin (36, 37), though thiol groups may also be a target. Another important consideration in the binding of metals to ligands is their coordination geometry, as both metals can form a variety of complexes, but Co^{2+} prefers octahedral and sometimes tetrahedral, while Ni^{2+} forms predominantly octahedral and square planar complexes (33, 34, 38–41), a difference which leads to binding at different sites in human serum albumin (HSA) (35).

Additionally, the size and electronegativity of metal ions affect their ability to complex ligands. A summary of various mono-, di-, and trivalent ions tabulated by Nightingale (1959) (42) and Allred (1961) (43) are shown in Figure 2:

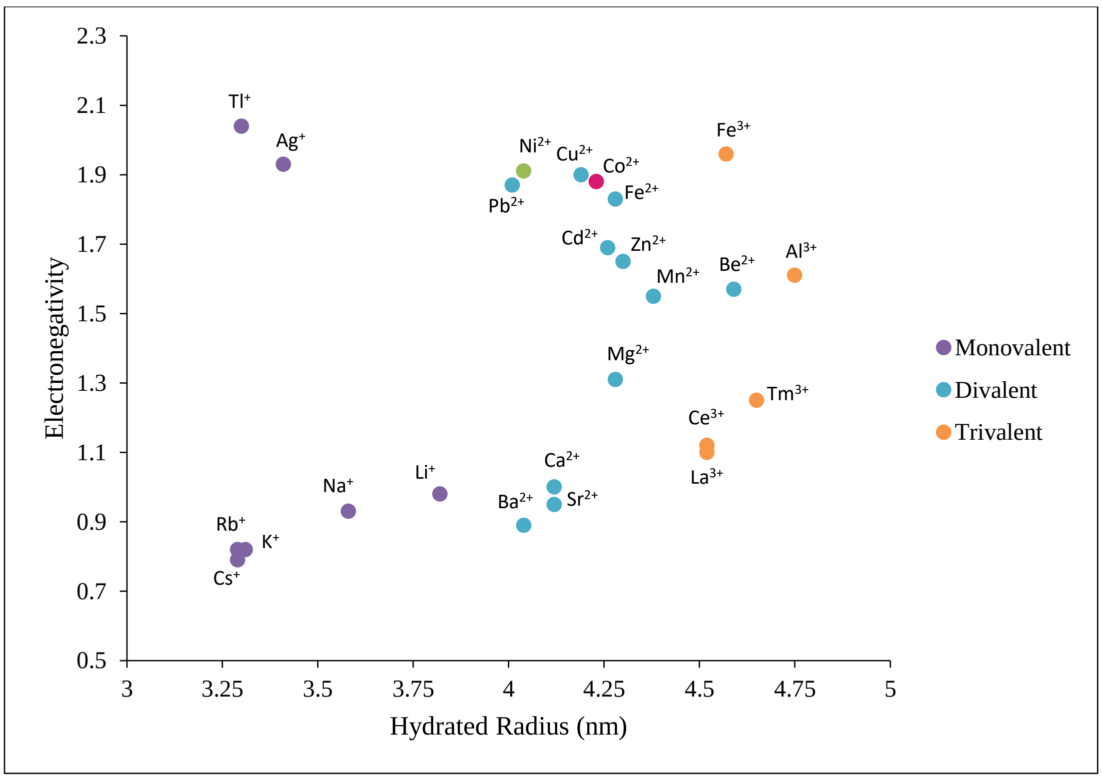

Figure 2. Metal ions plotted according to their hydrated radius (42) and electronegativity (43).

It is apparent that Ni^{2+} ions are relatively small and strongly electronegative compared to most other divalent ions, and that Co^{2+} is very similar to other biologically-relevant ions such as Cu^{2+} and Fe^{2+}. These properties may allow them to bind many important biomolecules.

The effects of Co^{2+} and Ni^{2+} in the human body share some similarities with other metals, but also cause unique effects. Co^{2+} and Ni^{2+} are redox-active metals which are known to produce general oxidative stress in the cell, similarly to many other metals (44, 45). The mechanism of oxidative stress is potentially due to the formation of hydroxyl radicals via Fenton-like chemistry of Co^{2+} and Ni^{2+} ions themselves (44, 46), but may also be due to the substitution for, and release of, highly redox-active metals such as Fe^{2+}, Cu^{2+}, or Cr^{3+} within proteins (3, 23, 39).

$$M^{(n+1)+} + O_2^{\cdot-} \rightarrow M^{n+} + O_2$$

$$M^{n+} + H_2O_2 \rightarrow M^{(n+1)+} + {}^{\cdot}OH + OH^-$$

Figure 3. Scheme for production of hydroxyl radicals via Fenton-like chemistry, in which M may be Co, Ni, Fe, Cu, Cr (44, 45).

Hydroxyl radicals may then go on to cause non-specific damage to many biomolecules including: DNA, proteins, and lipids (44, 47–49). Lipid peroxidation is initiated by hydrogen abstraction by hydroxyl radicals, which generally occurs on hydrogens adjacent to double bonds in acyl chains (50). Thus, polyunsaturated acyl chains are particularly susceptible to lipid peroxidation (50).

On the other hand, an interaction which appears to be specific to Co^{2+} and Ni^{2+} is the induction of the hypoxic stress response pathway, stimulating red blood cell production (51). This appears to be due to activation of the HIF-1 transcription factor, potentially in an Fe^{2+}-dependent oxidative stress mechanism (51, 52).

There may be many underlying mechanisms of carcinogenesis/genotoxicity, but it has been found that Co^{2+} and Ni^{2+} both cause oxidative damage to DNA (53, 54), as well as inhibition of DNA repair systems (55, 56). Ni^{2+} treatment has also been found to enhance overall DNA methylation, and thus gene silencing, despite its ability to inhibit cytosine 5-methyltransferase (57). In a study with human lung epithelial cells, Ni^{2+} was found to induce rapid apoptosis, whereas Co^{2+} was highly tolerated and accumulated by the cells (58).

1.3 Introduction to Lipid Membranes

1.3.1 Lipid structural considerations

While there has been more study devoted to interactions of metals with DNA and proteins, there is less understanding of the interactions and effects of metals with lipid membranes. The lipid membrane bilayer constitutes the cellular or organellar barrier to the outside environment, and should thus be considered, as toxic effects of metals may occur through changes to the properties and integrity of membranes. As well, the membrane is responsible for transport and signaling functions which may also be impaired by metals obstructing lipid accessibility or altering membrane composition. This thesis is primarily focused on the effects of Co^{2+} and Ni^{2+} on the relative fluidity of lipid membranes.

The main features of an amphipathic lipid molecule include a head group, backbone, and acyl chains, giving rise to great structural variability. The main classifications of lipids considered in this thesis include: phospholipids, sphingolipids, and sterols, as illustrated in Figure 4.

(A)

(B)

(C)

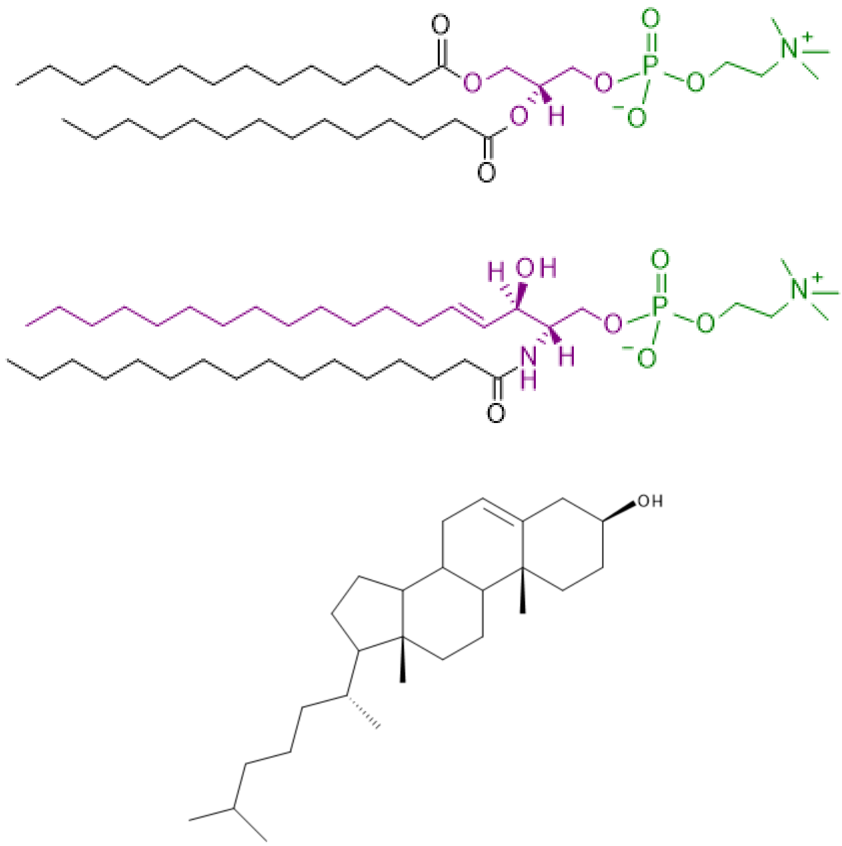

Figure 4. Representative structures of (A) phospholipids, (B) sphingolipids, and (C) sterols with head groups (green), backbones (purple), and acyl chains (black).

The classes of lipids discussed in this thesis are described in Table 1, having a variety of head groups as well as acyl chains, which are annotated according to the chain length (*l*), and number (*n*) and position (*x*) of double bonds as $l{:}n\ \Delta^{x}$. Lipid name abbreviations are given as acyl chains, followed by head group.

Table 1. Lipids considered in this study in terms of (A) acyl chains (B) and head groups.

A

Name	Structure	Abbreviation
Palmitoyl	16:0	P
Oleyl	$18{:}1\Delta^{9}$	O
Myristoyl	14:0	M
Stearoyl	18:0	S
Arachidonoyl	$20{:}4\ \Delta^{5,8,11,14}$	A

B

Negatively-charged	Zwitterionic	Neutral
Phosphatidic acid (PA)	Phosphatidylcholine (PC)	Cholesterol (Chol)
Phosphatidylglycerol (PG)	Phosphatidylethanolamine (PE)	Ergosterol (Ergo)
Phosphatidylserine (PS)	Sphingomyelin (SM)	Ceramide (Cera)
Phosphatidylinositol (PI)		Cerebroside (Cere)
Cardiolipin (CL)		Diacylglycerol (DAG)
		Triacylglycerol (TAG)

Zwitterionic phospholipids (PC, PE, SM) and sterols (Chol, Ergo) constitute the major structural components of biological membranes, while negatively-charged (PA, PS, PG, CL, PI) and other neutral lipids (Ceramide, Glycolipids, DAG, TAG, free fatty acids) constitute minor components (59–63). However, the presence and availability of these minor lipids are critical for many synthesis and signalling pathways, as well as protein regulation, often having unique roles in different cellular compartments (64–67). Mammalian lipids contain a variety of saturated, mono-, and polyunsaturated acyl chains, varying in prevalence with tissues and membrane type (68). As well, biological lipid bilayers have an asymmetric compositional distribution, such that some lipids are nearly exclusively localized to inner or outer leaflets (59, 69), which is maintained and modulated by specific lipid transport enzymes: flippases, floppases, and scramblases (70).

Lipid membranes exhibit phase behaviour, such that the relative fluidity and properties of the membrane changes with temperature, transitioning gradually from a relatively rigid “gel” phase to a fluid “liquid crystalline” phase (71, 72).

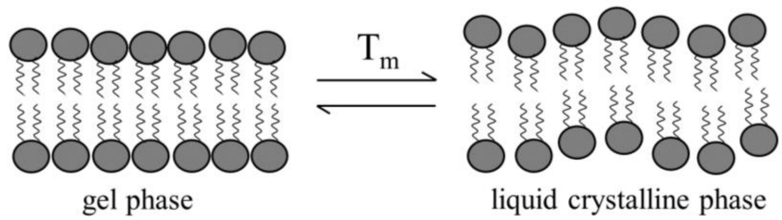

Figure 5. Schematic of lipid membrane phase transition. T_m represents the melting temperature.

The fluidity of membranes is also affected by local lipid composition and the surrounding environment (71), which includes ions in solution (73, 74).

1.3.2 Known interactions of Co^{2+} and Ni^{2+} with lipids

There has been some previous study on the direct binding interactions of Co^{2+} and Ni^{2+} with simple lipid membranes, finding that the interactions with zwitterionic lipids are weak in nature (75), while stronger electrostatic binding occurs with negatively-charged lipids such as PS and PG (76, 77), and that Co^{2+}, along with other metal ions, affects the transition temperature of tetra-palmitoyl cardiolipin (TPCL) (73). Additionally, it has been observed that Co^{2+} and Ni^{2+} stimulate iron-dependent lipid peroxidation *in vitro* under specific conditions (78, 79), which may be due to the ability of Co^{2+} and Ni^{2+} to bind and cluster lipids (80, 81). Co^{2+} on its own has also been found to be a very strong catalyst of linoleic acid (18:2) peroxidation (82). Previous studies have also reported direct lipid interactions of $CdCl^{+}/Cd^{2+}$ (83, 84), $HgCl_3^{-}/HgCl_4^{2-}$ (85),

Th^{3+} (86), Ca^{2+} (87, 88), $PbCl^{+}$/Pb^{2+} (89, 90), and Cu^{2+} (91), suggesting that lipids may indeed constitute a target for metal interactions.

1.4 Complex membranes

1.4.1 Commercial polar lipid extracts

In addition to interactions with simple lipid systems, it is interesting to consider complex models and lipid extracts to further characterize metal interactions in biologically-relevant systems. One set of complex membranes studied were polar lipid extracts of the brain, heart, liver, *S. cerevisiae*, and *E. coli*, which are commercially-available from Avanti Polar Lipids (Alabaster, AL), as these extracts are reproducible, and the composition is mostly defined. The polar extracts were expected to contain various ratios of potential lipid binding targets for Co^{2+} and Ni^{2+} (92–98). Compositions of these cells/tissues from experimental studies is given in Figure 6, demonstrating the large differences. The compositions of the commercially-available extracts from Avanti Polar Lipids themselves are presented in Ch 2.

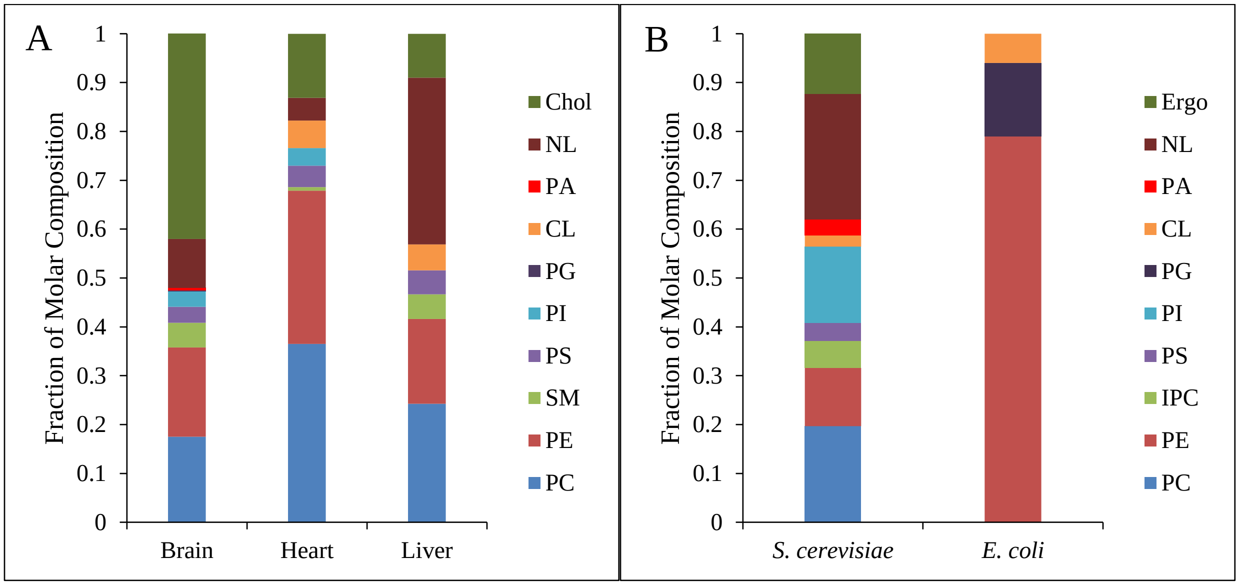

Figure 6. Average molar composition of (A) mammalian and (B) microbial lipid extracts experimentally-determined from: human brain by Chan *et al*. (2012) (92), rat heart by Homan and Anderson (1998) (93), human liver by Puri *et al.* (2007) (94), *S. cerevisiae* by Casanovas *et al.* (2015) (95) (at 24hrs), and *E. coli* by Morein *et al.* (1996) (98).

There are some clear differences in lipid composition. The brain and liver tissues appear similar, yet the brain extract is expected to be more rigid due to a high Chol content (61, 92, 94). The heart extract is expected to contain a large portion of CL and neutral lipid, likely a result of high mitochondrial content (93, 99, 100). The *S. cerevisiae* extract is expected to be strikingly enriched in PI lipids (95, 96), while the composition of *E.coli* extract is very simple, containing only PE, CL, and PG (98). One important consideration for this thesis is the overall amount of negatively-charged lipid present. The brain, heart, and liver tissues are expected to contain low amounts of around 7% (92), 14% (93), and 10% (94), respectively, while *S. cerevisiae* and *E. coli* cells may contain much more, at 30% (95) and 21% (98), which would suggest much stronger interactions of Co^{2+} and Ni^{2+} with the microbial extracts. However, the identity of the negatively-charged lipids as well as the sterol and neutral lipid/phospholipid ratios are expected to play a large role in the interactions observed.

1.4.2 Lung surfactant

Another complex membrane considered was lung surfactant (LS), which is a lipid monolayer that coats the inner surface of the lungs, providing a semi-permeable barrier for gas exchange, as well as modulating responses to foreign particles (63). The physical properties and lipid composition of LS are crucial to mediating its function (63), so a metal-induced disturbance would be expected to be detrimental. LS is a highly specialized monolayer, and differs greatly from cellular biomembranes, in that it is primarily a lipid monolayer containing fully-saturated DPPC and the only major occurrence of PG in mammalian systems (63, 101, 102). The phospholipid species in LS are shown in Figure 7.

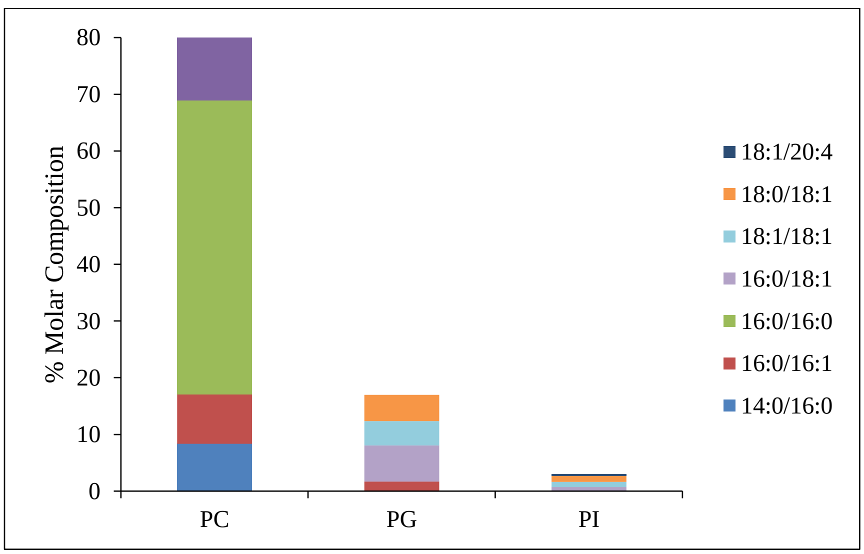

Figure 7. Distribution of human LS phospholipids according to a mass spectrometry study by Postle *et al*. (2001) (101). The composition presented here is simplified to show the four most prevalent acyl chain combinations per head group type.

In addition to the major phospholipids, human LS contains 5–10% (*wt/wt*) cholesterol, which is necessary for mediating its fluidity and function (103). The only proteins present in LS are referred to as Surfactant Proteins (SP) A, B, C, and D (63, 103).

In this thesis, Bovine Lipid Extract Surfactant (BLES Biochemicals Inc., London, ON) was used as a biological comparison with various synthetic models, as bovine lung surfactant is similar to human (101). LS was considered to be a particularly relevant target for Co^{2+} and Ni^{2+} given the damaging and specific effects of the metals on the lungs (4, 104, 105). It is currently not known whether Co^{2+} and Ni^{2+} are able to directly bind to and induce changes in LS. However, previous studies with rabbits have identified that exposure to Co^{2+},Ni^{2+}, or metallic Ni dust leads to overproduction of DPPC (105, 106), suggesting that the metals have at least an indirect effect on LS properties.

1.4.3 Red blood cells (RBCs)

Erythrocyte membranes were also considered as a potential target for toxicity, as solubilized Co^{2+} and Ni^{2+} are transported in the body via the bloodstream, potentially having direct interactions with RBCs (23, 36, 107). The RBC plasma membrane contains major phospholipids (59, 108) which are summarized in Figure 8, as well as Chol at 40–50% (109, 110). The vast majority of negatively-charged lipids are localized on the inner leaflet (111).

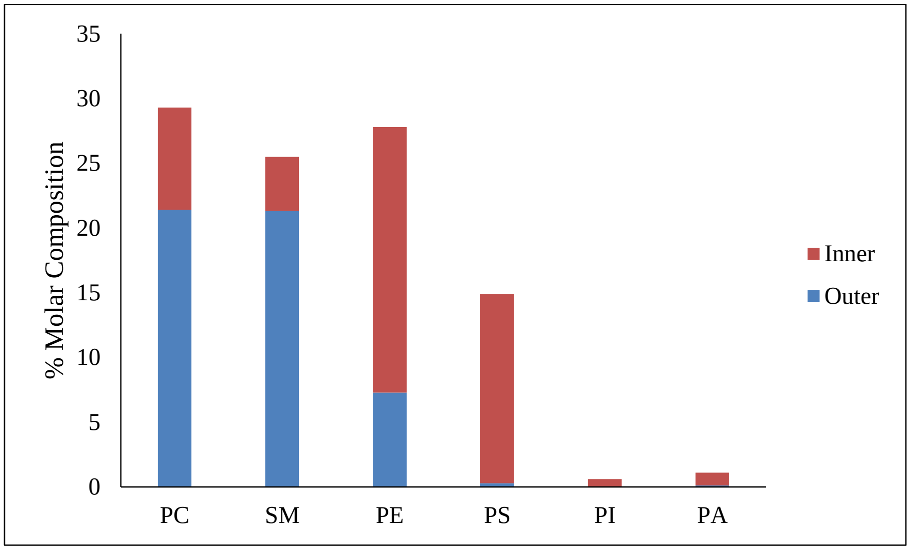

Figure 8. Average phospholipid composition of human RBCs according to a gas chromatography study by Dodge and Phillips (1967) (108). Inner and outer leaflet distributions are an average of those presented by Virtanen *et al.* (1998) (59) and Zachowski (1993) (111).

A previous study using a membrane fluidity dye called Laurdan found that, compared to other toxic and essential metal ions, Co^{2+} and Ni^{2+} caused the strongest relative rigidification of human RBC membranes, with Co^{2+} having the apparently unique effect of rigidification prior to the addition of an ionophore (112). This suggests that Co^{2+} binds uniquely strongly to the outer leaflet of the membrane or crosses the membrane on its own. As well, it has been observed that Co^{2+} and Ni^{2+} are able to induce changes in RBC shape (112), including Ni^{2+}-induced echinocyte formation (113). However, in a complex system it should be considered there are many other binding partners present in the whole blood and inside the cell, as it has been found that Co^{2+} uptake into RBCs is essentially irreversible, suggesting binding to intracellular components (36). Therefore, in this thesis, competition for binding to the membrane was assessed in the presence of low concentrations of glutathione (GSH) and bovine serum albumin (BSA). Rabbit blood was used for experiments, though it should be noted that human and rabbit RBCs are not compositionally-identical, but rather rabbit RBCs have been found to contain ~5% less SM and slightly more PC/PE (114).

1.5 Toxicity Testing with *S. cerevisiae*

1.5.1 Yeast as a model organism

The eukaryotic organism *Saccharomyces cerevisiae* (Baker's yeast) is a very common model organism which has been used extensively for various growth and drug testing studies. *S. cerevisiae* was employed in this project for: growth, viability, and respiration assays, live-cell imaging, lipid extractions, and mitochondria isolation. *S. cerevisiae* has been previously used in many studies regarding metal toxicity (115–117), providing a convenient and comparable system for understanding how Co^{2+} and Ni^{2+} affect live cells.

The primary means by which wild-type *S. cerevisiae* generates energy is through glycolysis coupled to alcoholic fermentation (118). Unless otherwise compromised, *S. cerevisiae* maintains the ability to utilize oxidative phosphorylation, but with a fermentable carbon source such as glucose, this pathway is used secondly to fermentation (118). However, growth media containing a non-fermentable carbon source such as glycerol or ethanol (119) forces cells to respire and grow more slowly. The laboratory strain BY4741 was used for most of this thesis, as it represents a common, haploid, wild-type strain.

A drawback to using yeast for toxicity studies is mainly in terms of direct comparison to human cells; yeast are single-celled organisms which contain a cell wall, preferentially utilize fermentation, and contain different genes and regulatory systems (120). Thus, any conclusions from the present study should likely not be fully extended to explain toxic effects in humans.

However, the manipulability of *S. cerevisiae* and eukaryotic cell structure makes it a very useful and economic system for screening and identifying potential *in vivo* targets.

1.5.2 Essentiality and toxicity of Co and Ni to S. cerevisiae

Co^{2+} and Ni^{2+} are both part of the metallome of *S. cerevisiae*, though their molecular functions are still not well-understood (121). It is known that excess Co^{2+} or Ni^{2+} cause inhibition of growth and possibly cell death, the exact characteristics of which strongly depend on growth conditions and cell strains (115, 116, 122). Previous studies have reported varying values for Co^{2+} and Ni^{2+} toxicity, with sublethal or inhibitory concentrations ranging from 0.1–3 mM (115–117, 122–130). The detoxification of excess Co^{2+} and Ni^{2+} is thought to mainly occur in the vacuole (121, 131), but other details of their cellular interactions in yeast as well as humans are unclear.

1.5.3 Mitochondria as a metal target in live cells

Mitochondria may constitute a target of Co^{2+} and Ni^{2+} in live cells as they, along with other metals, have been found to trigger the opening of the mitochondrial permeability transition pore (MPTP), likely a result of oxidative stress (132–135). As mitochondria are a natural center of oxidative stress in the cell, mitochondrial membranes were considered as potentially vulnerable to redox-active metal exposure (81, 136). As mentioned previously, the preferential utilization of the fermentation pathway by *S. cerevisiae* means that cells can survive under fermenting conditions with non-functional mitochondria, becoming the designation "petite" (137). Previous studies with Co^{2+} and Ni^{2+} have shown that these metals do cause respiratory deficiency in yeast (138, 139), and that Co^{2+} accumulates in the mitochondrial matrix (140) but whether this is specifically implicated in toxicity, and the mode by which it occurs, is currently unknown.

1.5.4 Lipid metabolism and membrane regulation in S. cerevisiae

The lipid metabolic network in *S. cerevisiae* is regulated similarly to humans, but yeast are much more adaptable in their lipid composition (141), and may thus be able to better manage metal stress. Thus, in addition to direct lipid-metal interactions, it was important to consider the indirect effects of Co^{2+} and Ni^{2+} on membrane properties in terms of metal-induced changes to lipid composition in live cells. Like in mammalian cells, the general composition of yeast membranes differs by cellular compartment, though yeast contain ergosterol (Ergo) as the main sterol lipid (141, 142), which has been reported at a 12–50% molar composition (95, 96, 143, 144). Yeast also contain unique inositol phosphorylceramide (IPC) sphingolipids which contain a PI head group and may be glycosylated (95, 96). The main phospholipids in yeast organelles are summarized in Figure 9, again reflecting the relatively high PI content, as mentioned previously (95, 96).

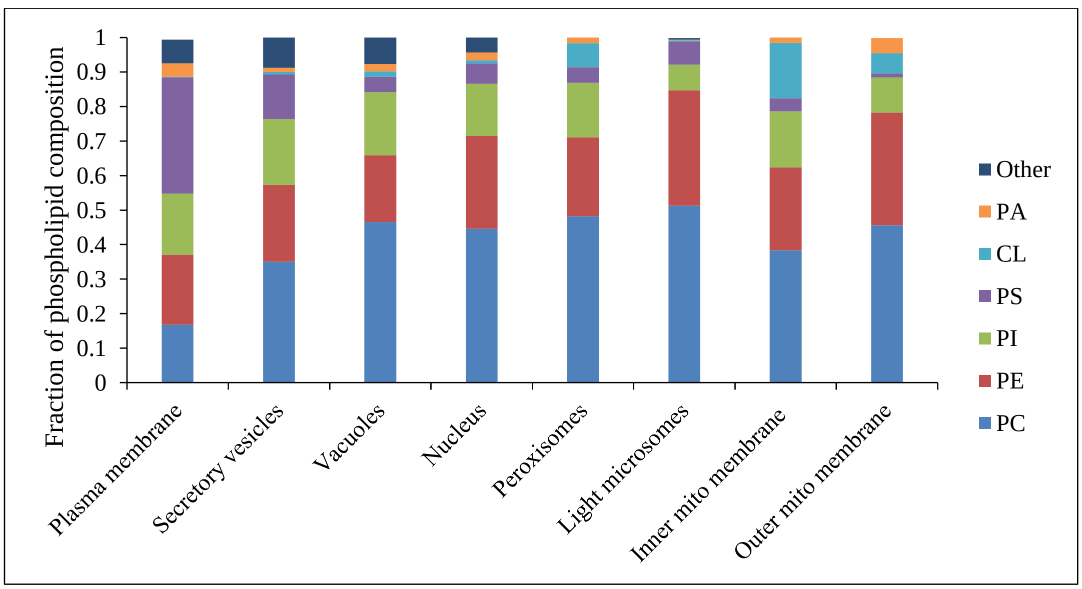

Figure 9. Distribution of phospholipids in subcellular structures of *S. cerevisiae* according to a quantitative TLC study by Zinser *et al.* (1991) (142).

A unique feature in yeast is that nearly all fatty acid chains are composed of 16 or 18 carbons, with one or no double bonds (141). Yeast also contain lipid droplets, which serve as pools of mainly sterol esters (SE) and triacylglycerols (TAG) (145). A previous study found that exposure of *S. cerevisiae* to Co^{2+} resulted in a decrease in sterols and unsaturated fatty acids, while Ni^{2+} also induced a decrease in unsaturated fatty acids, though with much lower efficiency (146). Thus, the metals may have an indirect effect on membranes by affecting lipid metabolism.

1.6 Project Goals and Hypothesis

In summary, the purpose of this thesis was a biophysical investigation of the interactions and effects of Co^{2+} and Ni^{2+} with simple lipid membranes as well as the potential consequences of interaction with complex biomembranes and cells, relevant to Co^{2+} and Ni^{2+} toxicity. The investigation was divided into several sections:

1. Investigate the biophysical effects of Co^{2+} and Ni^{2+} on simple lipid systems in terms of their impact on: membrane fluidity (using Laurdan fluorescence), vesicle size (using DLS), and binding affinity (using Calcein for metal detection) to determine individual lipid targets.
2. Investigate the biophysical effects of Co^{2+} and Ni^{2+} on complex biological models and lipid extracts to assess the relevance of metal-lipid interactions in mixed membranes.
    a. Polar lipid extracts
    b. Lung Surfactant (LS)
    c. Red Blood Cells (RBC)
3. Investigate the toxic or inhibitory effects of Co^{2+} and Ni^{2+} on *S. cerevisiae* cells in terms of their effects on: growth, viability, morphology, mitochondrial damage, and membrane

composition. This was done by using: growth curves and viability assays under various conditions, fluorescence live cell imaging, lipid extractions, and thin layer chromatography (TLC).

As mentioned, the speciation of $CoCl_2$ and $NiCl_2$ into divalent positive ions (32), suggested a preference for negatively-charged moieties. Based on previous studies with various metals and lipids, it was hypothesized that Co^{2+} and Ni^{2+} would selectively bind to and induce rigidity in membranes with negatively-charged lipids (76, 83, 112). It was expected that similar effects would carry on into complex membranes, yet be diminished due to the fact that negatively-charged lipids constitute a relatively small portion of biomembranes (59–61, 63), and that any proteins present may be a metal-binding sink (147). It was hypothesized that the experiments with *S. cerevisiae* would demonstrate that Co^{2+} and Ni^{2+} exposure results in mitochondrial damage (132, 133, 138), leading to growth inhibition and cell death, along with an alteration in lipid composition as a stress response to combat rigidification and lipid peroxidation (44).

Chapter Two: Materials, Methods, and Theory

2.1 Reagents

Pure lipid powders and polar lipid extracts were purchased from Avanti Polar Lipids (Alabaster, AL) including: 1-palmitoyl-2-oleoyl-*sn*-glycero-3-phosphocholine (POPC); 1,2-dimyristoyl-*sn*-glycero-3-phosphocholine (DMPC); 1,2-dipalmitoyl-*sn*-glycero-3-phosphocholine (DPPC); 1-myristoyl-2-palmitoyl-*sn*-glycero-3-phosphocholine (MPPC); 1-palmitoyl-2-oleoyl-*sn*-glycero-3-phosphoethanolamine (POPE); 1-palmitoyl-2-oleoyl-*sn*-glycero-3-phosphate (POPA); 1,2-dimyristoyl-*sn*-glycero-3-phosphate (DMPA); 1',3'-bis[1,2-dioleoyl-*sn*-glycero-3-phospho]-*sn*-glycerol (TOCL); 1',3'-bis[1,2-dimyristoyl-*sn*-glycero-3-phospho]-*sn*-glycerol (TMCL); 1-palmitoyl-2-oleoyl-*sn*-glycero-3-phospho-(1'-*rac*-glycerol) (POPG); 1,2-dimyristoyl-*sn*-glycero-3-phospho-(1'-rac-glycerol) (DMPG); 1,2-dipalmitoyl-*sn*-glycero-3-phospho-(1'-*rac*-glycerol) (DPPG); 1-stearoyl-2-oleoyl-*sn*-glycero-3-phospho-(1'-*rac*-glycerol) (SOPG); 1-palmitoyl-2-oleoyl-*sn*-glycero-3-phospho-L-serine (POPS); 1,2-dimyristoyl-*sn*-glycero-3-phospho-L-serine (DMPS); 1-stearoyl-2-arachidonoyl-*sn*-glycero-3-phosphoinositol (SAPI); N-palmitoyl-D-*erythro*-sphingosylphosphorylcholine (Palmitoyl-SM); Egg SM (Chicken); Brain SM (Porcine); N-palmitoyl-D-*erythro*-sphingosine (16:0 Ceramide); D-glucosyl-ß-1,1'-N-palmitoyl-D-erythro-sphingosine (Glucosyl ceramide); Total Brain Cerebroside (Porcine); (3β)-cholest-5-en-3-ol (Cholesterol, Ovine); cholest-5-en-3ß-yl nonadecanoate (19:0 Cholesteryl Ester); ergosta-5,7,9(11),22-tetraen-3ß-ol (Dehydroergosterol); 1-2-dioleoyl-*sn*-glycerol (18:1 DAG); 1,2,3-tri-(9Z-octadecenoyl)-glycerol (18:1 TAG/Triolein); Brain Polar Extract (Bovine); Liver Polar Extract (Bovine); Heart Polar Extract (Bovine); Yeast Polar Extract (*S. cerevisiae*); and *E. coli* Polar Extract.

Laurdan (6-Dodecanoyl-2-Dimethylaminonaphthalene), Calcein (Fluorescein-bis(methyliminodiacetic acid)), MitoTracker Green-FM, and MitoSOX Red Mitochondrial Superoxide Indicator were purchased from Molecular Probes (Eugene, OR). $NiCl_2$, Hepes (4-(2-hydroxyethyl)-1-piperazineethanesulfonic acid), Krebs-Ringer buffer, phosphate assay reagents ($Mg(NO_3)_2 \cdot 6H_2O$, Ascorbic acid, $(NH_4)_6Mo_7O_{24} \cdot 4H_2O$), reduced glutathione (GSH), and BSA were purchased from Sigma-Aldrich (Oakville, ON). $CoCl_2$ was purchased from Allied Chemical (Morristown, NJ). Yeast media components were purchased from MP Biomedicals (Santa Ana, CA), dextrose from EMD (Burlington, MA), glycerol and Triton X-100 from Fisher Scientific (Pittsburgh, PA).

2.1.1 Structures

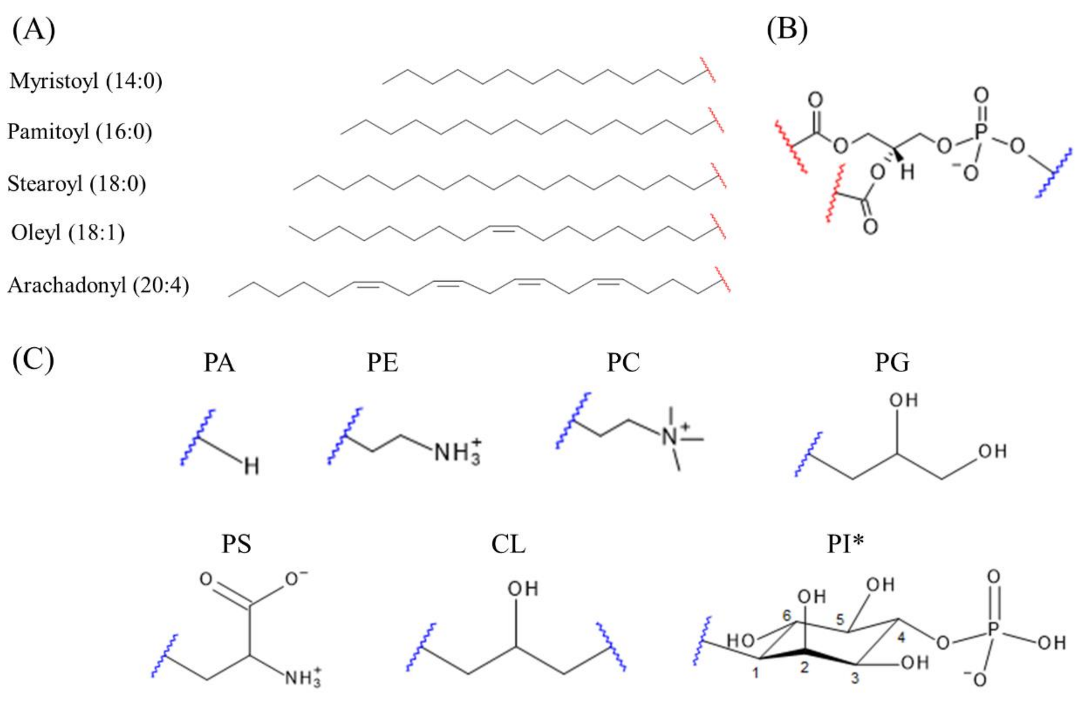

Figure 10. Summary of phospholipid structures referred to in this thesis, as combinations of: (A) acyl chains, (B) phosphoglycerolipid backbone, and (C) head groups. *PI lipids may be phosphorylated at any combination of positions: 3’, 4’, and 5’, or not at all.

(A)
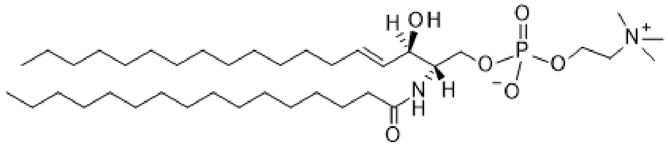

(B)
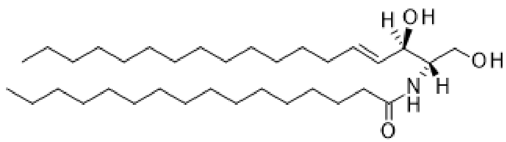

(C)
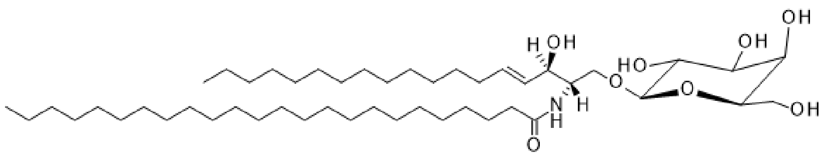

(D)
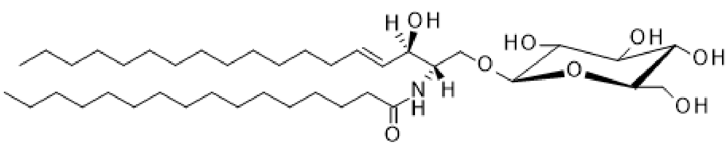

Figure 11. Summary of representative sphingolipid structures referred to in this thesis: (A) sphingomyelin, (B) 16:0 ceramide, (C) cerebroside, (D) 16:0 glucosyl-β-ceramide

(A)
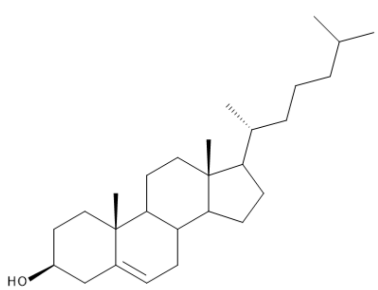

(B)
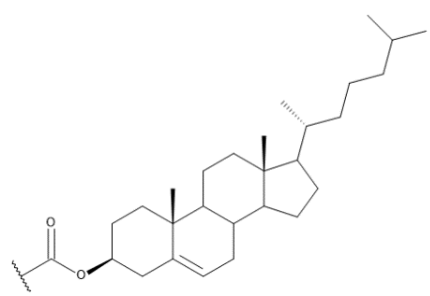

(C)
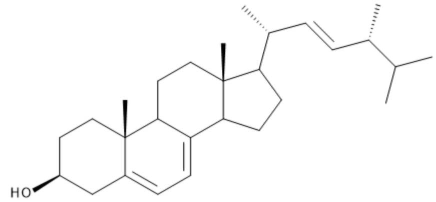

(D)
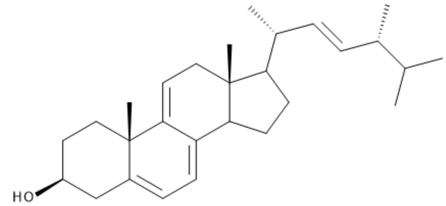

(E) 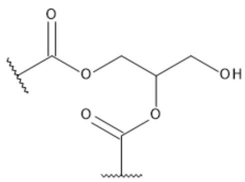 (F) 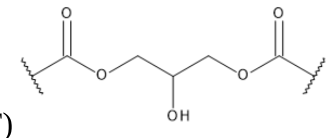 (G) 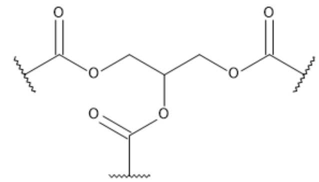

Figure 12. Summary of neutral lipids referred to in this thesis: (A) cholesterol, (B) cholesteryl esters, (C) ergosterol, (D) dehydroergosterol, (E) 1,2-diacylglycerol, (F) 1,3-diacylglycerol, (G) triacylglycerol.

(A) 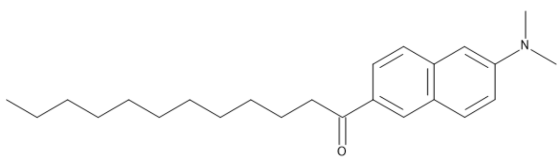 (B) 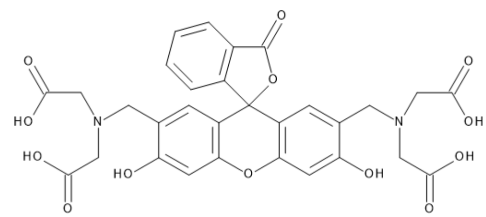

Figure 13. Structures of dyes used in this thesis. (A) Laurdan, (B) Calcein.

2.2 Vesicle Preparation

2.2.1 LUV Preparation

Lipid powders at defined molar ratios were dissolved in 7:3 (*v/v*) $CHCl_3$/methanol and sonicated to fully solubilize. As required, Laurdan in $CHCl_3$ was added to the film at a 1:275 Laurdan/lipid molar ratio (83, 148), which allowed for sufficient signal, as it was found that Co^{2+} and Ni^{2+} quenched the dye, decreasing the emission intensity, but the emission peak was not shifted (Appendix A). The solution was dried to a film under argon gas, followed by storage in a vacuum chamber overnight. Lipid films were hydrated in 20 mM Hepes, 100 mM NaCl buffer at pH 7.4 and removed from the glass by sonication, vortexing, and freeze-thaw cycles to form multilamellar vesicles (MLVs). Hepes buffer was used, as it has been previously-found to not complex Co^{2+} or Ni^{2+}, by use of isothermal titration calorimetry (ITC) (35). The MLV solution was passed 30 times through an extruder (Avanti Polar Lipids, Alabaster, AL) containing Whatman Nucleopore polycarbonate filters of 100 nm diameter (Maidstone, UK).

2.2.2 MLV Preparation

Alternatively, for preparation of washed MLVs for binding assays, the resuspended MLV solution was centrifuged at 21,000 g for 15 min in a ThermoIEC MicroMax (Fisher Scientific, Pittsburg, PA) which lead to formation of a visible MLV pellet. The supernatant was removed and replaced with fresh buffer to remove any LUVs or lipid fragments formed during sonication and freeze-thaw. The pellet was resuspended by gentle pipette mixing.

2.2.3 Phospholipid concentration: Ames assay

In order to determine phospholipid concentration following LUV or MLV preparation, the procedure of Ames (149) was followed, which is based on the colorimetric determination of a phosphomolybdate complex. 5 µL of samples were pipetted onto the bottom surface of glass test tubes in triplicate. 20 mM Hepes, 100 mM NaCl buffer at pH 7.4 was used as the negative control, and 2 mM phosphate as the positive control. To these tubes 30 µL of 10% $Mg(NO_3)_2$ in 95% ethanol were added and ashed over a Bunsen burner until all the ethanol evaporated and a white film formed in the tube. 300 µL of 0.5 M HCl was added to each tube followed by vortexing to dissolve the white coating. The tubes were capped with tin foil and boiled on a hot plate for 15 min. During this step, $Mg(NO_3)_2$ and HCl cleave phosphate from phospholipids. Following boiling, 0.6 mL of 0.42% ammonium molybdate in 1M H_2SO_4 and 100 µL of 10% ascorbic acid in ddH_2O were added to each tube. The tubes were vortexed and then incubated at 37°C for 1 hour in an Isotemp 500 incubator (Fisher Scientific, Pittsburgh, PA). The resulting blue colour of the phosphomolybdate complex was measured at 820 nm on a Shimadzu UV-1700 UV-VIS Spectrophotometer (Shimadzu Corporation, Kyoto, Japan). The absorbance of the negative control is subtracted from the positive and sample absorbances. The positive controls are used to create a linear standard curve that is used to quantify the samples.

2.3 Experiments with LUVs

2.3.1 Laurdan theory

Laurdan is a polarity-sensitive fluorescent probe which spontaneously incorporates into lipid bilayers based on its amphipathic structure (Figure 13A) (150). The fluorescence of Laurdan is due to the formation of a partial charge separation across the naphthalene moiety in the excited state (150). The emission peak of Laurdan depends on the environment polarity, as energy is lost to reorientation of solvent molecules around the excited state in increasingly polar solvents (150). Thus, the emission peak of Laurdan in a lipid bilayer shifts from 440 nm in the gel phase to 490 nm in the liquid crystalline phase as water accessibility is increased (150). The ratio of intensities between these peaks provides a useful parameter to assess the relative rigidity of a membrane, referred to as Generalized Polarization (GP) (Equation 1).

$$GP = \frac{I_{440\ nm} - I_{490\ nm}}{I_{440\ nm} + I_{490\ nm}}$$

Equation 1. Formula for generalized polarization (GP).

Membranes that are relatively rigid have a higher GP value, while membranes that are more fluid have a lower GP value (150). A schematic diagram showing the relationship between Laurdan and membrane fluidity is shown in Figure 14:

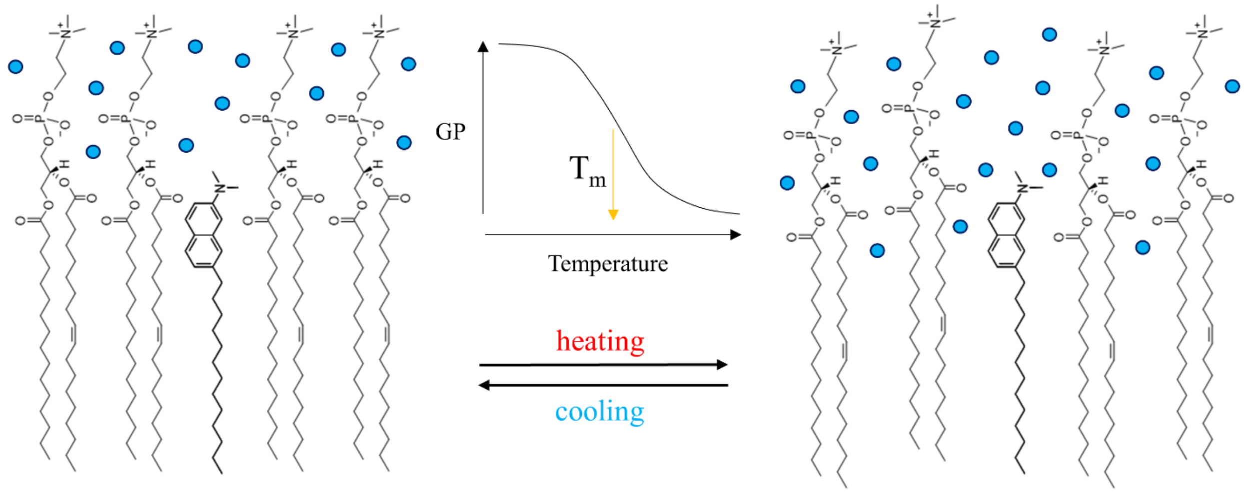

Figure 14. Schematic of Laurdan in a POPC membrane in the gel phase (left) or the liquid crystalline phase (right). Blue circles represent water molecules. The melting curve shows how GP changes with membrane melting.

2.3.2 Laurdan fluorescence measurements

A Cary Eclipse fluorimeter (Agilent Technologies, Santa Clara, CA) was used to measure Laurdan fluorescence by excitation at 340 nm. Emission was measured at 440 nm and 490 nm, with slit widths of 5 nm, recording the average of 4 measurements each for triplicate samples. LUVs at 0.3 mM and various concentrations of $CoCl_2$ or $NiCl_2$ were combined in small volume quartz cuvettes (Starna Scientific Ltd, Atascadero, CA) at room temperature. The fluorimeter sample holder temperature was maintained by a Cary water bath temperature controller (Agilent Technologies, Santa Clara, CA). Fluorescence measurements were recorded between 10 and 60°C, depending on the membrane T_m, but always passing through physiological temperature at 37°C. For each 1°C increase in temperature, the samples were allowed to equilibrate for 1 min. As applicable, OriginPro 8 software (151) was used to determine the T_m's by fitting GP curves to the Boltzmann function (Equation 2). The initial and final temperature values are denoted by A_1 and A_2, with x_0 representing the T_m at the inflection point.

$$Y = A_2 + \frac{A_1 - A_2}{1 + exp^{\frac{(x - x_0)}{dx}}}$$

Equation 2. Boltzmann function used to fit GP curves.

2.3.3 Dynamic light scattering (DLS) size measurements

A Zetasizer Nano-ZS instrument (Malvern, Worcestershire, UK) was used to measure mean liposome radius. 0.3 mM LUVs were incubated for at least 15 minutes at room temperature with various concentrations of $CoCl_2$ or $NiCl_2$, and triplicate measurements were averaged.

2.3.4 Dynamic light scattering (DLS) phase transition

The membrane phase transitions of select lipid systems were determined by DLS, as scattering properties of the membrane change with melting (152), to further validate the results with Laurdan (Appendix A). 0.3 mM LUVs with various concentrations of $CoCl_2$ or $NiCl_2$ were added to small volume quartz cuvettes (Starna Scientific Ltd, Atascadero, CA). Using the Size-Temperature Trend protocol, the derived count rate was recorded as the average of 3 measurements per 1°C increase to construct a melting curve.

2.3.5 Zeta potential measurements

The zeta potential refers to the potential which develops around a charged entity at the interface of the associated ions and bulk solution, dependent upon the intrinsic charge and the attraction to the surrounding solution (153). It can be used as an estimate of relative surface charge and stability of suspensions (154). The Zetasizer Nano-ZS instrument (Malvern, Worcestershire, UK) was used to measure zeta potential of select samples at 0.3 mM lipid. The derived zeta potential was recorded as the average of at least 100 runs of 4 measurements (5 V applied) in triplicate.

2.4 Experiments with Calcein

2.4.1 Using calcein for detection of Co^{2+} and Ni^{2+}

The dye Calcein is a well-known membrane-impermeant Ca^{2+} indicator (155) but is also extensively used in liposome fusion/leakage assays due to its self-quenching properties at high concentrations (156). The fluorescence of Calcein is also strongly quenched by Co^{2+} and Ni^{2+}in a 1:1 stoichiometry (157), thus proceeding to completion when metal is slightly in excess. Experimentally, both Co^{2+} and Ni^{2+} were found to be very effective quenchers of Calcein; while the interaction with Co^{2+} proceeds to completion almost immediately, Ni^{2+} quenches at a substantial, but slower rate over 1 hour (Appendix A).

2.4.2 Calcein permeability assays

In contrast to typical liposome permeability assays which encapsulate self-quenching concentrations of Calcein (156), this thesis used a low encapsulated concentration which could therefore be noticeably quenched by Co^{2+} or Ni^{2+} (157) upon dye release or metal entry into the liposome (Figure 15).

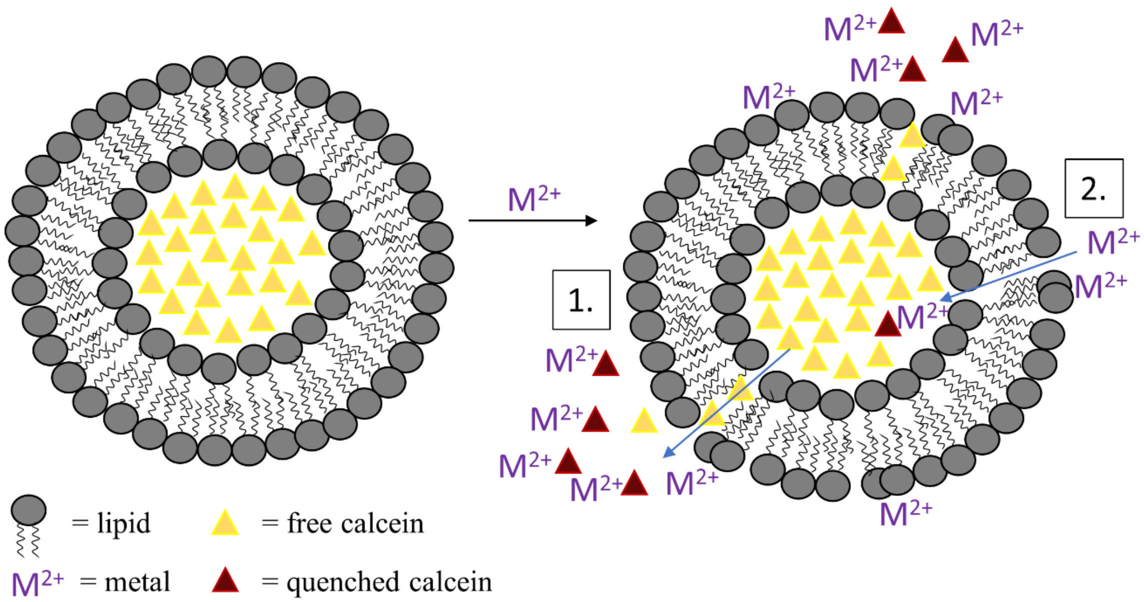

Figure 15. Schematic for the adapted Calcein permeability assay, with liposomes containing fluorescent Calcein. The addition of metal (M^{2+}) may lead to the quenching of Calcein by: 1) release of the dye into bulk solution, or 2) permeation of metal into the encapsulated volume.

Select lipid films were prepared and rehydrated in 20 mM Hepes, 100 mM NaCl pH 7.4 containing 0.6 mM Calcein, and extruded to form LUVs. The approximate concentration of encapsulated Calcein was 130 nM, a non-self-quenching concentration. The LUVs were then separated from free Calcein by passage through a Sephadex G-25 column (GE Healthcare, Mississauga, ON) calibrated with blue dextran (Sigma Aldrich, Oakville, ON) and the phospholipid concentration was determined as in Section 2.2.3. 0.15 mM LUVs were prepared in small volume quartz cuvettes (Starna Scientific Ltd, Atascadero, CA). Calcein fluorescence was measured by excitation at 495 nm and emission at 514 nm with slit widths of 5 nm. Injections of 5 µL of buffer/5 mM metal were made every 2 minutes and fluorescence was monitored continuously over 20 injections. 0.002% Triton was added at the end to release remaining encapsulated Calcein and allow for total quenching by Co^{2+} and Ni^{2+} to confirm that Calcein-encapsulated liposomes were formed properly.

For each injection, intensities were averaged over 2 min equilibration periods and converted to stepwise percentage decreases. The equation for percent release is determined from the intensity upon injection (I_x) and initial intensity (I_i) (Equation 3). The term for the fully-quenched Calcein baseline was taken as the low background signal for a blank sample (I_N).

$$\%\ Release = \frac{I_x - I_N}{I_i - I_N}$$

Equation 3. Formula for percent release of encapsulated Calcein from liposomes.

Significant difference is determined from the slopes of the resulting curves compared to the buffer control, which simply represents dilution/ photobleaching effects.

2.4.3 Calcein-metal quenching standard curves

Standard curves for Co^{2+} and Ni^{2+} determination using Calcein quenching used 0.3 µM Calcein in UV-plastic cuvettes to a volume of 2.5 mL in 20 mM Hepes, 100 mM NaCl buffer at pH 7.4. The linear range for metal response under these conditions was 20–125 nM for both $CoCl_2$ and $NiCl_2$. Following metal addition, the samples were pipette-mixed and incubated at room temperature in the dark for 1 hour, to ensure intensities had equilibrated (Appendix A). A Cary Eclipse fluorimeter (Agilent Technologies, Santa Clara, CA) was used to measure Calcein fluorescence by excitation at 495 nm, emission at 514 nm, and slit widths of 5 nm.

2.4.4 MLV centrifugation and binding assay

50 µM MLVs were added to 1.5 mL Eppendorf tubes along with various concentrations of $CoCl_2$ or $NiCl_2$ in the range of 5–250 µM. The samples were gently vortexed for 4 seconds to

mix, then incubated at 37°C for 15 min in an Isotemp 145D Dry Bath (Fisher Scientific, Pittsburg, PA). The samples were then centrifuged at 21,000 g for 10 min in a ThermoIEC MicroMax (Fisher Scientific, Pittsburg, PA). The supernatants, or a dilution, were added to a 2.5 mL total volume containing 0.3 µM Calcein, such that the signal fell within a range corresponding to 20–125 nM metal. The fraction of metal bound to the MLVs at each concentration point was calculated from the standard curves based on the quenching of Calcein by the remaining metal in the supernatant.

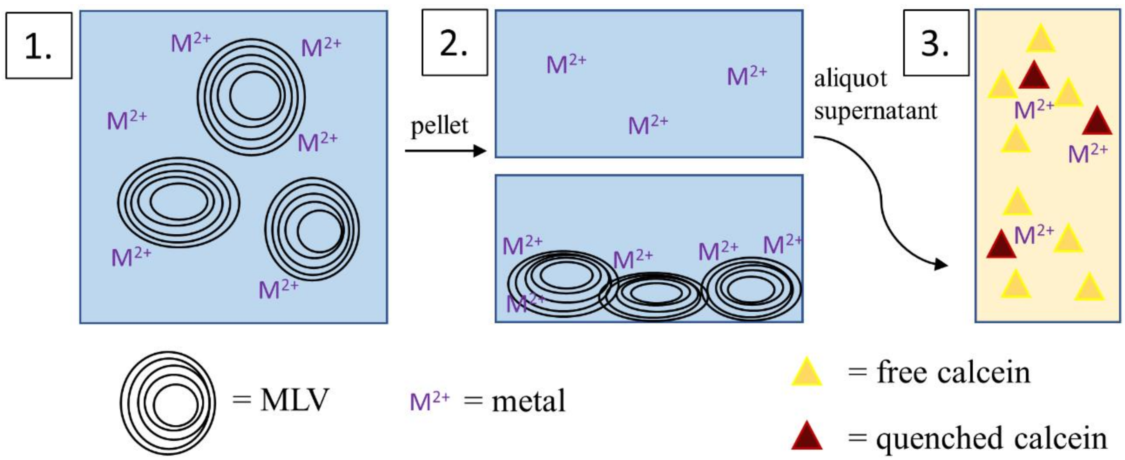

Figure 16. Schematic diagram of MLV centrifugation binding assay. 1) MLVs are incubated with metal, 2) MLVs and bound metal are pelleted by centrifugation, and 3) remaining metal is determined by Calcein quenching.

Binding curves were analyzed by constructing Scatchard plots to estimate the binding constants and cooperativity (158, 159).

2.5 Complex biomimetics and extracts

2.5.1 Polar lipid extracts (Avanti)

Polar lipid extracts commercially available from Avanti Polar Lipids (Alabaster, AL) were used to make LUVs (Section 2.2.1). The compositions of the extracts are provided on the Avanti Polar Lipids website as % wt/wt lipid. A conversion to molar percentages using approximate molecular weights yields these rough molar compositions (Figure 17):

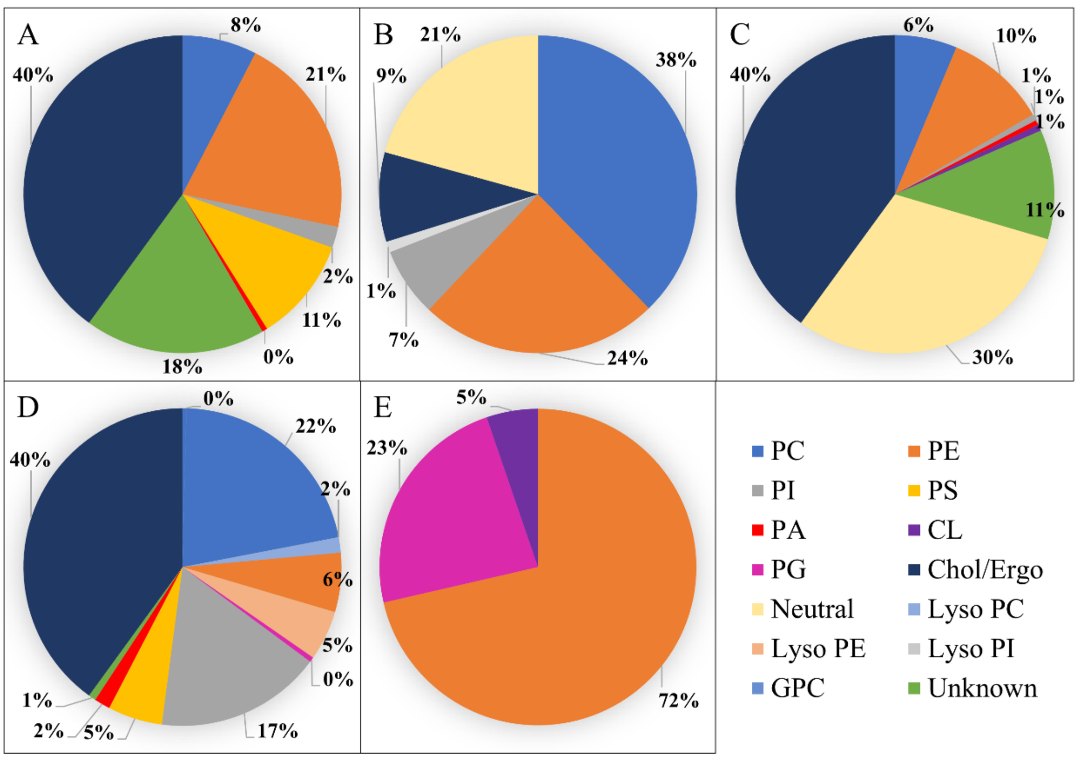

Figure 17. Approximate conversion to molar % composition of (A) Brain polar extract (bovine), (B) Liver polar extract (bovine), (C) Heart polar extract (bovine), (D) *S. cerevisiae* polar extract, and (E) *E. coli* polar extract from Avanti Polar Lipids.

These molar compositions do not necessarily reflect the true ratios, as in cases in which Chol/Ergo content was not stated, it was assumed to be 40% (60, 61, 143).

2.5.2 Lipid peroxidation and extraction

Lipid oxidation was performed by incubating 1 mg/mL of lipid in 20 mM Tris pH 7.4, 0.15 mM NaCl, 1.45 mM $CaCl_2$, 0.63 mM EDTA, 29 mM H_2O_2, and 0.65 mM metal (Fe^{2+}/Co^{2+}/Ni^{2+}alone or in mixtures) for 24 hrs at 37°C shaking at 180 rpm in an Excella E24 Incubator Shaker (Eppendorf, Mississauga, ON) (160). For each type of metal treatment, a separate lipid film and incubation buffer was made to ensure that, upon rehydration, the metal/H_2O_2/EDTA ratio was maintained in every compartment within the MLV structure. After the 24-hr incubation, lipid samples were transferred to screw-capped glass test tubes and recovered by organic extraction. 1 mL of 7:3 (*v/v*) $CHCl_3$/methanol was added to each sample and mixed by vortexing and sonication. The phases were separated by centrifugation at 2500 rpm for 10 min at 4°C in a Sorvall Legend X1R Centrifuge, as shown in Figure 18.

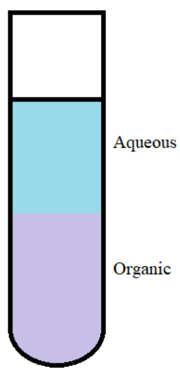

Figure 18. Schematic of organic and aqueous phase separation in lipid extractions.

The aqueous phase was pipetted off and transferred to a new glass tube, while the organic phase containing lipid was collected with a 1 mL Hamilton syringe and transferred to another tube. The aqueous phase was extracted a second time following the same procedure. The combined organic phases were then dried under argon. Lipid oxidation was monitored by TLC, as will be detailed in Section 2.6.

2.5.3 Lung surfactant mimics and BLES

Lung surfactant mimics were prepared with various compositions to determine how the presence or absence of certain lipid components affect the interactions of Co^{2+} and Ni^{2+}. An initial model was roughly based on a composition presented in a review, as exact lipid species were not discussed (63):

Table 2. Molar composition of Lung Surfactant Mimic 1 (LSM1) (63).

Component	Percent (%)
DPPC	55.6
POPC	18.9
POPG	7.8
POPE	4.4
SAPI	2.2
SM	2.2
POPS	3.3
Chol	5.6

A revised set of mimics were prepared according to a mass spectrometry study, maintaining negatively-charged lipid at a 20% molar ratio in each model (101).

Table 3. Molar composition of revised Lung Surfactant Mimics (101).

Component	LSM 2	LSM 3	LSM 4
DPPC	67.9	59.8	67.9
POPC	12.1	10.6	12.1
POPG	17.1	10.5	14.6
DPPG	2.9	1.8	2.4
MPPC	-	9.6	-
SOPG	-	7.7	-
SAPI	-	-	2.0
POPS	-	-	1.0
Chol*	5	5	5

*Chol was added to lipid films as 5% wt/wt (103).

The LSM 2 model was the simplest of the models, only containing the major PC and PG species, and cholesterol. The LSM 3 model incorporated different acyl chains for PC and PG to investigate the effects of a more complex packing arrangement on metal interaction. The LSM 4 model replaced 3% of the negative charge of PG with PI and PS to determine if the minor presence of strong binding targets affects metal interaction.

A 27 mg/mL sample of BLES (Bovine Lipid Extract Surfactant) from BLES Biochemicals Inc. (London, ON) was prepared into a film by Dr. Patrick Lai according to a previously described procedure (103). A portion of the BLES film was dissolved in 7:3 (*v/v*) $CHCl_3$/methanol and aliquoted into tubes for an Ames assay (Section 2.2.3). The $CHCl_3$ was left to evaporate overnight to avoid any possible interference with the assay. 5% wt/wt Chol was added to the BLES film (103). BLES differs from the mimics in its lipid complexity as well as the presence of hydrophobic lung surfactant proteins SP-B and SP-C (161). The phospholipid composition of BLES, as stated in the product monograph, is largely PC- and PG-based, with minor amounts of other lipids (Table 4) (162).

Table 4. Molar composition of BLES according to the product monograph (162).

Component	Percent Range (%)
PC	75-85
PG	12-17
PE	1-5
PI	0-2
PS	0-2
SM	0-5
Lyso-PC	0-2.5
Lyso-bis-PA	0-2.4

2.5.4 Microscopy of RBCs

Rabbit blood cells were collected by centrifugation in a Sorvall Legend X1R Centrifuge at 1600 rpm for 10 min at 4°C and resuspended in Krebs-Ringer buffer with 1.26 g/L sodium bicarbonate at pH 7.4 (3 mL per 6 mL initial). Cells were washed 4x in Krebs-Ringer buffer and then diluted to A_{280} 4.0. Cells were incubated at 37°C with 1 mM Co^{2+} and Ni^{2+}. 5 µL of cells at a given time point was pipetted onto a 3 x 1" glass slide and covered with a 0.15 mm cover slip (Fisher Scientific, Pittsburgh, PA). Cells were visualized using a Motic BA 200 Microscope (Motic, Richmond, BC) and images collected using Motic Images Plus 2.0 software.

2.5.5 RBC absorbance assay

Rabbit blood cells in Krebs-Ringer buffer at A_{280} 4.0 were incubated with 0.5–1 mM Co^{2+} and Ni^{2+} at 37°C for 8 hrs, alongside a positive control containing 1% Triton. After incubation, cells were collected by centrifugation at 10,000 g for 1 min in a ThermoIEC MicroMax (Fisher Scientific, Pittsburg, PA). The absorbance spectrum of the supernatant was measured from 250–650 nm on a Shimadzu UV-1700 UV-VIS Spectrophotometer (Shimadzu Corporation, Kyoto, Japan) using UV Probe 2.42 software.

2.5.6 RBC lipid extraction

Rabbit blood samples were frozen at -80°C for storage. The initial steps towards lipid extraction were performed using a protocol for isolation of red blood cell ghosts, which are intact membranes with retained lipid asymmetry and proteins (163). As the blood was frozen, ghosts could not be isolated, but the preliminary procedure was done in attempt to minimize protein contamination, which was found to be a problem in a previous extraction. Blood was thawed and split into 5 mL fractions in sodium heparin blood collection tubes (BD Vacutainer, NJ); 1 mL of Krebs-Ringer buffer with 1.26 g/L sodium bicarbonate at pH 7.4 was added to each. The samples were centrifuged in a Sorvall Legend X1R Centrifuge at 1600 rpm for 10 min at 4°C to pellet the RBCs. Likely because of membrane damage upon freezing, some of the tubes did not contain a visible pellet. 2 mL more of Krebs-Ringer buffer was added to each tube and centrifuged again. Again, only some of the tubes contained a pellet, while others were dark red throughout; thus the separation of red and white blood cells was unsuccessful. The supernatants and pellets were recovered into 40 mL high-speed centrifuge tubes and centrifuged at 20,000 g at 4°C for 40 min in a Sorvall RC SC Plus Centrifuge (Thermo Scientific, Ottawa, ON). A significant pellet was recovered from the supernatants. The supernatant was removed and 5 mM phosphate buffer at pH 7.4 was added at roughly 9:1 (*v/v*) to the remaining pellet, which was centrifuged at 20,000 g at 4°C for 40 min for 5 washes. The pellets were lastly washed with 100 mM NaCl to remove phosphate buffer which complexes the metals.

The aqueous phase was split into glass vials along with an equal volume of 7:3 (*v/v*) $CHCl_3$/methanol. The phases were mixed by vortexing, sonication, and Pasteur pipette mixing and then separated by centrifugation at 1000 rpm at 4°C for 5 min in a Sorvall Legend X1R Plus Centrifuge (Thermo Scientific, Ottawa, ON).

The lipid-containing organic phase was collected using a 1 mL Hamilton syringe. The aqueous phase was washed 4 times with 7:3 (*v/v*) $CHCl_3$/methanol, then the collected organic phase was washed 2 times with distilled water. The volume of the organic phase was reduced by evaporation and gentle heating until it could be transferred into a small vial. Sodium sulfate was added to remove traces of water. The film was dissolved in 2 mL $CHCl_3$ and the concentration determined by the Ames assay (Section 2.2.3), approximating the phospholipid fraction as 50% of total lipids (164), though this has been reported to vary between 50-60% (109, 110).

The blood extract film was prepared into LUVs (Section 2.2.1). The absorbance spectrum of the LUVs showed a small shoulder around 280 nm, suggesting slight protein contamination. The RBC lipid extraction was only completed in one replicate.

2.6 Thin Layer Chromatography (TLC)

Compositional analysis of lipid mixtures and complex extracts was performed by thin layer chromatography (TLC), which allows for identification and relative quantitation of components by use of lipid standards. TLC separates components in a mixture due to their relative interactions with a stationary and mobile phase. 5 x 10 cm Silica gel TLC plates on Al matrix (Sigma Aldrich, Oakville, ON) were marked with pencil at 10 mm and 90 mm to designate the spotting location and solvent front endpoint.

2.6.1 Separation of polar lipids

The plates were initially run in a 3-component solvent mixture consisting of 80:16:4 (*v/v*) dichloromethane/ethyl acetate/acetone, then in an 8-component solvent mixture of 30:6:6:6:16:28:6:2 (*v/v*) $CHCl_3$/ethyl acetate/acetone/isopropanol/ethanol/ methanol/water/acetic acid to wash the plate. These solvents are known to be effective for the separation of polar lipids (165). 20–100 µg lipid samples and standards were then loaded on the 10 mm line by spotting with 10 µL capillary tubes (Fischer Scientific, Pittsburgh, PA), or with Hamilton syringes (Hamilton, Reno, NV) for quantitative spotting. The solvent front was run to 90 mm in the 3-component solvent, followed by the 8-component solvent. The plates were left to dry fully for 15 minutes. For visualization of all lipid components, the plates were sprayed with 2% H_2SO_4 and charred on a hot plate at ~100°C until spots became dark (166).

2.6.1.1 Specific visualization techniques

Alternatively, for visualization of phospholipid components alone, the plates were sprayed with a 6:1 (*v/v*) 0.21% ammonium molybdate in 0.5 M H_2SO_4 and 5% ascorbic acid in H_2O, as the phosphomolybdate complex turns blue, as described for the Ames assay (Section 2.2.3) (149). The plates were then developed by incubation at 37°C in an Isotemp 500 incubator (Fisher Scientific, Pittsburgh, PA) for 30–35 minutes. The plates were photographed immediately to avoid background colour development on the silica plate. The plates could subsequently be charred to visualize non-phospholipids as described above.

For visualization of lipid peroxides, plates were sprayed with 1:4 (*v/v*) 4% KI/1% acetic acid, allowed to dry for 6 min under vacuum, then sprayed with 2% cornstarch (167, 168). Peroxidised lipids appear as purple-brown spots. The starch solution was prepared by boiling in 0.2 M NaOH to dissolve, and then neutralized with HCl.

2.6.2 Separation of neutral lipids

The separation of neutral lipids was performed according to a previously-described procedure (165). Plates were washed with 6:4 (*v/v*) methanol/ethyl acetate prior to loading (165). The plates were run to 40 mm and subsequently 55 mm in 80:16:4 (*v/v*) dichloromethane/ethyl acetate/acetone, to 68 mm in 90:10 hexane/ethyl acetate, to 80 mm in 95:5 hexane/ethyl acetate, and to 90 mm in hexane (165), drying for 10 min between each run. Plates were then sprayed with 2% H_2SO_4 as described in Section 2.6.1.

2.6.3 Separation of DAG regioisomers

The separation of 1,2- and 1,3-DAG regioisomers was performed according to a previously-described procedure (169). Silica gel plates were modified by rinsing the surface with 2.3% boric acid in ethanol and then heated at 100°C for 10 min. Plates were washed with and then run in 96:4 (*v/v*) $CHCl_3$/acetone to 90 mm and sprayed with 2% H_2SO_4 as described in Section 2.6.1. To make a 1,3-DAG standard, 1,2-DAG was dissolved in $CHCl_3$ with 5% acetic acid, as DAG spontaneously isomerizes to 1,3-DAG under acidic conditions (170).

2.7 Growth Experiments with *Saccharomyces cerevisiae*

2.7.1 Yeast strains

Table 5. Yeast strains and genotypes used in this thesis. Genotype information was retrieved from Saccharomyces Genome Database (SGD).

Strain	Genotype	Experimental uses
BY4741	MATa his3Δ1 leu2Δ0 met15Δ0 ura3Δ0	General use (wild-type strain)
YPH499	MATa ura3-52 lys2-801_amber ade2-101_ochre trp1-Δ63 his3-Δ200 leu2-Δ1	Mitochondria isolation
W303	*MATa/MATα {leu2-3,112 trp1-1 can1-100 ura3-1 ade2-1 his3-11,15} [phi+]*	Respiration assay

2.7.2 Yeast media

SC (synthetic complete) media represents the simplest media which supports the growth of *S. cerevisiae*, though the carbon and nitrogen sources may be varied. The composition is entirely defined, which makes it ideal for controlled growth experiments. SD (synthetic defined) media is the same as SC but it is a selective media with a dropout component, in this case lacking uracil. YPD (yeast extract peptone dextrose) media is the richest media, such that all viable cells can grow on YPD. YPG (yeast extract peptone glycerol) is a selective media, identical to YPD, except containing glycerol instead of dextrose, which is a non-fermentable carbon source, only supporting the growth of respiring cells (119). It was found that growth of BY4741 in YPG was very slow when pH was unadjusted (~7.1), so pH was adjusted to 5.0.

Table 6. Types of yeast media used in this thesis.

Media	Abbreviation	Carbon source	Nitrogen source	Other components
Synthetic Complete	SC	2% dextrose	0.5% ammonium sulfate	/
Synthetic Complete + Yeast Extract	SC+YE	2% dextrose	0.5% ammonium sulfate	0.5% yeast extract-B
Synthetic Complete (Glutamate)	SC Glu	2% dextrose	0.5% glutamate	/
Synthetic Defined	SD-ura	2% dextrose	0.5% ammonium sulfate	No uracil
Yeast Extract Peptone Dextrose [a]	YPD	2% dextrose	0.5% ammonium sulfate	2% YEP
Yeast Extract Peptone Glycerol [a]	YPG	3% glycerol	0.5% ammonium sulfate	2% YEP pH 5.0

[a] For preparation of solid media plates, 2% agar was added prior to autoclaving.

2.7.3 Metal-media interactions

Various types of yeast media were tested for precipitating interactions with $CoCl_2$, $NiCl_2$, $MnCl_2$, and $Pb(NO_3)_2$. 50% (*v/v*) media was added to 5 mM $CoCl_2$, $NiCl_2$, $MnCl_2$, or $Pb(NO_3)_2$ and the OD_{600} was measured immediately, after 1 hr incubation at room temperature, and at pH 3. Further testing was performed with lower concentrations of $Pb(NO_3)_2$, as well as monitoring OD_{600} over shorter time increments. 50% (*v/v*) media was incubated with 0.5 mM metal for 1 hr at room temperature, then centrifuged at 21,000g for 15 min in a ThermoIEC MicroMax (Fisher Scientific, Pittsburg, PA). The fraction of free metal in the supernatant was measured by the quenching of Calcein, using standard curves as described in Section 2.4.3. $Pb(NO_3)_2$ was completely complexed by all media, so it was not pursued further for yeast growth experiments.

2.7.4 Growth curves

A single colony of *S. cerevisiae* BY4741 was transferred from YPD agar to liquid media and grown overnight (approx. 16 hrs) at 30°C shaking at 200 rpm in an Innova 44 Incubator Shaker (Eppendorf, Mississauga, ON). Cultures in YPG were grown for 2 days overnight. The overnight culture was diluted the following morning to an OD_{600} of ~0.2, as measured on a Genesys 30 UV/Vis Spectrophotometer (Thermo Scientific, Ottawa, ON), then incubated for an additional 2 hrs to ensure the cells were in log phase growth. After incubation, the culture was diluted to an OD_{600} of 0.1–0.2 for use in experiments. 4.5 mL of yeast culture were aliquoted into culture tubes along with 0.5 mL of $CoCl_2$, $NiCl_2$, or ddH_2O. Metal stock solutions were not autoclaved, but prepared by dissolving in sterile water. The cultures were incubated at 30°C shaking at 200 rpm and OD_{600} was monitored every 2 hrs for the first 10 hrs and then at 24 hrs. Controls of each metal concentration with media alone were incubated alongside to check for contamination or precipitation. Growth curves were performed in triplicate and confirmed with another independent culture.

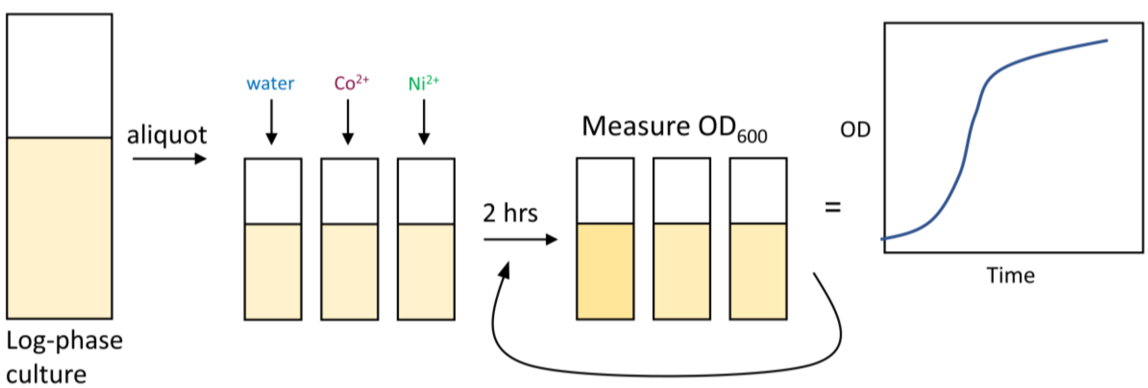

Figure 19. Schematic diagram for measurement of yeast growth in liquid culture.

2.7.5 Brightfield microscopy of S. cerevisiae

Cell morphology was monitored using brightfield microscopy. 5 µL of culture at a given time point was pipetted onto a 3 x 1" glass slide and covered with a 0.15 mm cover slip (Fisher Scientific, Pittsburgh, PA). Cells were visualized using a Motic BA 200 Microscope (Motic, Richmond, BC) and images collected using Motic Images Plus 2.0 software.

2.8* Respiration and Viability of *S. cerevisiae

2.8.1 Red/White spot plate assay with W303

W303 is a strain of yeast which contains a mutation in its adenine biosynthesis pathway, leading to the accumulation of oxidized ribosylaminoimidazole in the mitochondria, which is red in colour (171). After sufficient growth on YPD, respiring colonies visibly turn red/pink, while non-respiring colonies remain white (172).

An overnight culture of W303 was incubated with various concentrations of $CoCl_2$ and $NiCl_2$ for 6 hrs. Cells were then pelleted at 10,000 g for 1 min in an Eppendorf 5415R Centrifuge (Eppendorf, Mississauga, ON), counted using a hemocytometer (Hausser Scientific, Horsham, PA) and resuspended at 10^8 cells/mL in sterile water. 5 µL of stock and serially-diluted cells (up to D1000) were spotted onto a YPD plate (Table 6) and then incubated at 30°C in an Isotemp Incubator (Fisher Scientific, Pittsburgh, PA) for ~16 hrs (YPD) or 2 days (YPG). The plates were then stored at 4°C to allow for colour development. Plates were imaged on a Gel Doc XR+ (Bio-Rad, Hercules, CA) and analyzed with Quantity One software (Bio-Rad, Hercules, CA).

2.8.2 Viability assays

Viability refers to the number of live cells left following a treatment. A metal or drug treatment may be cytostatic (inhibiting growth), but not necessarily cytotoxic (causing cell death). Conditions which produced a decrease in cell density of W303 in the Red/White assay were analyzed by viability assays, incubating samples of BY4741 in SC with metal for 4 hrs. Cells were collected by centrifugation, washed with sterile water to remove metal and media, and counted with a hemocytometer, as in Section 2.8.1. Cells were then diluted such that 200 µL containing ~400 cells were plated on YPD or YPG, using sterile glass beads to spread. The plates were incubated at 30°C in an Isotemp Incubator (Fisher Scientific, Pittsburgh, PA) for 2 days (YPD) or 4 days (YPG). The colonies were then counted and the ratio of viable colonies on YPG/YPD was determined for each treatment.

2.8.3 Isolation of mitochondria

The following isolation procedure was performed by Brittney Kozlowski and the isolated membranes were then investigated in this thesis. An overnight culture of YPH499 in YPG was diluted to OD_{600} 0.03 and grown for ~28 hrs to OD_{600} 2.0. Cells were pelleted in pre-weighed containers by centrifugation at 3000 g for 5 min in a Sorvall Legend RT Centrifuge (Thermo Scientific, Ottawa, ON), which were then washed with dH_2O and combined to determine wet pellet weight. Cells were resuspended in pre-warmed DTT buffer (100 mM Tris-H_2SO_4, 10 mM DTT pH 9.4) at 2 mL/g, and then shaken at 80 rpm at 30°C for 20 min. Centrifugation was repeated 2x more, by resuspending in Zymolyase buffer (1.2 M sorbitol, 20 mM KH_2PO_4 pH 7.4) which lyses cell walls (173), at 8 mL/g, and then subsequently in 3 mL/g of 20T-Zymolase, shaking at 30°C as before. Degradation of the cell wall was confirmed by assessing the clarity of the solution by mixing 50 µL of culture before and after Zymolyase treatment with 2 mL dH_2O.

Cells were collected and washed once more with Zymolyase buffer (7 mL/g), then collected and resuspended at 4°C in Homogenization buffer (0.6 M sorbitol, 10 mM Tris-HCl, 1 mM EDTA, 1 mM PMSF, 0.2% (*w/v*) fatty acid-free BSA pH 7.4) at 6.5 mL/g. Spheroplasts, or cells without cell walls, were then homogenized by 15 passes in a glass-Teflon homogenizer and diluted 2x in Homogenization buffer. Cell debris was eliminated by pelleting at 1500 g for 5 min, and then the supernatant was spun again at 4000 g for 5 min, and pellet was discarded again. The supernatant was spun once more at 12,000 g for 15 min to collect the crude mitochondrial fraction. The pellet was then resuspended in SEM buffer (250 mM sucrose, 1 mM EDTA, 10 mM MOPS-KOH pH 7.2), and the 4000 g and 12,000 g steps were repeated. Protein yield in the crude extract was determined by a BCA assay (174), diluted to 5–10 mg/mL protein and stored at -80°C.

Purified mitochondria were isolated from the crude extract by sucrose density centrifugation. The crude extract was homogenized once more with 10 passes. The homogenate was loaded onto a step gradient in EM buffer (1 mM EDTA, 10 mM KOH-MOPS pH 7.2): 60, 32, 23, 15% sucrose, which was spun at 134,000 rpm at 2°C for 1 hr in an ultracentrifuge with a Beckman SW41 Ti rotor. The mitochondrial fraction was recovered from the 60/32% interface using a Pasteur pipette. Samples from each tube were pooled and diluted 2x with SEM. Mitochondria were pelleted at 10,000 g at 2°C, protein concentration determined and adjusted again to 5–10 mg/mL protein prior to storage at -80°C.

2.8.4 Laurdan experiments with mitochondria

Purified mitochondrial fractions were pelleted by centrifugation at 10,000 g, and resuspended in 250 mM sucrose, 10 mM Hepes at pH 7.2, as both Mops and EDTA complex Co^{2+} and Ni^{2+} and needed to be removed (175). Approximately 120 µg/mL protein weight of mitochondria were incubated with 0.5 µM Laurdan in DMSO (0.05% *v/v* final) at 37°C for 30 min, which lead to a sufficient signal without overwhelming the membrane with Laurdan or DMSO (176–178). Initial range finding was performed at 30°C by titrating in Co^{2+} or Ni^{2+} starting at 0.5 µM. Experiments were only completed in one replicate due to limited sample.

The effects of Co^{2+} and Ni^{2+} on isolated mitochondrial membranes were compared to a liposome mimic based on yeast mitochondrial lipid composition.

Table 7. Molar lipid composition of yeast mitochondrial membrane mimic based on Zinser and Daum (1995) (179) and Horvath and Daum (2013) (99).

Component	Molar fraction (%)
POPC	28.2
POPE	19.0
SAPI	10.6
POPS	2.1
TOCL	9.2
POPA	1.4
C16 glucosyl ceramide	12.9
Ergo (DHE)	16.7

C16 glucosyl ceramide was used to represent the sphingolipid contribution, as it bears some resemblance to the inositol phosphorylceramide (IPC) sphingolipids in yeast (96), which are not commercially-available. The mimic was resuspended in the 250 mM sucrose, 10 mM Hepes pH 7.2 buffer alike to the mitochondria. Laurdan was excited at 360 nm to avoid interference of dehydroergosterol (DHE).

2.8.5 Fluorescence live-cell imaging of S. cerevisiae

2.8.5.1 MitoTracker Green FM

MitoTracker Green-FM (MTG-FM) was used to monitor mitochondrial morphology. MTG-FM is a mitochondria-specific dye which fluoresces upon localization in the mitochondrial matrix, presumably activated by reaction with protein thiols (180). Images are thus relatively free of background signal. However, a drawback is that the potential direct quenching interaction with Co^{2+} and Ni^{2+} cannot be tested, as MTG-FM is not fluorescent on its own in buffer.

An overnight culture of BY4741 in SC media (Table 6) was incubated with 2 mM $CoCl_2$ and $NiCl_2$ for 4 hrs, then collected by centrifugation at 10,000 g for 1 min in an Eppendorf 5415R Centrifuge (Eppendorf, Mississauga, ON). The cells were resuspended in a small volume of 10 mM Hepes, 5% (*w/v*) glucose pH 7.4 buffer and adjusted to OD_{600} of 1.2. 150 nM MTG-FM (Molecular Probes, Eugene, OR) in DMSO was then added to each sample, which was incubated at room temperature in the dark for 20 min. 3 µL of cells were spotted onto a 2% agarose slab containing the resuspension buffer on a 75 x 25 mm glass slide and covered with a 1.5 mm coverslip.

Fluorescence microscopy experiments were performed on an Axio Imager.Z2 fluorescence microscope (Zeiss, Oberkochen, Germany), and samples were imaged with the brightfield channel as well as an appropriate channel for MTG-FM (Ex 490 nm, Em 516 nm). Exposure and laser power were auto-adjusted for the intensity of the control slide, and absence of background intensity was checked with an unlabelled control slide. Images were taken at 1000x magnification. Three independent samples were made in which 50–100 cells were counted per trial, and z-stack images were taken over a 5 µm range to assess the 3D structure of the mitochondrial network. Images were analyzed using Fiji software (181). The structure of mitochondria in each cell were categorized as either “tubular” or “fragmented”. Dead cells were not counted.

2.8.5.2 MitoSOX Red Superoxide Indicator

MitoSOX Red (MSR) is another mitochondrial-specific dye which allows for detection of mitochondrial-localized oxidative stress, as it only becomes fluorescent upon oxidation by superoxide and subsequent binding to mitochondrial DNA (182). Again, this allows for images with low background signal, but the direct effects of Co^{2+} and Ni^{2+} on the fluorescence of the dye itself cannot be tested.

Cells were prepared similarly to with MTG-FM, but instead incubated with 5 µM MSR for 20 min at 37°C in the dark before spotting on a slide. Images were taken as with MTG-FM, but with an appropriate channel (Ex 510 nm, Em 580 nm). Analysis was performed by manually measuring the average intensity of the mitochondrial structure in each cell using Fiji software (181). The intensities of each replicate were normalized according to the control for that replicate, to account for any changes in intensities between trials which may result from slight differences in cell number, dye degradation, and/or agarose bed consistency.

2.8.5.3 C1-GFP for diacylglycerol (DAG) monitoring

A BY4741 strain transformed with a plasmid encoding C1-GFP was used to monitor DAG localization in cells through GFP fluorescence (Ex 488 nm, Em 509 nm), as the C1-domain is a DAG-binding motif (183). The transformation was performed by Suria Ganesan from the Zaremberg lab; I have used the strain for fluorescence microscopy. Cells were grown in SD-ura and prepared as with MTG-FM, but SD-ura media was used instead of resuspension buffer, and no dye was added. The location of DAG and number of vacuoles were recorded for each cell.

2.9 Lipid Extracts from *S. cerevisiae*

2.9.1 Extraction of total lipids

Total lipids were extracted from *S. cerevisiae* using a modified Folch's method (184). An overnight culture (200 mL) in SC at OD_{600} 0.1 was prepared and aliquoted into 3 flasks containing: $CoCl_2$, $NiCl_2$, or ddH_2O to a final metal concentration of 1 mM. The cultures were grown in the presence of metal for 4 hrs to a final OD_{600} of ~0.4 and then placed on ice. Cells were pelleted by spinning at 2500 g in a Sorvall Legend RT Centrifuge (Thermo Scientific, Ottawa, ON) for 5 min at 4°C, and the supernatant was decanted. The cells were washed twice in 1 mL of cold 1 M sorbitol and pelleted for 1 min at 10,000 g in an Eppendorf 5415R Centrifuge (Eppendorf, Mississauga, ON) to wash away excess media, which was decanted. 1 mL of 1:1 (*v/v*) $CHCl_3$/methanol was added to the pellet to transfer the samples into a 2 mL bead beater vial filled 1/8 with 0.5 mm acid washed beads. The pellet was then homogenized in a BioSpec Bead Beater (Bartlesville, OK) for 60 sec at 4°C to disrupt the cell wall. The cell extract was transferred to a capped glass test tube, and the beads were rinsed with 1 mL 2:1 (*v/v*) $CHCl_3$/ methanol, which was added to the total volume. To each test tube 0.5 mL 2:1 (*v/v*) $CHCl_3$/ methanol, 0.5mL $CHCl_3$, and 1.5mL H_2O were added. The tubes were vortexed to fully mix the organic and aqueous phases, then spun at 2500 rpm for 10 min at 4 °C in a Sorvall Legend X1R Centrifuge (Thermo Scientific, Ottawa, ON). The top aqueous layer and protein interface were aspirated off, and the organic phase was collected and transferred into a clean test tube with a 1 mL Hamilton syringe. The organic phase was washed twice to remove aqueous-soluble contaminants with 2.5 mL of 3:48:47 (*v/v*) $CHCl_3$/ methanol/ H_2O, which was spun and collected as before. The organic phases of each treatment were pooled into a single test tube and a small amount of sodium sulfate was added to remove traces of water. The solvent was then evaporated under argon by heating gently at 50°C, and then overnight in a vacuum chamber to form a lipid film of yeast total lipid extract (YTE), which was transferred into a small pre-weighed glass vial. Lipid yield was determined by weight difference of the vials. Extractions were performed on independent duplicates, each consisting of 6 technical replicates which were combined. The independent replicates were not combined but run separately on TLC to confirm reproducibility.

2.9.2 Separation of neutral and polar lipids

It was found that YTE contained a large abundance of neutral lipids and did not form liposomes, so yeast polar lipid extracts (YPE) were prepared from YTE by an adapted procedure for the extraction of neutral lipids (185, 186). Approximately 0.5 mg of YTE was dissolved in a minimal amount of 7:3 (*v/v*) $CHCl_3$/methanol, deposited onto the bottom of a 10 mL glass screw-cap test tube, and dried to a film under argon. 5 mL of cold acetone was added and the neutral lipids in the film were solubilized by repeated vortexing and sonication (185), while polar lipids remained as visible fine particulates. The sample was then bubbled with argon for 1 min to prevent lipid oxidation, and then sealed with Parafilm and stored at 4°C overnight, allowing for further precipitation and settling of polar lipids (185). The sample was briefly spun at 2500 rpm for 10 min at 4°C in a Sorvall Legend X1R Centrifuge (Thermo Scientific, Ottawa, ON) to pellet any suspended particulates. The acetone-soluble fraction was carefully removed into another glass tube with a Pasteur pipette, leaving the acetone-insoluble polar lipids behind (185, 186). Remaining acetone was evaporated under argon, leading to formation of films in both fractions, which were soluble in 7:3 (*v/v*) $CHCl_3$/methanol. TLC of each fraction was run to confirm separation of neutral lipids; the procedure was optimized using YTE from Avanti Polar Lipids. Unfortunately, some polar lipids were found to remain soluble in acetone, reducing the overall yield, but none of the neutral lipids were found to precipitate in acetone, suggesting that the method would work for the extraction of a bilayer-forming polar lipid extract (Figure 20).

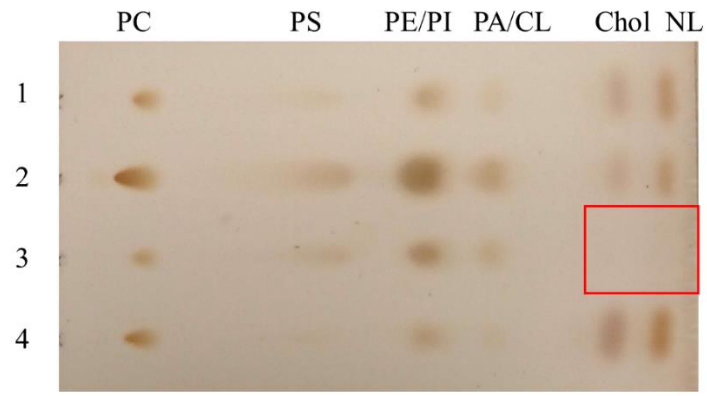

Figure 20. Polar lipid TLC separation of (1) Avanti YTE, (2) Avanti YPE, (3) acetone-insoluble fraction of Avanti YTE, and (4) acetone-soluble fraction of Avanti YTE. The red box indicates the removal of neutral lipids (NL) in the acetone-insoluble fraction.

Lipid compositions of both YPE and neutral extracts were analyzed by TLC (Section 2.6) spotting 100 µg of each for comparative analysis. The YPE was used to form liposomes (Section 2.2.1) for Laurdan and DLS experiments.

2.10 Statistics

In all figures presented, results are the average of at least triplicates with error bars representing ± standard deviation, unless otherwise noted. Significance is denoted by asterisks (*) $p < 0.05$, (**) $p < 0.01$, (***) $p < 0.001$, (****) $p < 0.0001$.

Chapter Three: Interactions of Co^{2+} and Ni^{2+} with Simple LUVs and MLVs

Firstly, simple lipid systems were considered to determine binding targets of Co^{2+} and Ni^{2+}, and the relative strength of interactions. A portion of this chapter discussing Laurdan and DLS experiments with PA, CL, PG, PS, and PC is adapted from Umbsaar *et al.* (2018) (187).

3.1 Effects of Co^{2+} and Ni^{2+} on the Fluidity of Zwitterionic Lipid Membranes

3.1.1 Background on zwitterionic lipids

Zwitterionic lipids and sterols constitute the structural components of cell membranes, with PC, SM, PE, and Chol/Ergo comprising the majority of the membrane (59, 71). These lipids are, therefore, very important in dictating the properties of the membrane. PC and SM are canonical bilayer-forming phospholipids, as the cylindrical geometry allows them to pack with minimal defect, whereas the non-bilayer forming lipid PE induces membrane curvature, important in fusion and protein accommodation (71, 188). The presence of sterols contributes to a tighter-packing liquid crystalline phase, as the highly-hydrophobic structure interacts favourably with lipid acyl chains (189). In the context of this project, zwitterionic/neutral lipids were tested as negative controls for Co^{2+} and Ni^{2+} interaction, as the interactions were hypothesized to be electrostatic in nature (32). The head groups of PC, SM, and PE all contain a negative charge on the phosphate backbone, but the more accessible positive charge in the headgroup is likely to repel Co^{2+} and Ni^{2+}.

3.1.2 Laurdan GP of zwitterionic membranes

Laurdan GP (Section 2.3.2) was used to assess the effects of Co^{2+} and Ni^{2+} on the fluidity/rigidity of lipid membranes (150). Various zwitterionic and neutral lipids were tested to assess these interactions including: POPC, DMPC, POPE, Chol, SM, ceramide, and cerebroside.

The GP melting curves of the various systems demonstrate large differences in the relative fluidity of each membrane with temperature. Some of the systems had a measurable inflection point (T_m) above 10°C, while others underwent a transition at a lower temperature, so the curve simply represents an increasingly-fluid liquid crystalline phase as shown in Figure 21:

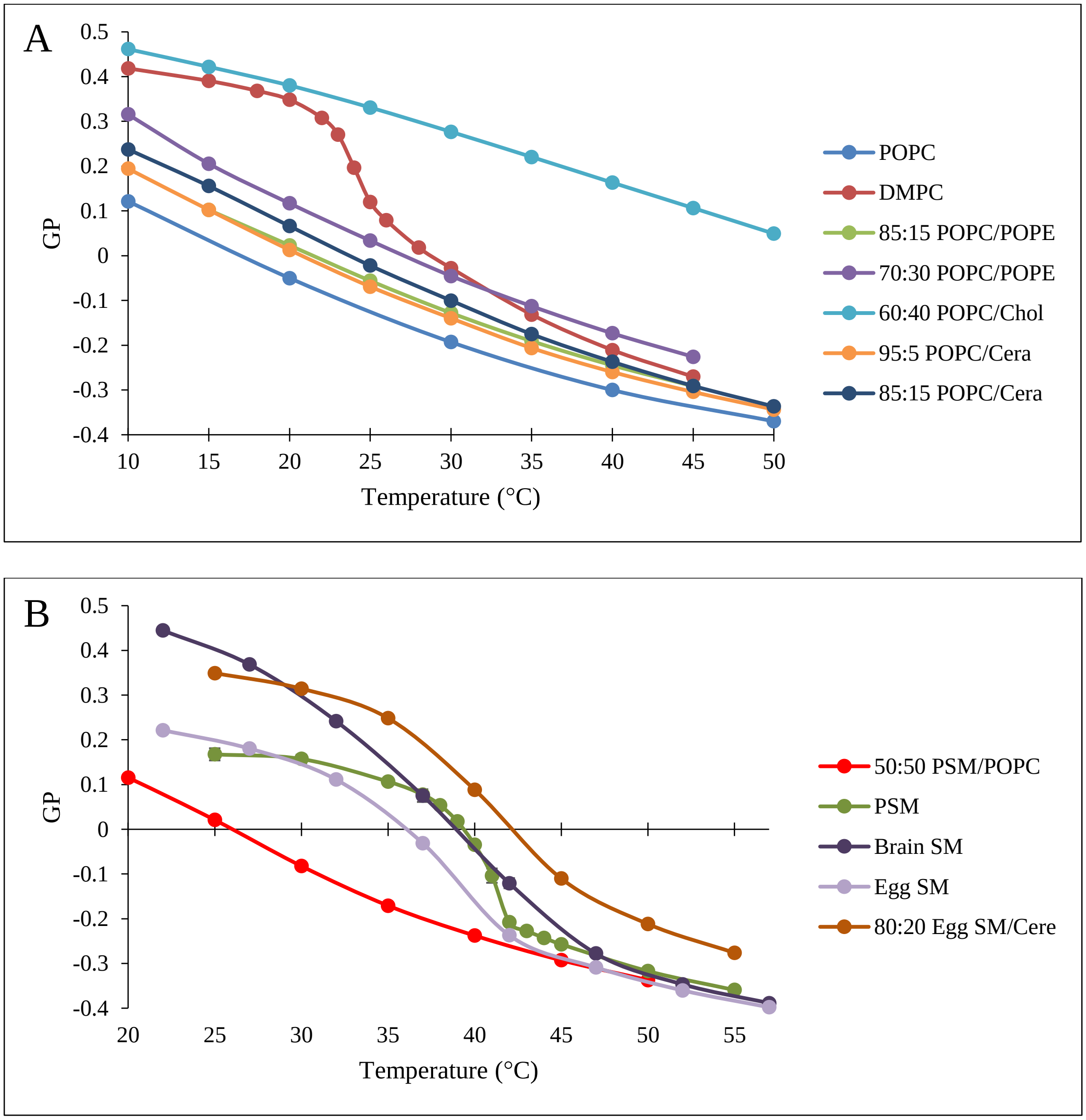

Figure 21. Laurdan GP melting curves of simple zwitterionic/ neutral membranes which are (A) PC-based, or (B) SM-based in 20 mM Hepes, 100 mM NaCl pH 7.4.

POPC and 50:50 PSM (palmitoyl-SM)/POPC were the most fluid systems tested, while the addition of POPE, ceramide, and most notably Chol to POPC caused the membrane to become significantly more rigid (Figure 21A), as expected (189). The lipid which was able to adopt the tightest gel phase packing was Brain SM. Co^{2+} and Ni^{2+} had minimal effects on any of the systems tested, but if interaction occurred, it was at higher temperatures in the liquid crystalline phase. A representative summary of the GP change between controls and metal exposed samples (ΔGP) in these systems is shown in Figure 22:

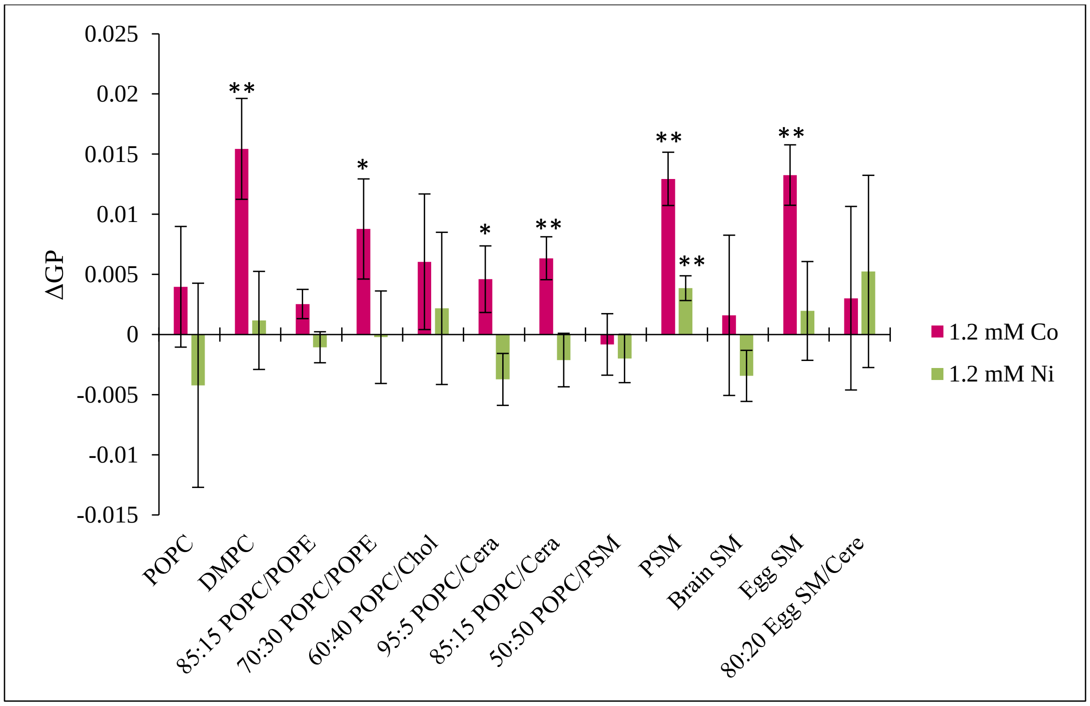

Figure 22. Change in GP at 40°C (or 50°C for SM-containing membranes) induced by 1.2 mM Co^{2+} or Ni^{2+} in various zwitterionic/neutral lipid liposomes (0.3 mM) in 20 mM Hepes, 100 mM NaCl pH 7.4.

The overall effect of Co^{2+} and Ni^{2+} on zwitterionic/ neutral lipids was minor, as the highest concentration of metal tested (1.2 mM), generally induced little to no change in GP values (Figure 22). The ΔGP shown for PC- and SM-based membranes is given at 40 and 50°C, respectively, to reflect comparable liquid-crystalline phases (Figure 21), in which significant interactions were observed. While Ni^{2+} showed only a minor rigidifying effect with PSM, 1.2 mM Co^{2+} was able to induce minor changes in: DMPC, Egg SM, PSM, 70:30 POPC/POPE, and 95:5 or 85:15 POPC/ceramide, suggesting a weak affinity for these lipids and/or packing arrangements. The greatest rigidifying effect was observed between Co^{2+} and DMPC, along with a T_m shift of +0.1°C. A previous study using DSC to investigate interactions of NaCl and LiCl with DMPC (15 mM Hepes pH 7.0) found that 100 mM metal also increased the T_m very slightly (190), though much lower metal concentrations were used in this thesis. Despite interactions with DMPC, neither Co^{2+} nor Ni^{2+} affected POPC, suggesting that the tighter packing of acyl tails allows for better interactions with the PC head group, though these are still very minor effects. The weak interactions with PC in general is supported by an ^{31}P NMR study which found a dissociation constant of 1.2 M for both Co^{2+} and Ni^{2+} with Egg PC (75). Structurally speaking, it is likely that the bulkiness and positive charge of the choline group is too repulsive to allow Co^{2+} and Ni^{2+} binding to the phosphate group.

A comparable effect by Co^{2+} was observed for Egg SM and PSM, yet surprisingly not for the tighter packing Brain SM, again suggesting that the acyl chain identity plays a role in the interaction with choline head groups. According to the Avanti Polar Lipids product information, Egg SM contains approximately 86% 16:0 (palmitoyl) SM, while Brain SM contains notably 50% 18:0 (stearoyl) and 21% 24:1 (nervonoyl) SM. The average chain length of Egg SM is 16 C, while that of Brain SM is 20 C, suggesting that Brain SM would create a more rigid membrane. This is clearly reflected in the raw GP data, as in the gel phase at 22°C, Egg SM has a GP value of 0.221, while Brain SM has a GP value of 0.447. Altogether, this suggests that the binding of

Co^{2+} and Ni^{2+} to PC or SM membranes depends on an optimal spacing between head groups. POPC appears to be too intrinsically disordered to allow for any interaction, while the head groups in Brain SM may be too close together.

In the case of Co^{2+}, it was also observed that mixed liposomes containing POPC with POPE or ceramide (Cera) also allowed for minor interactions, suggesting either that: PE and ceramide are targets, and/or that the change in packing arrangement allows for interaction with PC. A previous study on Egg PE found that 3 mM Co^{2+} or Ni^{2+} were able to cause aggregation of PE vesicles, suggesting some propensity for interaction with PE (191). Steric considerations could also play as role, since the smaller primary amine of PE, as compared to the quaternary amine of PC, may allow access for metal binding to the backbone phosphate. Direct binding of Co^{2+} to Cera has not been reported, but in terms of structure, it is again possible that the small head group of Cera allows Co^{2+} binding to the phosphate of PC. It is also possible that Co^{2+} is able to weakly associate with the electron-rich oxygen and nitrogen atoms in ceramide itself. Yet, these interactions are likely all biologically negligible given that 1.2 mM metal was used, which is 4x in excess of lipid concentration. It is also likely that much stronger binding occurs with other cellular targets such as negatively-charged lipids (76) or proteins (35, 147).

3.2 Effects of Co^{2+} and Ni^{2+} on the Fluidity of PA Membranes

3.2.1 Background on PA

PA lipids were considered as the structurally most simple of the negatively-charged lipids, containing a single exposed phosphate group. It was expected that the high accessibility of the negative charge would allow for strong interactions with Co^{2+} and Ni^{2+}. Despite being present as a very minor component of most membranes (60), PA is physiologically-relevant in many mammalian cell functions such as regulating cell survival, vesicular trafficking, and cell differentiation (65). It has been suggested that localization of certain proteins to the cell membrane may be due to direct PA-protein interactions (65). Additionally, PA is an important precursor in the synthesis of other lipids (65), making it necessary for cell function.

3.2.2 Laurdan GP of PA membranes

Monounsaturated POPA and fully saturated DMPA were considered to assess the effect of acyl chain identity on metal lipid interactions, as they are structurally-identical apart from the acyl chains. Firstly, POPA was found to have a T_m of 20.5°C, lower than a DSC study which determined a T_m of 24°C in 150 mM NaCl, 10 mM Tris at pH 7.40 (192). As the T_m determined for this thesis was 3.5°C lower than a literature value, POPA melting was also tested in 20 mM phosphate, 100 mM NaCl pH 7.4, yielding the same result (Appendix A). Next, the fully-saturated DMPA was considered. The T_m of DMPA was determined to be 47.5°C, which is consistent with a previous study reporting a T_m of 47.3°C in 25 mM PIPES, 100 mM NaCl pH 7.4 by Differential Scanning Calorimetry (DSC) (193). The control melting curves of POPA and DMPA are shown in Figure 23:

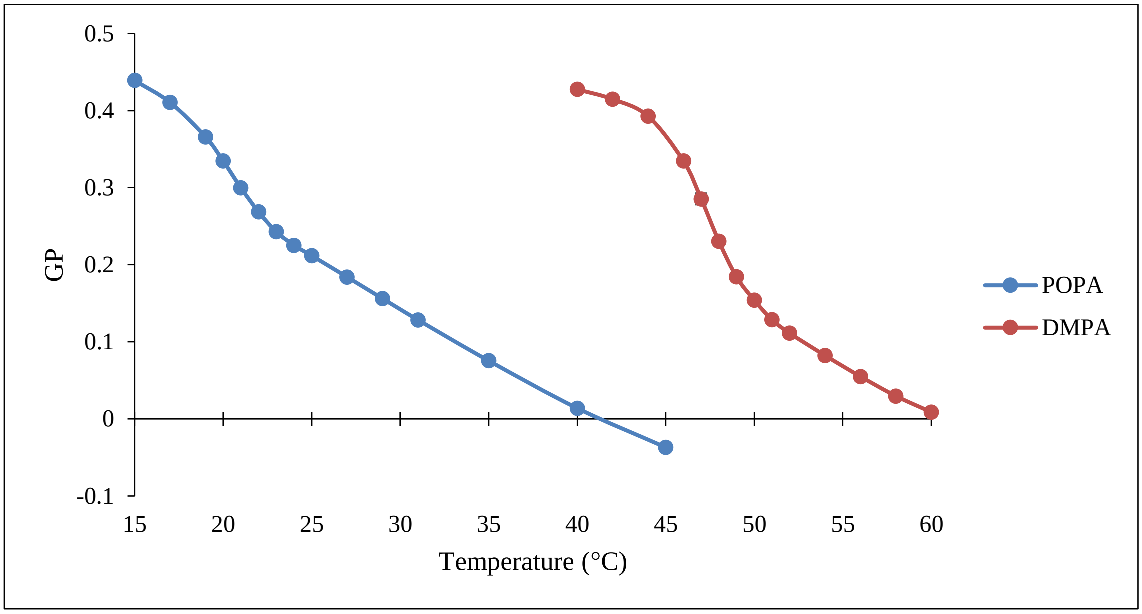

Figure 23. Laurdan GP melting curves of PA lipids in 20 mM Hepes, 100 mM NaCl pH 7.4.

The melting curves clearly reflect that DMPA is much more rigid than POPA, melting over a higher temperature range. As well, the melting transition of DMPA is sharper than POPA. A summary of the metal-induced ΔGPs for POPA is presented in Figure 24.

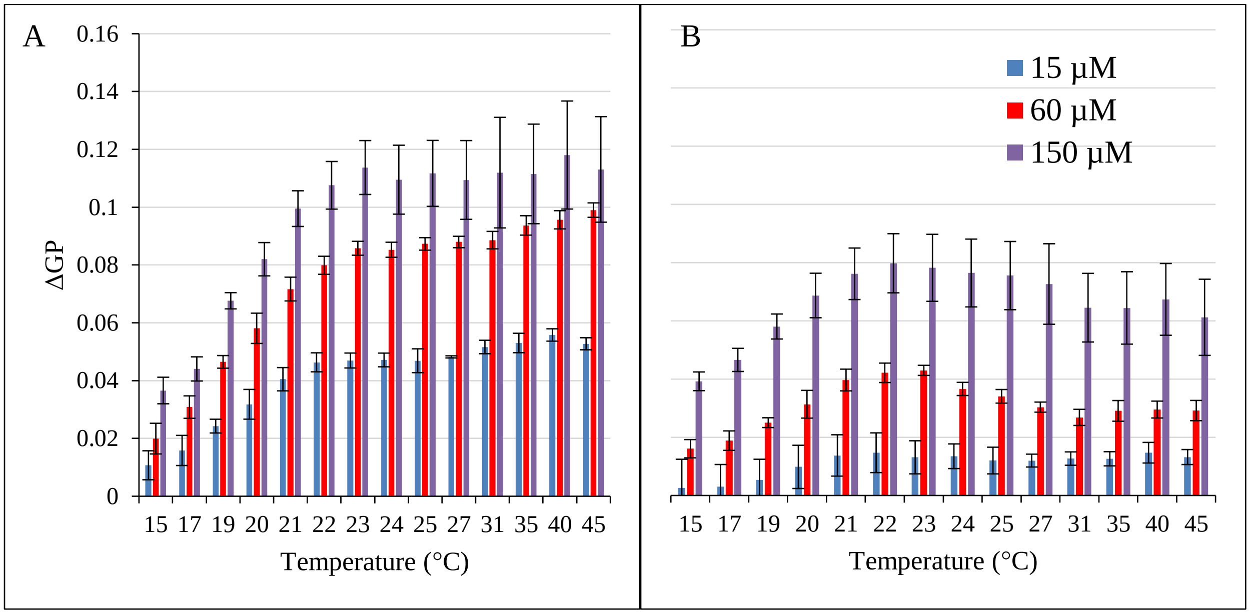

Figure 24. Change in GP induced by (A) Co^{2+} or (B) Ni^{2+} in 0.3 mM POPA liposomes in 20 mM Hepes, 100 mM NaCl pH 7.4.

Both Co^{2+} and Ni^{2+} induced significant rigidification of POPA, as shown by positive ΔGP values, indicating a maintenance of gel phase-like fluidity in which the 440 nm emission peak of Laurdan dominates (150). It is clear that the effects of Co^{2+} are stronger for a given metal concentration, and that the effect of both metals show a temperature-dependence, having greater effects at higher temperature. In comparing 150 µM metal, the effects of Co^{2+} and Ni^{2+} are greatest after the membrane melts (ΔGP of 0.11 and 0.08 at 24°C) and the effects of Ni^{2+} decrease slightly with higher temperatures. This suggests that Co^{2+} and Ni^{2+} more preferably bind to disordered POPA in the liquid crystalline phase. The effects of Co^{2+} and Ni^{2+} on the fully-saturated DMPA are summarized in Figure 25:

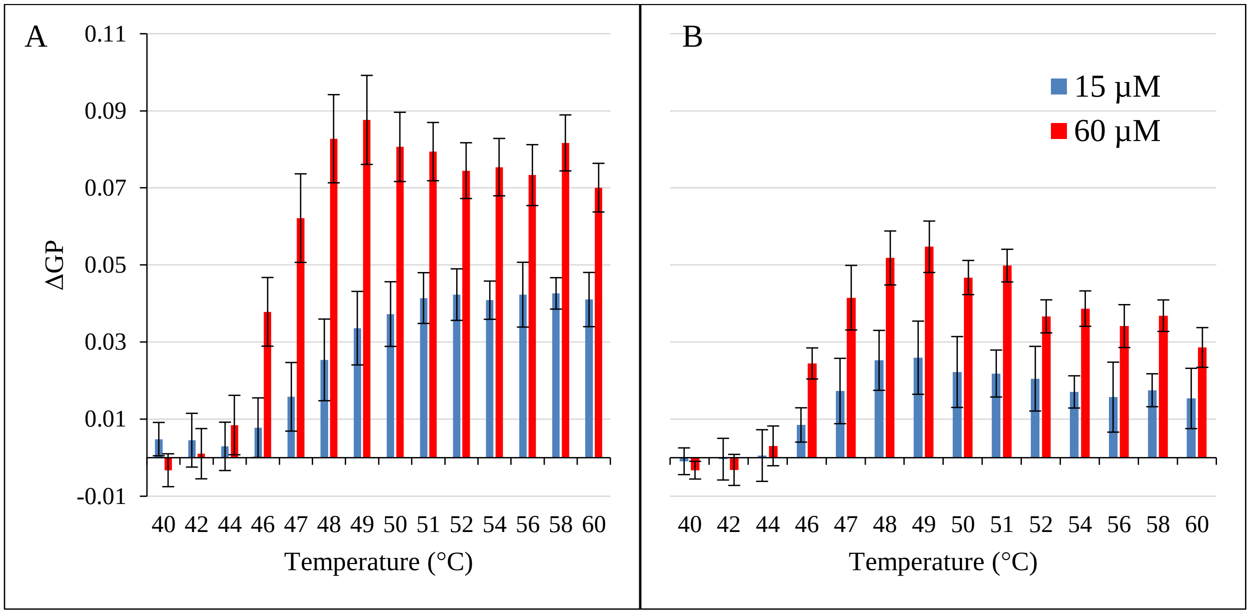

Figure 25. Change in GP induced by (A) Co^{2+} or (B) Ni^{2+} in 0.3 mM DMPA liposomes in 20 mM Hepes, 100 mM NaCl pH 7.4.

Co^{2+} and Ni^{2+} are unable to induce changes in the gel phase of DMPA (40–44°C), suggesting that the metals may not be able to bind to tightly-packed PA. However, the relative strength of metal effect on DMPA in the liquid crystalline phase is quite similar to that of POPA. 60 µM Co was able to cause a maximum ΔGP of 0.098 and 0.088 in the liquid crystalline phases of POPA and DMPA, while 60 µM Ni caused a maximum ΔGP of 0.043 and 0.055. This suggests that the metals do not have a strong preference for binding either one. This is in contrast to previous work with Cd^{2+} (83) and Pb^{2+} (90) in this Lab, which showed preference for DMPA. It is possible that the speciation of Co^{2+} and Ni^{2+} into entirely divalent cations allows for strong interaction with PA regardless of acyl chains, as $CdCl_2$ and $Pb(NO_3)_2$ both largely speciate into monovalent forms, MCl^+ (32).

Interestingly, the trends observed for Co^{2+} and Ni^{2+} and POPA are also present in DMPA, in that the effects of Ni^{2+} reach a maximum just after membrane melting. The cause of this effect is not clear, but it could be based on differences in the preferred coordination environment of Co^{2+} and Ni^{2+} ions, suggesting that the binding of Ni^{2+} depends on a certain arrangement of lipids, most favourable around the T_m. Ni^{2+} tends to form square planar and octahedral geometry (39, 41), while Co^{2+} favours octahedral and tetrahedral geometries (38, 41). It may be that the constraints of a square planar Ni^{2+} ion are best met in the partly-disordered melting transition.

3.3 Effects of Co^{2+} and Ni^{2+} on the Fluidity of CL Membranes

3.3.1 Background on CL

Cardiolipin (CL) is a structurally-unique lipid class which is localized in the mitochondria, but also constitutes a large component of many bacterial membranes (66, 98). CL is functionally important for the mitochondrial membrane, as it influences the membrane structure and activates some enzymes in the respiratory chain (194). Structurally, it can be envisioned as two PA lipids joined by a glycerol linker. The phosphate portion of the headgroup is relatively small and the phosphate conformation is sterically limited, such that it is unlikely to be able to interact with nearby lipids, a feature which has been suggested to leave the head group available to bind with other molecules (194). Under physiological conditions, the CL head group is fully deprotonated, carrying a charge of -2.0 (195); thus, Co^{2+} and Ni^{2+} were expected to bind.

3.3.2 Laurdan GP of CL membranes

TOCL was considered firstly, as it is a highly-fluid membrane with 4 oleyl chains. The T_m of TOCL could not be recorded, as it is below 0°C (196), so the representative temperature scan simply shows an increasingly-fluid liquid crystalline phase. This is in contrast to TMCL, which was found to have a T_m of 40.2°C, which is in agreement with a previous DSC study that reported a T_m of 38.9°C in 50 mM Tris, 150 mM NaCl at pH 7.40 (197). The melting curves of control CL membranes are shown in Figure 26:

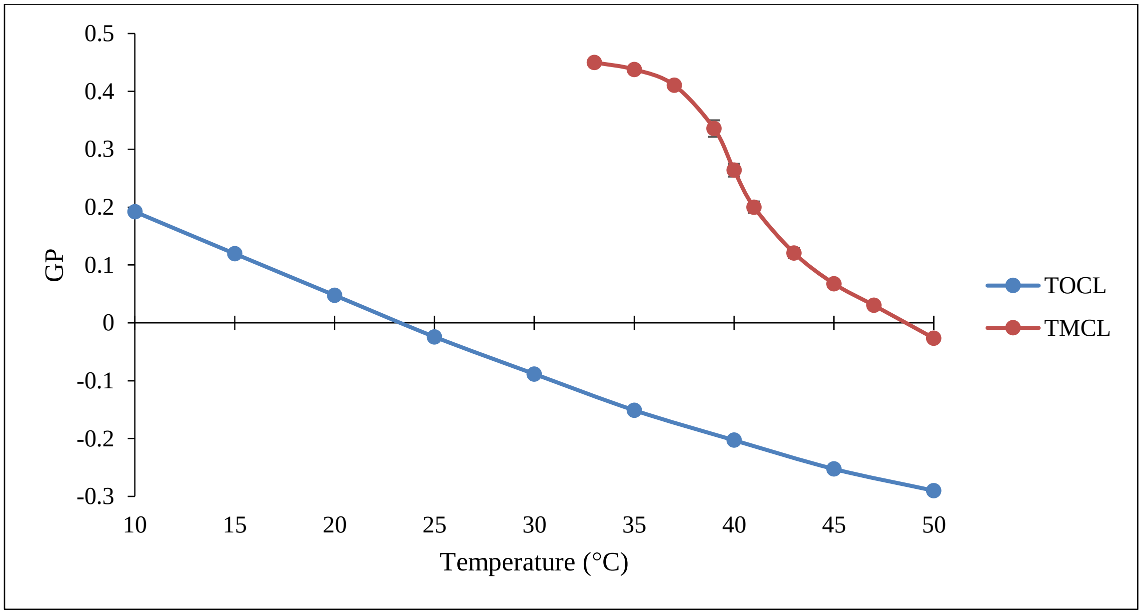

Figure 26. Laurdan GP melting curves of CL lipids in 20 mM Hepes, 100 mM NaCl pH 7.4.

The melting curve of TOCL shows nearly a linear trend , reflecting the fact that the membrane is fully-melted even at 10°C. On the other hand, TMCL is much more rigid, maintaining a gel phase up to ~35°C before undergoing a sharp phase transition. The effects of Co^{2+} and Ni^{2+} on TOCL are summarized in Figure 27:

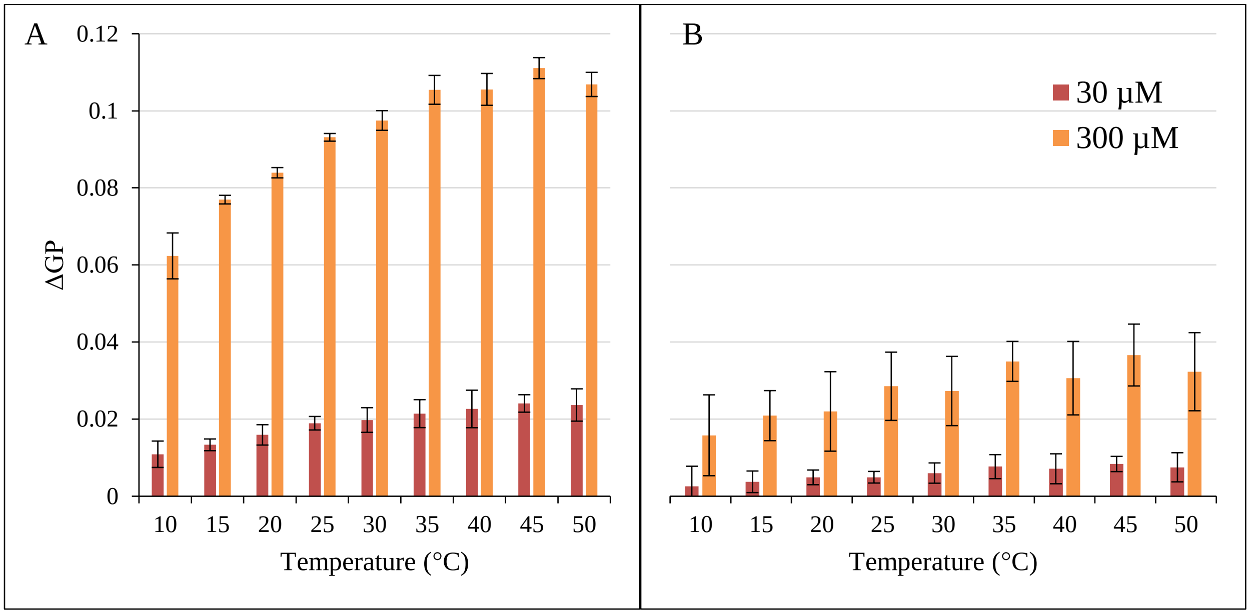

Figure 27. Change in GP induced by (A) Co^{2+} or (B) Ni^{2+} in 0.3 mM TOCL liposomes in 20 mM Hepes, 100 mM NaCl pH 7.4.

The effects of Co^{2+} and Ni^{2+} on TOCL are quite different between the ions, as Co^{2+} causes strong rigidification that increases with concentration and slightly with temperature (up to ΔGP of 0.111 at 45°C), while the effects of Ni^{2+} are very minimal in comparison (up to ΔGP of 0.037 at 45°C). The interactions with Ni^{2+} appeared to be saturated at 300 µM, as they did not increase further with the addition of 600 µM total. The effects of Co^{2+} are remarkably strong compared to similar studies with Cd^{2+} which also reported weak effects (83), as seen for Ni^{2+}. The interactions of Co^{2+} with fluid CL may have some biological relevance, as polyunsaturated linoleic (18:2) acyl chains are most common in mammalian mitochondria (198). The effects of Co^{2+} and Ni^{2+} on TMCL are summarized in Figure 28:

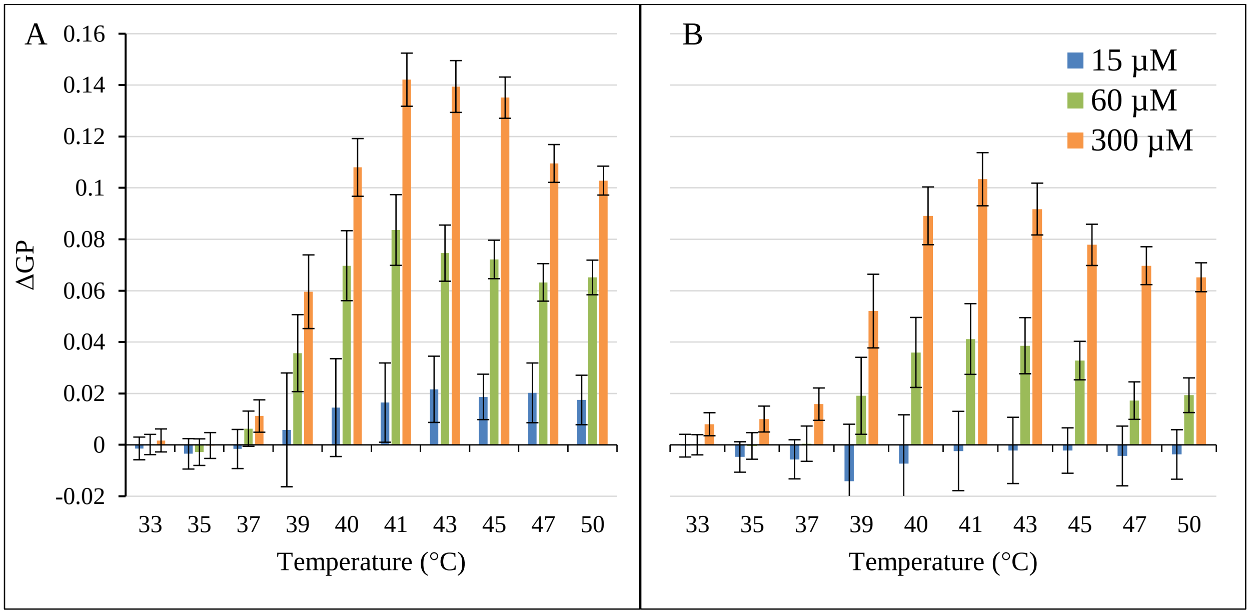

Figure 28. Change in GP induced by (A) Co^{2+} or (B) Ni^{2+} in 0.3 mM TMCL liposomes in 20 mM Hepes, 100 mM NaCl pH 7.4.

Alike to the interactions with DMPA, Co^{2+} and Ni^{2+} were unable to induce changes in the gel phase of TMCL, suggesting again that the packing is too tight and does not allow access for the metals to bind. However, as was observed for Ni^{2+} with PA, the strongest effects of both Co^{2+} and Ni^{2+} occur just after the membrane melts at 41°C, with 300 µM Co^{2+} and Ni^{2+} causing ΔGPs of 0.142 and 0.103, respectively. While the effects of Co^{2+} are relatively comparable to that with TOCL, Ni^{2+} appears to show stronger interaction with TMCL. This preference has also been reported for Cd^{2+} (83), suggesting that Cd^{2+} and Ni^{2+} may share a similar binding geometry which favours a tightly-packed CL arrangement. The rigidifying interactions of metal ions with CL may have considerable consequences for mitochondrial membrane function, as CL is the major negatively-charged lipid (199). The acyl chain composition of CL is actively remodeled post-synthesis by an enzyme called tafazzin, which senses and regulates local membrane fluidity (199). A disturbance to local membrane fluidity may theoretically affect this process.

3.4 Effects of Co^{2+} and Ni^{2+} on the Fluidity of PG Membranes

3.4.1 Background on PG

PG lipids were considered next in terms of structural complexity, as they contain a neutral glycerol head group attached to the negative charge of the backbone phosphate. The ability of metal ions to bind to the phosphate group may thus depend on steric factors. The relevance of PG in mammalian systems is nearly entirely limited to lung surfactant (LS), in which POPG and other minor PG species are present at about 20% of the total lipid composition (63, 101). DPPC is the main modulator of LS structure and function; however, a complex lipid composition including PG appears to be necessary to allow for rapid spreading of the LS layer during breathing (200). The exact role of PG is not clear, but the ratio of PG to other lipids has been found to be altered in several lung diseases (63), highlighting the importance of PG in healthy LS composition. PG is also present as a very minor component of mitochondrial membranes, as it is a precursor of CL (201).

In contrast to eukaryotic cells, bacterial cell membranes contain a significant portion of PG, at about 20% of their lipid content (98). Both experimental and molecular dynamics simulation studies have found that the presence of PG appears to be important in increasing the stability of bacterial cell membranes through hydrogen bonding with PE (202, 203).

3.4.2 Laurdan GP of PG membranes

Monounsaturated POPG was considered first and, like TOCL, the T_m of POPG was too low to be measured with this experimental setup (192), so the melting curve represents the liquid crystalline phase. On the other hand, DMPG was found to have a sharp T_m of 23.2°C, comparable to a value of 23°C obtained by DSC in 10 mM HEPES, 100 mM NaCl pH 7.40 (204). The control melting curves of POPG and DMPG are shown in Figure 29:

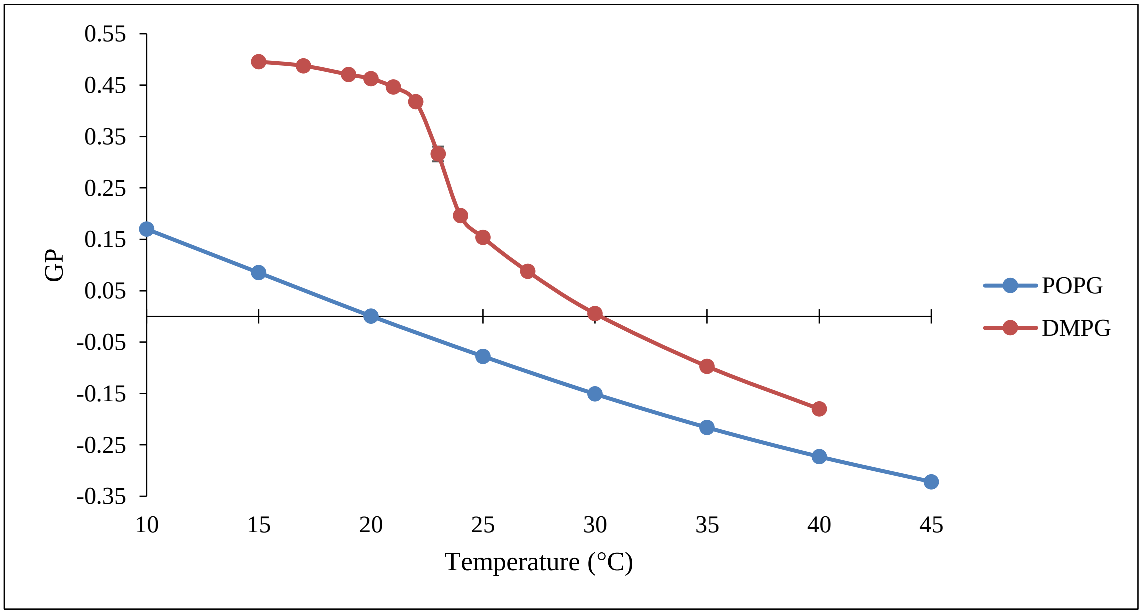

Figure 29. Laurdan GP melting curves of PG lipids in 20 mM Hepes, 100 mM NaCl pH 7.4.

Again, the melting curves are similar to the CLs in that POPG does not show a phase transition over this temperature range with similar GP values to TOCL, while DMPG undergoes a sharp transition (23.2°C), though at a lower temperature than TMCL, which melted at 40.2°C. The interactions of Co^{2+} and Ni^{2+} with POPG are shown in Figure 30:

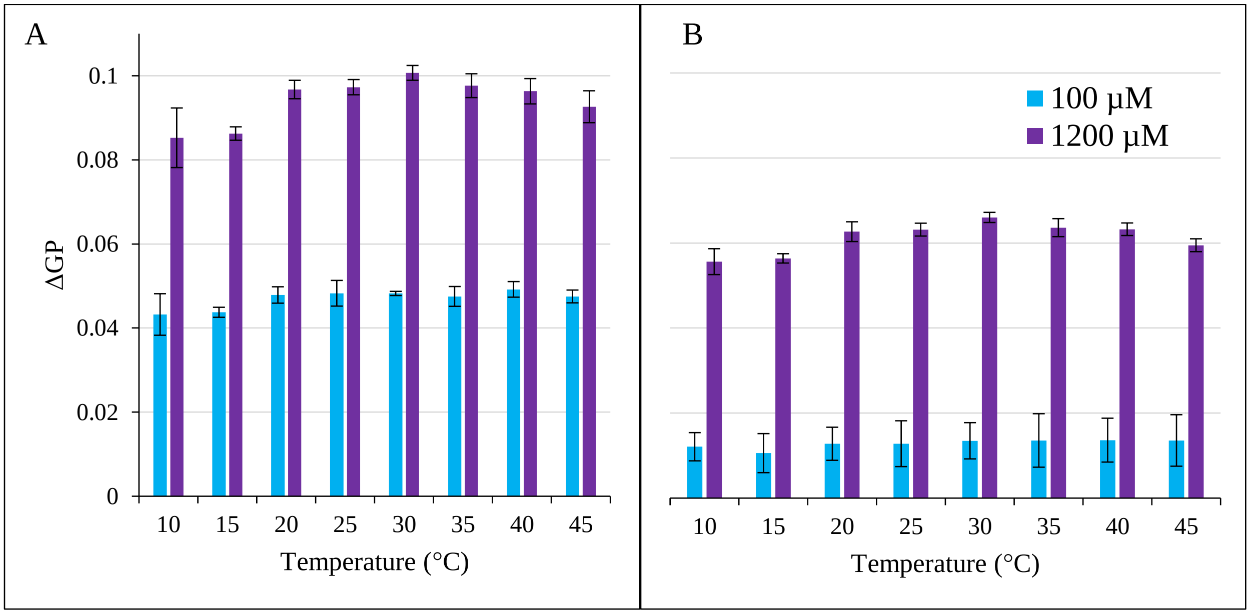

Figure 30. Change in GP induced by (A) Co^{2+} or (B) Ni^{2+} in 0.3 mM POPG liposomes in 20 mM Hepes, 100 mM NaCl pH 7.4.

In other systems, the metal concentrations used were limited because of aggregation or excessive Laurdan quenching. However, this was not a problem with POPG, so excess metal could be tested up to 1200 µM, which is 4x the lipid concentration at 300 µM. The effects show no temperature-dependence, reflecting the fact that it is a fully-melted membrane. As was the case for the other lipid systems, the effects of Co^{2+} were stronger than the effects of Ni^{2+} (ΔGP of 0.10 vs. 0.07 at 30°C with 1200 µM metal). Despite the higher concentrations tested, the effects of Co^{2+} on TOCL were greater than on POPG, while the effects of Ni^{2+} were comparable. The interactions of Co^{2+} and Ni^{2+} with the more rigid DMPG are summarized in Figure 31:

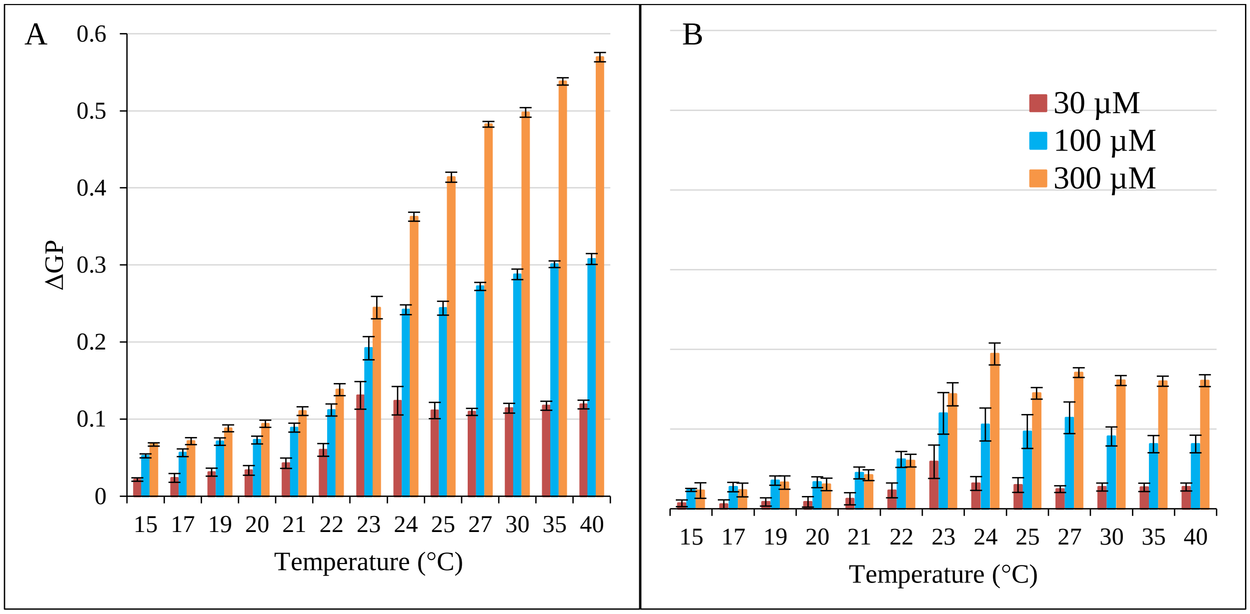

Figure 31. Change in GP induced by (A) Co^{2+} or (B) Ni^{2+} in 0.3 mM DMPG liposomes in 20 mM Hepes, 100 mM NaCl pH 7.4.

As was the case with the other DM lipids tested, the interactions of Co^{2+} and Ni^{2+} reached their full effect once the membrane transitioned to the liquid crystalline phase (after 23°C). However, in contrast to DMPA and TMCL, both Co^{2+} and Ni^{2+} were able to induce significant rigidification in the gel phase of DMPG (15–21°C) suggesting that the gel phase packing of DMPG is still able to accommodate the metals. The rigidifying effects of both Co^{2+} and Ni^{2+} were remarkably strong, as 300 µM Co^{2+} maintained GP values similar to a gel phase-like membrane even after melting (ΔGP of 0.54 at 35°C). A comparison of the results for both PG lipids, clearly shows that the tighter-packing acyl chains of the DM lipids are much more preferable for metal binding, which has also been observed with Cd^{2+} (83). A previous study has found that Co^{2+} and Ni^{2+} associate with PG lipids with 1:1 association constants of 7.5 M^{-1} (Ni^{2+}) and 6.5 M^{-1} (Co^{2+}) in 1 mM Mops, 100 mM NaCl, 10 µM X-537A (ionophore) at pH 7.5 (77), suggesting the metals have at least a weak affinity. As well, a previous Laurdan study with various metal ions including Co^{2+} and Ni^{2+} found weak rigidifying effects on 91:9 DPPC/DPPG liposomes (ΔGP of 0.01–0.02) (112). The much stronger effects observed in this thesis were likely a result of using pure PG liposomes, as PC has been identified as a weak/negligible target (Section 3.1.2). The structure of the PG head group may constitute a protected binding pocket which results in strong rigidifying effects in a pure PG system.

3.5 Effects of Co^{2+} and Ni^{2+} on the Fluidity of PS Membranes

3.5.1 Background on PS

PS lipids were studied next, having a zwitterionic serine head group in addition to the negative charge on the phosphate, so the overall charge is -1.0. The serine carboxyl group was expected to be highly-accessible for metal binding, and indeed this has been previously found to be the case, as a ^{31}P-NMR and ^{13}C-NMR study with Co^{2+} found that 86% of metal complexed with the carboxyl alone or carboxyl and amine (205). PS is a biologically-relevant target to consider as it is a significant component of the plasma membrane, nearly exclusively localized to the inner leaflet (206–208). The externalization of PS to the outer leaflet is known to be a marker for apoptosis (207), a process which may be initialized by oxidation of PS as a result of oxidative stress (206). It can thus be envisioned that metal binding and possible oxidation of PS may affect this signaling process.

3.5.2 Laurdan GP of PS membranes

POPS was considered firstly, and a T_m of 13.6°C was observed, comparable to a DSC study which found a T_m of 13.9°C in 5 mM phosphate, 5 mM EDTA and pH 7.0 (209). The more rigid DMPS membrane exhibited a T_m of 36.9°C, again in agreement with a previous DSC study reporting 36.5°C in 10 mM HEPES, 100 mM NaCl, 0.1 mM EDTA pH 7.4 (210). The control melting curves of POPS and DMPS are shown in Figure 32:

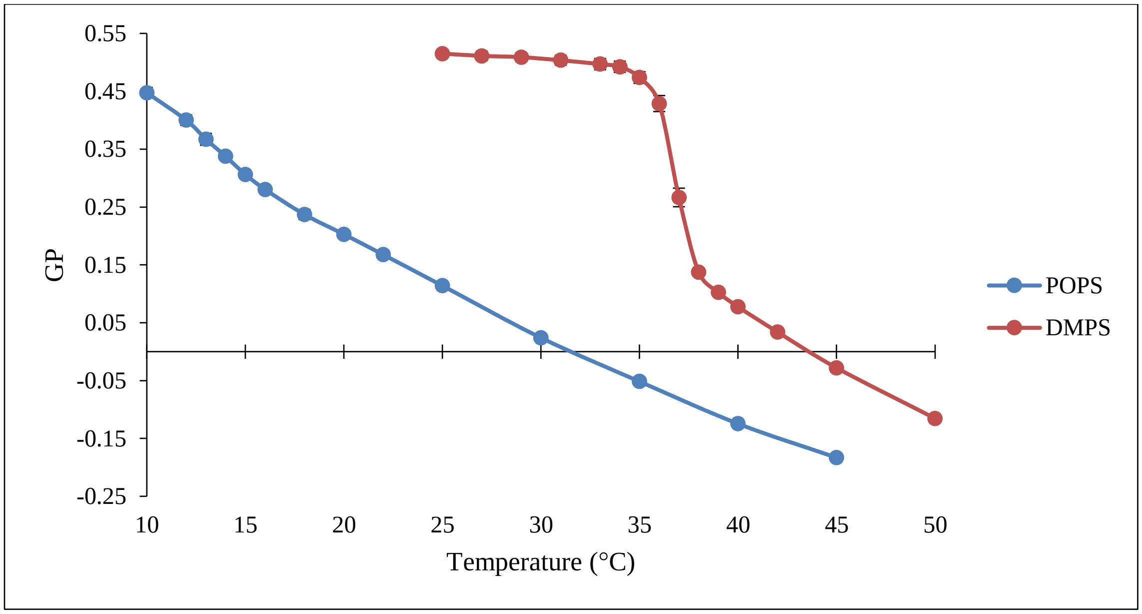

Figure 32. Laurdan GP melting curves of PS lipids in 20 mM Hepes, 100 mM NaCl pH 7.4.

The T_m's of both PS lipids were measurable, with POPS having the broadest melting transition observed, occurring very gradually over a long range, while DMPS had the sharpest transition observed, changing abruptly from a very rigid gel phase to a very fluid liquid crystalline phase. The interactions of Co^{2+} and Ni^{2+} with POPS are summarized in Figure 33:

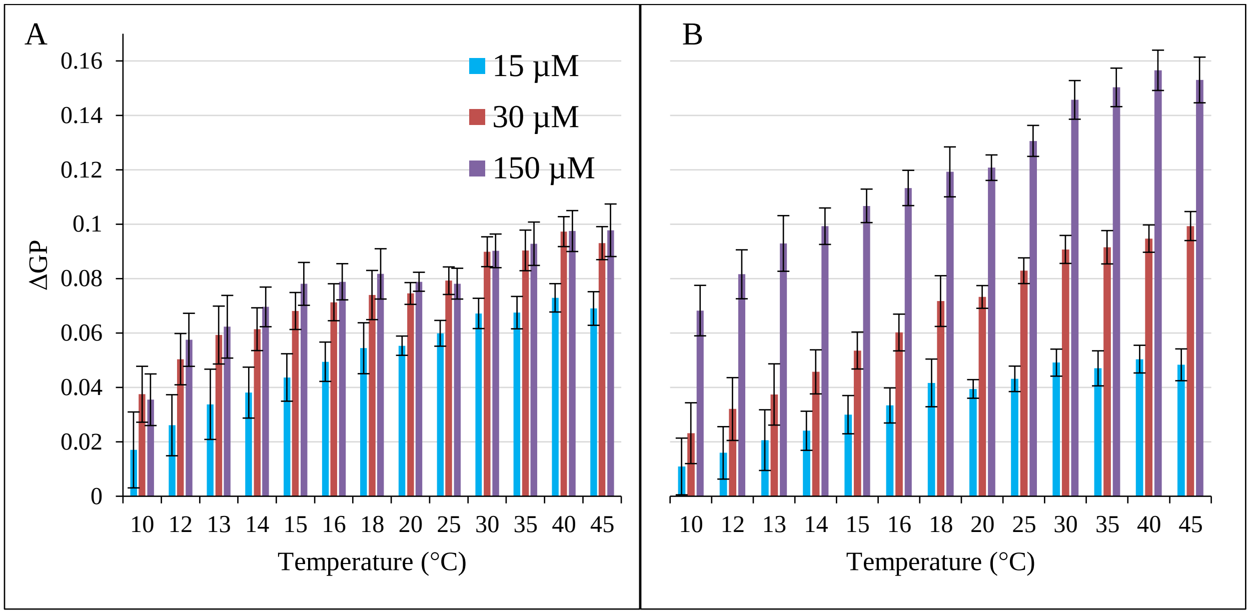

Figure 33. Change in GP induced by (A) Co^{2+} or (B) Ni^{2+} in 0.3 mM POPS liposomes in 20 mM Hepes, 100 mM NaCl pH 7.4.

The interactions with POPS stand in contrast to the results with the other negatively-charged lipids, in that the effects of Ni^{2+} were higher than that of Co^{2+}, due to the fact that the effects of Co^{2+} saturated at the low metal/lipid ratio of 0.1 (Figure 33). Below the saturation point (15 µM), the effects of Co^{2+} were still slightly stronger (ΔGP of 0.07 vs. 0.05 at 35°C), but above (150 µM), the effects of Ni^{2+} were much stronger (ΔGP of 0.09 vs. 0.15 at 35°C). This indicates that the binding capacity of the membrane for Co^{2+} is low. As well, likely due to the broad phase transition, the effects of the metals show a gentle temperature-dependence, similar to POPA. The effects of Co^{2+} and Ni^{2+} on DMPS are shown in Figure 34:

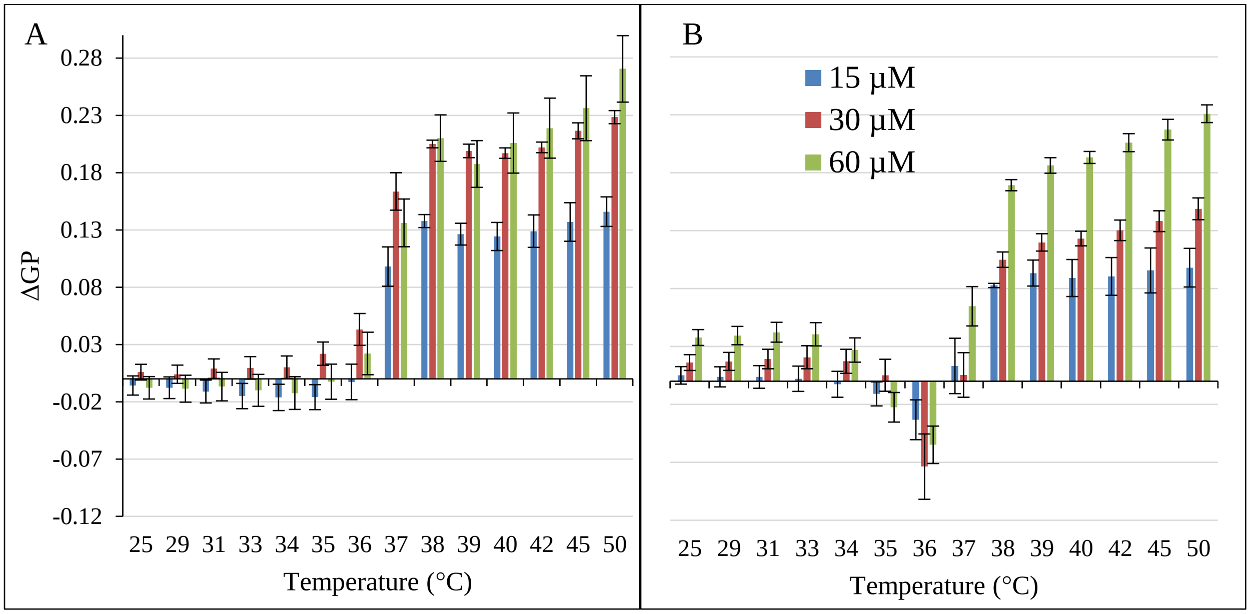

Figure 34. Change in GP induced by (A) Co^{2+} or (B) Ni^{2+} in 0.3 mM DMPS liposomes in 20 mM Hepes, 100 mM NaCl pH 7.4.

As with the other DM lipids, there is a strong temperature-dependence in the interactions with DMPS, but in this case > 30 µM Ni^{2+} was able to cause slight rigidification of the gel phase (25–34°C). Alike to the PGs, both metals cause greater effects on the DM version of the lipid. A very surprising finding with DMPS was that Ni^{2+} was able to slightly lower the T_m, leading to negative ΔGP values at the phase transition (36°C). This effect is uncharacteristic in metal-lipid interactions, which are generally found to increase or broaden the phase transition by bringing lipids closer together (83, 211). It is possible that the complexation geometry of Ni^{2+} is again affecting the interactions at the melting transition, as suggested for the interactions with PA lipids. The square planar geometry of Ni^{2+} (39) may interact with DMPS in such a way that it destabilizes the gel phase and causes it to melt early.

Like with POPS, the effects of Co^{2+} appear to saturate at the low metal/lipid ratio of 0.1, while the effects of Ni^{2+} increase further (Figure 34). However, the effects of 60 µM Co^{2+} and Ni^{2+} are quite comparable, causing ΔGPs of 0.21 and 0.19 at 40°C, respectively. In general, the large rigidifying effects observed with low concentrations of metal suggests that PS is the strongest binding target compared to the other lipid head groups. This is in agreement with previously-determined binding constants of Co^{2+} and Ni^{2+} to PS, at 28 M^{-1} and 40 M^{-1}, respectively, in 1 mM MOPS, 100 mM NaCl, pH 7.4 (76). As well, PS has been found to be a strong binding target of Cu^{2+}, suggesting that the accessibility of PS may be favourable for metal association overall (91).

3.6 Effects of Co^{2+} and Ni^{2+} on the Fluidity of PI Membranes

3.6.1 Background on PI

PI lipids have the most complex negatively-charged head group considered, consisting of an inositol ring which may be phosphorylated at any combination of positions: 3', 4', or 5' (64). PIs are among the major signaling lipids in the cell, involved in a wide variety of processes including cell survival, secretion and trafficking, and membrane regulation (64, 212). The lipid highlighted in this thesis is PI(4)P, which constitutes the largest pool of monophosphorylated PI in mammalian cells, being the main precursor to PI(4,5)P_2 (212). PI(4)P is localized in the plasma membrane and Golgi following its synthesis in the ER (212). PI(4)P is expected to carry a charge of -3.0 at pH 7.4, due to deprotonation of both the backbone and ring phosphates (213), as has been previously reported for PI(4)P at pH 8.0 (214). Thus, a single head group may have considerable metal-binding capacity.

3.6.2 Laurdan GP of PI membranes (work performed by Robyn)

A detailed screen of all PI lipids with various metals was performed by Robyn Mundle using a 99:1 POPC/DOPI model. I have analyzed her data for DOPI(4)P with which Co^{2+} had remarkably strong interactions. Results are shown below. I have also performed the data analysis and the discussion that is presented here.

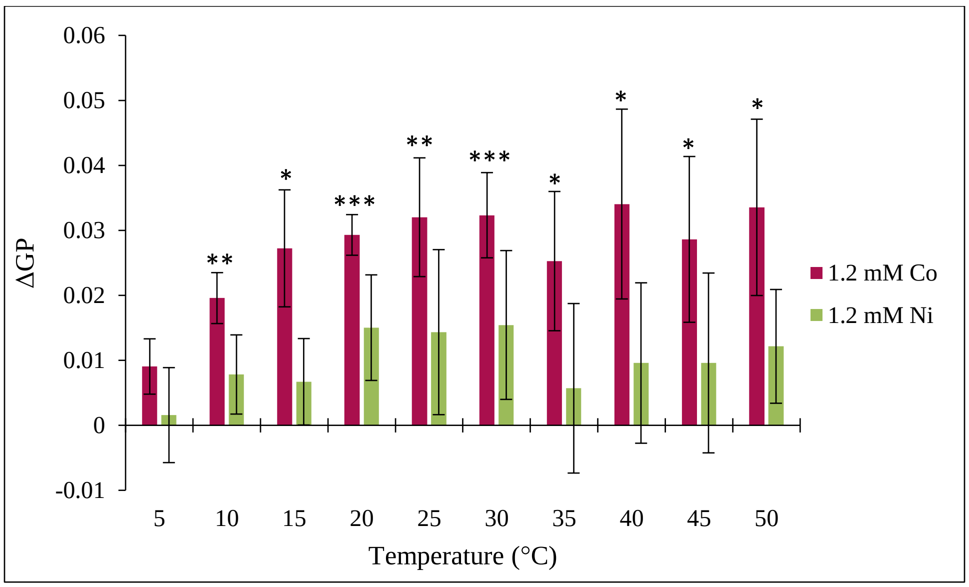

Figure 35. ΔGP induced by (A) Co^{2+} or (B) Ni^{2+} in 0.3 mM 99:1 POPC/DOPI(4)P liposomes in 100 mM NaCl pH 7.4.

The effects of Co^{2+} especially were found to be remarkably strong, given that only 1% PI was present in the membrane. For comparison, 1.2 mM Co^{2+} only induced a ΔGP approximately 3x larger in pure POPG (Section 3.4.2), suggesting that PI(4)P is a relatively strong binding target. The 4' position of the inositol ring is the furthest from the membrane backbone, and the results suggest that this is a highly-accessible position (215). Direct interactions of Co^{2+} and Ni^{2+} with PI(4)P have not been studied, but previous studies have suggested strong binding capacity of Ca^{2+} with $PI(3,4)P_2$ and $PI(4,5)P_2$ (216, 217). Given that Co^{2+} especially was able to affect membrane fluidity with only a physiological concentration of 1% PI present, it is quite possible that these interactions have biological relevance (212). Disruption to PI(4)P may have downstream effects on $PI(4,5)P_2$ signalling pathways and sphingolipid synthesis (212, 218).

3.7 Effects of Co^{2+} and Ni^{2+} on Liposome Size

Dynamic light scattering was used to monitor the liposome size in order to assess if Co^{2+} and Ni^{2+} are able to cause fusion/aggregation, which has been observed for metals such as Ca^{2+} (88) and Cd^{2+} (83).

3.7.1 Sizes of zwitterionic/neutral liposomes

The sizes of zwitterionic/neutral liposomes were found to be between 54–62 nm in radius and the polydispersity of the controls were <15%, unless otherwise stated. The changes in sizes of these liposomes incubated with 1.2 mM metal are summarized in Figure 36.

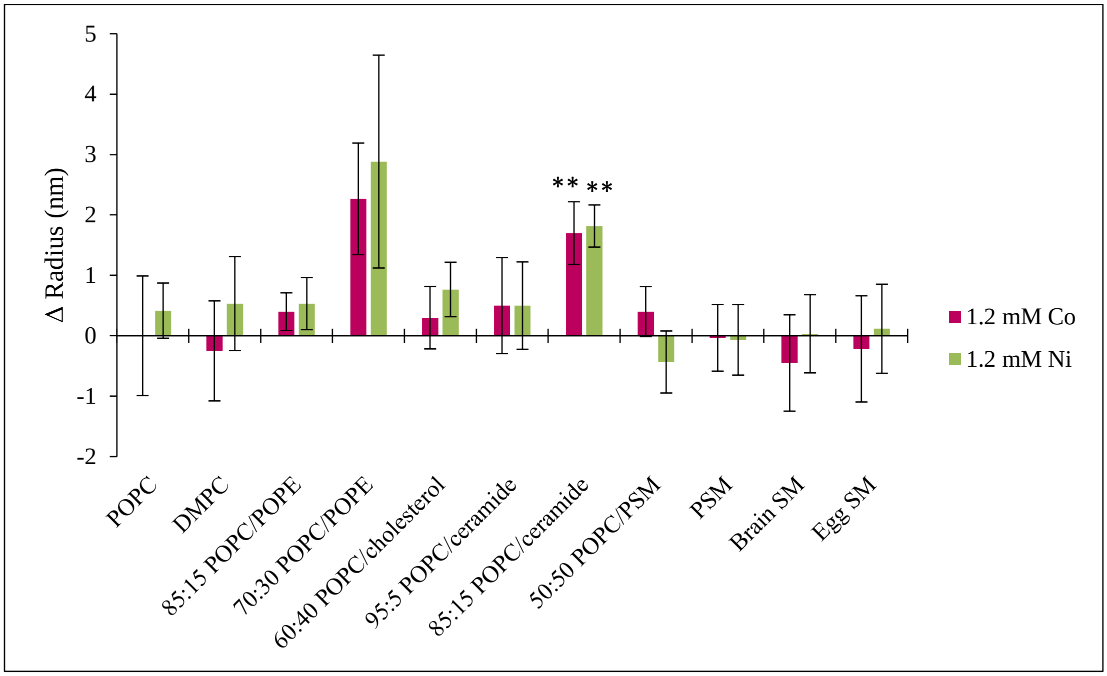

Figure 36. Change in liposome radius at 20°C induced by 1.2 mM Co^{2+} or Ni^{2+} in various zwitterionic/neutral lipid liposomes (0.3 mM) in 20 mM Hepes, 100 mM NaCl pH 7.4.

The results of DLS sizing data complement the general lack of interaction with zwitterionic/neutral lipids as observed with Laurdan GP (Section 3.1.2), showing only one significant effect of 1.2 mM Co^{2+} and Ni^{2+} with 85:15 POPC/Cera. However, the polydispersity index (PDI) >15% for the control indicated that forming these liposomes with a 50 nm radius was unfavourable, so the sizes may have been more easily perturbed by the metals. Although the minor size increases in 70:30 POPC/POPE are not significant, both metals were able to cause an increase in PDI % (Control: 12.7±0.55, Co^{2+}: 15.8±0.84, Ni^{2+}: 19.0±3.34) suggesting that they are able to cause slight swelling of PE, as previously reported for pure PE vesicles (191). The sizing data for 80:20 Egg SM/cerebroside has been excluded because of large aggregation in the control, suggesting that this composition is not stable as 50 nm liposomes.

3.7.2 Sizes of negatively-charged liposomes

In contrast, Co^{2+} and Ni^{2+} were found to have significant effects on the sizes of some negatively-charged lipid systems, PA and PS, which are shown in Figure 37:

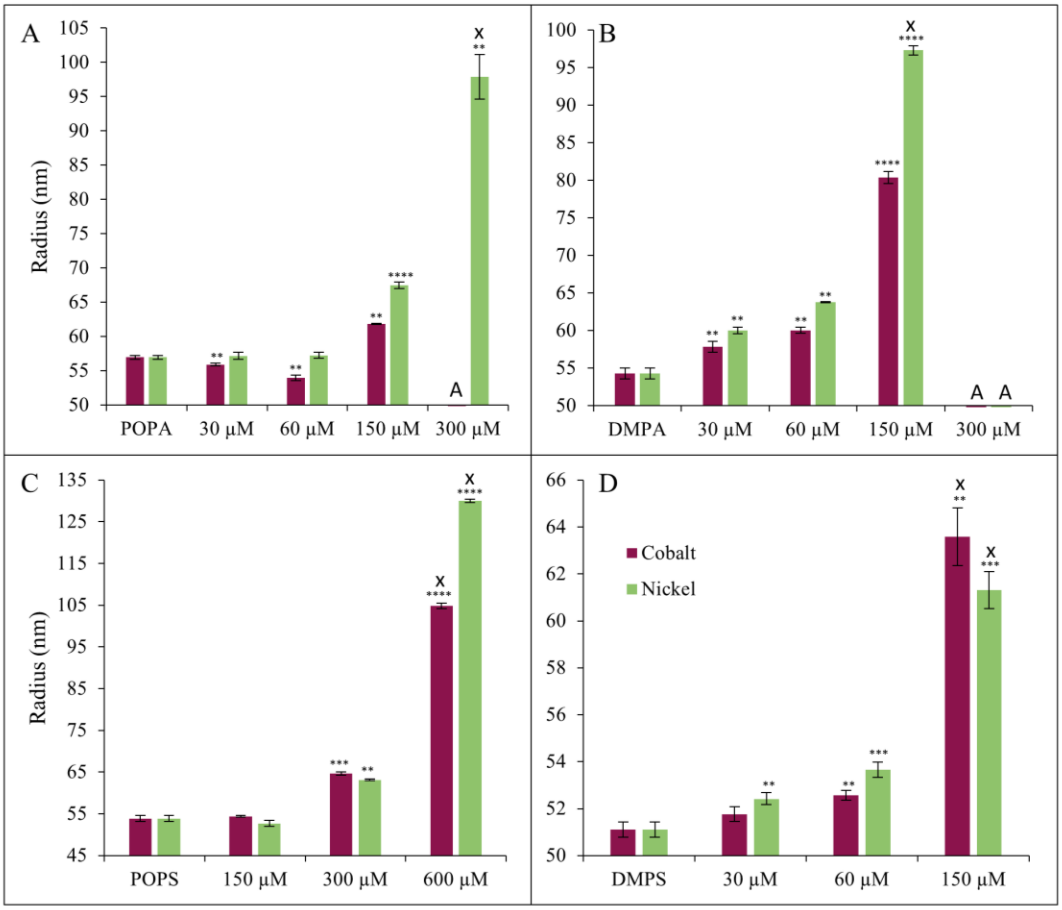

Figure 37. Sizes of liposomes (A) POPA, (B) DMPA, (C) POPS, (D) DMPS incubated with various concentrations of Co^{2+} and Ni^{2+} in 20 mM Hepes, 100 mM NaCl pH 7.4 at 20°C. (x = polydispersity >15%, A = aggregation).

The amount of metal required to induce size changes and aggregation differed with each lipid system. The system which aggregated at the lowest concentration for both metals was DMPS, in which 150 µM metal significantly increased the polydispersity despite only a 10 nm increase in average size (Figure 37D). Although Ni^{2+} also began aggregation of DMPA at this concentration. In contrast, POPS only exhibited significantly swelling at 300 µM metal which is equimolar to the lipid concentration. Aggregation only occurred when the metal was in excess. This agrees with the Laurdan data which suggested a stronger metal effect for DMPS over POPS. This trend was also seen for PA lipids, as similar concentrations induced greater swelling in DMPA over POPA, eventually leading to precipitation in both systems. However, lower concentrations of Co^{2+} (<60 µM) were found to cause minor shrinking of POPA liposomes, which suggests that the membrane may pack together more tightly, possibly due to head group dehydration (219). Swelling and aggregation/fusion of PA and PS liposomes has been previously reported for other ions such as Cd^{2+} (83) and Ca^{2+} (88, 220). Co^{2+} and Ni^{2+} appear to have a stronger propensity to induce size changes than Cd^{2+}, which may be due to the fact that $CdCl_2$ speciates into 66% $CdCl^{+}$, 27% $CdCl_2$, and 7% Cd^{2+} (83), while Co^{2+} and Ni^{2+} are almost entirely divalent (32). The fact that swelling and rigidifying effects occur simultaneously may suggest that metal complexation results in increased spacing between lipid head groups which increases liposome size but limits mobility overall.

Interestingly, though the sizes of PA and PS liposomes were significantly affected by Co^{2+} and Ni^{2+}, little-to-no change was induced in PG and CL, aside from minor shrinking of DMPG (3–4 nm decrease with excess metal). This lack of effect on PG and CL has also been reported for Cd^{2+}, though 2 mM Cd^{2+} was able to cause swelling in TMCL (83). This may suggest that the structure of PG and CL head groups do not allow effective intra-liposome complexation. It is possible that the protected phosphate of PG and the low surface charge density of CL does not support head group bridging by metal ions. Additionally, minor shrinking was observed by Co^{2+} and Ni^{2+} with 99:1 POPC/DOPI(4)P.

3.8 Effects of Co^{2+} and Ni^{2+} on Membrane T_m

Another property of pure lipid membranes which may be affected by metal binding is the phase transition temperature, which was determined by Laurdan GP melting curves. The changes in T_m induced by the metals are summarized in Table 8:

Table 8. Change in melting temperatures (ΔT_m) of lipid membranes incubated with various concentrations of Co^{2+} and Ni^{2+} in 20 mM Hepes, 100 mM NaCl pH 7.4, as determined by Laurdan GP. (n.s.) refers to measured changes which were not significant and (-) refers to concentrations that were not measured for that system.

System	Metal	ΔT_m (°C)					
		15 µM	30 µM	60 µM	100 µM	150 µM	300 µM
POPA (20.5±0.1°C)	Co^{2+}	0.4±0.2	-	0.6±0.1	-	1.4±0.2	-
	Ni^{2+}	0.2±0.1	-	0.6±0.1	-	0.8±0.1	-
DMPA (47.4±0.2°C)	Co^{2+}	n.s.	0.8±0.1	1.2±0.2	-	-	-
	Ni^{2+}	0.3±0.1	-	0.8±0.1	-	-	-
TMCL (40.4±0.2°C)	Co^{2+}	n.s.	-	1.0±0.2	1.2±0.2	-	2.7±0.2
	Ni^{2+}	n.s.	-	0.5±0.2	-	-	1.6±0.2
DMPG (23.2±0.1°C)	Co^{2+}	-	0.6±0.1	0.9±0.1	1.8±0.1	-	5.7±0.1
	Ni^{2+}	-	n.s.	-	1.5±0.1	-	2.0±0.1
POPS (13.6±0.1°C)	Co^{2+}	n.s.	0.6±0.2	-	-	1.0±0.3	-
	Ni^{2+}	n.s.	-0.4±0.2	-	-	0.5±0.1	-
DMPS (36.9±0.1°C)	Co^{2+}	0.4±0.2	0.6±0.1	n.s.	-	-	-
	Ni^{2+}	n.s.	-1.0±0.2	-1.5±0.1	-	-	-

In general, Co^{2+} and Ni^{2+} had small effects on the T_m, increasing by 1–2°C in a concentration-dependent manner. The metals generally caused the phase transition to become less sharp, indicating of a less-cooperative melting process (221), which has been previously found for the interaction of Ca^{2+} with DMPS in a DSC study (222). This may be explained as the metal-induced disruption of membrane homogeneity by creating patches of highly-rigid clustered lipids and subsequent voids. A previous study measured the effects of metal ions on the T_m of TPCL, which is a fully-saturated membrane like TMCL, and found that Co^{2+} induced the smallest T_m shift (+11.8°C), while Ca^{2+} induced the largest shift (+48.8°C) from the sodium salt, a trend which appeared to be correlated with the ion size (73). This agrees with the finding that the smaller ions Co^{2+} and Ni^{2+} shifted the T_m of TMCL to a lesser extent than has been previously shown for the larger ion Cd^{2+} (83).

The largest T_m shifts observed here were for DMPG, in which 300 μM Co^{2+} and Ni^{2+} increased the T_m by 5.7 and 2.0°C, respectively. A previous study using Cd^{2+} similarly found dramatic increases in the T_m of DMPG whereby the sharp transition was maintained (83). The effects of Co^{2+} and Ni^{2+} were instead accompanied by significant broadening of the transition. The strong effects of metals on DMPG may be a quality of the lipid itself, as the phosphate binding position may provide a protected binding pocket. As mentioned in the Laurdan GP section for PS (Section 3.5.2), there was the remarkable finding that Ni^{2+} was able to decrease the T_m of DMPS by 1.5°C (60 μM). Again, this does suggest that the binding of Ni^{2+} causes early gel phase destabilization.

The melting trends of DMPA and DMPG in the presence of metals were also verified with DLS data during temperature scans, and the determined T_m's agreed within 2% with the Laurdan T_m's (Appendix A).

3.9 Binding of Co^{2+} and Ni^{2+} to MLVs

3.9.1 Background on membrane binding and dehydration

Although changes in Laurdan GP can indicate relative strength of effect on various membranes, the technique reports on the hydration of the membrane (150), and as such, does not distinguish between direct binding/clustering effects versus disruption of associated water . It has been previously shown that Ca^{2+} induces dehydration in DPPG (223) and DMPS (209). The association and coordination of metals within the water layer depends on the metal ion as well as the lipid (219). *In vivo*, the net negative charge of the membrane attracts counterions such as Na^{+} and Ca^{2+} such that the layer surrounding the membrane contains different local concentrations of ions than the bulk, which would also affect the attraction of Co^{2+} and Ni^{2+} to the membrane (224). It was suspected that Co^{2+} and Ni^{2+} may affect the relative fluidity of the membrane by disrupting/displacing water molecules associated with the membrane surface along with direct binding, as binding constants have been reported to be quite weak (75–77). An additional consideration is that metal ions themselves are hydrated, as Co^{2+} and Ni^{2+} coordinate H_2O octahedrally with hydration free energies of -272.5 and -292.6 kcal/mol, respectively (225, 226).

The binding capacity of Co^{2+} and Ni^{2+} to the various classes of lipids was assessed by: incubating MLVs with metal, pelleting MLVs, and assaying the supernatant for remaining Co^{2+} and Ni^{2+} by Calcein quenching, as this avoids the complication of ternary lipid-metal-dye interactions (227). A preliminary screening tested PO and DM versions of PA, PS, PG, CL, and PC lipids upon incubation at 25 or 37°C with metal at a 1:1 molar ratio. The results suggested that PA/PS had the most associated metal (50% bound), while PG was the least-associated lipid (<10% bound) (aside from the negative control PC), and that there was no difference with incubation temperature (Appendix A).

However, it became clear that there were some drawbacks to the assay, such as vesiculation of MLVs into LUVs even after washing, as well as differences in pelleting efficiency between lipid systems and upon treatment by Co^{2+} and Ni^{2+}. Thus, the results are likely not useful for quantitative analysis but rather provide insight into the relative affinities. By measuring the MLV size using DLS and assuming a bilayer thickness of 5.4 nm (228) and 4 bilayer structures within each MLV, it was calculated that approximately 27% of lipid would be accessible for binding on the outer leaflet (Appendix A). This approximation may be generous, as previous theoretical approximations have suggested only 11% exposed due to formation of 5–10 bilayers in an MLV of radius 700 nm (229). However, the MLVs obtained in the present study were smaller and, as such, likely contained fewer bilayers. A previous experimental study using various external lipid marker assays with PC/PE MLVs found that, on average, 23% of lipid was exposed (230), which is in better agreement with the approximation. The sizes of the MLVs and the remaining lipid fragments in the supernatant are shown in Figure 38:

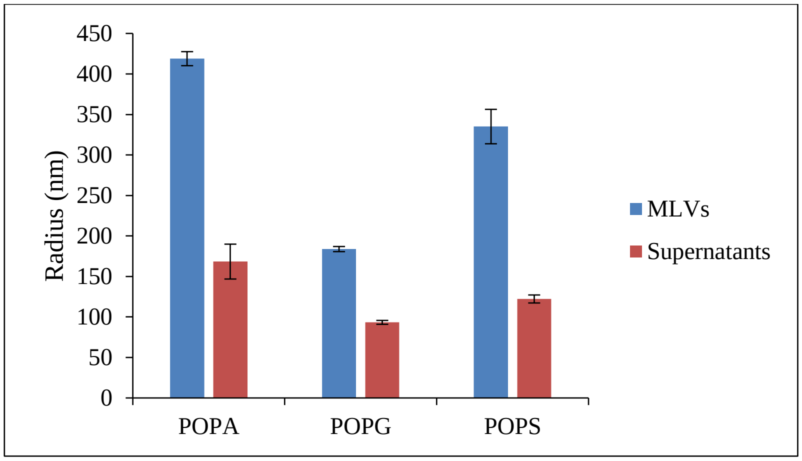

Figure 38. Radii (nm) of washed MLVs and remaining supernatants of lipid suspensions, as measured by DLS.

The POPA and POPS MLVs had larger radii than the than the POPG MLVs, but all samples showed detectable LUVs in solution after washing, which appear to have been a result of spontaneous vesiculation. Using the DLS-derived count rate as a rough approximation for concentration, POPG was also found to have the lowest pelleting efficiency (76%), compared to POPA and POPS (90%) (Appendix A). Thus, POPG appears to naturally form the smallest structures in solution (231, 232). The pelleting efficiencies of POPA and POPS were significantly increased by Co^{2+} and Ni^{2+}, but POPG was relatively unaffected (Appendix A), which was expected based on the lack of size change observed in LUVs (Section 3.7.2).

3.9.2 Binding to POPA MLVs

The highly-accessible POPA lipid was considered first, and it was found that a surprisingly large portion of Co^{2+} was able to bind, while Ni^{2+} also bound nearly all of the accessible sites (Figure 39).

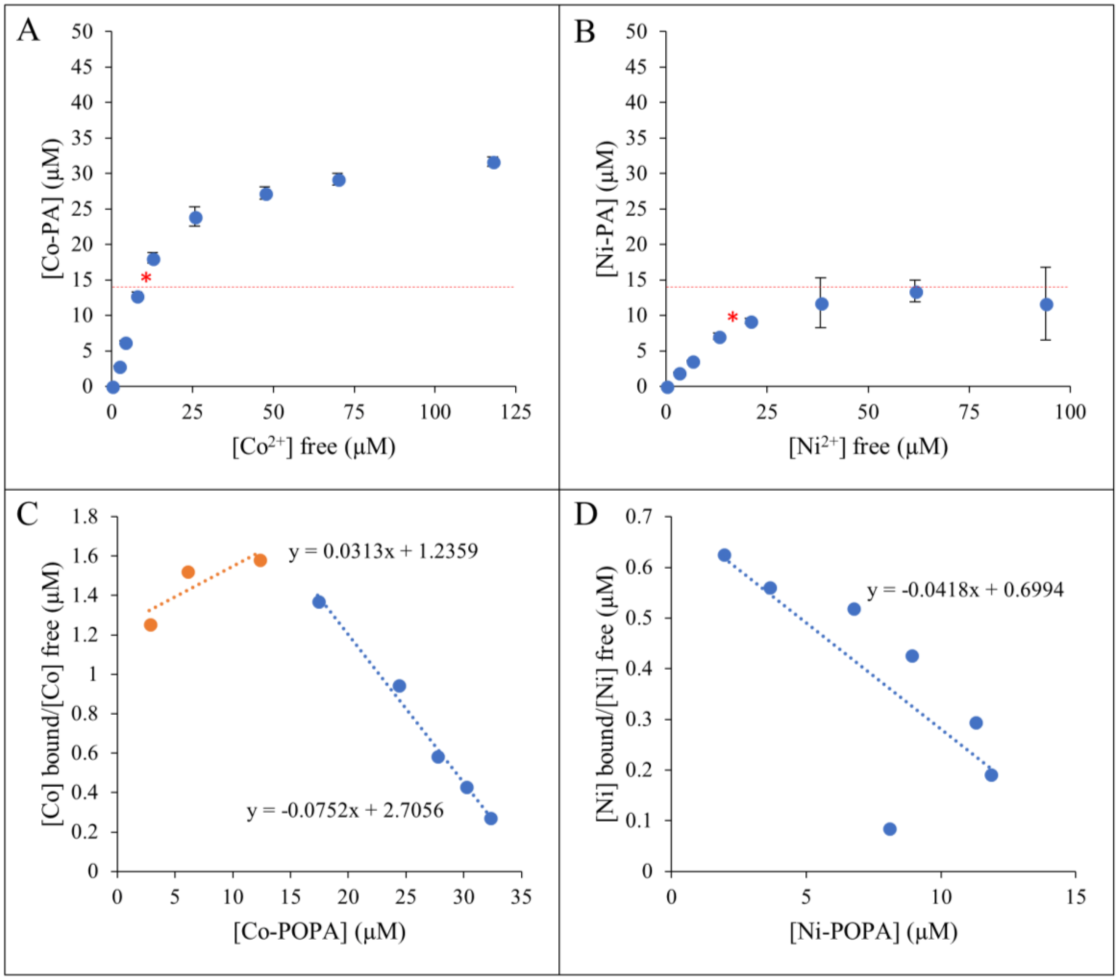

Figure 39. (A,B) Binding curves and (C,D) Scatchard plots of (A,C) Co^{2+} and (B,D) Ni^{2+} to 50 µM POPA MLVs in 20 mM Hepes, 100 mM NaCl pH 7.4. The expected accessible lipid is shown with a dashed red line. The point at which LUVs were found to swell is indicated by (*) (Section 3.7.2).

The binding of Co^{2+} surprisingly showed a pattern of positive cooperativity, in that regions of upward and downward slopes were present in the Scatchard plot (159). It is not clear why this occurs, but it is possible that a tighter lipid packing upon initial metal binding causes the membrane to become favourable for further binding. Additionally, assuming a 1:1

stoichiometry of binding, it was surprising to find that the amount of bound Co^{2+} was twice the expected accessible lipid. This suggests that: the amount of metal per lipid is higher, metal preferentially associates near the pelleted MLVs (219), and/or that MLV structure is severely disrupted upon binding, exposing more binding sites. All of these options may be possible explanations, as DLS indicated significant changes in the size and count rate detected by the instrument upon metal incubation. The point at which bound Co^{2+} increased past the expected threshold was upon incubation of 50 µM POPA with 20 µM Co^{2+}, which is nearly equivalent to the ratio at which significant swelling was observed in LUVs (Section 3.7.2). As well, the results do appear to complement the Laurdan GP data overall in that the affinity of Co^{2+} appears to be higher than that of Ni^{2+}.

3.9.3 Binding to POPG MLVs

Next, POPG was investigated, and the results were able to support the idea that membrane dehydration may be involved in rigidifying effects, as Co^{2+} was found to not significantly bind the membrane, even when present in 3x excess, such that the binding curve and Scatchard plot were flat (Figure 40).

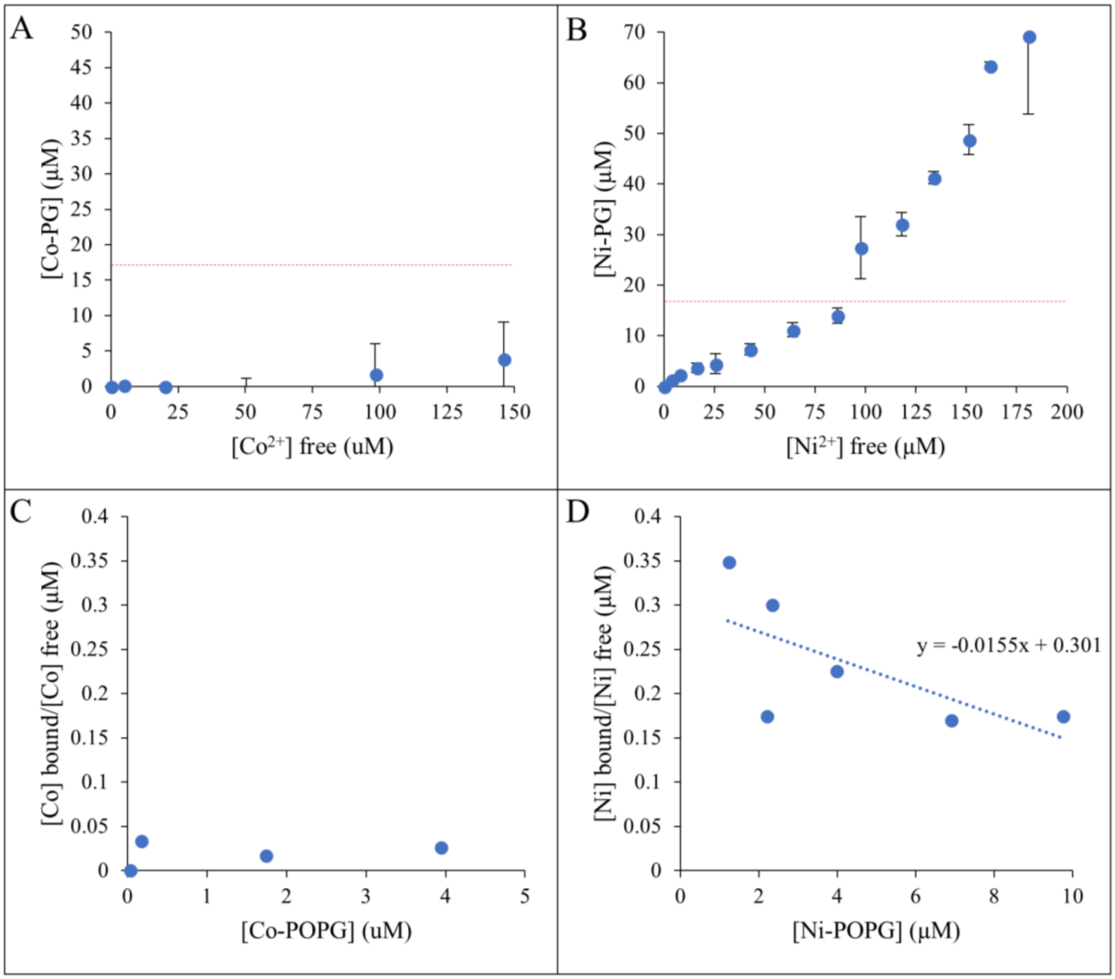

Figure 40. (A,B) Binding curves and (C,D) Scatchard plots of (A,C) Co^{2+} and (B,D) Ni^{2+} to 50 μM POPG MLVs in 20 mM Hepes, 100 mM NaCl pH 7.4. The expected accessible lipid is shown with a dashed red line.

Despite rigidification observed in Laurdan GP (Section 3.4.2), it appears that Co^{2+} does not strongly associate with POPG, as nearly all the input Co^{2+} was still measured in the supernatant. It is also possible that Co-PG binding is too weak to withstand the force of centrifugation, such that it is not measured by this assay. On the other hand, the binding of Ni^{2+} did fit the Scatchard plot poorly for the initial portion of the curve, showing weak binding.

Additionally, Ni^{2+} was apparently able to bind more lipid than was predicted to be accessible, and even past the total lipid (50 µM) in seemingly separate events. The same reasoning for this unexpected result may be applied as with Co^{2+} and POPA, though in this case only minor structural disruption was indicated in DLS (Appendix A). Therefore, this observation could suggest that a higher concentration of Ni^{2+} is localized near the membrane or that Ni^{2+} is able to bind to multiple sites on a single head group, thus causing apparent binding to exceed a 1:1 ratio. Either way, this complements the results of Laurdan GP, which found that rigidifying effects continued to increase past the 1:1 metal/lipid ratio (Section 3.4.2). As with POPA, the binding of Ni^{2+} does not appear to follow a cooperative mechanism.

The results thus suggest that the association of Co^{2+} and Ni^{2+} with POPG are different. Ni^{2+} appears to bind weakly to/around the membrane with high capacity, while Co^{2+} may only associate very weakly near the membrane, disrupting the water layer to cause rigidification. Water content is important for the phase behaviour of lipid membranes, so disruption would be expected to show effects on relative fluidity (233). A molecular dynamics simulation of a POPG membrane has suggested that water molecules are involved in the majority of hydrogen bonds in PG (234). Additionally, a DSC study found that the ejection of water allows for phosphate-glycerol hydrogen bonding which is accompanied by a more rigid phase (232), supporting the idea that removal of water may induce rigidification.

3.9.4 Binding to POPS MLVs

Next, the more complex serine head group of POPS was assessed for binding and, alike to Ni^{2+} with POPG, there appeared to be separate binding events occurring past an initial saturation point, though the binding of both metals was relatively strong (Figure 41).

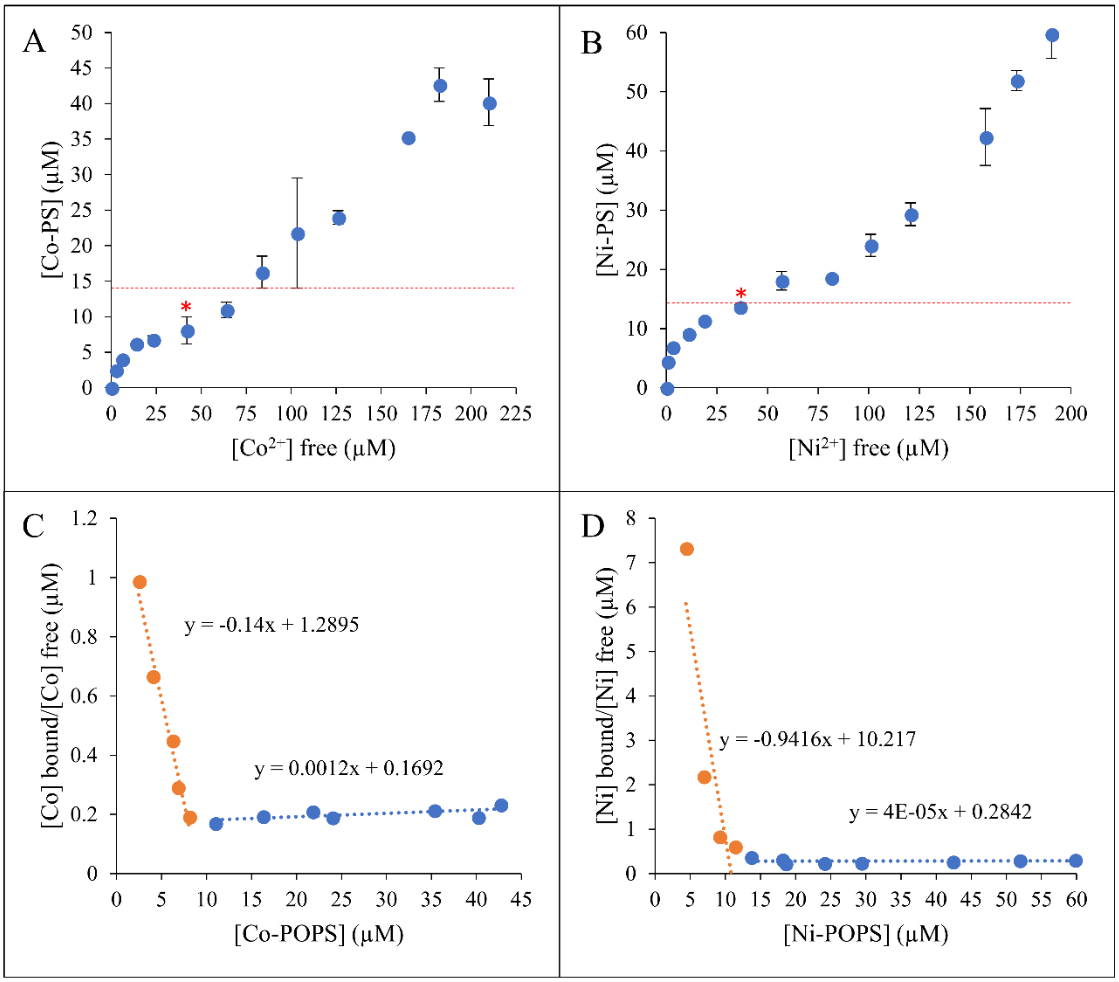

Figure 41. (A,B) Binding curves and (C,D) Scatchard plots of (A,C) Co^{2+} and (B,D) Ni^{2+} to 50 µM POPS MLVs in 20 mM Hepes, 100 mM NaCl pH 7.4. The expected accessible lipid is shown with a dashed red line. The point at which LUVs were found to swell is indicated by (*) (Section 3.7.2).

The Scatchard plots for the binding of Co^{2+} and Ni^{2+} to POPS indicate a strong interaction at low metal concentrations, which reaches rapid saturation following a negative cooperativity pattern (159). This suggests that the binding of metal decreases the favourability for further binding events, likely due to neutralization of membrane surface charge. The binding capacity of Ni^{2+} to POPS was found to be greater than that of Co^{2+}, again consistent with Laurdan GP findings. Interestingly, the secondary binding events began to occur around the LUV swelling point (Section 3.7.2), especially for Co^{2+}, which suggests that structural disruption may contribute to the secondary binding/association. Alike to POPG, the apparent bound Ni^{2+} was found to exceed that of the total lipid, again potentially due to greater than 1:1 binding or association within the water layer. The stronger affinity of Co^{2+} and Ni^{2+} for PS over PG has been previously demonstrated (76, 77).

3.9.5 Binding summary

There were several flaws with the assay including: differences in pelleting efficiency, possible removal of metal by centrifugation, and the inability to distinguish binding from "association" of metal ions with the pelleted region. However, differences between lipids and metals were apparent and generally provided support for previous results. The approximate K_d values and concentration of initial complex formation are given in Table 9:

Table 9. Dissociation constants (K_d) and saturated complex concentration for MLV systems tested using the centrifugation binding assay with 50 µM lipid in 20 mM Hepes, 100 mM NaCl pH 7.4. K_d were determined by the inverse slope of the Scatchard plot, and $[ML]_{saturated}$ was approximated from the binding curves.

System	K_d (µM)		$[ML]_{saturated}$ (µM)	
	Co^{2+}	Ni^{2+}	Co^{2+}	Ni^{2+}
POPA	13.3	23.9	30	12
POPG	n.d.	64.5	n.d.	10
POPS	7.1	1.1	8	15

The results indicate that the relative binding affinity for both metals follows the trend: PS > PA > PG, which is consistent with the strength of effect observed with Laurdan GP and previous studies (76, 77). However, the K_d values found here suggest a much higher affinity than the previously reported millimolar K_d values for Co^{2+} and Ni^{2+} binding to PS and PG based on zeta potential and ^{31}P-NMR studies (76, 77). This is likely because the binding assay used in this thesis also includes "associated" ions, which may not be directly bound. A previous ITC study on the binding of $CdCl_2$ and $HgCl_2$ to various membranes also found millimolar K_d values (235), aside from the binding of Hg to plasmalogens, which is in the range of 4–30 µM (85). However, in the absence of NaCl, Cu^{2+} has been previously reported to have incredibly high-affinity interactions with PS, in the picomolar range with 20% PS membranes, suggesting that metal-lipid interactions may be very strong (236).

One interesting result found in this thesis was the case of Co^{2+} with POPG, finding that Co^{2+} may not associate strongly with the membrane, despite changes in membrane fluidity. This suggests that Co^{2+} may affect membrane hydration without significant binding/ association, but binding may also just be disrupted in the assay by centrifugation, and thus was not observed. There were several cases in which the apparent bound metal was greater than the accessible and, sometimes, total lipid. The reasoning for this may be due to structural disruption of MLVs and/or association of metal near the hydration layer of the membrane in addition to direct binding. It is quite possible that a gradient of metal ions exists in the sample once the lipid is pelleted, such that any small portion of supernatant is an inaccurate measure of total supernatant. The assay requires quite a bit of improvement for further use.

3.10 Summary of Interactions with Simple Lipid Systems

The results for a variety of simple lipid systems have supported the hypothesis that metal-lipid interactions are electrostatic in nature, as little-to-no effects were observed with zwitterionic lipids, but instead with negatively-charged lipids to varying extents. For both metals, the strongest effects were observed in the liquid crystalline phase, suggesting that binding is more favourable in a disordered membrane. It is also possible that the gel phase cannot be made more rigid by metal binding. A summary of ΔGP induced by Co^{2+} and Ni^{2+} in the liquid crystalline phase of various pure systems is shown in Figure 42:

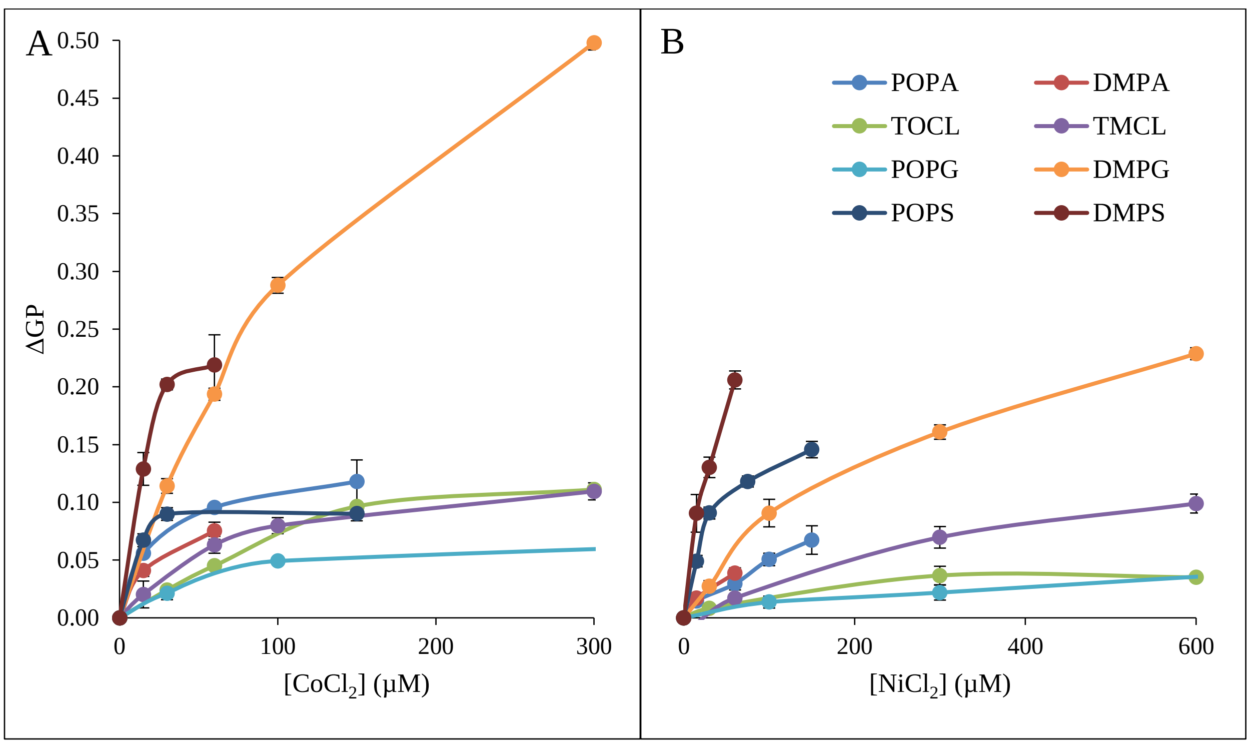

Figure 42. ΔGP induced by (A) Co^{2+} and (B) Ni^{2+} in the liquid crystalline phase of 0.3 mM: POPA (40°C), DMPA (54°C), TOCL (45°C), TMCL (47°C), POPG (40°C), DMPG (30°C), POPS (30°C), DMPS (42°C) in 20 mM Hepes, 100 mM NaCl pH 7.4.

While metal concentrations were limited to a lower range because of aggregation and/or Laurdan quenching, it is also clear that the effects of Co^{2+} saturated in nearly every system by 150 µM metal, at half the total lipid amount used for liposome preparation. This suggests that Co^{2+} likely binds most of the accessible lipid on the outer leaflet of liposomes.

The effects of Ni^{2+} were weaker overall in every system, except in POPS/DMPS in which they were higher or comparable to Co^{2+}. Also, in contrast to Co^{2+}, Ni^{2+} did not show such rapidly-saturating effects, suggesting that Ni^{2+} may bind with a 2:1 metal/lipid ratio, which seems unlikely given that it is divalent. It is also possible that simply the presence of additional Ni^{2+} in the local environment affects the fluidity. This was also suggested in the MLV binding data in which the apparent bound Ni^{2+} was sometimes greater than the accessible and total lipid.

At low concentrations, the effects of both metals on DMPS were by far the greatest, while at high concentrations, the effects on DMPG continued to increase, accompanied by the largest T_m shifts observed. The reasoning for this may be partially due to dehydration effects, which may account for the changes in POPG, as the binding assay suggested very weak association by Co^{2+} (Section 3.9.3). Ni^{2+} also had the unusual effect of decreasing the T_m of DMPS; the physical explanation for this is yet unclear but may be due to optimal binding geometry.

The Laurdan GP, sizing, and binding data have suggested that PS is a strong binding target for Co^{2+} and Ni^{2+}, which may be due to the high accessibility of the negative charge at the carboxyl group. For PG and PS, both metals also caused stronger rigidifying effects with the fully-saturated version of the lipid, which suggests that the tighter packing of the membrane allows for greater metal interaction. This was also observed for Ni^{2+} with CLs, but not for Co^{2+} which caused relatively strong effects on highly-fluid CL. Co^{2+} and Ni^{2+} only induced significant liposome size changes in PS and PA, suggesting that inter-liposome interactions are more favourable than with PG and CL.

Overall, both metals were found to induce significant changes in all types of pure negatively-charged membranes (187). As negatively-charged lipids are present as minor components in all cell membranes, it is difficult to predict their involvement in specific toxic effects, though certain lipids are highly-localized such as PG in lung surfactant (63) and CL in mitochondria (66). Thus, it was then considered if these effects would be maintained in complex biologically-relevant systems and what the consequence of such effects may be.

Chapter Four: Interactions of Co^{2+} and Ni^{2+} with Complex Membranes

Chapter Three investigated the interactions of Co^{2+} and Ni^{2+} with simple lipid membranes and showed that the metals interact with negatively-charged lipids PA, CL, PG, PS, and PI, while interactions with zwitterionic/neutral lipids are essentially negligible. The results suggested that PS especially is a relatively high-affinity target. While it was informative to firstly consider the effects in pure systems, it was also of interest to test the effects on complex biologically-relevant membranes which have minor amounts of negatively-charged lipids in varying proportions. The presence and availability of negatively-charged lipids is often important in signaling and protein function in the membrane. Thus, many processes may be affected by metal complexation. The complex membranes considered in this thesis included: commercially-available polar lipid extracts, model lung surfactant (LS), and red blood cells (RBCs).

4.1 Effects of Co^{2+} and Ni^{2+} on the Fluidity of Polar Lipid Extracts

The first set of complex membranes considered were liposomes composed of commercial polar lipid extracts from Avanti Polar Lipids (Alabaster, AL). The melting curves of the Brain, Heart, Liver, *S. cerevisiae*, and *E. coli* polar extracts are shown in Figure 43:

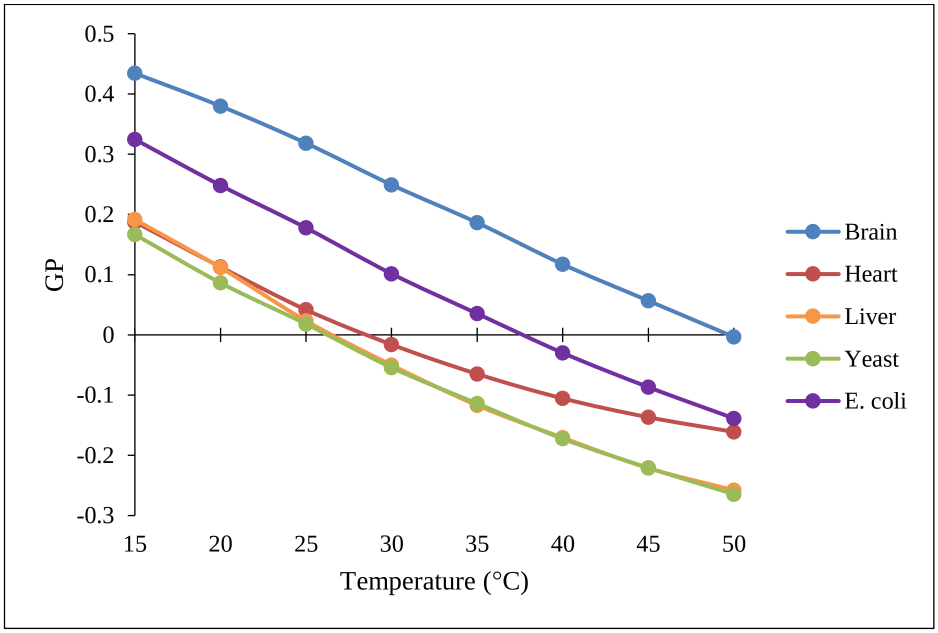

Figure 43. Laurdan GP melting curves of liposomes of Avanti Polar Lipid Extracts in 100 mM NaCl pH 7.4.

The Brain polar extract was found to be the most rigid of the extracts, likely a result of saturated acyl chains and cholesterol content, which was assumed to be 40% for the Ames assay (61, 92), as this was not explicitly stated. *E. coli* polar extract was also considerably rigid despite not containing sterols. This may instead be due to hydrogen bonding between PE and PG head groups, leading to a more rigid membrane (202, 203). The melting curves of Liver and *S. cerevisiae* polar extracts were quite similar despite large differences in composition, which suggests that membrane fluidity is not a sensitive indicator of compositional difference for complex membranes. The curves are all comparable to previous work in this lab (237, 238), though minor deviations (ΔGP of ~0.05) may indicate slight degradation of stock lipids. Based on the results with simple systems, which showed greater metal effects on the liquid crystalline phase, it was expected that the more fluid systems may be more easily impacted by Co^{2+} and Ni^{2+}. In addition to intrinsic fluidity, it is also necessary to consider the amount and nature of negatively-charged lipids, which are summarized in Table 10:

Table 10. Approximate molar percent negatively-charged lipid and major negative lipid component in each extract, as indicated in compositions of Avanti Polar Lipid extracts.

Polar Extract	% Identified negative	Main negative lipid
Brain	13.3	PS
Heart	1.8	CL
Liver	8.1	PI
S. cerevisiae	24.6	PI
E. coli	28.6	PG

The *E. coli* polar extract was expected to contain the greatest proportion of negatively-charged lipid, but the major species are PG, followed by CL (Section 2.5.1), which were identified as weaker targets, so effects were not expected to be strong. On the other hand, Brain, Liver, and *S. cerevisiae* polar extracts were expected to contain a larger proportion of high-affinity targets PS and PI. Lastly, Heart polar extract was reported as containing only a very small amount of negatively-charged lipid, with CL as the major species, though a substantial portion was also reported as unknown. Thus, the least effects were expected for Heart polar extract and the greatest effects for *S. cerevisiae* polar extract based on composition alone. As aggregation and Laurdan quenching were not found to be a problem in complex mixtures, metal concentrations below (30 µM), above (1.2 mM), and at the lipid concentration (300 µM) were tested, as well as 1.2 mM of each metal to test for relative competition.

4.1.1 Interactions of Co^{2+} and Ni^{2+} with Brain Polar Extract

The rigid Brain polar extract was considered first, and the effects of Co^{2+} and Ni^{2+} are shown in Figure 44.

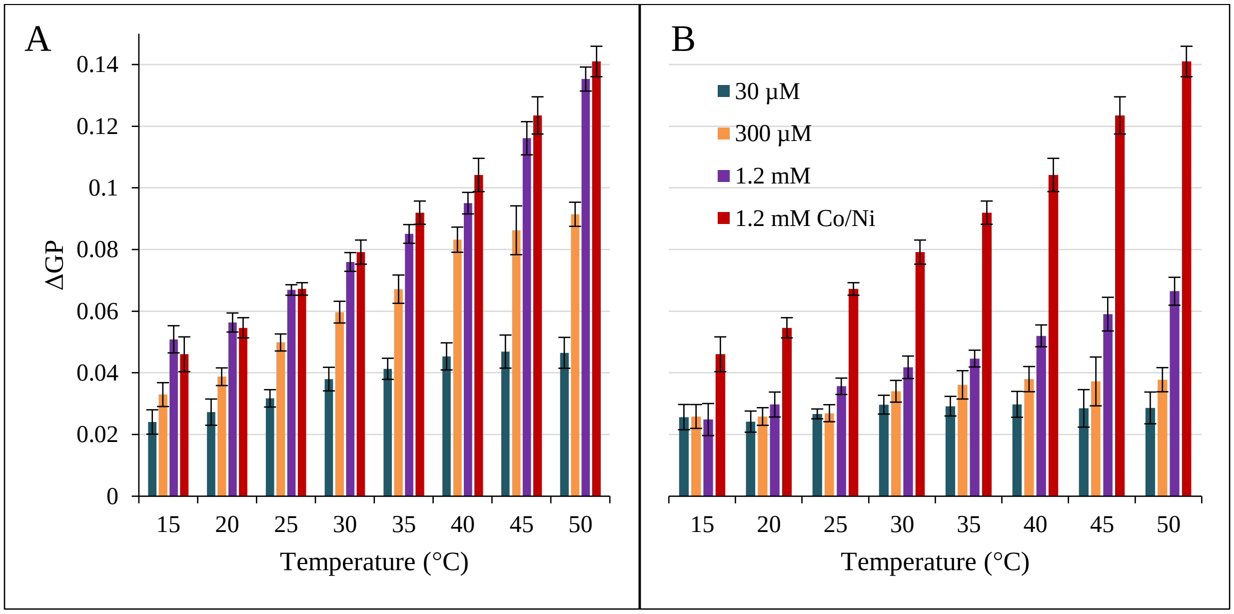

Figure 44. Change in GP induced by (A) Co^{2+} or (B) Ni^{2+} in 0.3 mM Brain polar extract liposomes in 100 mM NaCl pH 7.4.

Both Co^{2+} and Ni^{2+} induced significant rigidification at all concentrations and temperatures tested. Alike to the pure lipid systems, the overall effects of Co^{2+} were stronger than that of Ni^{2+}. However, the effects of Ni^{2+} appeared to nearly saturate at 30 µM, only increasing further at higher temperatures (30–50°C), suggesting high affinity as previously seen for pure PS. When 1.2 mM Co^{2+} and Ni^{2+} are present together, the effects are the same as that of 1.2 mM Co^{2+}, suggesting that Co^{2+} out-competes Ni^{2+} for the binding sites. The fact that the effects of Co^{2+} especially increase upon addition of excess metal suggests that the effects may represent interactions in addition to electrostatics, as only a small portion of the membrane is negatively-charged (Table 10). It is possible that dehydration effects may also occur to cause further membrane rigidification, or that the binding equilibrium requires excess metal. The effect of 30 µM of either metal is higher than would be expected if the ΔGP for pure PS is multiplied by the reported fraction of negatively-charged lipid. At 40°C, the theoretical ΔGP values are 0.013 for both Co^{2+} or Ni^{2+}, while the actual values are 0.045 and 0.030, respectively. This suggests that there may be additional high-affinity targets present in the "unknown" fraction of the composition, and/or that the complex mixture actually allows for more favourable metal interaction than a pure system. A previous study tested the interactions of various metal ions on rat neuronal membranes using electron spin resonance spectrometry and found that both Co^{2+} and Ni^{2+} increased the rigidity of the membrane, as observed here (74).

4.1.2 Interactions of Co^{2+} and Ni^{2+} with Heart Polar Extract

Next, Heart polar extract was tested, which was assumed to show little interaction due to the low negatively-charged lipid reported in the composition, as well as the high neutral lipid content. The ΔGP caused by Co^{2+} and Ni^{2+} is summarized in Figure 45:

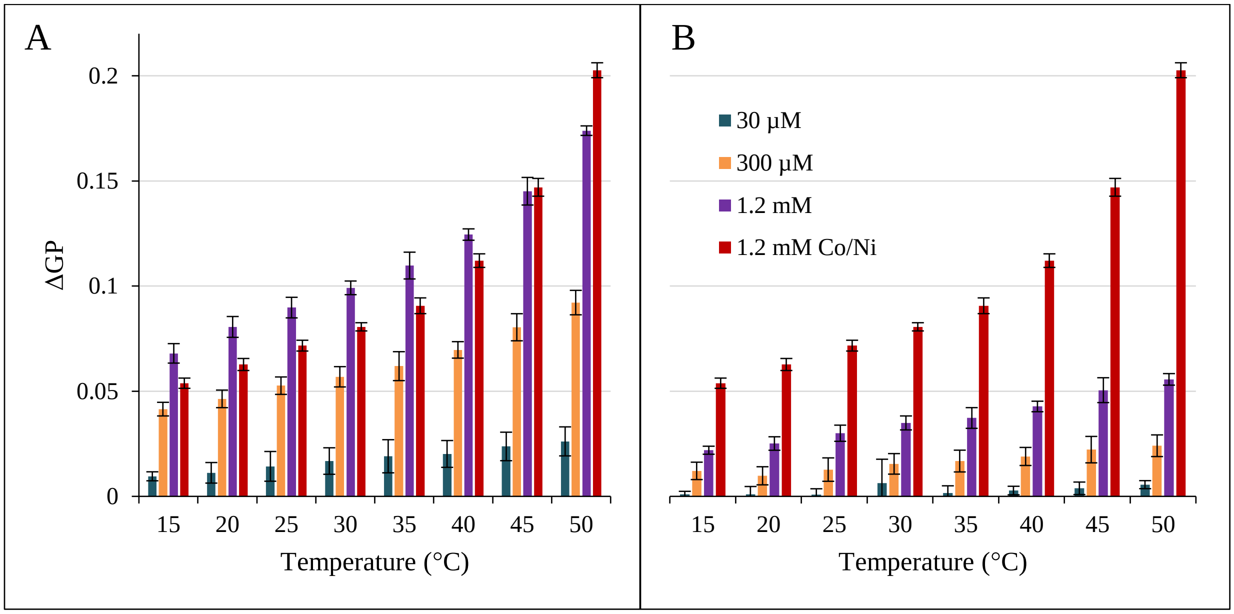

Figure 45. Change in GP induced by (A) Co^{2+} or (B) Ni^{2+} in 0.3 mM Heart polar extract liposomes in 100 mM NaCl pH 7.4.

Given the composition, the effects of Co^{2+} and Ni^{2+} on Heart polar extract were uncharacteristically strong, as only ~2% of the molar composition was reported as negatively-charged. In contrast to the effects with Brain polar extract, the effects of 1.2 mM Co^{2+} and Ni^{2+} together were generally slightly lower than with Co^{2+} alone. Again, the lack of saturation suggests that Co^{2+} and Ni^{2+} may also dehydrate the membrane or require excess metal to cause effects past the 1:1 metal/lipid ratio. However, the effects of 30 μM Co^{2+} and Ni^{2+} (ΔGP of 0.020 and 0.003 at 40°C) are lower than with Brain polar extract (ΔGP of 0.045 and 0.030 at 40°C), presumably due to a low amount of high-affinity binding targets like PS.

A surprisingly large effect on Heart polar extract has also been previously seen with Cd^{2+} (237). The Avanti lipid profile reports a portion of “unknown” lipid which was previously shown to have a negative zeta potential and was characterized by TLC using a reagent for phospholipid visualization (Section 2.6.1.1) (237). The unknown spot was stained blue, demonstrating that it is a phospholipid, and it ran to the same location as PG (237). The fact that there may be unreported negative charge present as PG/degraded CL helps to partly explain the very strong effects observed with Co^{2+} and Ni^{2+}. Pure DMPG was found to be very strongly rigidified by both metals, even though PG was found to be a weaker binding target compared to PS and PA. PS was also not reported in the composition but was indicated by TLC, thus it may also be part of the "unknown" content contributing to negatively-charged lipid. The neutral lipid content also appears to contain free fatty acids (237), which would carry a negative charge at pH 7.4. (239).

4.1.3 Interactions of Co^{2+} and Ni^{2+} with Liver Polar Extract

Next, the Liver polar extract was tested, and the effects are shown in Figure 46:

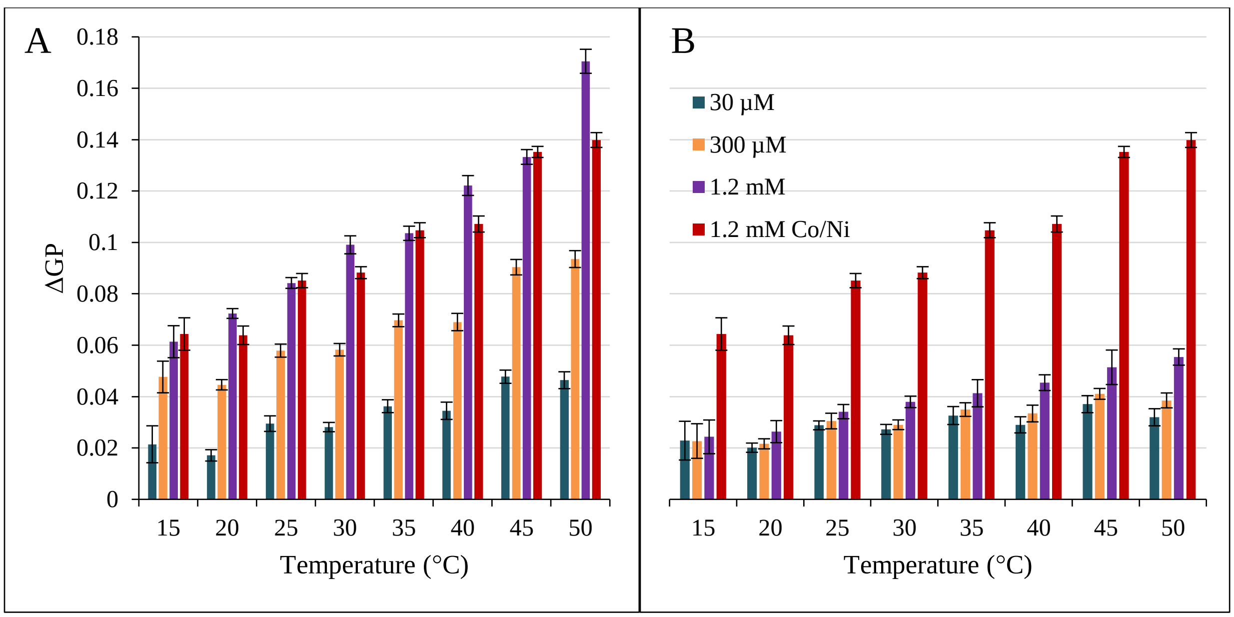

Figure 46. Change in GP induced by (A) Co^{2+} or (B) Ni^{2+} in 0.3 mM Liver polar extract liposomes in 100 mM NaCl pH 7.4.

The pattern observed in the interactions was similar to the Brain polar extract, especially considering that the effects of Co^{2+} increased past the 1:1 ratio, while the effects of Ni^{2+} were again essentially saturated by 30 µM. This is fully expected if the amount of exposed negative lipid is completely bound by Ni^{2+}, which again suggests that Co^{2+} may induce dehydrating effects or requires excess metal to reach equilibrium. The interactions at 30 µM (ΔGP of 0.034 and 0.029 at 40°C) were again greater than with Heart polar extract (ΔGP of 0.020 and 0.003 at 40°C), likely due to the presence of PI, presumed to be a high-affinity target. When 1.2 mM of each Co^{2+} and Ni^{2+} were present together, the effects were either unchanged or slightly higher than 1.2 mM Co^{2+} alone, which, like with Brain polar extract, suggests that Co^{2+} is dominant in binding.

4.1.4 Interactions of Co^{2+} and Ni^{2+} with S. cerevisiae Polar Extract

Next, polar extract of *S. cerevisiae* was tested, which was expected to be the most greatly-affected extract due to the high PI content. The results are shown in Figure 47:

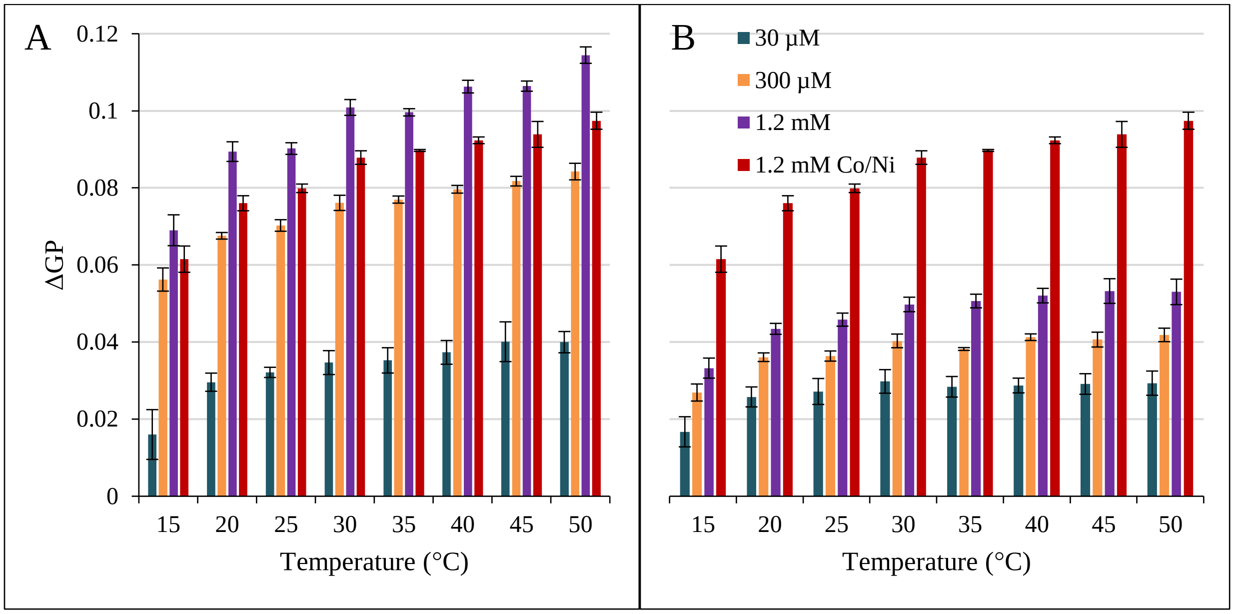

Figure 47. Change in GP induced by (A) Co^{2+} or (B) Ni^{2+} in 0.3 mM *S. cerevisiae* polar extract liposomes in 100 mM NaCl pH 7.4.

The effects on *S. cerevisiae* polar extract were not dramatically higher than Brain or Liver polar extracts at low concentrations, and certainly did not increase to the extent seen in Heart polar extract with high Co^{2+} concentrations. Thus, predicting effects appears to be more complicated than simply considering composition, as there are likely factors dealing with the packing of the complex membrane as a whole. One of the more interesting things which occurred, was that in the presence of 1.2 mM Co^{2+} and Ni^{2+}, the effects decreased relative to 1.2 mM Co^{2+} alone, suggesting that Ni^{2+} could out-compete Co^{2+} for binding sites. The targeted head group is not clear, but may be the fraction of PS, as Ni^{2+} was determined to have stronger binding affinity than Co^{2+} to POPS (Section 3.9.4) (76). A reason for why this may not have occurred in Brain polar extract could be due to the inherent fluidity of the membrane, as the Brain polar extract was much more rigid than the *S. cerevisiae* extract (Figure 43). It is possible that Ni^{2+} is only able to out-compete Co^{2+} in a sufficiently fluid membrane. This could be supported by the pure systems too, in that Ni^{2+} could affect POPS, but not DMPS, to a greater extent than Co^{2+} (Section 3.5.2).

4.1.5 Interactions of Co^{2+} and Ni^{2+} with E. coli Polar Extract

Lastly, the *E. coli* extract was tested, which contained the greatest fraction of negatively-charged lipid. The results are shown in Figure 48:

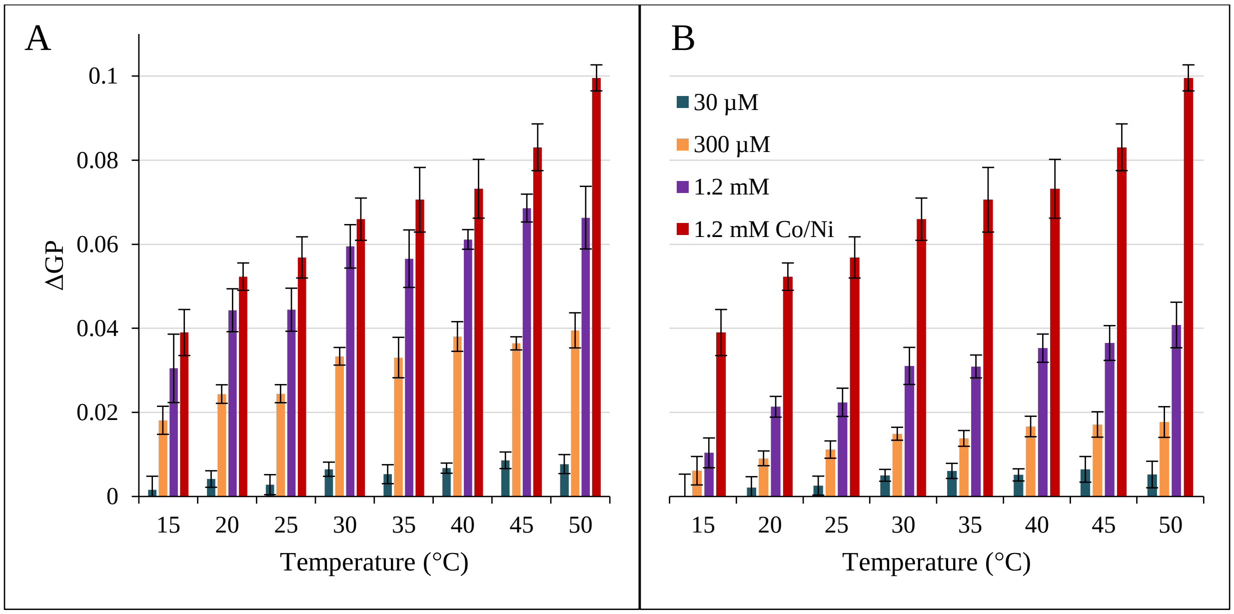

Figure 48. Change in GP induced by (A) Co^{2+} or (B) Ni^{2+} in 0.3 mM *E. coli* polar extract liposomes in 100 mM NaCl pH 7.4.

The effects on *E. coli* polar extract highlight the importance of the nature of the negatively-charged lipids, in that despite having the highest fraction of negative lipid, the effects were the weakest of the extracts. This is consistent with the finding that PG and CL were the weaker binding targets compared to PS and PA. Additionally, considerable hydrogen bonding within the bacterial lipids may shield head groups for interaction (202, 203). In contrast to the other systems, 30 µM metal induced little-to-no change in GP, suggesting much lower affinity than observed with other extracts. However, effects did continue to increase with higher concentrations, again suggesting that membrane dehydration or binding equilibrium plays a role. In a heterogenous membrane, inter-head group interactions will take place including electrostatics and hydrogen bonding which may influence the local membrane hydration (240). The effects of 1.2 mM Co^{2+} and Ni^{2+} together were slightly higher than Co^{2+} alone at high temperatures (40–50°C), suggesting that Ni^{2+} affects the membrane in addition to Co^{2+}.

4.1.6 Comparison of Polar Extracts

Overall, predicting effects based on composition alone were found to show some consistency, but there were also unexpected cases. If not for the uncharacteristically large effects of Co^{2+} on Heart polar extract, the prediction that *S. cerevisiae* extract would be most-affected, and *E. coli* extract would be weakly-affected generally holds. The effects of Co^{2+} and Ni^{2+} on the different extracts increased with metal concentration as well as temperature. A summary of Co^{2+} and Ni^{2+} effects near physiological temperature (40°C) are shown in Figure 49:

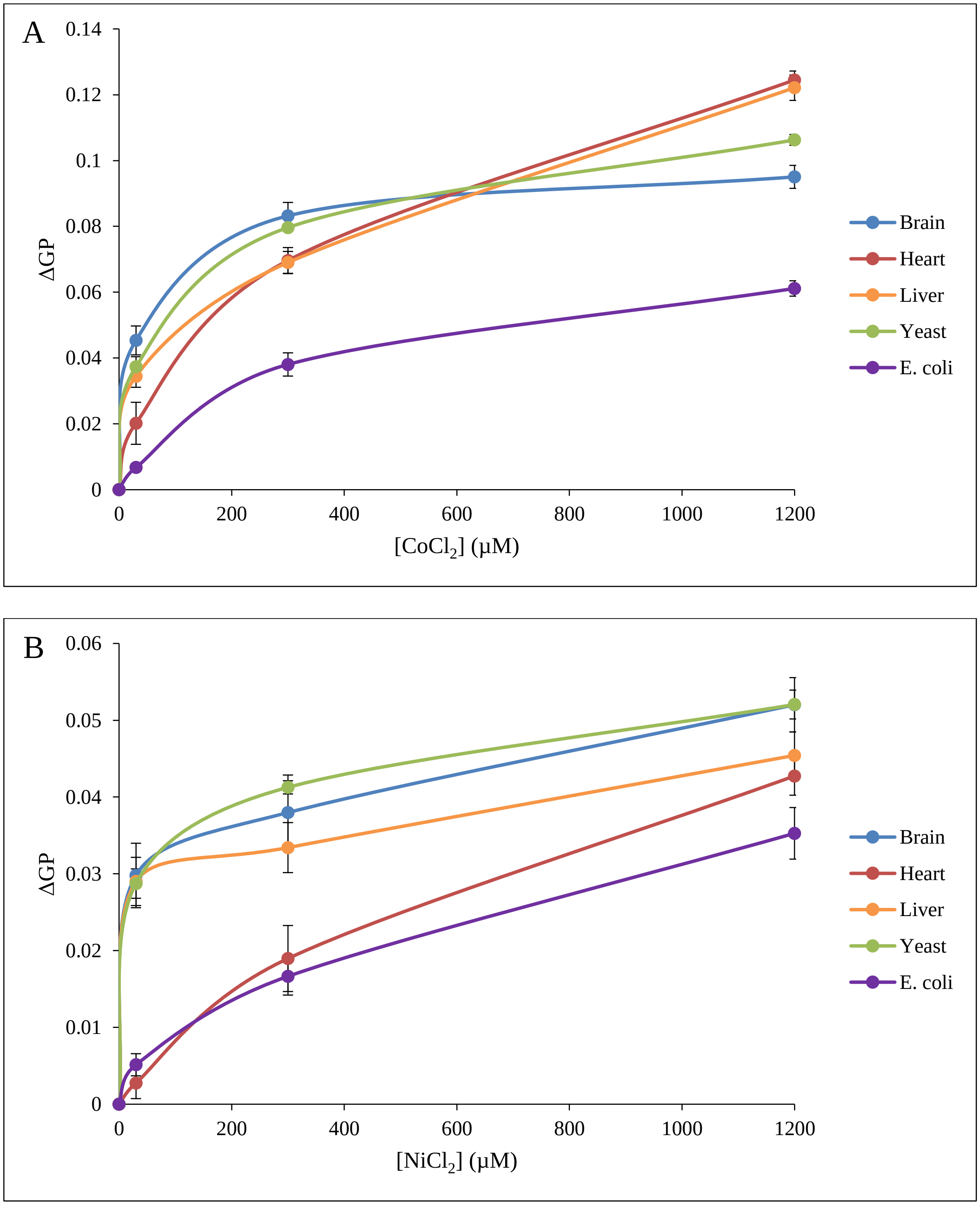

Figure 49. ΔGP induced by (A) Co^{2+} or (B) Ni^{2+} at 40°C in Avanti polar extracts in 100 mM NaCl pH 7.4.

At low concentrations, the effects on PS/PI-based systems (Brain, Liver, *S. cerevisiae*) are greatest, which is to be expected as these contain accessible, high-affinity targets. There did not appear to be an overall trend based on inherent fluidity of the whole membrane (Figure 43), suggesting that local packing and composition may be more important. The effects on the PS/PI-based systems generally follow similar patterns despite differences in amounts of negatively-charged lipid and inherent membrane fluidity. This suggests that even though *S. cerevisiae* extract contains much more PI than the others, the membrane packing may be relatively less favourable for binding. The PI of *S. cerevisiae* is different from the PI of mammalian cells in that sphingolipids in yeast also contain a PI head group, making it a structural lipid (141). Although, yeast do contain polyphosphorylated signaling PI as well (141). The major acyl chains present in *S. cerevisiae* are 16 and 18 C with one or no double bonds (141, 146), while Brain membranes generally contain longer-chained species with 18–22 C (241), and Liver membranes mainly contain 16, 18, and 20 C (60). The tighter packing expected in Brain and Liver extracts may allow for slightly stronger effects. Thus, this may compensate for the lesser amount of negatively-charged lipid compared to *S. cerevisiae*, as Co^{2+} and Ni^{2+} both showed greater effects on saturated vs. unsaturated PS. As well, at low concentrations the effects of Co^{2+} and Ni^{2+} are relatively similar, which may again be expected based on the comparable results for low metal concentrations with pure PS.

One characteristic which was quite different from pure systems was the saturating effect in PS/PI-based systems, as Co^{2+} was found to have large effects above 30 μM, while the effects of Ni^{2+} only increased slightly above 30 μM. Based on the pure systems, it would have been expected that the effects of Co^{2+} would saturate instead. This suggests that the favourability of metal association with the membrane surface is different for a complex membrane. It has been previously shown that ions such as Cu^{2+}, Be^{2+}, and Zn^{2+} significantly dehydrate POPC (219). Although Co^{2+} and Ni^{2+} were unable to affect pure POPC, it is possible that the heterogeneity of a complex membrane surface allows the metals to affect zwitterionic lipid head groups that otherwise would not be bound, leading to effects that were not predicted from pure systems alone. Additionally, the heterogeneity of the membrane likely results in packing defects (242) that may make complexation with negatively-charged head groups even more favourable.

The relative effects of Co^{2+} and Ni^{2+} on the fluidity of complex membranes were found to be higher than that shown for $CdCl_2$ and $HgCl_2$ in a previous study (237), and comparable or higher to that of $Pb(NO_3)_2$ (90). However, while the heavy metals were also able to induce changes in size of some of the polar extract liposomes (237, 238), Co^{2+} and Ni^{2+} were found to induce little-to-no change in the sizes or aggregation of any systems when 100 mM NaCl was present (Appendix B). This may suggest that the intra-liposome interactions are stronger than inter-liposome interactions, schematically represented in Figure 50.

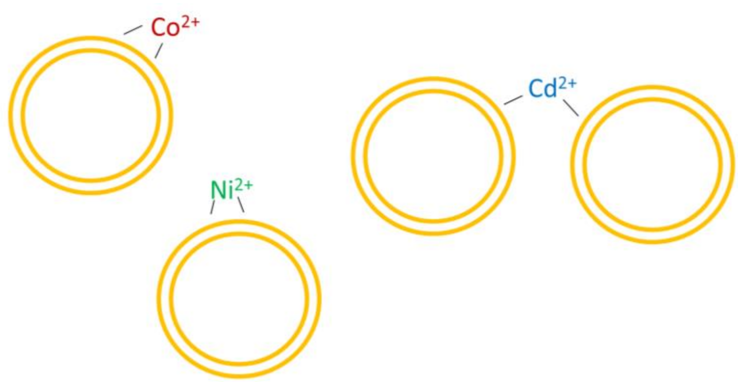

Figure 50. Schematic of intra-liposome interactions of Co^{2+} and Ni^{2+} compared to potential inter-liposome interactions of heavy metals such as Cd^{2+}.

The differences among these metals may be due to many factors including the size/electronegativity (Figure 2) (42, 43), complexation geometry (41), and speciation, as $CdCl_2$ and $Pb(NO_3)_2$ speciate mainly into MCl^+, while $HgCl_2$ speciates into $HgCl_2$ (35%), $HgCl_3^-$ (30%), $HgCl_4^{2-}$ (35%) (32) and does not interact with negatively-charged lipids, but instead targets plasmalogens (83, 85).

Overall, the induction of significant rigidifying effects in various complex membranes with low concentrations of Co^{2+} and Ni^{2+} suggests that these interactions may have some biological relevance. Considering various extracts is interesting to contrast compositional factors, but in terms of toxicity, it appears that membranes enriched in PS/PI lipids may be susceptible to direct Co^{2+} and Ni^{2+} binding, even when metals are present at low concentrations. The effects on Brain polar extract may have implications for neurotoxicity of Co^{2+} and Ni^{2+}. Both metals have been found to cause neurotoxic symptoms, though the mechanisms of this are unclear and may be due to reactive oxygen species, mitochondrial dysfunction, and genetic damage (18, 20). Additionally, Co^{2+} is known for its specific effects on the heart, resulting in cardiomyopathy (1). It is possible that a mechanism of this toxic effect stems from binding and disruption to the function of heart/mitochondrial membrane lipids.

4.2 Lipid Peroxidation of Heart Polar Extract

4.2.1 Background on lipid peroxidation via Fenton chemistry

It is well-understood that lipid peroxidation *in vivo* is a mechanism by which Co^{2+} and Ni^{2+} can exert damage to cell membranes (13, 46, 48). It is also understood that Co^{2+} and Ni^{2+} can undergo Fenton-like redox chemistry alike to Fe^{2+} (44, 81). However, many *in vitro* studies show contradictory results as to whether or not Co^{2+} and Ni^{2+} themselves undergo Fenton reactions to stimulate lipid peroxidation (78, 79, 81, 82). This suggests that reaction conditions matter greatly when making this assessment *in vitro* and then extending to *in vivo* consequences. Some of the conditions which may promote or inhibit this reaction include: buffer composition, pH, time, metal/H_2O_2/lipid/chelator ratios, and lipid composition (82, 243–245).

It has been previously found that Co^{2+} on its own is the strongest catalyst of peroxidation of linoleic and linolenic acid emulsions at pH 6–7 compared to other metals (82). Ni^{2+}, on the other hand, appears to only be strongly active when chelated by peptides such as carnosine or GSH (246).

For the following oxidation experiments, Heart polar extract (Avanti Polar Lipids, Alabaster, AL) was chosen as a model system, as it is likely enriched in mitochondrial lipids, which are one of the interests of this thesis. As well, it is a good model system as it is expected to contain many polyunsaturated acyl chains such as linoleic (18:2) and arachidonic (20:4) acids (62, 97), which undergo significant peroxidation (50). In contrast, preliminary experiments with Yeast polar extract demonstrated little-to-no peroxidation (Appendix B), likely due to the general lack of polyunsaturation (96).

4.2.2 TLC of oxidized lipids

Lipid oxidation was performed according to a previously-described procedure for the oxidation of BLES by Fe^{2+} (160). After a 24-hr oxidation period, lipids were recovered by organic extraction (Section 2.5.2) and run by TLC for the separation of polar lipids (Section 2.6.1). It should be noted that some of the breakdown products of oxidation may have been lost due to volatilization (247). The running location of peroxidised lipid was confirmed by a KI/starch spray (Appendix B). The TLC plate and spot distribution are summarized in Figure 51, in which the “expected” oxidized lipid in metal mixtures were calculated based on the oxidation induced in the respective single metal treatments.

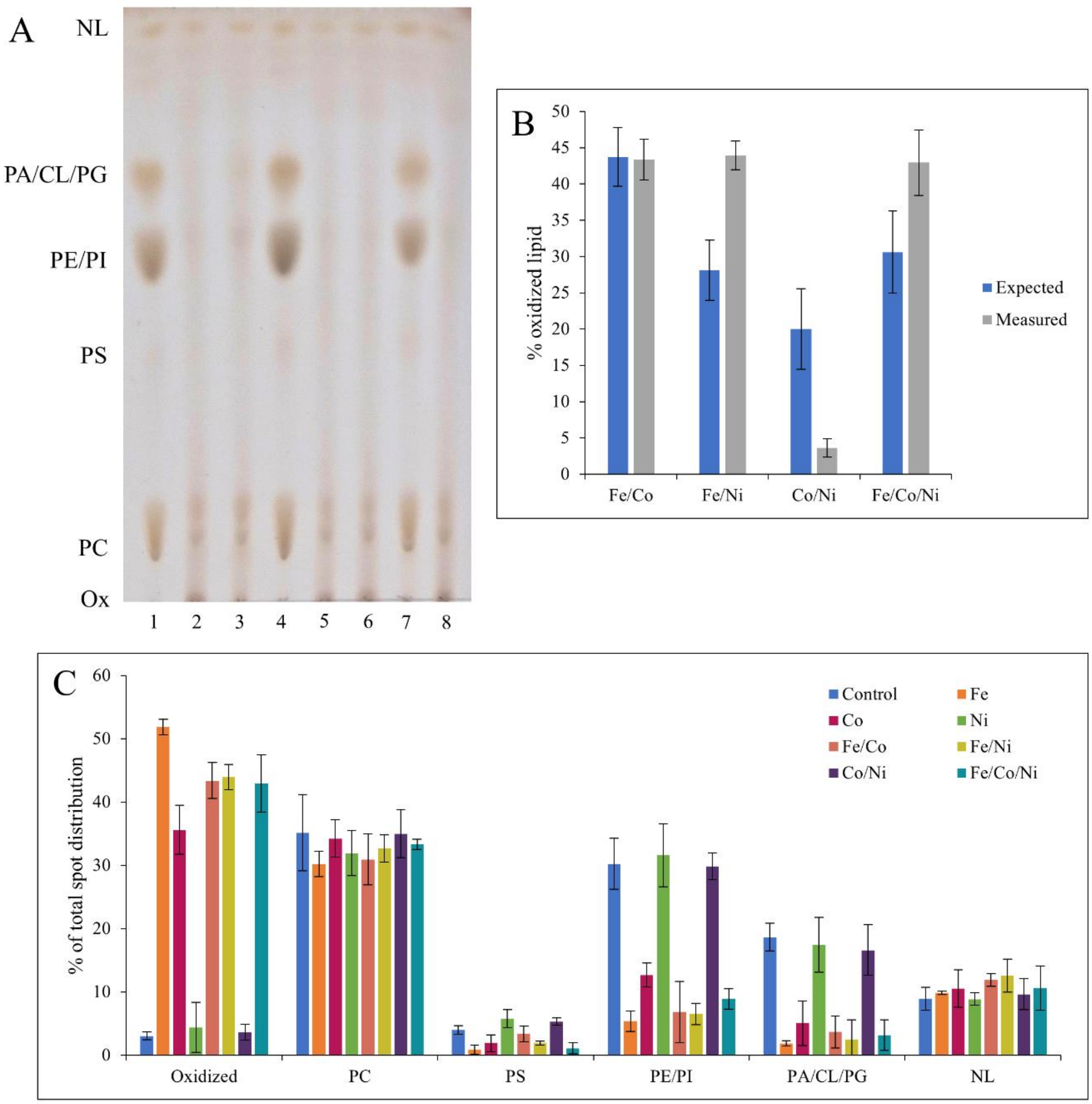

Figure 51. (A) Polar lipid TLC of Fenton-oxidized Heart polar extract lipid under conditions of varying metal catalyst. 1 = Control, 2 = $FeCl_2$, 3 = $CoCl_2$, 4 = $NiCl_2$, 5 = Fe/Co, 6 = Fe/Ni, 7 = Co/Ni, 8 = Fe/Co/Ni. (B) Expected and measured levels of oxidation in metal mixtures. (C) Spot distribution of lipids on TLC plate.

The highly-oxidized lipids likely contain polar peroxides, aldehydes, and ketones which remain at the origin, while other degradation products may have resulted in the smeared background along the plate. These were not observed in the control which underwent the same H_2O_2 treatment, suggesting that auto-oxidation was not occurring. The TLC plate clearly shows that Fe^{2+} and Co^{2+} alone are both able to catalyze lipid oxidation under these conditions, while Ni^{2+} cannot (Figure 51A, Lanes 2-4). This is potentially due to the absence of a suitable chelator (246), suggesting that Ni^{2+}-EDTA is not sufficiently Fenton-active. As the total metal concentration was held constant in the single-metal and multi-metal samples, the treatments can be directly compared (Figure 51B). This shows that Fe^{2+} and Co^{2+} have no activating/ inhibitory activity towards each other but behave as expected in a mixture. In contrast, though Ni^{2+} was not Fenton-active under these conditions, it was able to stimulate Fe^{2+}-catalyzed oxidation, potentially through binding and clustering lipids (78), a mechanism which would be suggested by the rigidifying interactions observed in this thesis (Ch 3). This occurred in both the Fe^{2+}/Ni^{2+} and $Fe^{2+}/Co^{2+}/Ni^{2+}$ treatments, but quite surprisingly, Ni^{2+} inhibited Co^{2+}-driven oxidation when just the two metals were present together. The reasoning for this is not clear, but potentially suggests that Ni^{2+} binds certain membrane targets and "protects" the membrane, as it was found that Ni^{2+} likely binds PS with greater affinity than Co^{2+} (Section 3.9.4), as has been previously reported (76). Perhaps another likely explanation is that Ni^{2+} may disrupt the EDTA/ metal ratio such that Co^{2+} loses its catalytic activity. The fact that the $Fe^{2+}/Co^{2+}/Ni^{2+}$ mixture produced levels of oxidized lipid comparable to Fe^{2+} alone is quite astounding, as it suggests that even if Fe^{2+} is the only Fenton-active metal present (at 1/3rd the concentration alone), Co^{2+} and Ni^{2+} stimulate the lipid peroxidation portion of the reaction.

Another interesting observation is that the oxidized products were primarily derived from the PE/PI, CL/PA/PG, and PS groups rather than PC (Figure 51C). It should be noted that the percent spot distribution only considers discrete spot locations. The loss of primarily negatively-charged lipid may indicate that the metals preferentially localize to, and exert damage at those sites, which would also be expected based on results from simple systems (Ch 3). A previous study has shown that membranes with a higher PE content are more susceptible to Cu^{2+}-induced lipid peroxidation, likely due to Cu^{2+}-PE complexes (248). However, the specific destruction of lipid classes through metal localization and Fenton-induced lipid peroxidation does not appear to have been studied. CL has been identified as being susceptible to peroxidation *in vivo*, but this has been attributed to the fact that most CL contains 18:2 acyl chains (249). Ideally, further experiments should be performed with a complex mixture containing identical polyunsaturated acyl chains to eliminate acyl chain bias. A preliminary oxidation experiment with a 1:1 POPC/POPA mixture suggested that, under conditions causing oxidation, PA is depleted to a greater extent than PC (Appendix B), supporting this idea.

4.3 Interactions of Co^{2+} and Ni^{2+} with Lung Surfactant

4.3.1 Background on Lung Surfactant

Lung surfactant (LS) is a lipid and protein monolayer which coats the inner surface of the lungs and regulates gas exchange (63). Co^{2+} and Ni^{2+} are both known to be specifically toxic to the lungs (2, 21); thus LS model systems were investigated. Various models were created to assess the importance of different lipid components on the interactions with Co^{2+} and Ni^{2+}. BLES was used as the biological comparison for LS as it contains the major lipid species in addition to surfactant proteins SP-B and SP-C (161). The melting curves of BLES and the LS models are shown in Figure 52:

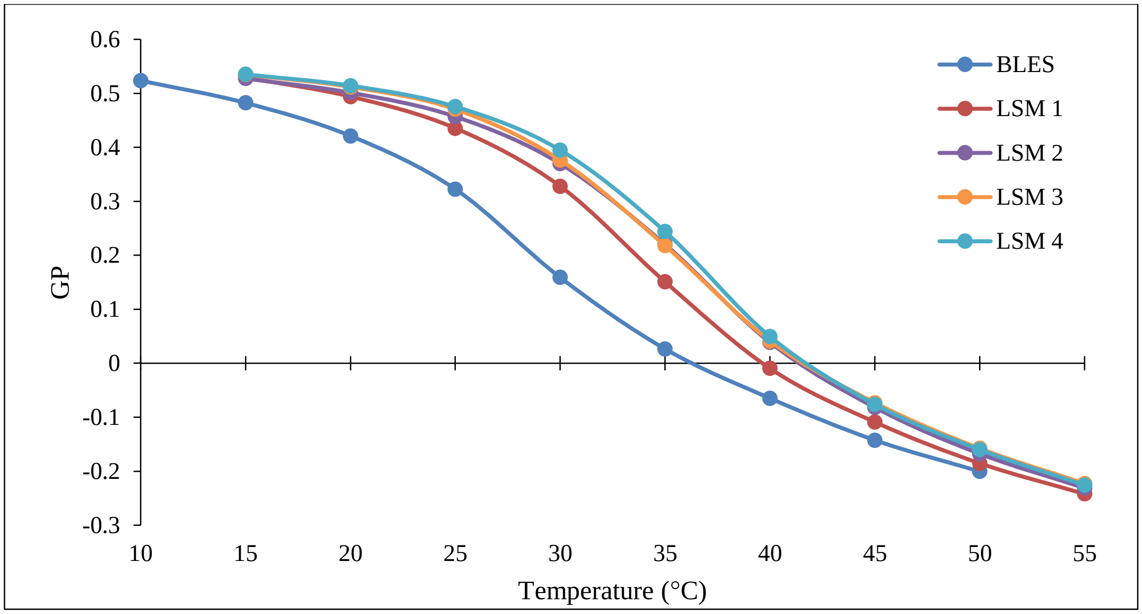

Figure 52. Laurdan GP melting curves of BLES and various LSM in 20 mM Hepes, 100 mM NaCl pH 7.4.

The melting of BLES was found to be considerably different from any of the LS mimics, as it is more fluid and has a lower and broader transition. The fact that the compositional variations tested with the models never resulted in a curve like BLES suggests that the melting of BLES may be partially influenced by the surfactant proteins (SPs), though present at low amounts (102, 250). Although this thesis used liposome models rather than biologically-accurate monolayer models, SP-B and SP-C present in BLES have been previously observed to enhance stability of the monolayer at the air-water interface (251). They may also have a role in regulating the local lipid composition, by allowing lipids to selectively "squeeze" in and out of the monolayer during compression of the film during breathing (250, 251). The lipid-protein interactions present in the LS monolayer likely also occur in a liposome model, such as the proposed electrostatic association of PG with SP-B (252). SP-B has been previously found to cause liposome destabilization and leakage in a 7:3 DPPC/ egg PG model (253), which may be expected to influence how Co^{2+} and Ni^{2+} interact with the membrane. As well, the interactions of Co^{2+} and Ni^{2+} with SPs alone are unknown, but they may constitute a binding target in addition to PG and minor amounts of PI/PS.

4.3.2 Effects of Co^{2+} and Ni^{2+} on fluidity of BLES and LS models (LSM)

The major compositional differences in the LS models are summarized in Table 11:

Table 11. Compositional summary of LSM. The compositions were presented in detail in Section 2.5.3.

LSM	Compositional Factor
1	Contains possible minor components (63, 162): 4% PE, 2% PI, 3% PS, 2% SM
2	Only DPPC/PG and POPC/PG*
3	LSM 2 + Additional acyl chain complexity in PC and PG*
4	LSM 2 + 2% PI and 1% PS*

*based on Postle et al. (2001) (101)

The effects of Co^{2+} and Ni^{2+} on BLES and various LS models were tested and the ΔGP results are summarized over the relevant physiological temperature range for Co^{2+} and Ni^{2+} below (30 µM), at (300 µM), and above (1.2 mM) lipid concentration (Figure 53–Figure 55). Significant difference is assessed between BLES and the various models to determine which model is the least-different and therefore able to most accurately predict the metal effects on biological LS.

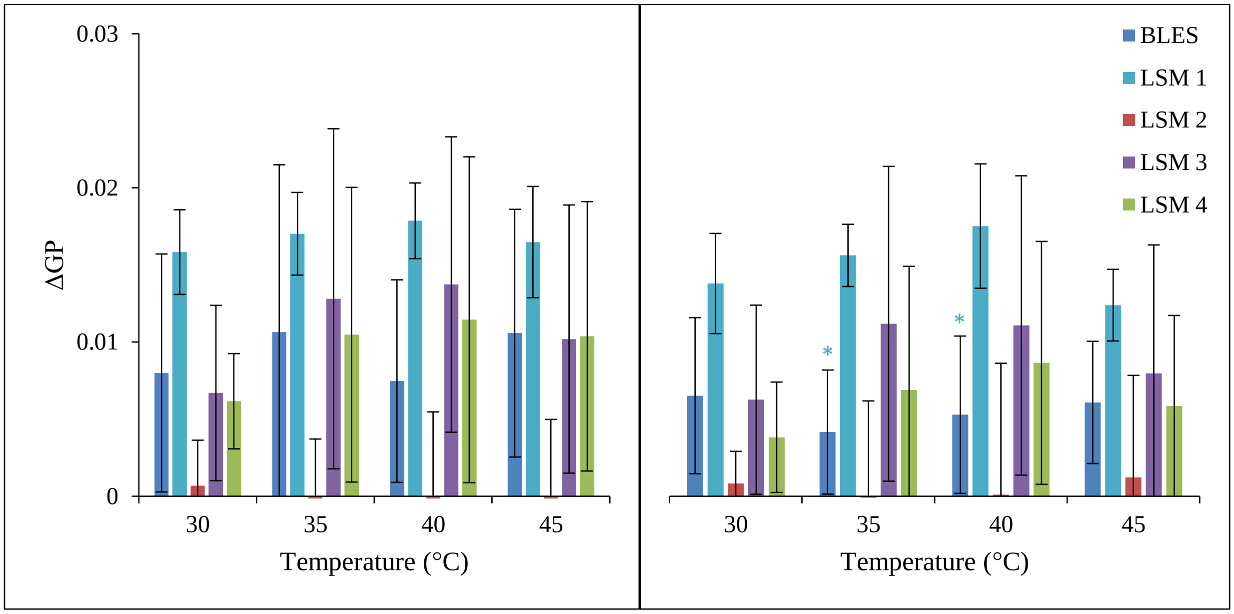

Figure 53. Change in GP induced by 30 µM (A) Co^{2+} or (B) Ni^{2+} in 0.3 mM liposomes of BLES or LSM in 20 mM Hepes, 100 mM NaCl pH 7.4 at 30–45°C.

Firstly, at 30 µM, neither Co^{2+} nor Ni^{2+} was able to induce considerable effects in BLES or various LSM, likely because the membranes are quite rigid, and the major lipid target present is PG, which appears to be a relatively weak binding target. However, in LSM 1, the metal effects are greater than in BLES, even significantly so with Ni^{2+}. This suggests that the minor lipid content in LSM 1 may be too high to be an accurate model for this application. On the other hand, LSM 2, which contained only major PC/PG species showed absolutely no effect, suggesting that this is also not a good model for this application. The effects of both LSM 3 and 4, which contained PC/PG with more complex acyl chains, or minor amounts of PS/PI, were both very comparable to BLES. The results with 300 µM metal are shown in Figure 54:

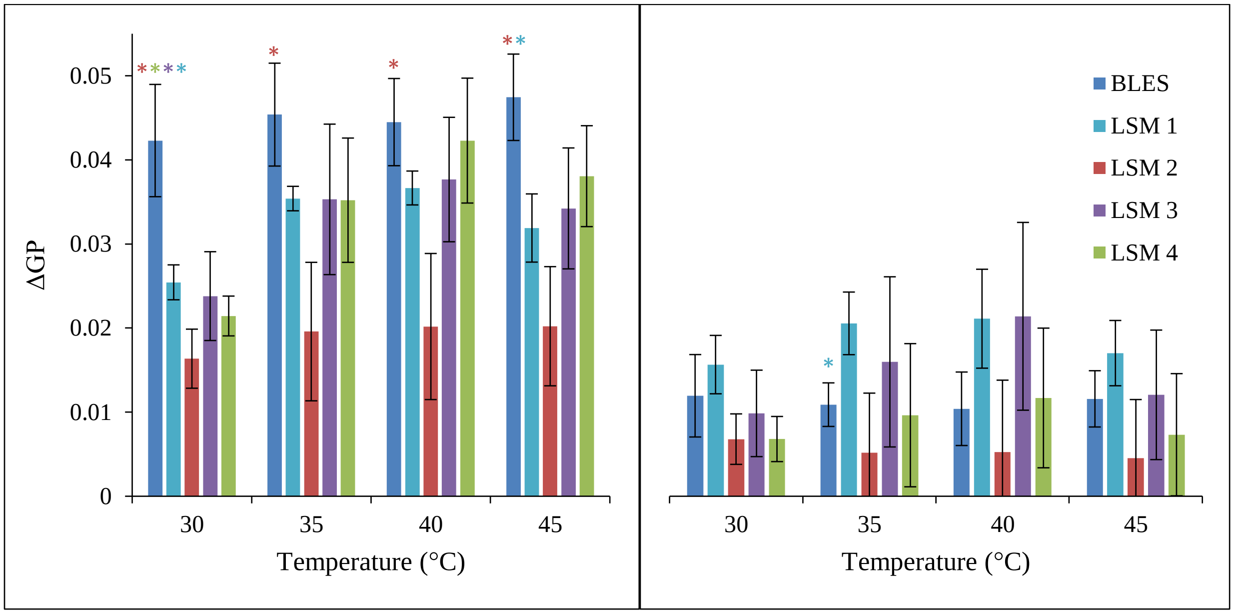

Figure 54. Change in GP induced by 300 μM (A) Co^{2+} or (B) Ni^{2+} in 0.3 mM liposomes of BLES or LSM in 20 mM Hepes, 100 mM NaCl pH 7.4.

At a 1:1 metal/lipid ratio, it is clear that the effects of Co^{2+} are much stronger than that of Ni^{2+} on BLES and all LSM. Again, LSM 2 (simple PC/PG model) proved to be the worst model compared to BLES, while LSM 1 again showed greater effects than BLES with Ni^{2+}. The suitability of either the complex acyl chain model or the minor PI/PS model still held well at this metal concentration, except for at 30°C with Co^{2+}, at which all of the models significantly under-predicted the interaction. This was also observed at temperatures below 30°C, possibly because the models are all too tightly packed to allow for Co^{2+} binding. Lastly, the effects of excess metal were considered.

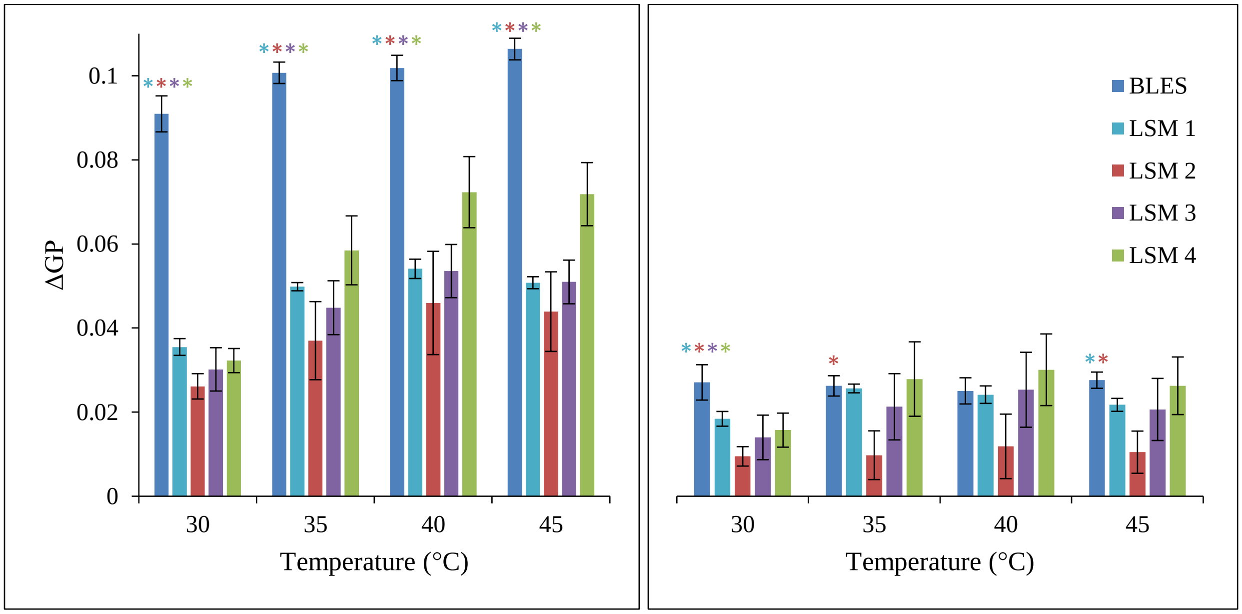

Figure 55. Change in GP induced by 1.2 mM (A) Co^{2+} or (B) Ni^{2+} in 0.3 mM liposomes of BLES or LSM in 20 mM Hepes, 100 mM NaCl pH 7.4.

When Co^{2+} is present in excess at 1.2 mM, the effects on BLES far surpass any of the models created. This suggests that: Co^{2+} interacts much more favourably with BLES because of its inherent fluidity and compositional differences, and/or that Co^{2+} interacts with SP-B or SP-C to cause additional rigidifiying effects. Along with that, it is also likely that the presence of SPs affects the local packing and sorting of lipids (252, 253), leading to more favourable metal binding sites. As far as the models go, LSM 4 (PI/PS model) was the best at predicting effects. The effects of Ni^{2+}, on the other hand, remained relatively well-predicted by either LSM 1, 3 or 4, with LSM 2 falling short again.

4.3.3 Discussion on lung surfactant

While the effects observed in the bilayer models were interesting to compare compositional differences, it should be noted that effects may be different in a monolayer model in which there is no curvature to the surface of the film. Yet, in testing various LS models, it became clear that a simple PC/PG model was a poor mimic for BLES in this application, as the simple composition lead to much lower metal-induced ΔGP values than with BLES. In contrast, the presence of more complex acyl chains (LSM 3) or minor amounts of high-affinity binding targets (LSM 4) resulted in ΔGP values more similar to that observed in BLES. It was somewhat surprising to find that a more complex packing arrangement in LSM 3 was sufficient to allow greater effects than on the simple PC/PG model. Yet, this agrees with Laurdan GP data with pure PG liposomes, which found a massive contrast in effects between POPG and DMPG (Section 3.4.2). Thus, this suggests that membrane packing is very important in allowing for metal-PG interactions, and a change in acyl chains may allow this to occur. Additionally, the LSM 1, which contained minor lipid components and less DPPC was again not as suitable, as it over-predicted the effects at lower metal concentrations. However, even though LSM 3 and 4 were the better models, the mechanism by which the metals exert their effects in the models versus BLES may be quite different, as the melting curve of BLES was far different from any of the models. Based on the strong effects of 1.2 mM Co^{2+} on BLES, it is quite possible that SPs also play a role in metal interaction, which is not observed in the lipid models. To my knowledge, there are no known interactions of Co^{2+} and Ni^{2+} with SP-B and SP-C, but it has been observed that Ba, Ti, and Cs oxide nanoparticles interact with SP-A (254).

A previous study on exposure of rabbits to inhaled $CoCl_2$ and $NiCl_2$ found that the metals stimulated an increase in phospholipids, specifically in DPPC, and that the combined effect of both metals was greater-than-additive (105). This effect is likely not a result of direct membrane-metal interactions, but rather appears to be due to effects on type II alveolar cells which produce surfactant (105). The results from this thesis suggest that the metals may also have direct interactions with LS itself, potentially altering the properties and thus the function. Complexation of PG by Co^{2+} and Ni^{2+} may have serious consequences, as the absence of PG in LS has been associated with respiratory distress syndrome (255). PG is thought to be involved in modulating the spreading of the monolayer (256), associating with SP-B (252), and may also be involved in immunity function (257). The effects of Co^{2+} and Ni^{2+} on more complex LS monolayer models, including interactions with SPs would be of interest for future study.

4.4 Interactions of Co^{2+} and Ni^{2+} with Whole Rabbit RBCs

Red blood cells (RBCs) were considered as another complex target membrane, as soluble Co^{2+} and Ni^{2+} are transported in the bloodstream, and levels may be elevated in patients with surgical metal implants (8). Co^{2+} and Ni^{2+} are known to induce a hypoxic stress response, thus stimulating the production of RBCs (4, 23), but the involvement of direct damage to RBCs pertaining to Co^{2+} and Ni^{2+} toxicity is not well-understood. It has been found that Co^{2+} and Ni^{2+} both bind to hemoglobin (Hb) in some capacity (36, 37).

4.4.1 Effects of Co^{2+} and Ni^{2+} on RBC shape

It has been previously reported that 1 mM Ni^{2+} stimulates the formation of echinocytes in human RBCs (113) and that metallic Co and Ni particles, but not ions, are strongly hemolytic compared to other metals (258). Additionally, it has been observed that Co^{2+} and Ni^{2+} induce changes in the Rayleigh scattering of RBCs upon cell entry, suggesting shape changes (112). The morphology of rabbit RBCs in Krebs-Ringer bicarbonate buffer was monitored over time upon incubation with 1 mM metal:

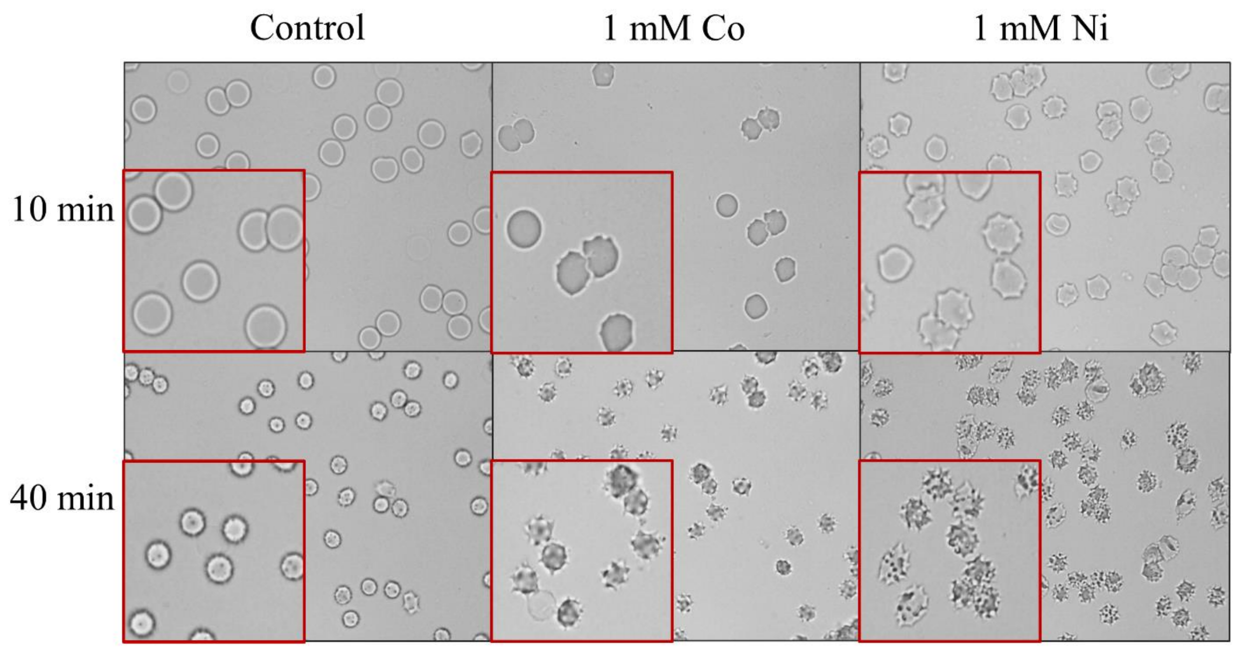

Figure 56. Images of rabbit RBCs in Krebs-Ringer bicarbonate buffer at pH 7.4 at 1000x magnification after incubation at 37°C after 10 and 40 min.

Upon treatment with 1 mM Co^{2+} or Ni^{2+}, the RBC membranes began to show small spiny defects within 10 mins, which were not present in the control. After 40 mins these spiny protrusions became very well-defined, especially for Ni^{2+}-treated cells. Unfortunately, the control cells did not appear to be very stable during this treatment, as some of the cells became smaller over time. Yet, the shape changes in the metal-treated cells were quite dramatic and suggest that Co^{2+} and Ni^{2+} may associate with the membrane. The shapes of the Co^{2+} and Ni^{2+}-treated cells were not identical, which may indicate different mechanisms or interactions.

Echinocyte formation has been observed for ions such as Ni^{2+} (113), Cd^{2+} (84, 237), Cu^{2+} (259), and Mn^{2+} (260). However, echinocyte formation appears to be triggered by a relatively wide array of mechanisms, including Mg^{2+}-depletion (261) or change in membrane potential

(262). Another possibility is the uneven association of metals/drugs with a single leaflet of the membrane, producing deformational strain (263). The formation of echinocytes would be predicted to occur with outer leaflet-association, while stomatocytes form with inner leaflet-association (89, 263). The association of Co^{2+} with lipids of the outer leaflet is certainly a possible explanation, as a previous study with Laurdan indicated that Co^{2+}, but not other metals including Ni^{2+}, was able to induce membrane rigidification of RBCs prior to the addition of an ionophore (112). However, there is very little negatively-charged lipid present on the outer leaflet of RBC membranes (59, 111), which may suggest that metal-membrane protein interaction also occurs. PI lipids constitute a very minor component (~3%) of RBC membranes, and previous study has suggested that 20% of PI is localized to the outer leaflet (264). Thus, it is possible that association with minor amounts of PI may have an effect (Section 3.6.2).

4.4.2 Effects of Co^{2+} and Ni^{2+} on membrane integrity using absorbance release assay

The ability of Co^{2+} and Ni^{2+} to disrupt RBC membranes and release cell components was tested by incubation with metal for 8 hrs, followed by pelleting and measuring absorbance of the supernatant. Complete release was induced by treatment with the detergent Triton X-100. This experiment was only performed in one replicate due to possible degradation of the blood sample over time. The absorbance spectra are shown in Figure 57:

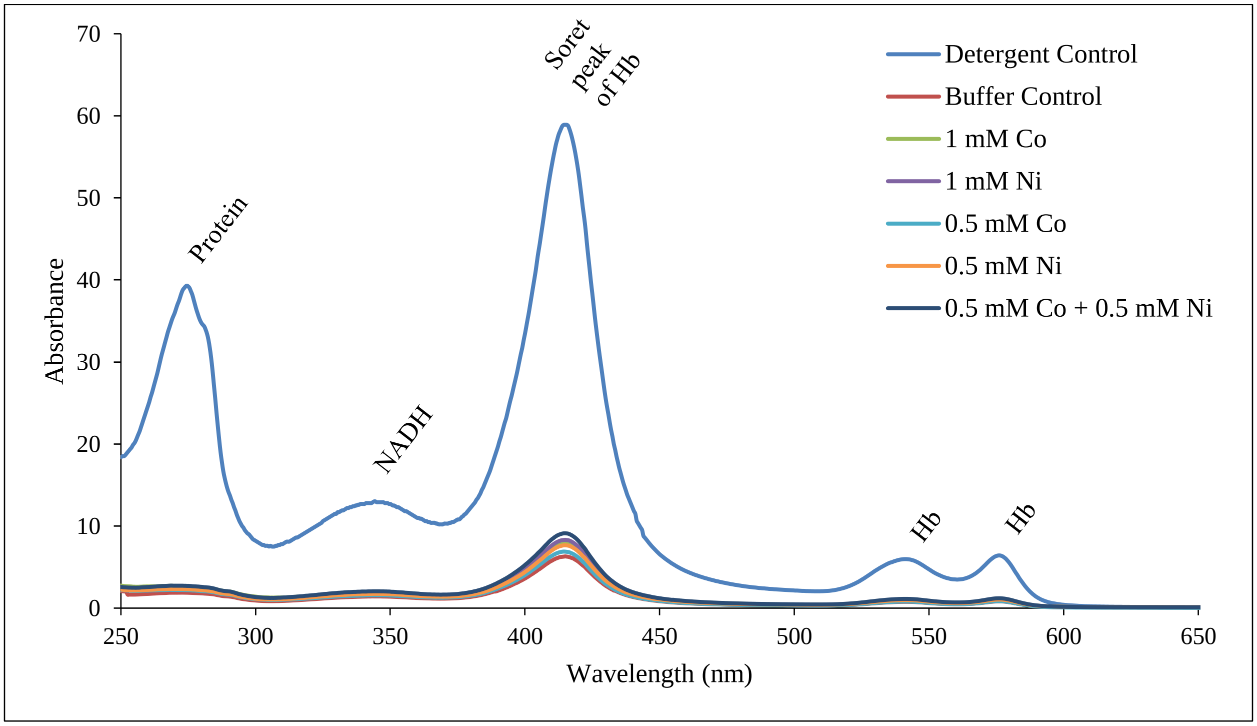

Figure 57. Absorbance spectra of supernatants from RBCs in Krebs-Ringer bicarbonate buffer pH 7.4 under various treatments for 8 hrs at 37°C.

Compared to the total possible release, the change in absorbance of the supernatant induced by the metals was very small, yet all treatments showed some effect. The percent release according to the absorbance of the Soret peak of Hb are given in Table 12:

Table 12. Percent change in absorbance of RBC supernatant at 415 nm under various treatments.

Treatment	% Increase
1 mM Co	3.1
1 mM Ni	3.8
0.5 mM Co	1.1
0.5 mM Ni	2.6
0.5 mM Co/Ni	5.4

The metal treatments caused a minor release of cell components, which increases with metal concentration. The rate at which this release occurs was not measured but is of interest for future study. Ni^{2+} appears slightly more potent, while the effects of Co^{2+} and Ni^{2+} together are greater-than-additive. This is consistent with the idea that the metals interact with RBCs slightly differently according to the shape changes observed and previous study (112), such that they do not overlap for binding targets. This experiment should be repeated with a fresh blood sample.

4.4.3 Investigating Co^{2+} and Ni^{2+} permeabilization of RBC models using calcein leakage

A previous paper reported specific rigidifying effects of Co^{2+} on RBCs prior to ionophore addition (112), yet the mechanism by which this occurred was not known. It was thus considered that either: Co^{2+} interacts with the outer leaflet of the membrane (lipid or protein) or that Co^{2+} crosses the membrane on its own to interact with high-affinity targets like PS. The ability of Co^{2+} and Ni^{2+} to permeabilize liposomes was tested by an adapted Calcein encapsulation and leakage assay detailed in Section 2.4.2, as Co^{2+} and Ni^{2+} are effective quenchers of Calcein (157). Liposomes composed of PC, 85:15 PC/PS, and 50:15:35 PC/PS/Chol (molar ratios) were tested as simple RBC models. It should be noted that this assay cannot confirm if metals permeabilize the membrane to release Calcein, or if the metals cross the membrane to quench Calcein. The effects on POPC are shown in Figure 58:

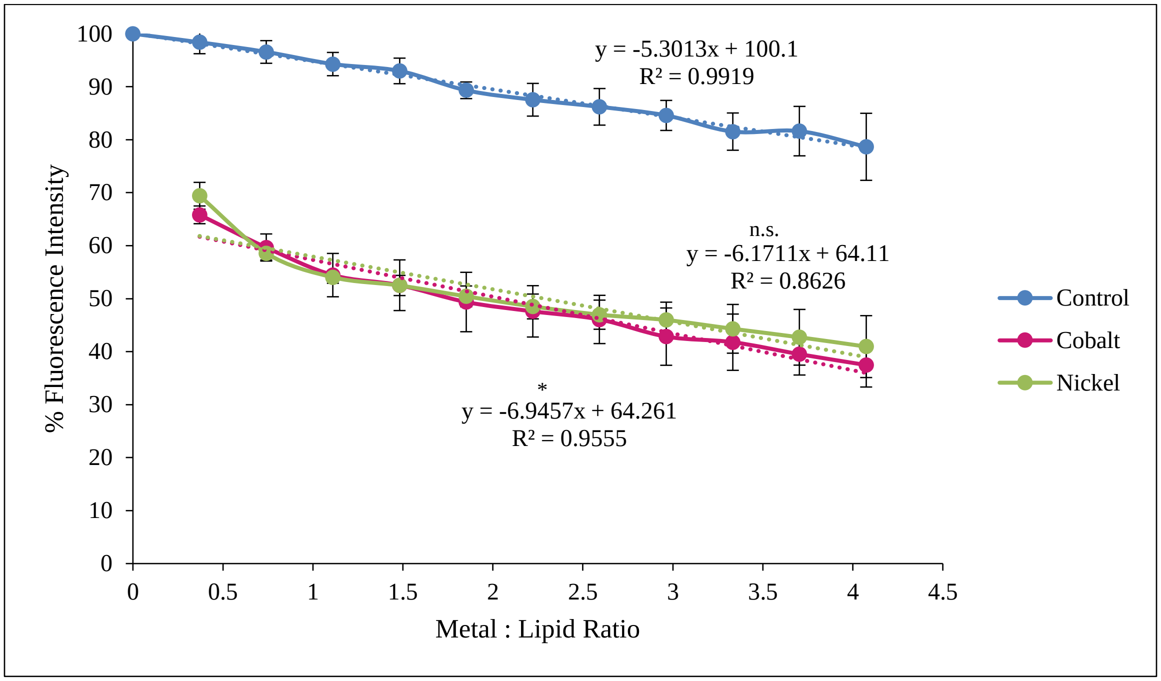

Figure 58. % Fluorescence intensity remaining of encapsulated Calcein in 0.15 mM POPC liposomes in 20 mM Hepes, 100 mM NaCl pH 7.4 upon injection of Co^{2+} or Ni^{2+} in 2 min increments.

The significantly steeper slope observed in the Co^{2+} curve suggests a slight permeabilization of POPC, leading to ~8% intensity loss, despite a lack of interactions observed in the Laurdan GP data (Section 3.1.2). The initial large drop (30%) in intensity was assumed to be due to the quenching of any remaining external free Calcein in solution. However, it is also possible that this overlaps with an initial permeabilization event, which does not largely increase in effect with further metal addition. There were significant dilution/ photobleaching/ leakage effects occurring even in the control, as seen by the loss of 20% intensity by the end. It is possible that the metals have very weak association with PC that disrupts the membrane slightly to release some Calcein without affecting overall fluidity (Section 3.1.2). 85:15 POPC/POPS liposomes were tested next to see if the presence of a high-affinity binding target at a relevant ratio for RBCs (59) would allow for significant membrane disruption. It should be noted that these liposomes are symmetric, and thus not a true representation of the asymmetric RBC membrane in which very little PS would be accessible (59, 111). The results are in Figure 59:

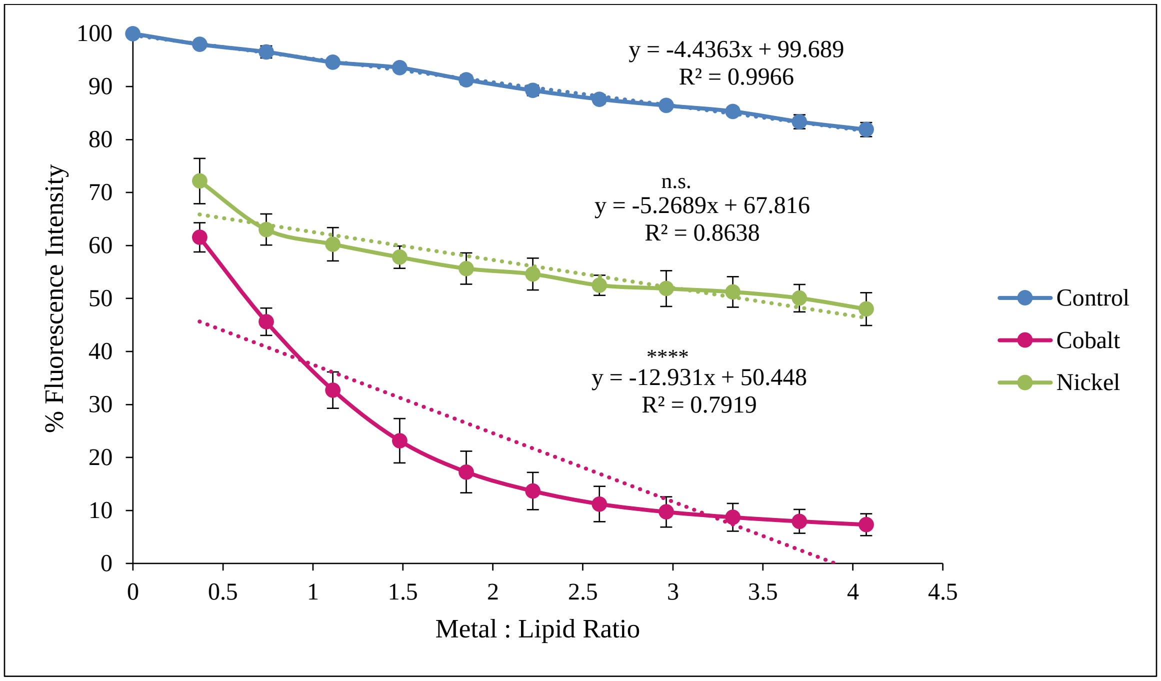

Figure 59. % Fluorescence intensity remaining of encapsulated Calcein in 0.15 mM 85:15 POPC/POPS liposomes in 20 mM Hepes, 100 mM NaCl pH 7.4 upon injection of Co^{2+} or Ni^{2+} in 2 min increments.

In contrast to pure POPC, the presence of just 15% PS (~7.5% accessible) lead to nearly complete quenching of Calcein by Co^{2+}, suggesting major membrane disruption. Again, it is not distinguishable whether this is due to leakage of Calcein from the liposome or permeation of Co^{2+} into the liposome. A previous study on liposome permeation by Co^{2+} used NBD-PE (nitrobenzoxadiaole-PE), which is a fluorescent lipid (265). They found that Co^{2+} was able to quench all NBD in 1:1 PE/PS liposomes, suggesting that Co^{2+} itself passes through the bilayer (265). However, this was only observed in small unilamellar vesicles (20–30 nm diameter) which have tight curvature which may allow for easier metal ion penetration (265). This suggests that a Co^{2+}-PS complex may create an ion passage in highly-strained membranes, as Co^{2+} was unable to pass into similar 1:1 PC-PE vesicles (265). The present results are fairly interesting in combination with these previous findings (112, 265), yet the effect still depends on the accessibility of PS to Co^{2+}. On the other hand, the effects of Ni^{2+} were again insignificant, though the large initial drop in intensity (30%) was observed as in POPC and suggests that some leakage may occur. To further improve the RBC model, Chol was added to make 50:15:35 POPC/POPS/Chol liposomes. The results are shown in Figure 60:

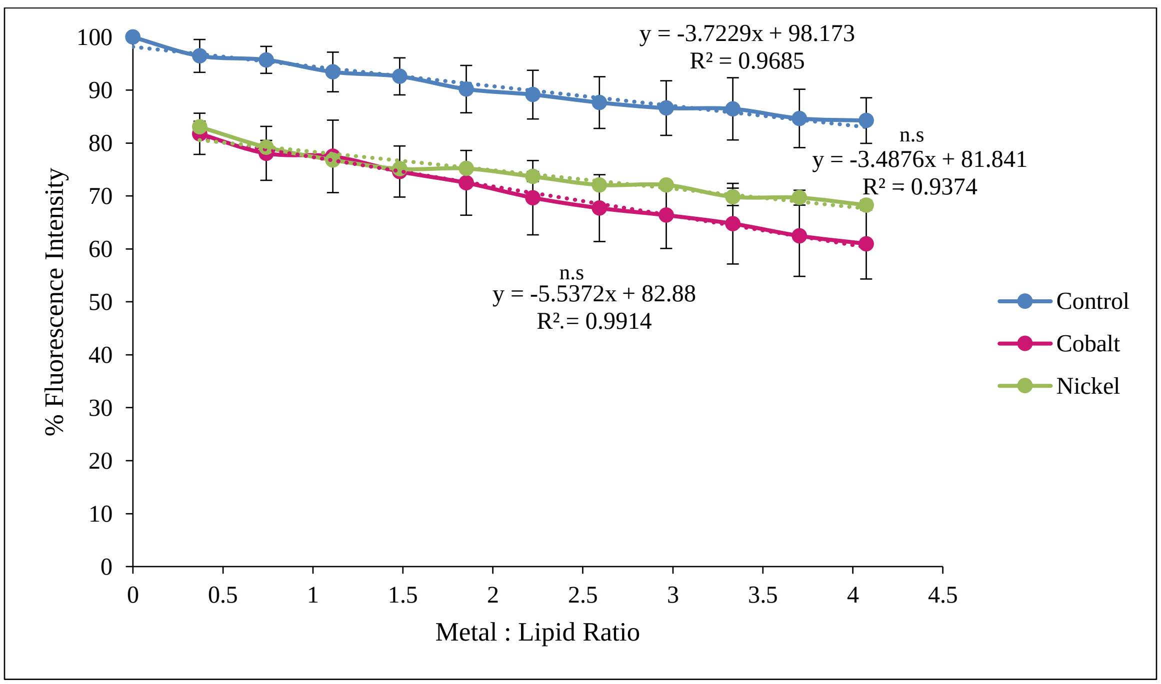

Figure 60. % Fluorescence intensity remaining of encapsulated Calcein in 0.15 mM 50:15:35 POPC/POPS/Chol liposomes in 20 mM Hepes, 100 mM NaCl pH 7.4 upon injection of Co^{2+} or Ni^{2+} in 2 min increments.

The presence of Chol significantly reduces the effect of Co^{2+}, though the slightly steeper slope indicates that some leakage may still be occurring (~5%). The slope of the Ni^{2+} curve, on the other hand, was clearly not different from that of the control. However, one interesting feature of these curves compared to the others, is that the initial quenching drop is not as large (only <20%). This may provide support for the idea that the initial drop observed in POPC and 85:15 POPC/POPS for both metals is partially a rapid permeabilization event, as the curves show a change in slope following the initial injection which is not observed when Chol is present (Figure 58–Figure 60). Thus, it seems that both Co^{2+} and Ni^{2+} may permeabilize non-Chol containing membranes upon immediate addition. Chol has been previously found to reduce membrane-permeabilizing effects of $HgCl_2$ (266), Rb^+ (267), as well as isolated serum components (268), so it is unsurprising to observe this protective effect. The permeabilizing ability of Co^{2+} on more complex membranes including PI (264), are of interest for further study.

4.4.4 Discussion on whole RBCs

The effects of Co^{2+} and Ni^{2+} on whole blood cells have shown that both metals induce echinocyte formation and disrupt cell membranes releasing Hb. It was hypothesized that Co^{2+} may have a direct membrane-disrupting mechanism, as it has been previously shown to have strong rigidifying effects prior to artificially-induced cell permeabilization, in contrast to 7 other divalent metals including Ni^{2+} (112). The Calcein leakage assay showed that the presence of PS allows for major leakage of liposome contents by Co^{2+}, possibly slightly so with Chol present. Both Co^{2+} and Ni^{2+} are expected to interact primarily with the inner leaflet of the membrane, where PS is mostly located (59, 111), but they may also interact with membrane proteins on either side. Thus, a potential pathway for Co^{2+} may follow: initial transport of Co^{2+} into RBCs (36), followed by complexation with PS causing rigidification (112), and possibly permeabilization (Figure 60), releasing Hb. Although, echinocyte formation still suggests primarily outer leaflet association (263). The pathway of Ni^{2+} *in vivo* may not involve metal-lipid induced permeabilization, as Ni^{2+} was not found to have permeabilizing effects in Chol-containing membranes (Figure 60). However, it is possible that Ni^{2+} interacts more with outer-leaflet membrane proteins, causing echinocyte formation (Figure 56) (113, 263), and release of cell components (Figure 57). The results have suggested that Co^{2+} and Ni^{2+} both have interactions and effects on whole RBC membranes, which warrant further study.

4.5 Interactions of Co^{2+} and Ni^{2+} with Rabbit Blood Lipid Extract

The lipids from rabbit RBCs were isolated to form liposomes to observe the direct metal-lipid interactions, which may occur. TLC identified the major lipid components including a large fraction of Chol (Figure 61):

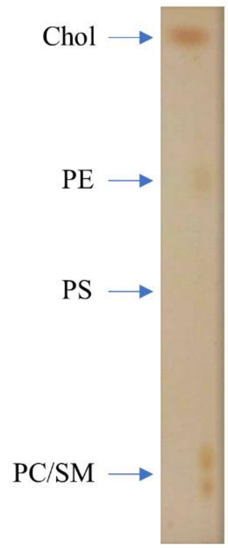

Figure 61. Polar lipid TLC of rabbit RBC extract visualized by 2% H_2SO_4 and charring. PC = phosphatidyl-choline, SM = sphingomyelin, PS = phosphatidylserine, PE = phosphatidylethanolamine, Chol = cholesterol.

4.5.1 Effects of Co^{2+} and Ni^{2+} on RBC extract membrane fluidity

The RBC lipid extract was found to be very rigid, as it maintained a GP above zero even at 50°C. Additionally, the melting of the RBC extract in the presence of GSH and BSA was measured, as these biomolecules would be expected to be near to or contact the cell membrane. The curves are shown in Figure 62:

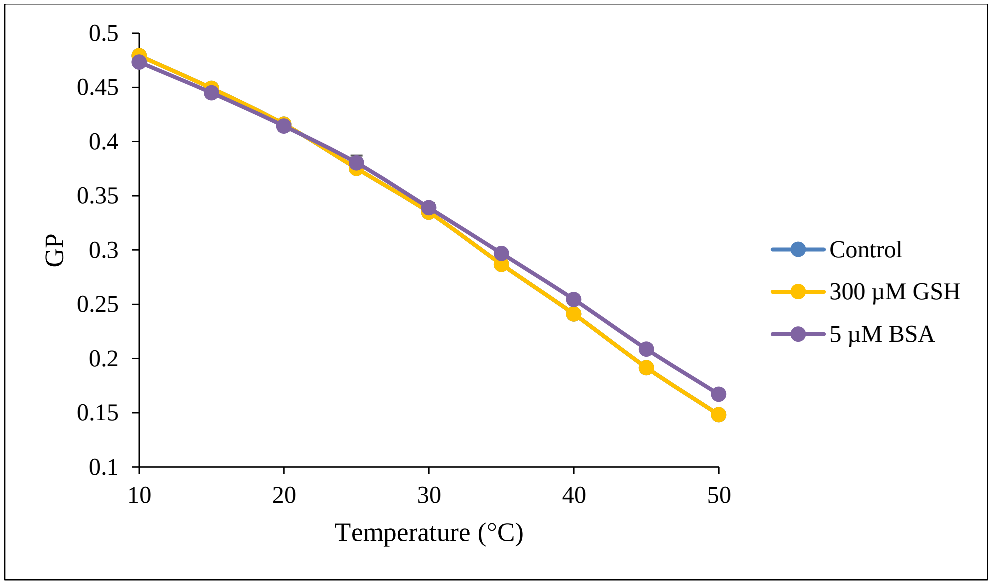

Figure 62. Laurdan GP melting curves of 0.3 mM Rabbit RBC extract liposomes in 20 mM Hepes, 100 mM NaCl pH 7.4 in the presence of 300 µM GSH or 5 µM BSA.

GSH at a 1:1 molar ratio did not affect the melting of RBC extract, but even a very low concentration of BSA (1:60 molar ratio) did cause changes to the melting. This suggests that BSA interacts with the membrane (269). The effects of Co^{2+} and Ni^{2+} on rabbit RBC extract are shown in Figure 63:

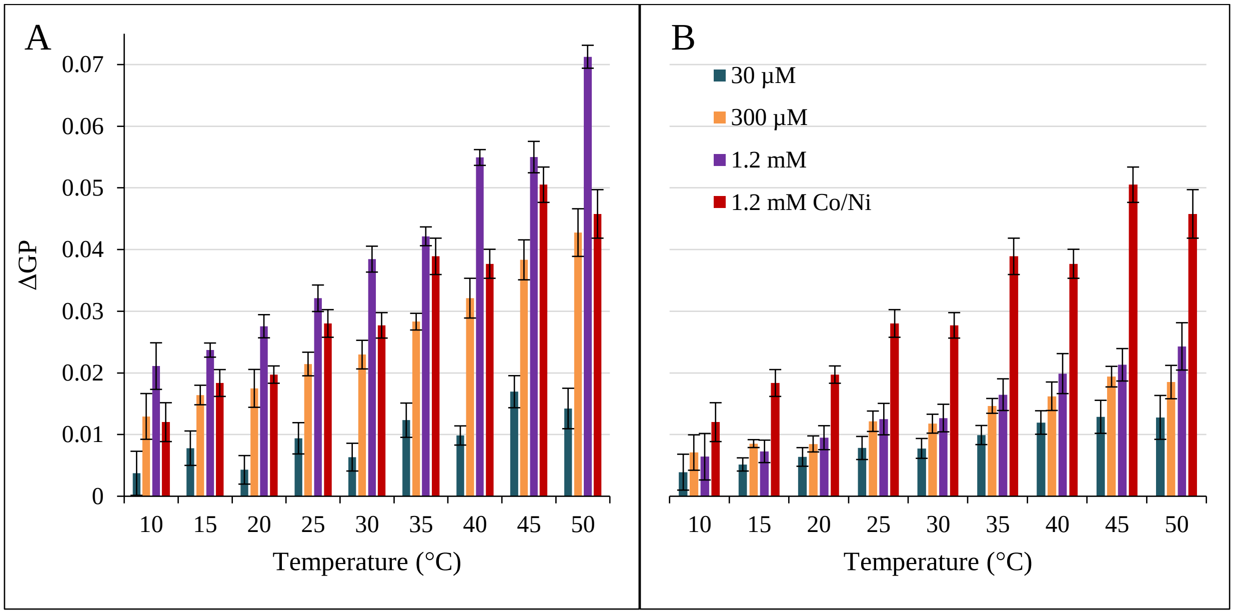

Figure 63. Change in GP induced by (A) Co^{2+} or (B) Ni^{2+} in 0.3 mM rabbit RBC extract liposomes in 20 mM Hepes, 100 mM NaCl pH 7.4.

The trends in effects observed are similar to that seen with Brain and Liver polar extracts (Section 4.1) in that the effects of Co^{2+} continue to increase with concentration and temperature, while the effects of Ni^{2+} saturate near 30 µM. This suggests that interaction likely occurs with similar high-affinity targets, PS and PI, which are expected to be the main targets in RBC lipids (59, 108). Interestingly, as observed with *S. cerevisiae* polar extract, the combined effects of 1.2 mM Co^{2+} and Ni^{2+} are lower than that of 1.2 mM Co^{2+} alone, which suggests that Ni^{2+} out-competes for some of the binding targets, likely PS (76), as the effects were found to be similar/greater in pure PS (Section 3.5.2). The effects of Co^{2+} and Ni^{2+} on RBC extract are overall lower than in comparison to the Avanti Polar Extracts. The absorbance spectrum of the RBC extract indicated slight protein contamination, so it is possible that membrane protein present may out-compete the lipids for metal binding, thus resulting in a lower overall effect. The RBC extract was also very rigid (Figure 62) and thus may have been less favourable to bind.

4.5.2 Effects of Co^{2+} and Ni^{2+} on RBC extract membrane fluidity in the presence of glutathione or BSA

It was then considered whether the presence of GSH or BSA would affect the binding of Co^{2+} or Ni^{2+} to the membrane, as these could be considered relevant competition for binding inside (GSH) or outside (BSA) of the cell. The effects are summarized in Figure 64:

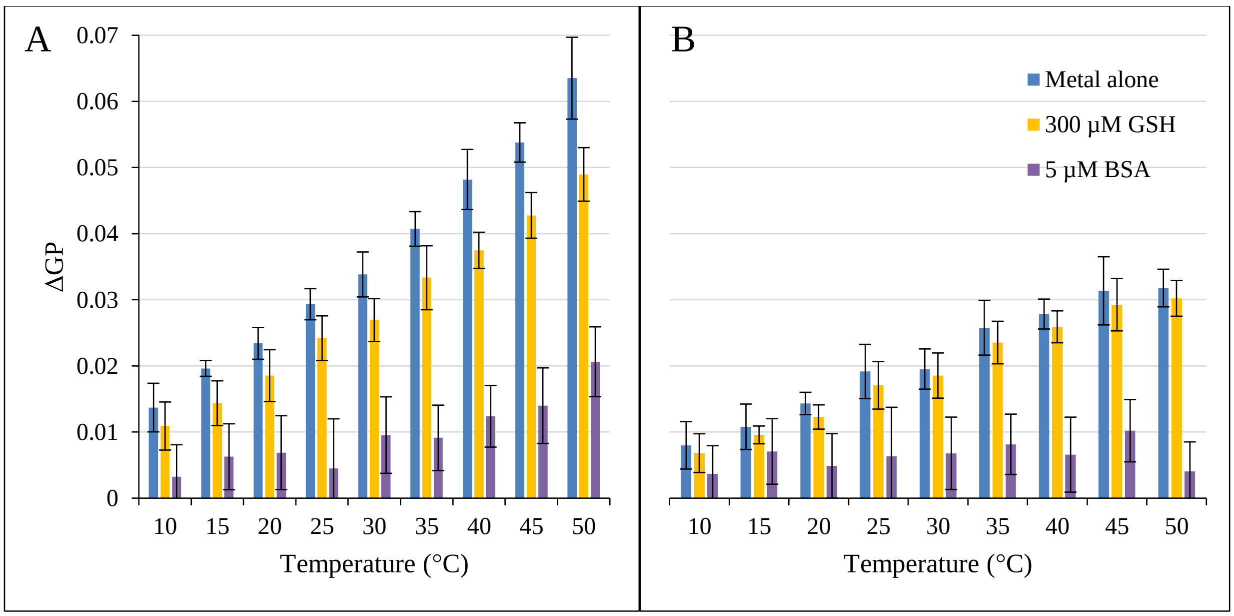

Figure 64. Change in GP induced by 300 µM (A) Co^{2+} or (B) Ni^{2+} in 0.3 mM rabbit RBC extract liposomes in 20 mM Hepes, 100 mM NaCl pH 7.4 in the presence of 300 µM GSH or 5 µM BSA.

The presence of 1:1 GSH to metal was found to significantly decrease the effects of Co^{2+} at higher temperatures (>40°C) but not affect the interactions of Ni^{2+}. This suggests that overall, the affinity of the metals for the membrane is higher than for GSH. However, GSH complexation may affect the speciation of Co^{2+} and Ni^{2+}, such that other lipids become targets leading to a "hidden" rigidifying effect.

In contrast, very low concentrations of BSA (1:60 molar ratio) lead to a significant decrease in metal effect, suggesting that the affinity of the metals for BSA is higher than for the membrane. HSA has been previously reported by isothermal titration calorimetry (ITC) to have three metal binding sites with K_d's 11, 90, and 111 μM for Co^{2+} (35) and 0.15 and 12.5 for Ni^{2+}, while Ni^{2+} does not bind the third site (107). Based on the PS K_d's determined in this study, it would not be expected that BSA could so decisively out-compete for binding when present at such a low concentration but may suggest metal is associated with BSA aside from the three binding sites. However, this is also likely due to the MLV binding assay reporting all weak association, while ITC is better at reporting tight binding, such that the metal-lipid binding constants determined in this thesis are likely inaccurate. Still, if Co^{2+} and Ni^{2+} were able to bind all 3 binding sites, this would only complex 15 μM of metal, leaving more than enough to bind the rest of the negatively-charged lipids. So, this suggests that the metals may weakly associate with BSA at many sites, such that the effects on the membrane are very reduced. However, in a 45:40:15 POPC/Chol/POPS system (not shown), 5 μM BSA was not as effective in decreasing the effect of 300 μM Co^{2+} or Ni^{2+}. It may be that the association of BSA itself with the RBC extract was different from the simple model. Perhaps BSA does not interact as closely with the RBC extract, such that bound metal is also further from the membrane and cannot exert an effect. Overall, it does appear that BSA is a very strong competitor for metal binding and would likely decrease the metal uptake into cells. Yet, the fact that the effect of GSH was so minimal may indicate that once inside the cell, the metals may be freer. However, it should be noted there are many intracellular peptides/ proteins which were not tested that may complex Co^{2+} and Ni^{2+} instead, potentially altering their effective speciation or availability.

4.5.2.1 Screening for effects of glutathione

It was suspected that interaction with GSH may affect the speciation of Co^{2+} and Ni^{2+}, such that the lipid targets may either be bound weaker or entirely differently. Various systems including: POPS, 50:50 POPC/POPS, 85:15 POPC/POPS, and 45:40:15 POPC/Chol/POPS were tested with 300 µM GSH and it was found that GSH never altered the effect of 300 µM Co^{2+} or Ni^{2+} on the membrane (Appendix B). Thus, it appears that GSH does not lead to a “hidden” effect by altering speciation. However, this suggests that the slight decrease in Co^{2+} effect observed in the RBC extract with GSH may be due to how the metal associates with the complex membrane, or due to the presence of membrane proteins, as the effect was not produced in any model system. In contrast, the same side experiments with Cd ($CdCl^+$ and Cd^{2+}) and Hg ($HgCl_3^-$ and $HgCl_4^{2-}$) showed that the effect of $CdCl^+/Cd^{2+}$ on POPS is reduced when GSH is present, while the effect of $HgCl_3^-/HgCl_4^{2-}$ on 85:15 POPC/POPS is greatly increased when GSH is present (Appendix B). This suggests that GSH complexation affects the charge of the polarizable heavy metals Hg and Cd species such that their affinity for different lipid targets changes. However, GSH seems to be a weak competitor for the transition metals Co^{2+} and Ni^{2+} compared to the lipid membrane. These results give additional support to the idea of lipids as a biologically relevant binding target for metals, and that other biomolecules in the system may dramatically change how they affect the membrane.

Chapter Five: Effects of Co^{2+} and Ni^{2+} on Respiration and Lipid Content of *S. cerevisiae*

Chapters Three and Four demonstrated that Co^{2+} and Ni^{2+} have significant direct interactions with lipid membranes in simple and complex systems. The interactions depend on the presence and identity of negatively-charged head groups but are also affected by acyl chain packing. The fact that low concentrations of Co^{2+} and Ni^{2+} can exert substantial changes to complex membranes *in vitro* warrants further study on interactions and effects *in vivo.* It has been previously suggested that one major effect of metal-lipid clustering interactions is the augmentation of lipid peroxidation reactions (78, 81). Thus, it was of interest to study metal toxicity in a simple *in vivo* system. *Saccharomyces cerevisiae* was employed as a model organism as it is eukaryotic and easily manipulated. One of the major differences to mammalian cells is its preferential usage of the fermentation pathway to generate energy (118).

In *S. cerevisiae*, excess Co^{2+} and Ni^{2+} is generally stored and detoxified in the vacuole, somewhat comparable to a lysosome (121, 128, 131, 270). However, Co^{2+} has also been found to localize to the yeast mitochondria (131, 140). It is thus possible that yeast preferentially allow damage to their superfluous respiratory chain to avoid excess Co^{2+} in other cellular compartments. Mitochondria are an organelle which are particularly sensitive to redox-active metals (44, 45, 81). This is likely due to the damaging effects of reactive oxygen species (ROS) on the respiratory chain and mitochondrial DNA, which lacks efficient repair systems (44, 81). Co^{2+} and Ni^{2+}, along with several other metals (135, 271, 272), have been previously identified as inducers of the mitochondrial transition pore (MPTP) in mammalian cells, a process which appears to be a result of oxidative stress (132, 133, 273). In mammals, the MPTP collapses the mitochondrial membrane potential and releases cytotoxic proteins, leading to cell death (274). Though this thesis is not specifically concerned with the MPTP, it should be noted that the pore is regulated differently in *S. cerevisiae*, (275) thus the same metal-induced effect may not occur. However, it is still possible that metal taken up into the cell is localized in the mitochondria and may interact with the membrane by complexing the major negatively-charged lipids: PI, PS, and CL (179). Along with direct metal-lipid interactions, it is also possible that Co^{2+} and Ni^{2+} cause effects on membranes indirectly by altering lipid metabolism, as Co^{2+} has been previously-found to affect sterol production (146).

Thus, the effects of Co^{2+} and Ni^{2+} on growth, viability, respiration, mitochondrial membranes, and lipid composition of *S. cerevisiae* were assessed, in collaboration with the Zaremberg lab.

5.1 Effects of Co^{2+} and Ni^{2+} on Growth of *S. cerevisiae*

Firstly, the possible inhibitory effects of Co^{2+} and Ni^{2+} on growth of *S. cerevisiae* were tested under various conditions including rich and minimal media with different carbon and nitrogen sources. The timeline for growth curve experiments is shown in Figure 65:

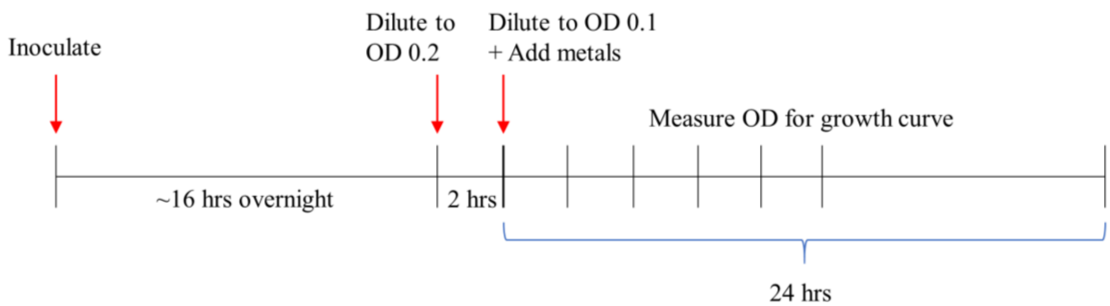

Figure 65. Timeline for standard growth curve experiments.

5.1.1 Growth curves in defined media

The first type of media considered was synthetic complete (SC) media, which is defined minimal media, containing a carbon and nitrogen source as well as any required amino acids, nitrogenous bases, and minor nutrients (276). Standard SC media contains glucose as a carbon source and $(NH_4)_2SO_4$ as a nitrogen source. The growth in SC is shown in Figure 66:

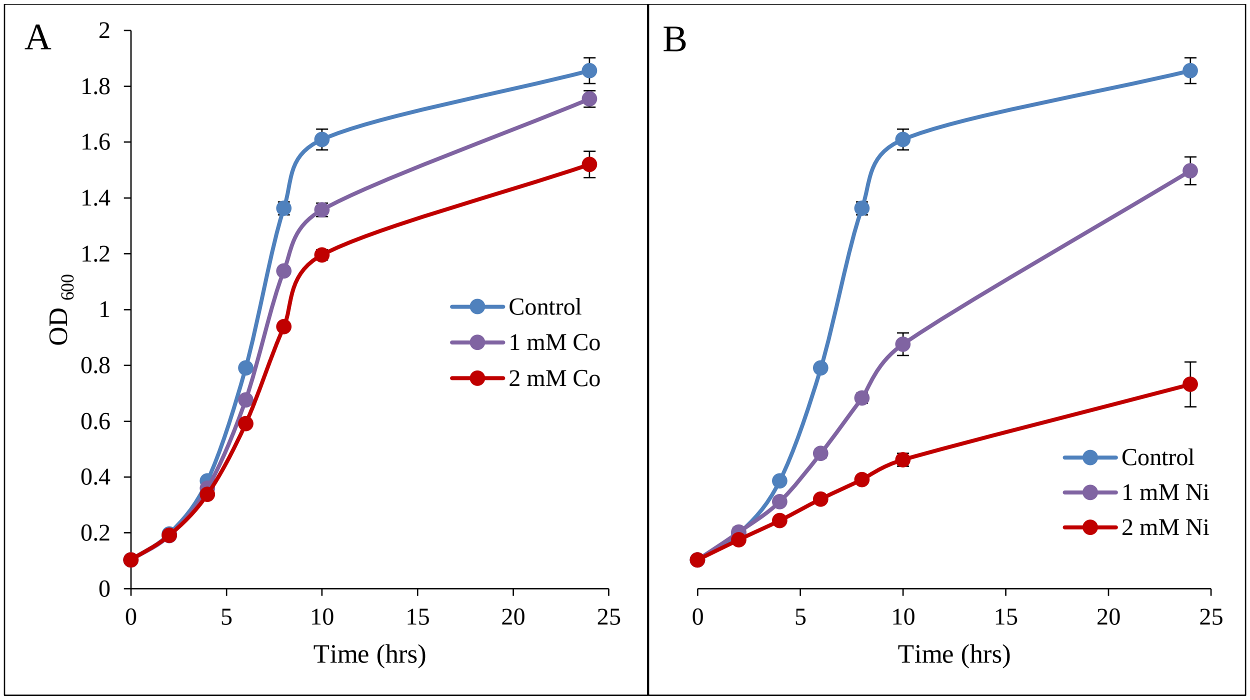

Figure 66. Growth curves of BY4741 in SC media at 30°C shaking at 200 rpm over 24 hrs with various concentrations of (A) Co^{2+} and (B) Ni^{2+}.

The growth curves indicated that both Co^{2+} and Ni^{2+} have significant inhibitory effects on growth in SC media, with Ni^{2+} being the more potent metal. Both Co^{2+} and Ni^{2+} show a maximum effect around 8 hrs (66% and 23% growth for 2 mM), but cells recover at least slightly by 24 hrs (81% and 36% growth). In a study under nearly identical conditions, an inhibitory effect of similar magnitude was been reported for 2 mM $CoSO_4$ (129), However, they found that the control cells reached a stationary phase OD_{600} near 7.0 (129), much higher than observed here, which seems uncharacteristically high for SC media (277, 278). Another study used S288C, a laboratory yeast strain from which BY4741 was derived (117). They incubated log-phase

S288C in SC media for 2 days and then reported the MIC_{90} for Co^{2+} and Ni^{2+} in SC to be 1.28 mM and 0.64 mM, respectively (117). The inhibitory effects observed in the present study are not quite as strong but still suggest that Ni^{2+} is more potent (117). Differences may be due to the strain used as well as culture conditions (117).

Growth in SC media was also tested with the addition of 0.05% yeast extract-B (MP Biomedicals, Santa Ana, CA) to assess if metals interact differently in a more complex media. Yeast extract-B is made from autolyzed yeast cells, and thus contains amino acids, peptides, carbohydrates, and water-soluble vitamins (MP Biomedicals, Santa Ana, CA). The results are shown in Figure 67:

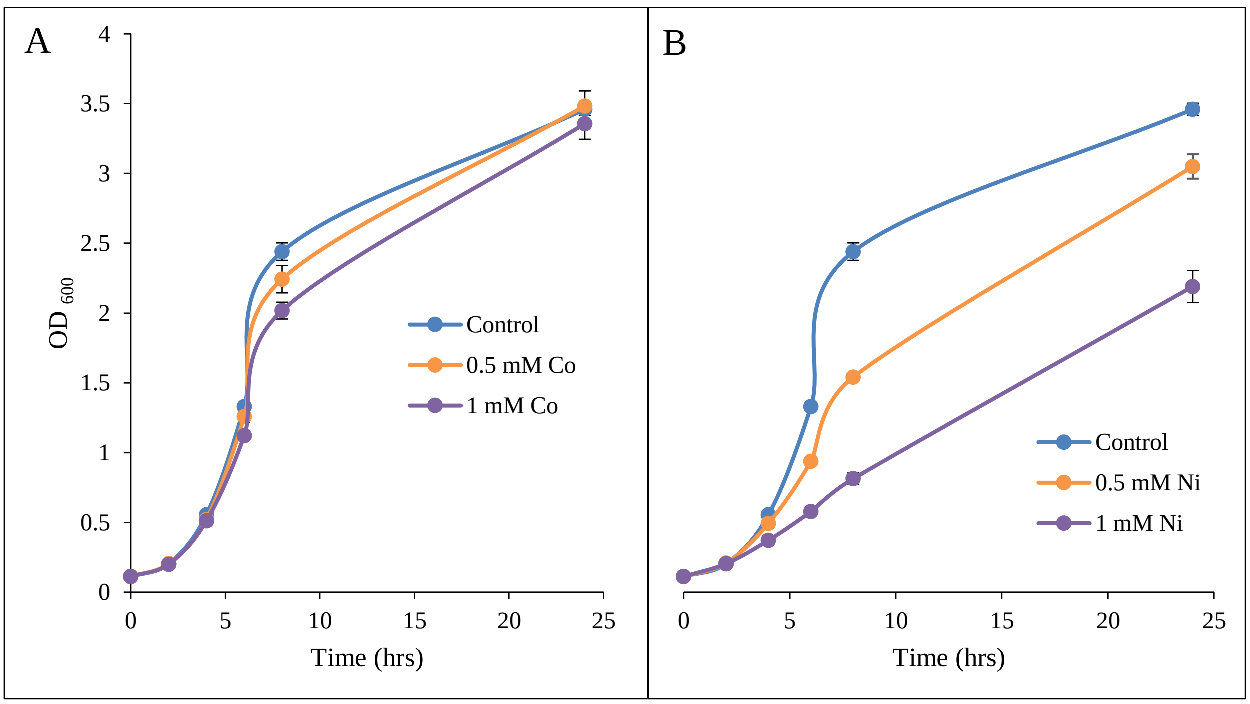

Figure 67. Growth curves of BY4741 in SC + 0.05% yeast extract-B media at 30°C shaking at 200 rpm over 24 hrs with various concentrations of (A) Co^{2+} and (B) Ni^{2+}.

The addition of 0.05% yeast extract-B had little effect on the inhibition of growth by Co^{2+}, as both showed 82% growth by 8 hrs for 1 mM Co^{2+}. However, an enhanced inhibitory effect was observed for 1 mM Ni^{2+} (46% growth in SC vs. 30% in SC+YE at 8 hrs). It has been previously shown that yeast extract complexes Co^{2+} and Ni^{2+} very effectively, thus increasing their bioavailability when precipitating agents are present (279). The reason for the enhanced inhibitory effect of Ni^{2+} may thus be due to complexation and increased uptake of metal (279), or complexation and depletion of media components. The fact that the effects of Co^{2+} were the same under either condition suggests that if metal-media complexation is occurring, it does not enhance the bioavailability of the metal or deplete essential components.

Although Co^{2+} and Ni^{2+} did not precipitate SC media, growth curves were also performed with glutamate as a nitrogen source (SCglu) shown in Figure 68:

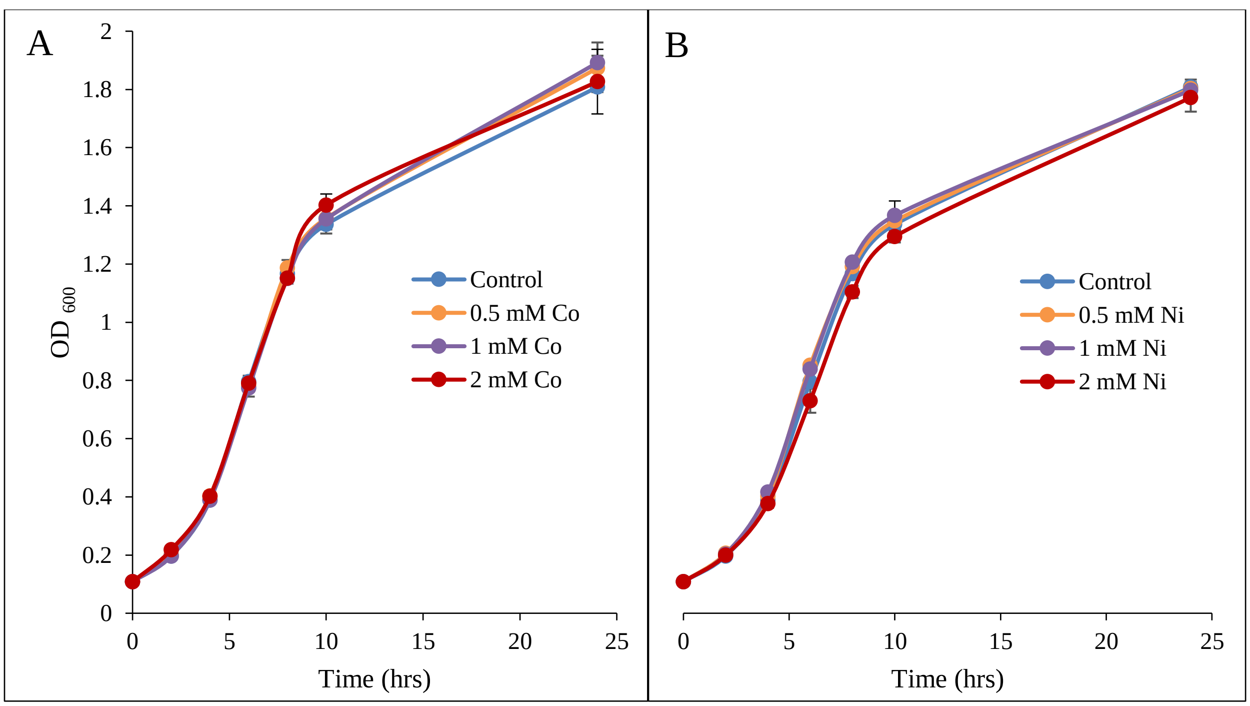

Figure 68. Growth curves of BY4741 in SCglu media at 30°C shaking at 200 rpm over 24 hrs with various concentrations of (A) Co^{2+} and (B) Ni^{2+}.

It was surprising to find that even at millimolar concentrations, Co^{2+} and Ni^{2+} did not affect the growth of BY4741 in SCglu. This was also observed for Mn^{2+} (Appendix C). The reasoning for this effect is not immediately clear, but there are several possibilities: 1) the metals may be chelated by glutamate itself, 2) the metals may not be taken up because the metal uptake pathway relates to nitrogen uptake, or 3) the nitrogen metabolism pathway of glutamate may confer inherent metal resistance. It has been reported that glutamate chelates Co^{2+} and Ni^{2+} in a 1:1 complex (280), but this is unlikely to completely explain the effect, as glutamate is only present at 0.5 mM. If chelation did occur, a decrease in growth would still be expected simply due to depletion of the nitrogen source. The uptake of metal was tested by pelleting treated cells in SC or SCglu and assaying the supernatant. The cell-associated Co^{2+} was unchanged in either media (~30%), while it was lower for Ni^{2+} (8% vs. 20%). It is possible that a reduced effect of Ni^{2+} is due to reduced uptake. As for the final possibility, it may be that the metabolic pathway of glutamate confers metal resistance. The use of glutamate compared to $(NH_4)_2SO_4$ as a nitrogen source has been reported to result in a massive increase in α-ketoglutarate production (64 vs. 0.5 mmol/mol glucose), as well as acetate, succinate, and pyruvate (281). α-ketoglutarate has been found to have direct antioxidant function, and may thus provide some resistance to redox-active metals (282). At this point, the involvement of the nitrogen source on Co^{2+} and Ni^{2+} growth inhibition remains unclear and requires further study.

5.1.2 Growth curves in rich media

Rich media for routine use is called YPD (yeast extract peptone dextrose), and it supports the growth of all viable yeast cells. It was suspected to contain many components which may complex the metals and is thus less informative for toxicity testing. Growth was tested at pH 7.1 (unadjusted) and at pH 5; the curves are shown in Figure 69:

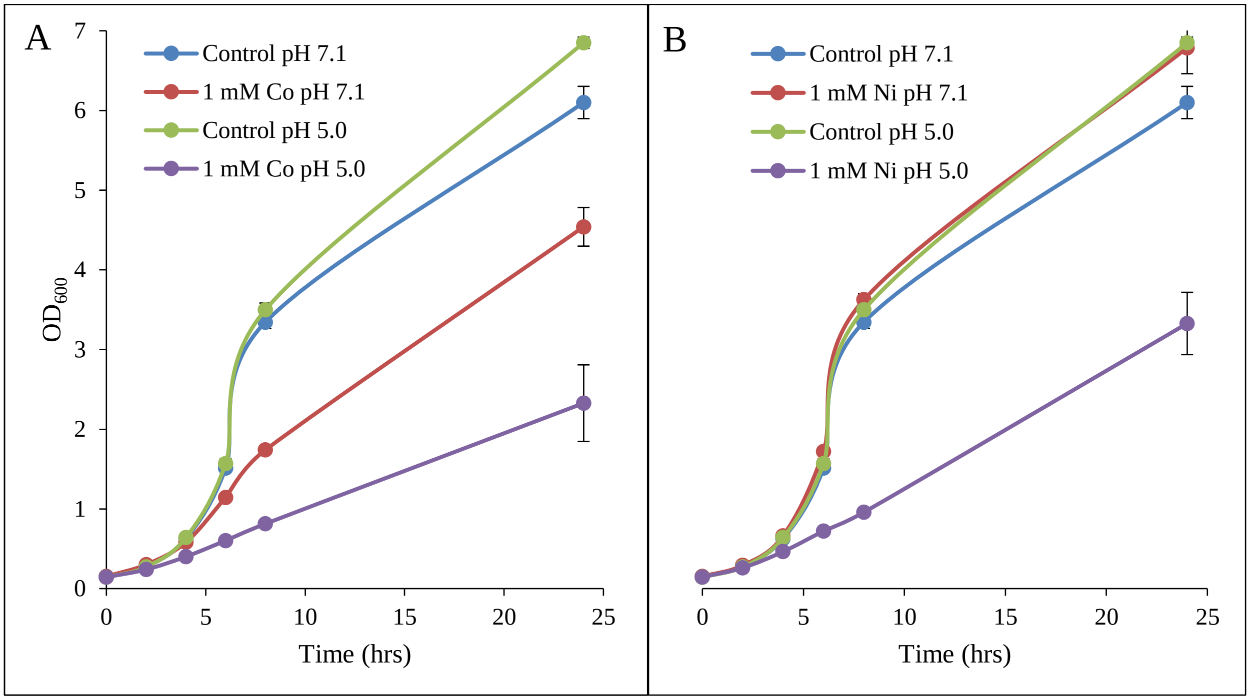

Figure 69. Growth curves of BY4741 in YPD media at pH 7.1 or 5.0 at 30°C shaking at 200 rpm over 24 hrs with 1 mM (A) Co^{2+} and (B) Ni^{2+}.

In contrast to the defined media, Co^{2+} had a stronger inhibitory effect than Ni^{2+}, but cells began to recover by 24 hrs in the standard pH 7.1 media. Ni^{2+} appeared to cause a slight increase in stationary phase OD_{600}, which may be due to alteration of the shape or size of the cells. The results highlight the importance of conditions when ranking metal potency, as Ni^{2+} was far more inhibitory in SC. A previous study which incubated log-phase S288C in YPD media for 2 days reported unspecific MIC_{90} for Co^{2+} and Ni^{2+} as >1.28 mM (117), suggesting that long-term inhibition is largely recoverable, as observed here. Another study with BY4741 using YPD media adjusted to pH 6.4 added metals at OD 0.8 and reported EC_{50}'s over 12 hrs for $CoCl_2$ and $NiSO_4$ to be 0.4 and 2 mM, respectively (122). This suggests that the metals have a stronger inhibitory effect on mid-log phase cells opposed to early-log phase used in this thesis, or that pH is also a factor. This agrees with the finding that the metals had a much stronger inhibitory effect in YPD adjusted to pH 5 (Figure 69), though recovery was also observed over time (up to 33% and 49% growth at 24 hrs for Co^{2+} and Ni^{2+}, respectively). The speciation of the metals themselves is not pH-dependent (32), so this suggests that at pH 5, the metals may complex a deprotonated media component which alters their effective speciation and/or increases their bioavailability.

YPG media was also considered, as it is routinely used for the identification of respiratory deficiency (RD), as it contains glycerol which cannot be fermented (119). The growth in non-fermentable media is slower, thus OD was also measured at 30 hrs. Growth was found to be very poor is unadjusted media, so the pH was set to 5. The results are shown in Figure 70:

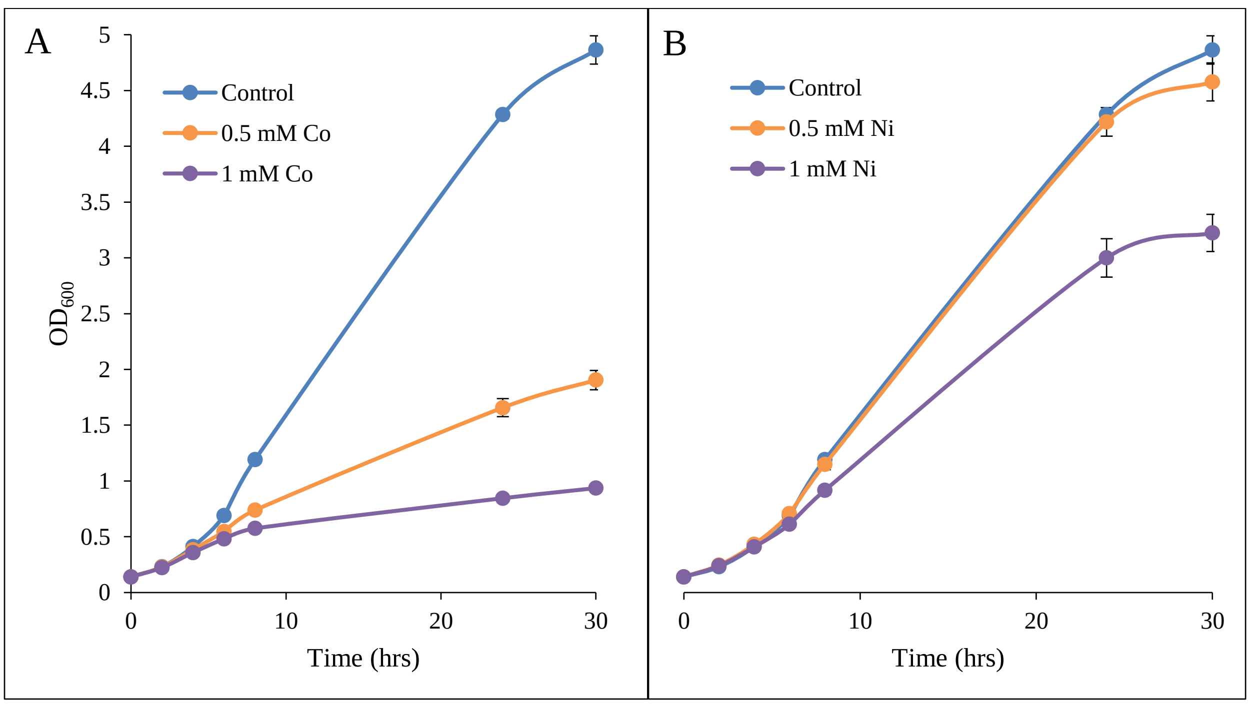

Figure 70. Growth curves of BY4741 in pH 5.0 YPG media at 30°C shaking at 200 rpm over 24 hrs with various concentrations of (A) Co^{2+} and (B) Ni^{2+}.

In direct comparison to unadjusted YPD, the effects of both metals were much greater, which suggests that the metals may induce RD. However, it was observed that the inhibitory effects of Co^{2+} and Ni^{2+} also showed a pH-dependence in rich media (Figure 69). As such, some of the inhibitory effects observed in YPG may simply be due to altered bioavailability at pH 5, in addition to damage to respiration. The effects of Co^{2+} were quite strong, as 1 mM Co^{2+} treatment resulted in only 19% growth by 30 hrs. Ni^{2+} was much less potent than Co^{2+}, but again had a fairly large effect (66% growth by 30 hrs). 1 mM Co^{2+} and Ni^{2+} have been previously reported to induce RD at rates of about 5 and 7%, respectively, after 24 hrs incubation in a customized rich glucose media (283). However, another study reported that 1 mM Co^{2+} induced 100% RD mutants after 24 hrs in a customized rich glucose media, and 2.1 mM Ni^{2+} induced 46% RD mutants (138).

5.1.3 Comparing growth conditions

To compare the relative inhibitory effects and recovery of growth under various conditions, results are summarized with 1 mM metal at 8 and 24 hrs in Figure 71:

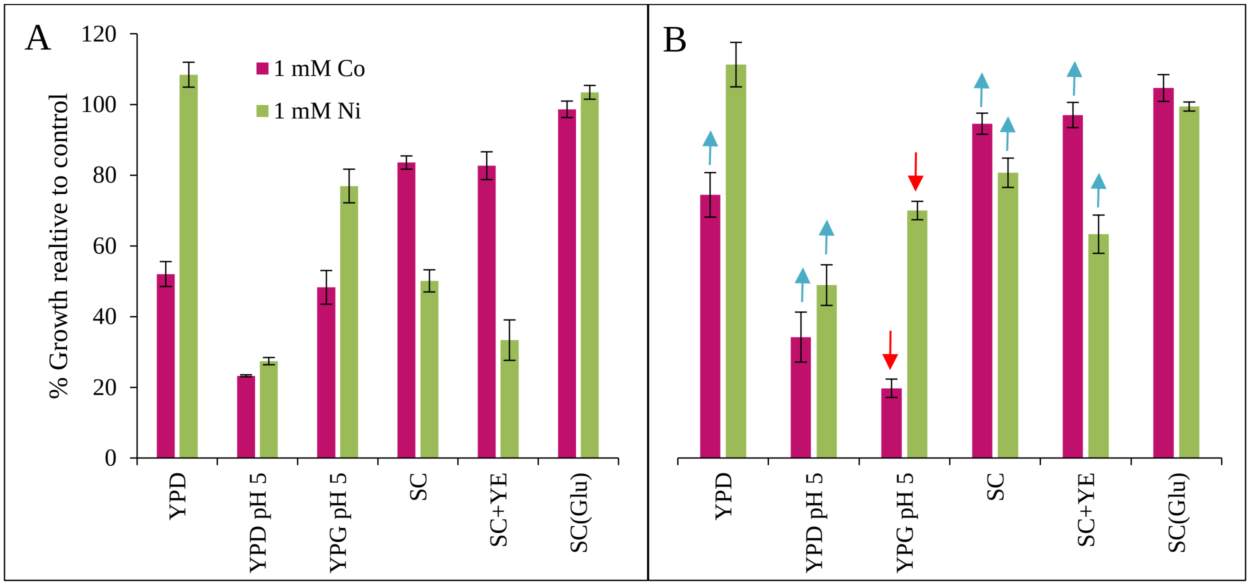

Figure 71. Summary of percent growth of BY4741 relative to control at (A) 8 hrs and (B) 24 hrs under various media conditions with 1 mM Co^{2+} or Ni^{2+}. Arrows in Panel B indicate a relative increase or decrease to values in Panel A.

One immediate observation was that the effects of either metal in YPG were not recoverable after 24 hrs, whereas growth increased or remained the same under other conditions. This supports the idea that mitochondria may be a target of Co^{2+} and Ni^{2+}. There were large differences between the metals in that Co^{2+} was more potent in complex rich media, while Ni^{2+} was generally more potent in synthetic defined media, and both metals caused stronger effects at pH 5. This suggests that components of rich media are depleted by Co^{2+} or enhance the bioavailability of Co^{2+} yet only have this effect with Ni^{2+} at pH 5 (279). Again, there is also the surprising finding that glutamate as a nitrogen source prevents any growth inhibition. The growth curves suggest, but are not entirely convincing, that respiration is a target which has been shown in previous studies (138, 283, 284). It is possible that the binding targets/chelators available at pH 5 in rich media cause Co^{2+} and Ni^{2+} to localize or speciate differently than under simpler conditions. Thus, further investigation was performed in SC media, in which mitochondrial damage would not necessarily manifest itself in growth inhibition but could result in condition-dependent loss of viability.

5.2 Effects of Co^{2+} and Ni^{2+} on Viability and Respiration of *S. cerevisiae*

Growth assays can provide information on inhibitory effects of test compounds but are not necessarily related to toxicity and cell death. It is possible that the presence of metal simply supresses growth, being cytostatic. Thus, it was considered if the cells maintain viability once Co^{2+} and Ni^{2+} are removed from the growth medium. The same incubation scheme was used as with the growth curves (Figure 65).

5.2.1 Spot plate assays with W303 and BY4741

The W303 strain turns red with functional mitochondria (172). After growing W303 for 6 hrs in SC in the presence of Co^{2+} or Ni^{2+}, cells were pelleted, resuspended in sterile water, and spotted onto YPD with increasing dilution.

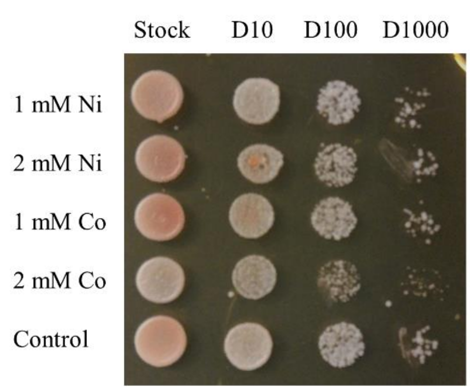

Figure 72. Spot plate assay of W303 grown for 6 hrs in SC spotted onto YPD in increasing dilutions, then grown for 2 days.

Firstly, the assay indicated that Co^{2+} and Ni^{2+} did not strongly affect the viability of W303 after removal from the growth medium. However, it is still clear that 2 mM Co^{2+} causes a slight decrease in cell density, suggesting that it is mildly cytotoxic to W303 in SC media. Additionally, the slightly white colour of the 2 mM Co^{2+}-treated cells suggests that Co^{2+} causes mitochondrial damage.

Growth of the wild type BY4741 was then tested for viability using the spot plate assay but was also spotted onto YPG to check if viability depends on respiratory capacity.

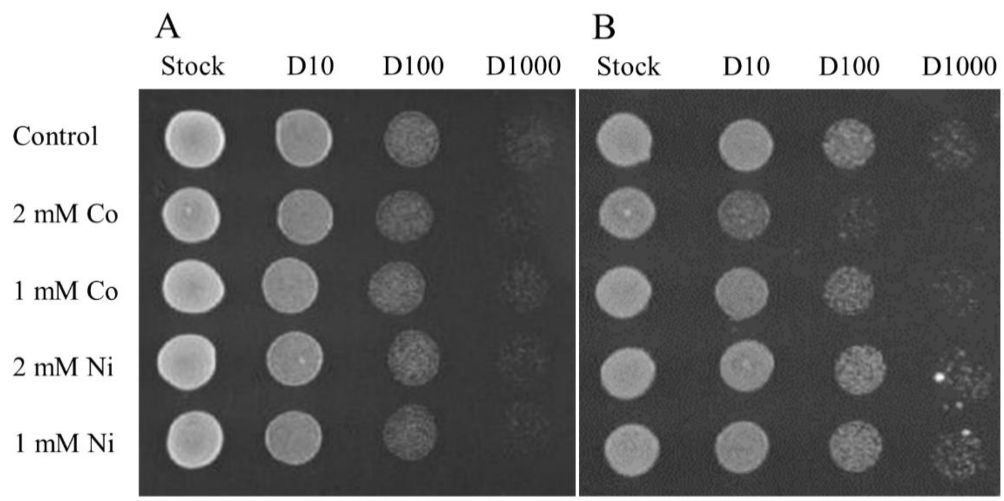

Figure 73. Spot plate assay of BY4741 grown for 6 hrs in SC spotted onto (A) YPD and (B) YPG in increasing dilutions, then grown for 2 days.

The pattern on YPD again suggested that Co^{2+} and Ni^{2+} have relatively little effect on viability under fermenting conditions. However, when the same samples were spotted onto YPG, the growth of the 2 mM Co^{2+}-treated sample was noticeably reduced, again suggesting that Co^{2+} especially affects the mitochondria. It was not clear from this assay if meaningful changes occurred with the other treatments, so a more sensitive assay was performed.

5.2.2 Viability on YPD and YPG

After 4 hrs growth in SC, ~400 cells were washed free of metal, counted, and identical samples were plated on both YPD and YPG. This eliminates possible error from cell counts. The growth ratio between these plates is shown in Figure 74:

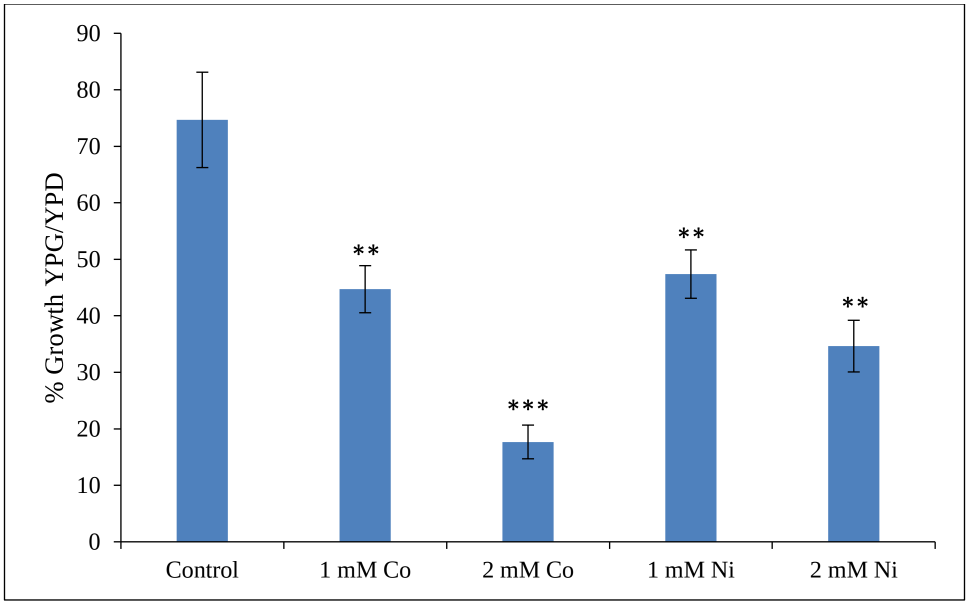

Figure 74. Ratio of colony counts on pH 5.0 YPG relative to that on YPD after 4 hrs growth in SC with various Co^{2+} or Ni^{2+} concentrations. YPD plates were incubated for 2 days, and YPG plates for 4 days. Significance is assessed relative to the control ((**) $p < 0.01$, (***) $p < 0.001$).

The growth ratios more clearly indicate that both Co^{2+} and Ni^{2+} cause greater decreases in viability when plated on YPG. This suggests that Co^{2+} and Ni^{2+} cause damage to mitochondria which impairs the respiratory capacity by some mechanism. The induction/selection of RD mutants observed in the present study by 2 mM Co^{2+} and Ni^{2+} (75% and 51%, respectively) is lower than has been previously reported for Co^{2+} (100%), but comparable to that for Ni^{2+} (46%) (138). However, this study used a different yeast strain, growth conditions, incubation time, and reporter method (138). Another previous study also found that Co^{2+} and Ni^{2+}, along with other carcinogens, showed a greater toxicity on YPG, with MICs ~43% lower than on YPD (284). It was surprising to observe that the control did not show 100% of colonies on YPG, as this suggests that there may have been mutations in the control, or that the plate incubation period was not sufficient to allow all colonies to grow to visible density. It was also qualitatively observed that the Ni^{2+}-treated cells began showing colonies on YPG earlier than the others, even though the overall density was lower. This may indicate mutation which leads to a higher growth rate of the surviving cells, as Ni^{2+} is known to be a potent mutagen (4).

5.2.3 Direct effects of Co^{2+} and Ni^{2+} on isolated mitochondrial membranes

While it appears that mitochondria are affected by Co^{2+} and Ni^{2+} (138, 283), it is not known if the metals localize/bind to the membrane itself, which is the target of interest for this thesis. Therefore, the direct effects of Co^{2+} and Ni^{2+} on the membrane fluidity of mitochondria isolated from *S. cerevisiae* by Brittney Kozlowski were tested and compared to model liposomes (Section 2.8.4). The metals were titrated into Laurdan-containing samples, with temperature held at 30°C.

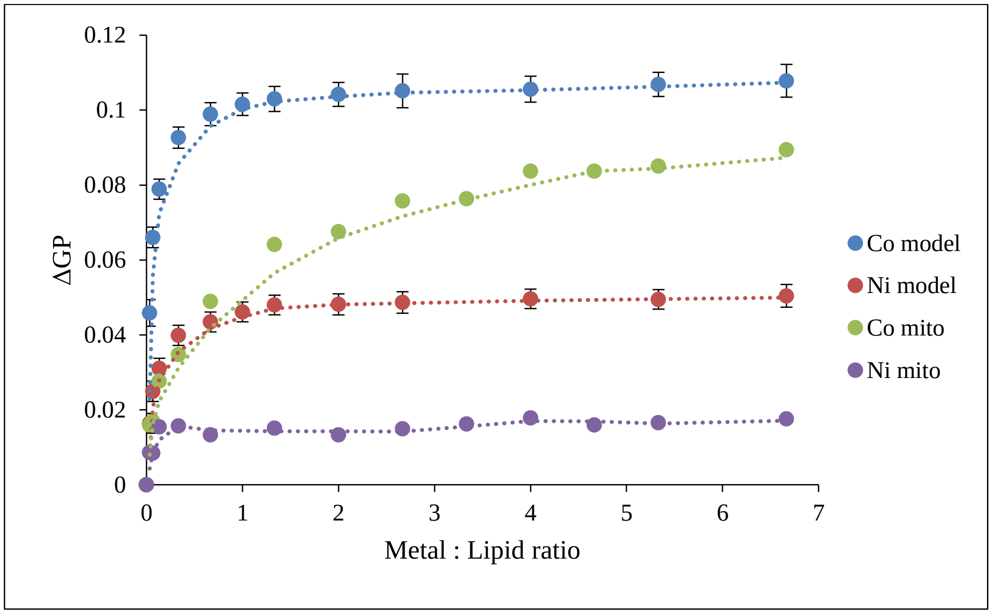

Figure 75. ΔGP in 0.12 mg/mL (protein weight) *S. cerevisiae* isolated mitochondrial membranes and 0.3 mM model mitochondrial membranes at 30°C upon titration of Co^{2+} or Ni^{2+} in 20 mM Hepes, 250 mM sucrose pH 7.2.

The initial titration indicated that Co^{2+} has very strong rigidifying interactions with the isolated mitochondrial membrane, saturating at about 4:1 Co^{2+}/lipid ratio. Ni^{2+}, on the other hand, showed very minor rigidifying effects which saturated at 1:5 Ni^{2+}/lipid ratio. In the model system, the effects of both Co^{2+} and Ni^{2+} showed a saturating pattern by about a 1:1 ratio. The effects observed in the model were much greater than in the isolated mitochondria, which are to be expected, as some lipid targets in mitochondria may be inaccessible, and some metal may be protein-bound.

While the effects observed in the isolated mitochondria cannot be compared directly to the lipid model because of the much greater complexity, the contrast provides insight into what may be occurring in the isolated mitochondria. The fact that the effects of Ni^{2+} saturate in a similar pattern to the model suggests that, in the mitochondria, Ni^{2+} initially binds to accessible lipid targets, but no further membrane binding occurs. The effects of Co^{2+} on the isolated mitochondria are very interesting in comparison to the model, as the effects require higher concentrations (or more time) to saturate but begin to approach the effects seen in the model. This suggests that the amount of accessible lipid targets may change as Co^{2+} binds to the membrane, or that Co^{2+} can pass through over time. It has been previously observed that Co^{2+} accumulates within the mitochondrial matrix in yeast cells (140), so it seems feasible that Co^{2+} could have access to inner-leaflet lipids, as suggested here.

5.3 Live-cell Imaging with Labelled Mitochondria

It was also of interest to monitor the effects of Co^{2+} and Ni^{2+} on mitochondrial structure and oxidative stress. As mentioned, Co^{2+} and Ni^{2+} have both been suggested to be inducers of oxidative stress in the mitochondria leading to the opening of the MPTP in mammalian cells (20, 132, 133). Mitochondrial-specific dyes were used to monitor mitochondria using fluorescence microscopy, according to the following timeline:

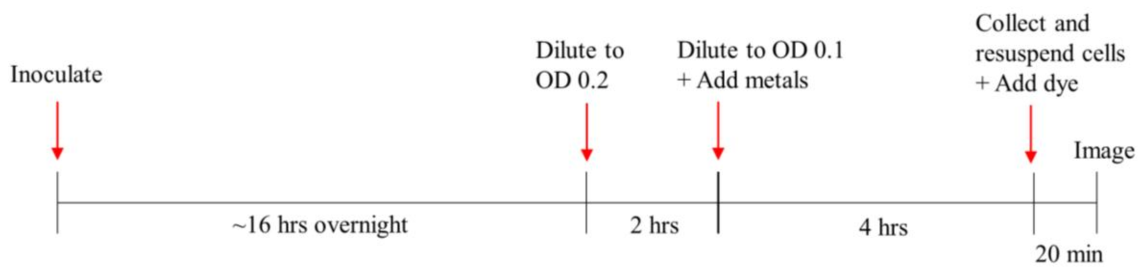

Figure 76. Timeline for fluorescence microscopy experiments.

5.3.1 Effects of Co^{2+} and Ni^{2+} on mitochondrial morphology

Yeast mitochondrial networks are arranged as tubules in healthy cells, but fragmentation has been found to correlate with respiratory deficiency and loss of mtDNA (285). The effects of Co^{2+} and Ni^{2+} on the morphology of BY4741 mitochondria were tested with MitoTracker Green-FM (MTG-FM). MTG-FM is a mitochondrial dye which is intended to localize to the mitochondria regardless of membrane potential (Molecular Probes, Eugene, OR), and becomes fluorescent upon binding to specific matrix proteins (180, 286). The effects of Co^{2+} and Ni^{2+} on the morphology of BY4741 are summarized in Figure 77:

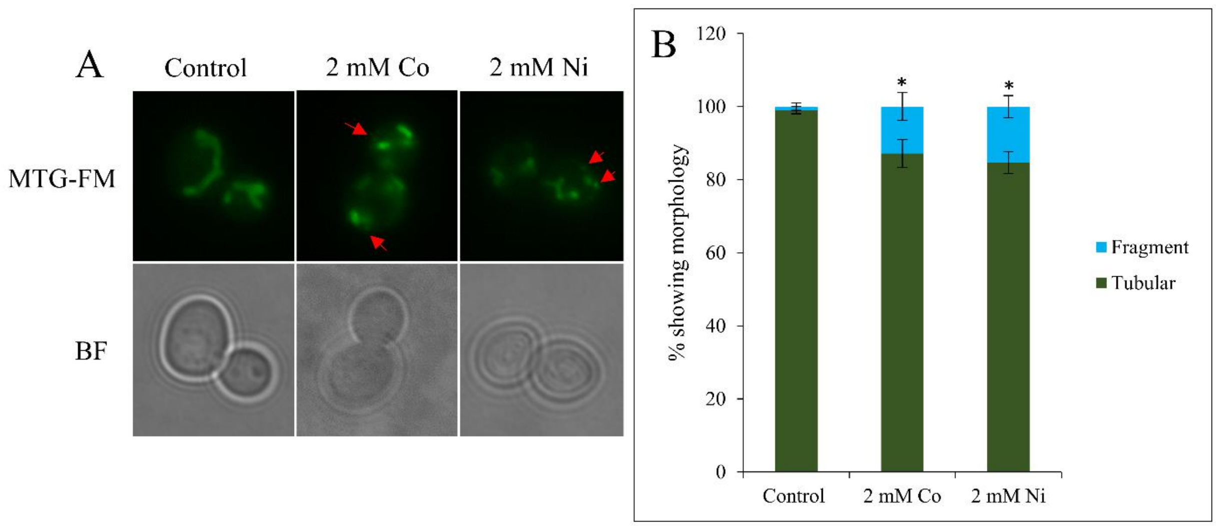

Figure 77. (A) Representative images of cells stained with 150 nM MitoTracker Green-FM (MTG-FM) (Ex 490, Em 516 nm) in 10 mM Hepes, 5% glucose pH 7.4 at 1000x magnification after 4 hrs growth in SC, along with corresponding brightfield (BF) images. Red arrows indicate fragments not attached to the mitochondrial tubule. (B) Percentage of cells showing tubular vs. fragmented morphologies.

In assessing the 3D structure, both 2 mM Co^{2+} and Ni^{2+} caused a significant portion of cells to show mitochondria as isolated pinpoints of fluorescence intensity, indicating fragmentation from the tubular network. The amount of fragmentation induced by both metals was low but relatively-similar, at about 15% (Figure 77). The fragmentation of mitochondria is suspected to be linked to an apoptotic response in yeast (285). The relatively low amount of fragmentation induced by these metals over 4 hrs suggests that they may be well-tolerated by the cell, thus potentially having a stronger mutagenic tendency rather than causing immediate cell death. Mitochondrial fragmentation has also been previously-reported for other metals including Cd^{2+} (287) and Ag^{+} (117), after growth to mid-log phase. Mitochondrial fragmentation is associated with disruption to respiration (117, 285, 288), and is thus consistent with the findings for viability ratios (Section 5.2.2). Although MTG-FM is supposed to accumulate independent of mitochondrial membrane potential, there is dispute in the literature (289, 290). Thus, it would be of interest to compare the results using cells transformed with mitochondrial GFP markers, in which the fluorescent probe would unquestionably be in the mitochondria (291).

5.3.2 Effects of Co^{2+} and Ni^{2+} on mitochondrial superoxide production

As has been mentioned, oxidative stress is one of the overarching themes of redox-active metal toxicity (81), so it was suspected that this may be one of the major sources of damage to the mitochondria caused by Co^{2+} and Ni^{2+}. The dye MitoSOX Red (MSR) is a specific indicator of oxidative stress in the mitochondria, as it becomes fluorescent upon oxidation by superoxide and then binding to mtDNA (292). The main reaction product of MSR oxidation is 2-hydroxyethidine, a derivative of ethidium (293). A summary of the results is shown in Figure 78:

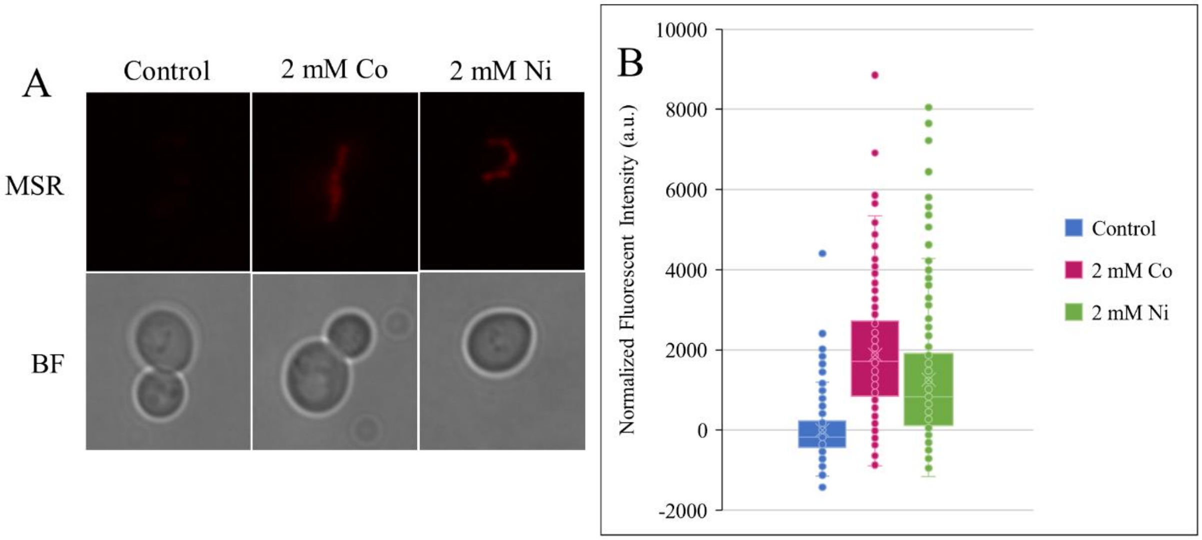

Figure 78. (A) Representative images of cells stained with 5 µM MitoSOX Red (MSR) (Ex 510, Em 580 nm) in 10 mM Hepes, 5% glucose pH 7.4 at 1000x magnification after 4 hrs growth in SC, along with corresponding brightfield (BF) images. (B) Control-normalized fluorescence intensities of mitochondria.

The intensities in each separate trial were normalized according to the control for that set to account for any differences in staining conditions. Both metals show an increase in the relative intensity generated by MSR, suggesting that they cause oxidative stress in the mitochondria. However, the spread in the intensity data was very large (Figure 78B). To confirm the significance of the increase, intensities were sorted into “bins” and the fraction of cells in each bin is shown in Figure 79:

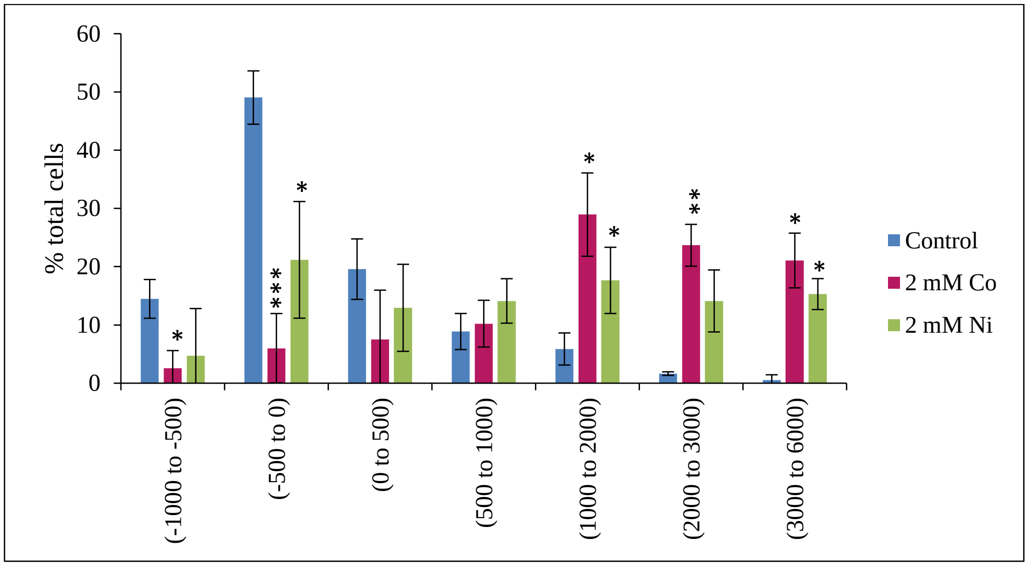

Figure 79. Control-normalized intensities of cells stained with 5 µM MSR in 10 mM Hepes, 5% glucose pH 7.4 sorted into intensity bins. ((*) $p < 0.05$, (**) $p < 0.01$, (***) $p < 0.001$).

The sorted intensities more clearly show that the metal-treated samples have fewer "dark" cells and more "bright" cells compared to the control. The effects of Co^{2+} appear to be greater than that of Ni^{2+} suggesting that Co^{2+} is a more potent inducer of oxidative stress in the mitochondria. This finding is consistent with the viability assays which showed that 2 mM Co^{2+} induced greater respiratory deficiency than 2 mM Ni^{2+} (Section 5.2.2). Previous reports have also found that excess H_2O_2 is generated by $NiSO_4$ in human lymphocytes (132), and Co^{2+} in isolated rat liver mitochondria (133), supporting the findings here that both metals induce mitochondrial oxidative stress.

However, it has been suggested that using MSR as a specific superoxide indicator can be misleading, as further reactions may occur with the 2-hydroxyethidium product (293). Therefore, the specific oxidation products should be characterized in order to exactly understand the type of

ROS produced (293), but it is still clear that general oxidative stress in the mitochondria occurs. Again, this is consistent with the current understanding of redox-active metal toxicity (44, 81). Increased oxidative stress in the mitochondria may have direct implications for membrane properties and function, as lipid peroxidation reactions may occur (81, 294).

5.4 Polar Lipid Extracts of *S. cerevisiae* Treated with Co^{2+} and Ni^{2+}

As it became clear that both Co^{2+} and Ni^{2+} exert inhibitory and toxic effects on *S. cerevisiae* related to respiration, it was of interest to determine if these effects were associated with inherent changes in polar lipid composition. Thus, whole cell lipids were extracted from log-phase cells treated with Co^{2+} or Ni^{2+} for 4 hrs in SC.

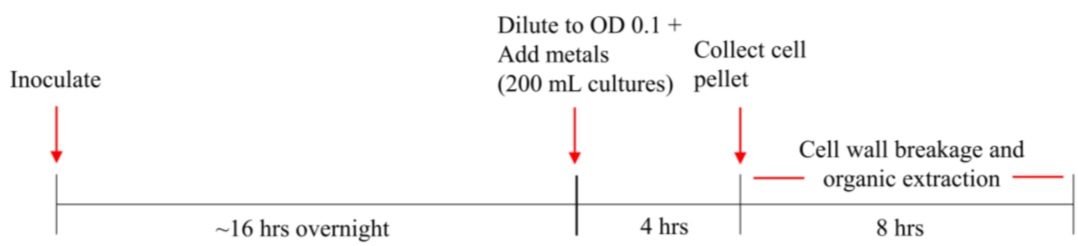

Figure 80. Timeline for lipid extractions from *S. cerevisiae.*

Co^{2+} and Ni^{2+} were added to the yeast culture in late log-phase. The total lipid extract of *S. cerevisiae* was rich in neutral lipid and did not form liposomes.

5.4.1 Polar lipid TLC of metal-treated extracts

The polar lipids were thus recovered by precipitation in acetone (185, 186), though the yield was poor, and the composition was assessed by TLC (165):

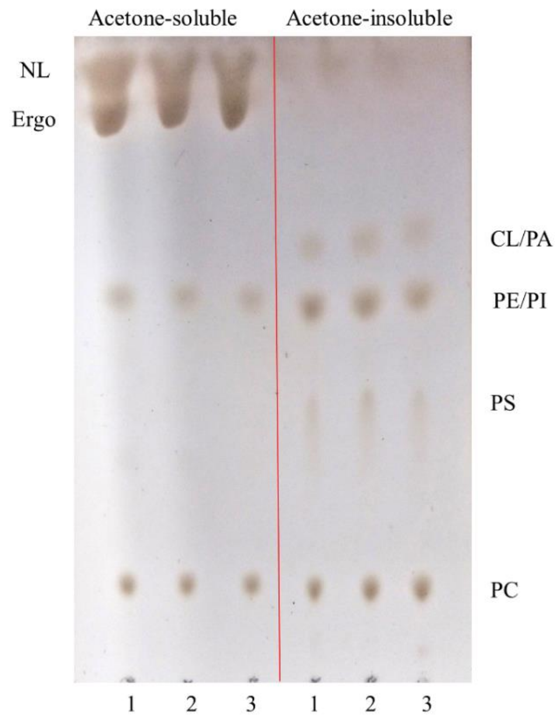

Figure 81. Polar lipid TLC of 100 µg of *S. cerevisiae* acetone-soluble/insoluble lipid extracts after 4 hrs treatment in SC media: 1) Control, 2) 1 mM Co^{2+}, 3) 1 mM Ni^{2+}. PC = phosphatidyl-choline, PS = phosphatidyl-serine, PE = phosphatidyl-ethanolamine, PI = phosphatidyl-inositol, CL = cardiolipin, PA = phosphatidic acid, Ergo = ergosterol, NL = neutral lipids.

It is clear that the large amount of neutral lipids and Ergo were removed in the acetone, yet there were still some PC and PE lipids which were not recovered. TLC did not clearly indicate compositional differences among the major phospholipids upon metal treatment, but there appears to be a shift in the PE/PI and PI/CL/PA spots upon Ni^{2+} treatment. This suggests a change in acyl chains towards a slightly less-polar nature. It is possible that this represents a shift to longer or more saturated acyl chains, but detailed characterization of these spots was not performed due to lack of time and proper equipment. The acetone-insoluble (polar) lipid extracts were used to prepare liposomes with Laurdan incorporated to see if the rigidity of the membrane was affected.

5.4.2 Laurdan GP of polar lipid extracts

The melting curve of the Control extract compared to the Avanti Yeast polar extract is shown in Figure 82:

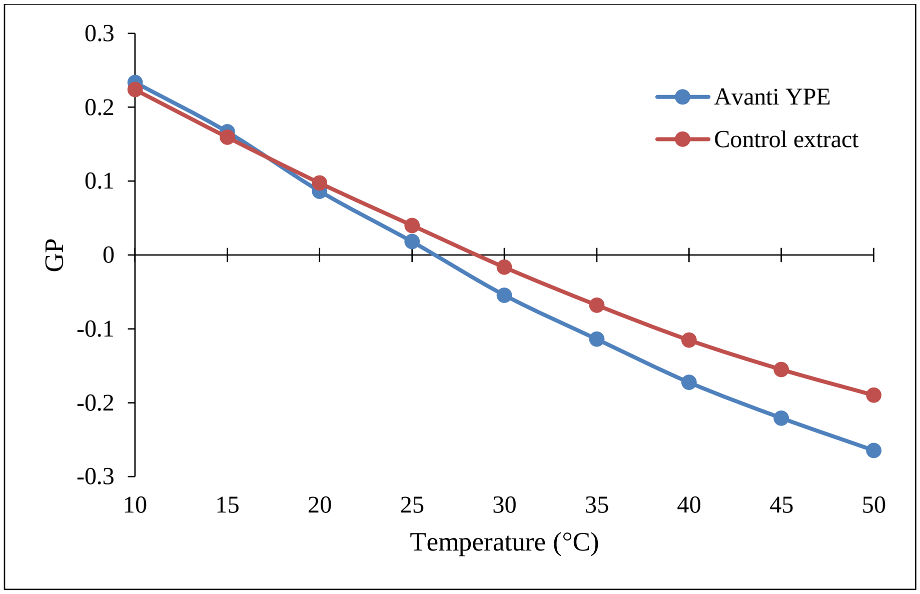

Figure 82. Laurdan GP melting curves of Avanti Yeast Polar Extract (YPE) and Control *S. cerevisiae* extract after 4 hrs in SC media in 20 mM Hepes, 100 mM NaCl pH 7.4. Liposomes were made with polar lipids from one independent extraction.

The melting curves of the Avanti polar extract and experimental extract were similar in fluidity, but differences were greater above 25°C. One of the major contributing differences may be the loss of some polar lipids (Figure 81) and the presence of Ergo in the Avanti extract (Appendix C), as it was mostly removed in the experimental extract. For a future experiment, it may be worthwhile to recover all the lost polar lipids by preparative TLC and add Ergo back to the extract. The difference of the Co^{2+} and Ni^{2+}-treated extracts from the Control are shown in Figure 83:

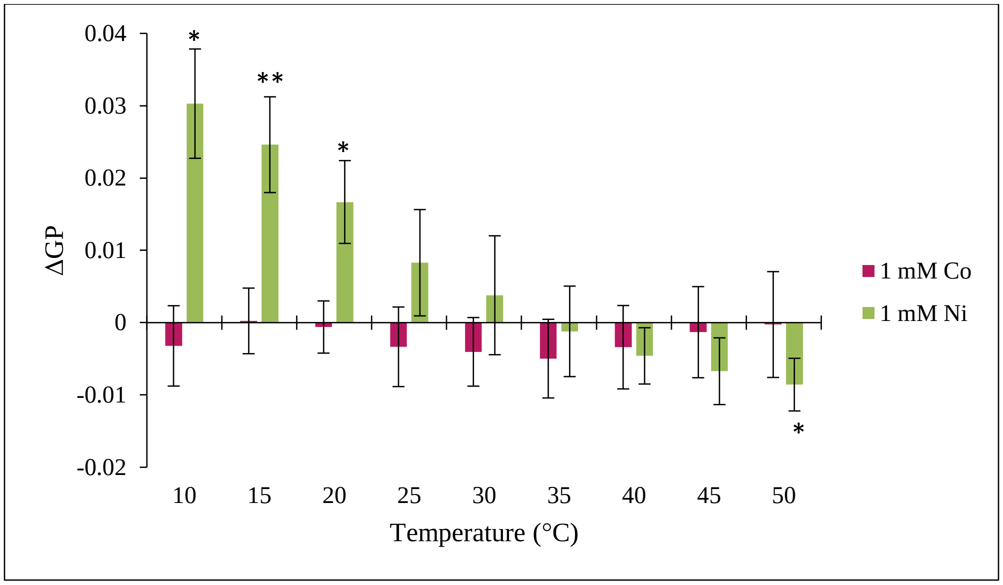

Figure 83. ΔGP of 1 mM metal-treated polar extracts relative to the control in 20 mM Hepes, 100 mM NaCl pH 7.4.

The melting of the Co^{2+}-treated polar extract was identical to the control, which makes sense given that the control and Co-treated extracts showed the same TLC pattern (Figure 81). Again, consistent with TLC is the finding that the melting of the Ni^{2+}-treated extract is minorly different from the control. It is slightly more rigid at low temperatures and slightly more fluid at high temperatures, but not different from the control at or around physiological temperature (30°C) (Figure 83). This suggests that slight changes in composition may be due to a stress response. It is possible that Ni^{2+} interacts directly with the membrane, thus *S. cerevisiae* alters the composition to make it less favourable for metal binding, without affecting membrane properties at 30°C. The liposome structure was also measured by DLS, and it was found that the

Co^{2+} liposome radii were not different from the control (48.9±0.7 nm), but the Ni^{2+} liposomes were slightly larger (52.1±0.4 nm). The reason for the slight size difference has not been deduced, yet may depend on different composition, hydration, and packing. A previous study on the response of *A. ferrooxidans* cytoplasmic membrane composition to Ni^{2+} stress found that, in general, most strains increased the saturated fatty acid content (295). Though a different organism, this supports the idea here that Ni^{2+} stress may prompt a slight alteration of acyl chain structure towards a less-polar nature. The change may be related to modulating oxidative stress, as saturated fatty acids would be less sensitive to lipid peroxidation (296).

However, the relatively minor effect observed on overall membrane properties may be sensible, as it is likely impractical and potentially detrimental for cells to dramatically change inherent membrane fluidity. It thus appears that, considering the total cell lipids, neither Co^{2+} nor Ni^{2+} significantly regulate polar lipid synthesis pathways, though it should be noted that changes in minor lipid components may not be detectable by TLC but require a more sensitive method such as HPLC. In a previous study on rat liver mitochondria, Co^{2+} was found to up-regulate CL production as CL synthases require a metal cofactor, of which Co^{2+} is the most potent activator in mammals (66, 297). However, the yeast CL synthases operate much more efficiently with Mg^{2+} over Co^{2+}, (66, 298) so Co^{2+}-treatment may instead cause CL down-regulation in yeast. It is possible that this effect in *S. cerevisiae* is too minimal to be detected by TLC of a total cell extract. Thus, investigation with a more sensitive method is of interest for future study.

5.5 Neutral Lipid Extracts of *S. cerevisiae* Treated with Co^{2+} and Ni^{2+}

As little change was observed in polar lipids, it was then considered if any effect may have occurred in the neutral lipid fraction. The major neutral lipids in *S. cerevisiae* include: storage lipids TAG and SE, structural sterols (mainly Ergo), and DAG (299). Neutral lipids are important as an energy reserve and as precursors for lipid synthesis (299). DAG also functions as a secondary messenger in signaling pathways (67, 299) and is involved in vesicular trafficking (300).

5.5.1 Neutral lipid TLC of metal-treated extracts

The acetone-soluble neutral lipid fraction was separated by TLC (165) and spots were identified using various standards:

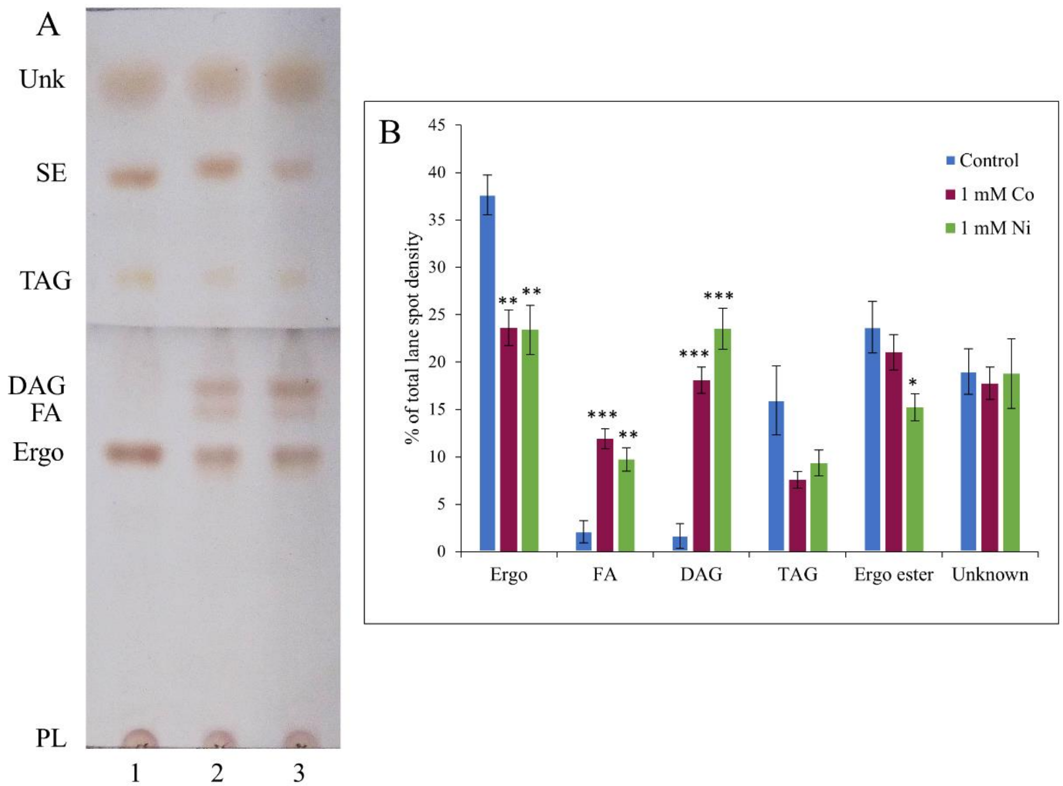

Figure 84. (A) Neutral lipid TLC of 100 µg of acetone-soluble lipid extracts from S. cerevisiae treated for 4 hrs in SC media: 1) Control, 2) 1 mM Co^{2+}, 3) 1 mM Ni^{2+}. (B) Background-corrected spot density distribution. PL = polar lipids, Ergo = ergosterol, FA = fatty acids, DAG = diacylglycerol, TAG = triacylglycerol, SE = sterol esters, Unk = unknown. Significant difference from the control is indicated. (*) $p < 0.05$, (**) $p < 0.01$, (***) $p < 0.001$

In contrast to the polar lipid composition, obvious major changes were detected in the neutral lipids. The Co^{2+} and Ni^{2+}-treated extracts showed a similar distribution pattern, with a large increase in DAG and free fatty acids relative to the control and decreases in Ergo and TAG (Figure 84). There was also a shift in the location of the SE spot towards a less polar nature. One large unknown spot running near the end of the plate is yet unidentified but does not appear to be affected. Additionally, the Co^{2+} and Ni^{2+}-treated neutral lipid extracts were pigmented compared to the colourless control. The absorbance spectra indicated large differences (Appendix C), yet the identities of the co-extracted pigmented compounds are yet unknown. To confirm that there were no biases in conclusions based on relative distribution of spots, various ratios were also measured. DAG, TAG, and FA content are intrinsically-linked, as well as Ergo/SE (299). The ratios are shown in Figure 85:

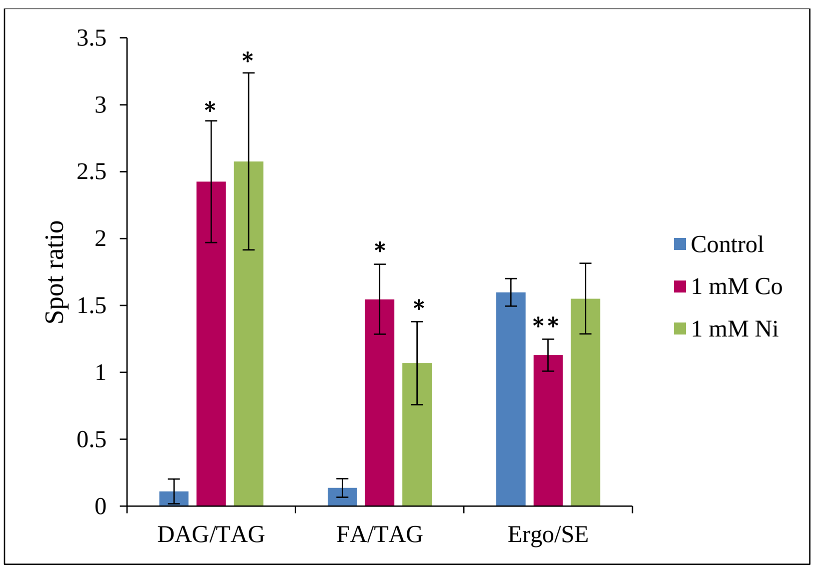

Figure 85. Spot density ratios between DAG/TAG, Ergo/SE, and FA/TAG for spots on neutral lipid extracts TLC. Significant difference from the control is indicated. (*) $p < 0.05$, (**) $p < 0.01$

The spot density ratios confirm that the apparent increase in DAG relative to TAG is real for both Co^{2+} and Ni^{2+}, showing ~22x more DAG than the control. An FA increase relative to TAG also occurs, with Co^{2+} causing a 10x and Ni^{2+} causing a 7x increase. Only Co^{2+} significantly decreased Ergo relative to SE (30% decrease), while Ni^{2+}-treatment maintained the Ergo/SE ratio, despite apparent changes in spot distribution (Figure 84B).

The zeta potential of 0.3 mM dispersions in 100 mM NaCl pH 7.4 showed that the control neutral lipid extract (-25.7±3.1 mV) was considerably different from that of the Co^{2+} and Ni^{2+}-treated extracts (-40.5±1.2 and -43.5±1.9 mV, respectively). This suggests that the metal-treated extracts are more negatively-charged, which is likely due to more fatty acids present.

5.5.1.1 Detection of DAG regioisomers

DAG has several isomeric forms which have different activity in the cell (301). The major distinction is between 1,2- and 1,3- regioisomers, which differ in the acylation position on the glycerol backbone (301). From the TLC method presented above, the isomeric form of DAG could not be determined, as 1,2- and 1,3-DAG ran identically. Thus, plates were modified with boric acid, which allows for separation of DAG regioisomers (169). The results are shown in Figure 86:

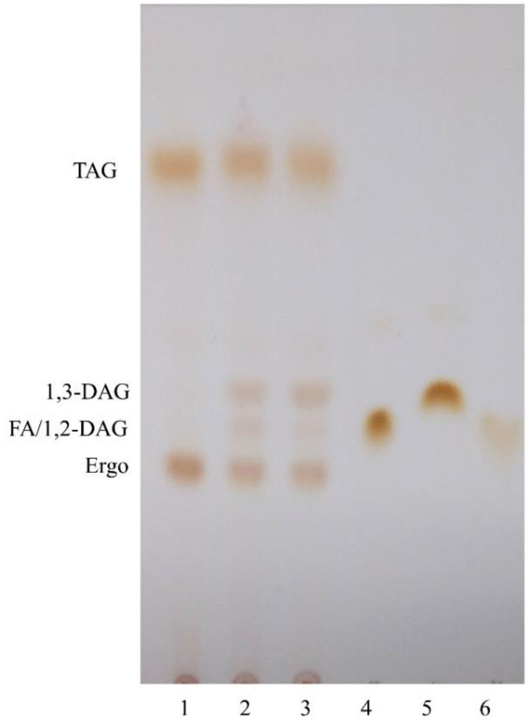

Figure 86. TLC of 100 µg neutral lipid extracts on 2.3% boric acid-modified plates with 96:4 chloroform/ acetone. 1) = control, 2) = 1 mM Co^{2+}-treated, 3) = 1 mM Ni^{2+}-treated, 4) = 1,2-DAG, 5) = 1,3-DAG, 6) = oleic acid.

The boric acid-modified TLC suggests that the DAG increase is due to accumulation of 1,3-DAG. The 1,2-DAG and FA spots run very similarly, but the band appears to correlate best with FA, suggesting that there is no detectable change in 1,2-DAG levels. This suggests that the metals may cause a preferential hydrolysis of TAG into the 1,3 form and it may get trapped in this thermodynamically-favourable isomer (302). It seems unlikely that the 1,3 form is an artefact, as there were no acidification steps during the extraction that would have promoted isomerization (170), but further experiments should be done to confirm that it is not an artefact. This is very interesting as 1,3-DAG is not the active signaling form of DAG, though it exerts similar effects on membrane properties (303). The following schematic shows how the insertion of DAG may lead to defects in normal bilayer packing:

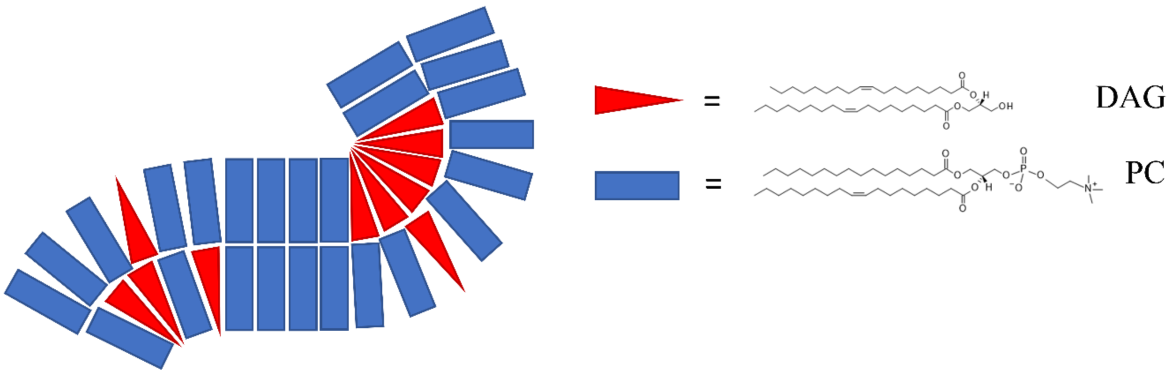

Figure 87. Schematic diagram of DAG accumulation in a PC bilayer.

The increase in DAG may be quite detrimental depending on where it localizes, as its cone-shaped geometry results in bilayer destabilization and conversion to hexagonal phase (233, 304). The introduction of packing defects in the membrane may affect permeability and membrane protein function.

5.5.2 Neutral lipids discussion

TAG is a major component of lipid droplets (LDs) in yeast, as it serves as an energy storage molecule and a substrate in lipid synthesis pathways (299). The TAG/DAG/FA content is intrinsically-linked as these molecules serve as substrates and precursors in lipid breakdown and synthesis (305, 306). It is thus possible that the changes in TAG/DAG/FA are due to a common interaction (299, 305–307), as the cycling pathways for neutral lipids are shown in Figure 88, with observed changes noted:

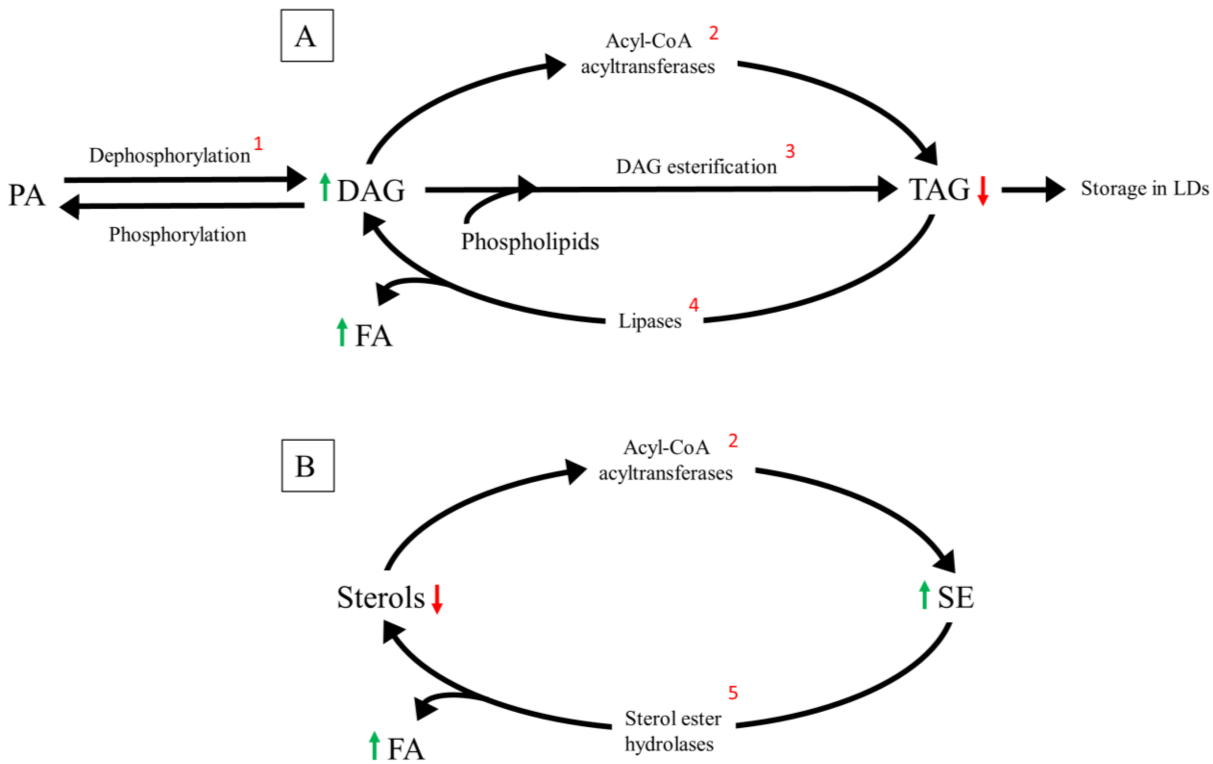

Figure 88. Major (A) DAG/TAG and (B) Ergo/SE cycling pathways in yeast (299, 306–308) with observed changes noted. Enzymes involved are: 1) Pah1p, Dpp1p, Lpp1p, 2) Are1p, Are2p, Dga1p (A only), 3) Lro1p, 4) Tgl3p, Tgl4p, Tgl5p, 5) Yeh1p, Tgl1p, Yeh2p (299, 307). This figure is adapted from Wagner and Daum (2005). (307)

As the changes in polar lipids were apparently minor, it seems more likely that Co^{2+} and Ni^{2+} affect DAG/TAG pathways at points 2 or 4 rather than involving phospholipids. Thus, this suggests that Co^{2+} and Ni^{2+} may lead to enhanced breakdown of TAG and/or inhibit formation of TAG. As the metals were added to the cells in late log-phase, it would be expected that the TAG content was increasing at the time of addition (309–311). Thus, a possible pathway to explain the increase of DAG/FA would be enhanced activation of lipases (Figure 88A). The lipases in *S. cerevisiae* require Mg^{2+} for function (312, 313), thus it is theoretically possible that Co^{2+} and

Ni^{2+} could substitute for Mg^{2+} (127, 314, 315) and may enhance their function. Another mechanism for lipase activation may be due to Co^{2+} and Ni^{2+} binding and recruiting lipases to a membrane surface, where they become activated (316). A specific lipase which may be affected is Tgl4p, which is a homologue to adipose triglyceride lipase in mammals that hydrolyzes TAG into 1,3-DAG specifically (301, 317).

Alternatively, Co^{2+} and Ni^{2+} may also block the conversion of DAG back to TAG by inhibiting DAG acyltransferase activity, as these enzymes also require Mg^{2+} (305, 311). Again, in terms of physiological consequences, DAG is a non-bilayer forming lipid, promoting the conversion to hexagonal phase (304), and thus destabilizing membranes (233) (Figure 87). Additionally, accumulation of FA may be toxic to cells and especially mitochondria, as they stimulate ROS production and lysosomal permeabilization (318–320). Thus, accumulation of DAG and FA in the cell may lead to membrane destabilization and various downstream toxic effects.

Similar enzyme inhibiting/ activating interactions may occur in the Co^{2+}-stimulated decrease in sterols (Figure 84B), but it is also possible that steps in the Ergo synthesis pathway itself are affected (321). A previous study with *S. cerevisiae* similarly reported that Co^{2+} treatment resulted in sterol depletion as seen here (146). Interestingly, by monitoring levels of sterol intermediates in the synthesis pathway of Ergo from squalene, they noted a correlation with inhibition of diiron enzymes (146). They also found that Co^{2+} caused an increase in saturated fatty acids and specifically targeted mitochondrial Fe-S enzymes (146). A previous study has found that *S. cerevisiae* accumulates TAG upon Cd^{2+} exposure, a process which appears to be due to disruption of Zn^{2+} and Ca^{2+} homeostasis (287, 322). Thus, substitution of

Co^{2+} and Ni^{2+} for other essential metals such as Fe^{2+} and Mg^{2+} may represent a feasible mechanism for changes in neutral lipid metabolism *in vivo*.

5.5.3 Live-cell imaging with C1-GFP to detect DAG localization

As DAG was found to be increased in metal-treated lipid extracts, it was of interest to determine if Co^{2+} and Ni^{2+} treatment also affected where DAG was localized in the cell. To do this, microscopy with a GFP reporter for DAG was used, graciously provided by the Zaremberg lab. The transformation of BY4741 with a plasmid encoding C1-GFP was performed by Suriakarthiga Ganesan, and transformed cells were selected by growth in SD-ura media (Table 6). The C1 domain contains a Zn^{2+}-dependent DAG binding motif, and has been previously used to visualize DAG pools in live yeast cells (183). In healthy cells, DAG is mainly localized in the vacuolar membrane, and polarized in the plasma membrane (PM) near the budding point (183). After 4 hrs treatment with metals in SD-ura media, the DAG pools were visualized by fluorescence microscopy, using the same timeline as in Section 5.3 (Figure 76) aside from the 20 min dye incubation period.

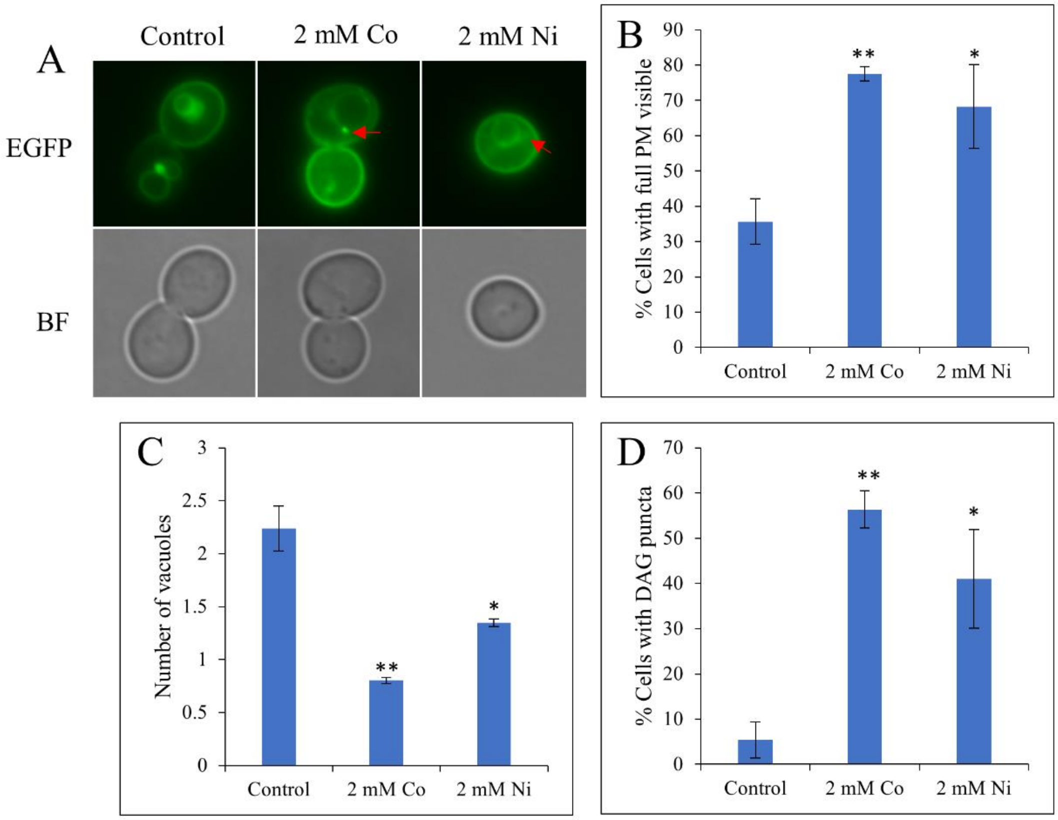

Figure 89. (A) Representative cell images of C1-GFP (Ex 488 nm, Em 509 nm) transformed into BY4741 after treatment for 4 hrs in SD-ura, with corresponding brightfield images. (B) Percentage of total cells with full plasma membrane visible by C1-GFP. (C) Average number of vacuoles visible per cell. (D) Percentage of cells showing irregular punctuated C1-GFP intensity.

It may have been expected that the relative intensity of C1-GFP would be vastly higher in the metal-treated cells, but this was not obviously apparent. This may support the finding of an increase in the 1,3-DAG isomer (Figure 86), which does not bind the C1 domain (303), and would thus not show a C1-GFP signal. Therefore, the changes observed in the C1-GFP patterns are due to 1,2-DAG, of which the localization appeared to be greatly-affected. The control cells showed the expected pattern in C1-GFP fluorescence, in that intensity was localized in vacuoles and usually polarized in the PM (183). However, the patterns were noticeably different upon treatment with Co^{2+} and Ni^{2+} in that both metals caused significant increases in the fraction of cells with total PM visible (Figure 89B), and the fraction of cells showing irregular speckled intensity (Figure 89D). DAG puncta refer to bright spots aside from the membranes, with examples indicated by arrows (Figure 89A). Additionally, both Co^{2+} and Ni^{2+} appeared to affect the vacuolar morphology, as fewer vacuoles were detected on average (Figure 89C). Co^{2+} treatment almost exclusively resulted in one large vacuole or none to be visible, and never more than two. Ni^{2+} generally caused this effect as well, but also caused some cells to show many (4–6) small vacuoles. So, the findings suggest that Co^{2+} and Ni^{2+} treatment induces localization of DAG to the PM over the vacuole. The reason for the preferential localization of DAG in the PM is not yet clear, but it suggests that the cells may be trapped in a “daughter-like” state. In normal cells, the budding daughter cell usually contains DAG in the full PM (observation) (183), distributed within the cell at about <4% of total lipids (96). This may suggest that once new cells are formed under Co^{2+} and Ni^{2+} stress, the DAG is not redistributed from the PM.

The speckled intensity pattern is also very interesting, as this was rarely observed in the controls (5%), but the majority of Co^{2+}-treated cells (56%), and many Ni^{2+}-treated cells (41%) showed this pattern of DAG localization. This suggests that a portion of DAG is not in the PM or vacuole, but rather highly-localized in small, dispersed structures. Although uncharacteristic for DAG localization, a potential structure are lipid droplets (LDs) which are primarily composed of TAG and SE (311). However, a recent study has shown that DAG is important in LD formation as it accumulates at the budding sites of LDs from the ER membrane (323). Subsequent depletion of DAG and replacement with lyso-lipids is then required for release of LDs from the surface of the ER due to alteration of membrane curvature (323). Another recent study has reported that LD-derived DAG may accumulate in the cell if endosomal/vacuolar sorting is non-functional (324). This provides an interesting possible explanation for the effects of Co^{2+} and Ni^{2+} on neutral lipid pathways. The observed increase in 1,3-DAG (Section 5.4.3) and localization of 1,2-DAG in punctuated points (Figure 89) may be due to Co^{2+} and Ni^{2+} keeping DAG associated with LDs at the ER, and/or accumulating DAG in LDs by some mechanism.

It is not yet clear if or how the metal-induced changes in neutral lipids may be associated with respiratory deficiency, yet a possible explanation may be that lipid distribution across organelles is disrupted, with mitochondria suffering as a result. A previous study has demonstrated that mutation in a vacuolar sorting protein resulted in mitochondrial defects due to problems with membrane contact sites (325). It is possible that metal interference at vesicle sorting and organelle communication sites affects a variety of pathways (326, 327). In both mammals and *S. cerevisiae,* mitochondrial-ER membrane contact sites are enriched in PS lipids (328), which have been identified as a relatively strong binding target of Co^{2+} and Ni^{2+}, and other toxic metals (83, 91). While this hypothesis requires much further study, it is possible that some of the *in vivo* effects observed come down to metal-lipid interactions in key sites.

Overall, this *in vivo* investigation has demonstrated that Co^{2+} and Ni^{2+} have significant effects on respiration and lipid regulation in *S. cerevisiae*. Thus, lipid membrane disruption appears to be a potential avenue for metal toxicity which may involve direct and indirect lipid-metal interactions.

Chapter Six: Summary, Conclusions, and Future Directions

6.1 Summary of Results

Lipid membranes were considered in this thesis as a potential point of interaction of Co^{2+} and Ni^{2+} which may be implicated in toxicity, as disruption to membrane properties and lipid dynamics may affect cell integrity and many cellular processes. The *in vitro* and *in vivo* studies have suggested significant interactions with, and effects of Co^{2+} and Ni^{2+} on biologically-relevant membranes.

Membrane rigidification as a result of direct lipid-metal interactions was observed in systems of purely negatively-charged lipids: PA, CL, PG, PS, and PI, while zwitterionic/ neutral lipids experienced negligible direct interaction (187). This can be attributed to the speciation of Co^{2+} and Ni^{2+} into divalent species under the experimental conditions (32). The simple systems showed that Co^{2+} nearly always caused stronger membrane-rigidifying effects than Ni^{2+}, except for POPS. PS was identified as a strong binding target for Co^{2+} and Ni^{2+}, likely a result of the highly-accessible negative charge at the carboxyl group and the potential for intra-lipid complexation. It is not yet known whether this interaction has physiological consequences, though externalization of PS is an important marker of apoptotic cells (206, 207). With PS and PG, both metals showed a stronger preference for the fully-saturated DM forms of the lipids, suggesting that tighter packing allows for greater metal complexation. This effect was not clearly observed with CL (for Co^{2+}) or PA. Dynamic light scattering also indicated the ability of Co^{2+} and Ni^{2+} to induce swelling and aggregation/fusion in pure PA and PS liposomes, but not for PG and CL.

The rigidifying effects observed in pure lipid systems were also present, but lesser, in complex multi-lipid and lipid-protein membranes. Some of the membranes studied included commercial Polar lipid extracts (Avanti Polar Lipids, Alabaster, AL), lung surfactant models, BLES (BLES Biochemicals Inc., London, ON), and RBCs. In general, the strength of effects on these membranes were dictated by the presence of higher-affinity targets, PS and PI lipids. The identity of the negatively-charged lipid content was found to be more important than the amount, as the *E. coli* extract was only weakly-affected though it contained the most negatively-charged lipid. In a lipid peroxidation assay with Heart polar extract, Co^{2+} was able to oxidize lipids similarly to Fe^{2+}, while Ni^{2+} stimulated the Fe^{2+}-catalyzed peroxidation and inhibited that of Co^{2+}, potentially due to binding certain lipid classes. Swelling and aggregation was not detected in complex membranes, suggesting that Co^{2+} and Ni^{2+} may not have a biologically-relevant ability to fuse membranes. However, Co^{2+} and Ni^{2+} were both able to affect the shape of RBCs and cause minor release of intracellular components, suggesting that they do disrupt erythrocyte membranes. In simplified RBC model systems, Co^{2+} was able to cause significant leakage in 15% PS-containing membranes, but the presence of Chol exerted a substantial protective effect.

In the experiments with *S. cerevisiae*, mitochondria were confirmed as a likely target for Co^{2+} and Ni^{2+} toxicity, as metal-treated cells incurred a reduced ability to grow with a non-fermentable carbon source, as well as greater loss in viability. This respiratory deficiency appeared to be associated with mitochondrial fragmentation and oxidative stress. Co^{2+} especially caused strong rigidifying effects on membranes of isolated mitochondria, suggesting that the lipid membranes themselves may constitute a binding target even in the presence of many complex proteins. Ni^{2+} did not cause very strong effects, suggesting the metals may have different pathways to generate the respiratory-deficient phenotype. While neutral lipids were unaffected in direct interactions, the lipid extractions showed that this was a major area of Co^{2+} and Ni^{2+} effects in live cells, causing accumulation of DAG in an uncharacteristic pattern. The consequences of this for membrane stability may be severe, as DAG is a non-bilayer forming lipid (304). Co^{2+} and Ni^{2+} may thus modulate neutral lipid synthesis, conversion, and transport pathways, having many potential consequences, which may or may not be linked to respiratory deficiency.

6.2 Future Directions

One future direction of interest is to further investigate the nature of the metal-lipid interactions. Many of the systems tested were rigidified as Co^{2+} and Ni^{2+} were increased past the 1:1 metal/lipid ratio, and the reasoning for this was not clear. It was thought that some of the rigidifying effects observed may be due to displacement of water at the membrane surface, thus leading to a response of the Laurdan probe as the surface environment changes (150). By complementing the experiments with an acyl chain-localized probe such as diphenylhexatriene (DPH), the effects of Co^{2+} and Ni^{2+} on lipid dynamics deeper in the membrane can be investigated (329). This may help to better understand if the effects of the metal interactions are surficial or extend into the bilayer. As well, the interactions of Fe^{2+}/Fe^{3+} with lipid membranes would also be of interest to study, as one of the ways in which Co^{2+} and Ni^{2+} may exert a toxic effect is by release of Fe^{2+}/Fe^{3+} from proteins (4, 23, 146, 330, 331).

It would also be of interest to improve the binding assay, as the MLV assay used in this thesis had many flaws which did not allow for accurate measurement of binding or determination of K_d. Ideally, it would be preferable to use LUVs to be able to better estimate the amount of accessible lipid. An obvious way to solve the problems in this assay would be ultracentrifugation, which will pellet LUVs (332), but this is a fairly impractical solution for a large amount of small-volume samples. Another possible solution is using a synthetic structure called ‘Lipobeads’, which consist of a polymeric hydrogel core with acyl chains attached for the self-assembly of a lipid coating (333, 334). This would solve the problems of size control and incomplete pelleting, as the Lipobeads can be synthesized as large particles up to 100 µm (333). The assay could then be performed much in the same way, without the problems of size changes, pelleting differences, and estimation of available lipid. An entirely different assay is also a possibility, as quenching of a Texas Red-DHPE (di-hexadecanoyl PE) fluorophore has previously been used to estimate binding of Cu^{2+} to PS liposomes (91). The authors have indicated that Ni^{2+} and Co^{2+} are both able to quench Texas Red as well, thus the method could be extended here (91). ITC is also a possible technique, though it has been previously found to be challenging to measure electrostatic metal-lipid interactions, or only show signals at very high metal concentrations (190, 335).

The lipid peroxidation assay could also be extended in many ways such as altering the chelator present, which may allow Ni^{2+} to catalyze the Fenton reaction (246). The composition of the lipid suspension could also be varied to determine if certain lipid classes truly are specifically-targeted for peroxidation by the metals. This could be done by making models with mixtures of head groups, with all lipids having identical acyl chains (18:2 preferably), such that there is no inherent preference based on susceptibility to peroxidation. The assay could then be performed in the same way to monitor lipid class depletion by TLC.

It would also be of interest to further investigate the membrane-permeating ability of Co^{2+} with more complex RBC models/extracts and compare this to other metals. It may be possible that the interaction observed here is specific, as the effect was not observed with Ni^{2+}. This may provide an explanation for the previously-reported unique interaction of Co^{2+} with RBCs, which rigidified the membrane without ionophore addition, in contrast to other metals

(112). Additionally, mitochondrial membrane mimics could be tested for permeating effects, as this may represent a mechanism of damage toward mitochondria.

The effects of Co^{2+} and Ni^{2+} on BLES and LS models suggested that the presence of surfactant proteins (SPs) may affect the interactions. It would thus be of interest to study the potential binding interactions of Co^{2+} and Ni^{2+} with SPs. Additionally, the effects of Co^{2+} and Ni^{2+} on monolayer models of LS would be an ideal experimental set-up, as this mimics the natural LS environment better than a liposome (63). This could be done using a Langmuir trough in which surface pressure can be monitored (336) in addition to using Brewster Angle microscopy for imaging of lateral domain organization (337). Another set of experiments which would be highly-relevant to Co^{2+} and Ni^{2+} toxicity would be to investigate the interactions of metal nanoparticles with LS. Co^{2+} and Ni^{2+} have both been found to be toxic to the lungs upon inhalation, and metal particulates in industry represent a potential source of exposure (1, 2, 4, 104, 338). Then, the strength of effects of solubilized Co^{2+} and Ni^{2+} versus particulate forms could be compared.

Lastly, the *in vivo* studies with *S. cerevisiae* leave many unanswered questions which are potentially meaningful. One of the major questions is to confirm the findings with the isolated mitochondria and to then understand the extent to which the membrane-rigidifying interactions observed in the pure mitochondrial fraction compare with that of other organellar fractions. This could be done by subcellular fractionation to separate various components of interest such as the vacuole, nucleus, ER, PM, and lipid droplets. Laurdan could then theoretically be incorporated as shown for mitochondria. As well, various fractions could be incubated with metal, pelleted, and the supernatant assayed for fraction of free metal. This could thus provide insight into preferable association with different fractions, as well as the effects on the membranes of each fraction. At present, it is not entirely clear if mitochondrial membranes themselves are truly a preferential target in whole cells, though the viability and microscopy experiments support this idea.

In terms of indirect effects on the membrane, another finding that opens many possible investigations is in the neutral lipid extracts, as the reasoning behind the increase in 1,3-DAG and the localization of DAG is not understood. It would be interesting to determine if the accumulation persists over time as the cells grow, or if it is just a temporary response. One of the possible pathways may be through activation of a specific lipase, potentially Tgl4p, which is a homologue to adipose triglyceride lipase in mammals which specifically produces 1,3-DAG (301, 313, 317). Thus, the direct interactions of Co^{2+} and Ni^{2+} with this enzyme may be a relevant consideration.

As well, the potential consequences of DAG and FA accumulation on membrane properties and toxicity is also a finding which warrants further study. If possible, it would be ideal to treat cells with Co^{2+} and Ni^{2+}, fractionate different components, then extract lipids from each fraction to confirm where the changes in neutral lipids are occurring. It would be very interesting to investigate if respiratory deficiency correlates with an alteration of neutral lipids in the mitochondria. This would be quite a bit of work, and it is not known whether the subcellular fractionation would occur correctly after metal treatment. It has been previously shown that substitution of Mg^{2+} for EDTA in the sucrose gradient leads to a completely different fractionation profile (339). Thus, if possible at all, much optimization may be needed to collect metal-treated fractions.

A potential way to firstly screen for metal localization may be to use fluorescence microscopy with a dye for Co^{2+} and Ni^{2+} detection. One such possible dye is a variant of Calcein used in this thesis called Calcein-AM (Molecular Probes, Eugene, OR), which is membranepermeable. The metal uptake and distribution could then be theoretically followed by Calcein quenching. Another possibility which has been previously used in plant cells for the detection of Ni^{2+} is Newport Green DCF, which can also detect Co^{2+} (340). This could provide an initial understanding of where the metals are localized in the whole cell.

Of course, it would then be meaningful to compare organellar localization, membrane effects, and lipid composition changes induced by Co^{2+} and Ni^{2+} to that of other toxic and essential metals, as effects of Co^{2+} and Ni^{2+} may or may not be specific. Then, a clearer picture of metal toxicity may emerge in terms of specificity for different organelles and the effects on membranes, both direct and indirect. This thesis has demonstrated that Co^{2+} and Ni^{2+} have significant effects on lipids and membranes *in vitro* and *in vivo*. The effects on lipids and membranes and their consequences as an avenue of metal toxicity in general is thus of interest for future study.

References

1. Barceloux, D. G. (1999) Cobalt. *J. Toxicol. Clin. Toxicol.* **37**, 201–216

2. Barceloux, D. G. (1999) Nickel. *J. Toxicol. Clin. Toxicol.* **37**, 239–258

3. Kobayashi, M., and Shimizu, S. (1999) Cobalt proteins. *Eur. J. Biochem.* **261**, 1–9

4. Denkhaus, E., and Salnikow, K. (2002) Nickel essentiality, toxicity, and carcinogenicity. *Crit. Rev. Oncol. Hematol.* **42**, 35–56

5. Czarnek, K., Terpilowska, S., and Siwicki, A. K. (2015) Selected aspects of the action of cobalt ions in the human body. *Cent. Eur. J. Immunol.* **40**, 236–242

6. Kräutler, B. (2005) Vitamin B12: chemistry and biochemistry. *Biochem. Soc. Trans.* **33**, 806–810

7. Ragsdale, S. W. (2009) Nickel-based enzyme systems. *J. Biol. Chem.* **284**, 18571–18575

8. Paustenbach, D. J., Galbraith, D. A., and Finley, B. L. (2014) Interpreting cobalt blood concentrations in hip implant patients. *Clin. Toxicol.* **52**, 98–112

9. Reynolds, E. (2006) Vitamin B12, folic acid, and the nervous system. *Lancet Neurol.* **5**, 949–960

10. Lexa, D., and Saveant, J. M. (1983) The Electrochemistry of Vitamin B12. *Acc. Chem. Res.* **16**, 235–243

11. Martens, J. H., Barg, H., Warren, M., and Jahn, D. (2002) Microbial production of vitamin B12. *Appl. Microbiol. Biotechnol.* **58**, 275–285

12. Stabler, S. P. (2013) Vitamin B_{12} Deficiency. *N. Engl. J. Med.* **368**, 149–160

13. Das, K. K., Das, S. N., and Dhundasi, S. A. (2008) Nickel, its adverse health effects & oxidative stress. *Indian J. Med. Res.* **128**, 412–425

14. Dabeka, R., and McKenzie, A. (1995) Survey of lead, cadmium, fluoride, nickel, and cobalt in food composites and estimation of dietary intakes of these elements by Canadians in 1986-1988. *J. AOAC Int.* **78**, 897–909

15. Berg, T., Petersen, A., Pedersen, G. A., Petersen, J., and Madsen, C. (2000) The release of nickel and other trace elements from electric kettles and coffee machines. *Food Addit. Contam.* **17**, 189–196

16. Gunshin, H., Mackenzie, B., Berger, U. V., Gunshin, Y., Romero, M. F., Boron, W. F., Nussberger, S., Gollan, J. L., and Hediger, M. A. (1997) Cloning and characterization of a mammalian proton-coupled metal-ion transporter. *Nature*. **388**, 482–488

17. Agency for Toxic Substances and Disease Registry (2017) *Substance Priority List*, [online] https://www.atsdr.cdc.gov/spl/index.html (Accessed January 2, 2018)

18. Catalani, S., Rizzetti, M., Padovani, A., and Apostoli, P. (2012) Neurotoxicity of cobalt. *Hum. Exp. Toxicol.* **31**, 421–437

19. Roth, J. A., and Salvi, R. (2016) Ototoxicity of Divalent Metals. *Neurotox. Res.* **30**, 268–282

20. Xu, S. C., He, M. Di, Zhong, M., Zhang, Y. W., Wang, Y., Yang, L., Yang, J., Yu, Z. P., and Zhou, Z. (2010) Melatonin protects against Nickel-induced neurotoxicity in vitro by reducing oxidative stress and maintaining mitochondrial function. *J. Pineal Res.* **49**, 86–94

21. Nemery, B., and Abraham, J. L. (2007) Hard metal lung disease: Still hard to understand. *Am. J. Respir. Crit. Care Med.* **176**, 2–3

22. Thyssen, J. P. (2011) Nickel and cobalt allergy before and after nickel regulation--evaluation of a public health intervention. *Contact Dermatitis*. **65**, 1–68

23. Simonsen, L. O., Harbak, H., and Bennekou, P. (2012) Cobalt metabolism and toxicology-A brief update. *Sci. Total Environ.* **432**, 210–215

24. Li, P., Ding, D., Salvi, R., and Roth, J. A. (2015) Cobalt-induced ototoxicity in rat postnatal cochlear organotypic cultures. *Neurotox. Res.* **28**, 209–221

25. Schaffer, A. W., Schaffer, A., Pilger, A., Engelhardt, C., Zweymueller, K., and Ruediger, H. W. (1999) Increased Blood Cobalt and Chromium After Total Hip Replacement. *J. Toxicol. Clin. Toxicol.* **37**, 839–844

26. Bishara, S. E., Barrett, R. D., and Selim, M. I. (1993) Biodegradation of orthodontic appliances. Part II. Changes in the blood level of nickel. *Am. J. Orthod. Dentofacial Orthop.* **103**, 115–9

27. Sunderman, F. W., Dingle, B., Hopfer, S. M., and Swift, T. (1988) Acute nickel toxicity in electroplating workers who accidently ingested a solution of nickel sulfate and nickel chloride. *Am. J. Ind. Med.* **14**, 257–266

28. Dahlstrand, H., Stark, A., Anissian, L., and Hailer, N. P. (2009) Elevated serum concentrations of cobalt, chromium, nickel, and manganese after metal-on-metal alloarthroplasty of the hip: A prospective randomized study. *J. Arthroplasty*. **24**, 837–845

29. Pelclova, D., Sklensky, M., Janicek, P., and Lach, K. (2012) Severe cobalt intoxication following hip

replacement revision: Clinical features and outcome. *Clin. Toxicol.* **50**, 262–265

30. Sunderman, F. W. (1981) Chelation therapy in nickel poisoning. *Ann. Clin. Lab. Sci.* **11**, 1–8

31. Flora, S. J. S., and Pachauri, V. (2010) Chelation in metal intoxication. *Int. J. Environ. Res. Public Health*. **7**, 2745–2788

32. Gustafsson, J. P. (2011) Visual MINTEQ 3.1

33. Singh, B. K., Sharma, R. K., and Garg, B. S. (2006) Cobalt(II) complexes of biologically active glutathione: Spectroscopic and molecular modeling studies. *Spectrochim. Acta - Part A Mol. Biomol. Spectrosc.* **63**, 96–102

34. Singh, B. K., Mishra, P., and Garg, B. S. (2007) Nickel(II) complexes of biologically active glutathione: Spectroscopic, kinetics of thermal decomposition and XRPD studies. *Spectrochim. Acta - Part A Mol. Biomol. Spectrosc.* **67**, 719–729

35. Sokołowska, M., Wszelaka-Rylik, M., Poznański, J., and Bal, W. (2009) Spectroscopic and thermodynamic determination of three distinct binding sites for Co(II) ions in human serum albumin. *J. Inorg. Biochem.* **103**, 1005–1013

36. Simonsen, L. O., Brown, A. M., Harbak, H., Kristensen, B. I., and Bennekou, P. (2011) Cobalt uptake and binding in human red blood cells. *Blood Cells, Mol. Dis.* **46**, 266–276

37. Levine, J., Weickert, M., Pagratis, M., Etter, J., Mathews, A., Fattor, T., Lippincott, J., and Apostol, I. (1998) Identification of a nickel(II) binding site on hemoglobin which confers susceptibility to oxidative deamination and intramolecular cross-linking. *J. Biol. Chem.* **273**, 13037–13046

38. Barszcz, B. (2005) Coordination properties of didentate N,O heterocyclic alcohols and aldehydes towards Cu(II), Co(II), Zn(II) and Cd(II) ions in the solid and aqueous state. *Coord. Chem. Rev.* **249**, 2259–2276

39. Coogan, T. P., Latta, D. M., Snow, E. T., and Costa, M. (1989) Toxicity and carcinogenicity of nickel compounds. *Crit. Rev. Toxicol.* **19**, 341–84

40. Taylor, M. K., Reglinski, J., and Wallace, D. (2004) Coordination geometry of tetradentate Schiff's base nickel complexes: The effects of donors, backbone length and hydrogenation. *Polyhedron*. **23**, 3201–3209

41. Rulíšek, L., and Vondrášek, J. (1998) Coordination geometries of selected transition metal ions (Co2+, Ni2+, Cu2+, Zn2+, Cd2+, and Hg2+) in metalloproteins. *J. Inorg. Biochem.* **71**, 115–127

42. Nightingale, E. R. (1959) Phenomenological theory of ion solvation. Effective radii of hydrated ions. *J. Phys. Chem.* **63**, 1381–1387

43. Allred, A. L. (1961) Electronegativity values from thermochemical data. *J. Inorg. Nucl. Chem.* **17**, 215–221

44. Valko, M., Rhodes, C. J., Moncol, J., Izakovic, M., and Mazur, M. (2006) Free radicals, metals and antioxidants in oxidative stress-induced cancer. *Chem. Biol. Interact.* **160**, 1–40

45. Stohs, S. J., and Bagchi, D. (1995) Oxidative mechanisms in the toxicity of metal ions. *Free Radic. Biol. Med.* **18**, 321–336

46. Kubrak, O. I., Husak, V. V., Rovenko, B. M., Storey, J. M., Storey, K. B., and Lushchak, V. I. (2011) Cobalt-induced oxidative stress in brain, liver and kidney of goldfish Carassius auratus. *Chemosphere*. **85**, 983–989

47. Nackerdien, Z., Kasprzak, K. S., Rao, G., Halliwell, B., and Dizdaroglu, M. (1991) Nickel (II)- and Cobalt (II)-dependent damage by hydrogen peroxide to the DNA bases in isolated human chromatin. *Cancer Res.* **51**, 5837–5842

48. Hasan, M., and Fatehyab Ali, S. (1981) Effects of thallium, nickel, and cobalt administration on the lipid peroxidation in different regions of the rat brain. *Toxicol. Appl. Pharmacol.* **57**, 8–13

49. Babu, K. R., Rajmohan, H. R. R., Rajan, B. K. M., and Kumar, M. K. (2006) Plasma lipid peroxidation and erythrocyte antioxidant enzymes status in workers exposed to cadmium. *Toxicol. Ind. Health*. **22**, 329–335

50. Halliwell, B., and Chirico, S. (1993) Lipid peroxidation : its mehcanism, measurement, and significance. *Am. J. Clin. Nutr.* **57**, 715S–725S

51. Salnikow, K., Donald, S. P., Bruick, R. K., Zhitkovich, A., Phang, J. M., and Kasprzak, K. S. (2004) Depletion of intracellular ascorbate by the carcinogenic metals nickel and cobalt results in the induction of hypoxic stress. *J. Biol. Chem.* **279**, 40337–40344

52. Triantafyllou, A., Liakos, P., Tsakalof, A., Georgatsou, E., Simos, G., and Bonanou, S. (2006) Cobalt induces hypoxia-inducible factor-1α (HIF-1α) in HeLa cells by an iron-independent, but ROS-, PI-3K- and MAPK-dependent mechanism. *Free Radic. Res.* **40**, 847–856

53. Robison, S. H., Cantoni, O., and Costa, M. (1982) Strand breakage and decreased molecular weight of DNA induced by specific metal compounds. *Carcinogenesis*. **3**, 657–662

54. Yamamoto, K., Inoue, S., Yamazaki, a, Yoshinaga, T., and Kawanishi, S. (1989) Site-specific DNA damage induced by cobalt(II) ion and hydrogen peroxide: role of singlet oxygen. *Chem. Res. Toxicol.* **2**, 234–9

55. Hartwig, A. (1998) Carcinogenicity of metal compounds: possible role of DNA repair inhibition. *Toxicol. Lett.* **102**–**103**, 235–9

56. Lynn, S., Yew, F. H., Chen, K. S., and Jan, K. Y. (1997) Reactive oxygen species are involved in nickel inhibition of DNA repair. *Environ. Mol. Mutagen.* **29**, 208–216

57. Lee, Y. W., Broday, L., and Costa, M. (1998) Effects of nickel on DNA methyltransferase activity and genomic DNA methylation levels. *Mutat. Res. - Genet. Toxicol. Environ. Mutagen*. **415**, 213–218

58. Green, S. E., Luczak, M. W., Morse, J. L., DeLoughery, Z., and Zhitkovich, A. (2013) Uptake, p53 pathway activation, and cytotoxic responses for Co(II) and Ni(II) in human lung cells: Implications for carcinogenicity. *Toxicol. Sci.* **136**, 467–477

59. Virtanen, J. A., Cheng, K. H., and Somerharju, P. (1998) Phospholipid composition of the mammalian red cell membrane can be rationalized by a superlattice model. *Proc. Natl. Acad. Sci. U. S. A.* **95**, 4964–4969

60. Ray, T. K., Skipiski, V. P., Barclay, M., Essner, E., and Archibald, F. M. (1969) Lipid Composition of Rat Liver Plasma Membranes. *J. Biol. Chem.* **244**, 5528–5536

61. O'Brien, J. S., and Sampson, L. E. (1965) Lipid composition of the normal human brain: gray matter, white matter, and myelin. *J. Lipid Res.* **6**, 537–544

62. Comte, J., Gautheron, D., Peypoux, F., and Michel, G. (1971) Lipid composition and endogenous respiration of pig heart mitochondria. *Lipids*. **6**, 882–888

63. Hamm, H., Fabel, H., and Bartsch, W. (1992) The surfactant system of the adult lung: physiology and clinical perspectives. *Clin. Investig.* **70**, 637–657

64. Balla, T. (2006) Phosphoinositide-derived messengers in endocrine signaling. *J. Endocrinol.* **188**, 135–153

65. Wang, X., Devaiah, S. P., Zhang, W., and Welti, R. (2006) Signaling functions of phosphatidic acid. *Prog. Lipid Res.* **45**, 250–78

66. Schlame, M., Rua, D., and Greenberg, M. L. (2000) The biosynthesis and functional role of cardiolipin. *Prog. Lipid Res.* **39**, 257–288

67. Bhalla, U. S., and Iyengar, R. (1999) Emergent Properties of Networks of Biological Signalling Pathways. *Science (80-.).* **283**, 381–387

68. Abbott, S. K., Else, P. L., Atkins, T. A., and Hulbert, A. J. (2012) Fatty acid composition of membrane bilayers: Importance of diet polyunsaturated fat balance. *Biochim. Biophys. Acta - Biomembr.* **1818**, 1309–1317

69. Manno, S., Takakuwa, Y., and Mohandas, N. (2002) Identification of a functional role for lipid asymmetry in biological membranes: Phosphatidylserine-skeletal protein interactions modulate membrane stability. *Proc. Natl. Acad. Sci. U. S. A.* **99**, 1943–8

70. Fadeel, B., and Xue, D. (2009) The ins and outs of phospholipid asymmetry in the plasma membrane: roles in health and disease. *Crit Rev Biochem Mol Biol*. **44**, 264–277

71. van Meer, G., Voelker, D. R., and Feigenson, G. W. (2008) Membrane lipids: where are they and how they behave. *Nature*. **9**, 112–124

72. Yu, W., So, P. T. C., French, T., and Gratton, E. (1996) Fluorescence generalized polarization of cell membranes : A two-photon scanning microscopy approach. *Biophys. J.* **70**, 626–636

73. Rainier, S., Jain, M. K., Ramirez, F., Ioannou, P. V., Marecek, J. F., and Wagner, R. (1979) Phase transition characteristics of diphosphatidylglycerol (cardiolipin) and stereoisomeric phosphatidyldiacylglycerol bilayers. Mono- and divalent metal ion effects. *BBA - Biomembr.* **558**, 187–198

74. Ohba, S., Hiramatsu, M., Edamatsu, R., Mori, I., and Mori, A. (1994) Metal ions affect neuronal membrane fluidity of rat cerebral cortex. *Neurochem. Res.* **19**, 237–241

75. McLaughlin, A., Grathwohl, C., and McLaughlin, S. (1978) The adsorption of divalent cations to phosphatidylcholine bilayer membranes. *BBA - Biomembr.* **513**, 338–357

76. McLaughlin, S., Mulrine, N., Gresalfi, T., Vaio, G., and McLaughlin, A. (1981) Adsorption of divalent cations to bilayer membranes containing phosphatidylserine. *J. Gen. Physiol.* **77**, 445–73

77. Lau, A., McLaughlin, A., and McLaughlin, S. (1981) The adsorption of divalent cations to phosphatidylglycerol bilayer membranes. *Biochim. Biophys. Acta*. **645**, 279–292

78. Repetto, M. G., Ferrarotti, N. F., and Boveris, A. (2010) The involvement of transition metal ions on iron-dependent lipid peroxidation. *Arch. Toxicol.* **84**, 255–262

79. Kilinç, K., and Rouhani, R. (1992) Cobaltous ion inhibition of lipid peroxidation in biological membranes. *Biochim. Biophys. Acta (BBA)/Lipids Lipid Metab.* **1125**, 189–195

80. Verstraeten, S. V, Nogueira, L. V, Schreier, S., and Oteiza, P. I. (1997) Effect of trivalent metal ions on phase separation and membrane lipid packing: role in lipid peroxidation. *Arch. Biochem. Biophys.* **338**, 121–7

81. Valko, M., Jomova, K., Rhodes, C. J., Kuča, K., and Musílek, K. (2016) Redox- and non-redox-metal-induced formation of free radicals and their role in human disease. *Arch. Toxicol.* **90**, 1–37

82. Wills, E. (1965) Mechanisms of lipid peroxide formation in animal tissues. *Biochim. Biophys. Acta - Lipids Lipid Metab.* **98**, 238–251

83. Kerek, E. M., and Prenner, E. J. (2016) Inorganic cadmium affects the fluidity and size of phospholipid based liposomes. *BBA - Biomembr.* **1858**, 3169–3181

84. Suwalsky, M., Villena, F., Norris, B., Cuevas, F., and Sotomayor, C. P. (2004) Cadmium-induced changes in the membrane of human erythrocytes and molecular models. *J. Inorg. Biochem.* **98**, 1061–1066

85. Kerek, E., Hassanin, M., Zhang, W., and Prenner, E. J. (2017) Preferential binding of Inorganic Mercury to specific lipid classes and its competition with Cadmium. *BBA - Biomembr.* **1859**, 1211–1221

86. del Carmen Puga Molina, L., and Verstraeten, S. V. (2008) Thallium(III)-mediated changes in membrane physical properties and lipid oxidation affect cardiolipin-cytochrome c interactions. *BBA - Biomembr.* **1778**, 2157–2164

87. Graber, Z. T., Shi, Z., and Baumgart, T. (2017) Cations induce shape remodeling of negatively charged phospholipid membranes. *Phys. Chem. Chem. Phys.* **19**, 15285–15295

88. Koter, M., De Kruijff, B., and Van Deenen, L. L. M. (1978) Calcium-induced aggregation and fusion of mixed phosphatidylcholine-phosphatidic acid vesicles as studied by 31P NMR. *BBA - Biomembr.* **514**, 255–263

89. Suwalsky, M., Villena, F., Norris, B., Cuevas, Y. F., Sotomayor, C. P., and Zatta, P. (2003) Effects of lead on the human erythrocyte membrane and molecular models. *J. Inorg. Biochem.* **97**, 308–313

90. Mundle, R. L. (2018) *Lead Interactions Affect the Fluidity and Lateral Organization of Complex Lipid Membranes*. Ph.D. thesis, University of Calgary

91. Monson, C. F., Cong, X., Robison, A. D., Pace, H. P., Liu, C., Poyton, M. F., and Cremer, P. S. (2012) Phosphatidylserine reversibly binds Cu 2+ with extremely high affinity. *J. Am. Chem. Soc.* **134**, 7773–7779

92. Chan, R. B., Oliveira, T. G., Cortes, E. P., Honig, L. S., Duff, K. E., Small, S. A., Wenk, M. R., Shui, G., and Di Paolo, G. (2012) Comparative lipidomic analysis of mouse and human brain with Alzheimer disease. *J. Biol. Chem.* **287**, 2678–2688

93. Homan, R., and Anderson, M. K. (1998) Rapid separation and quantitation of combined neutral and polar lipid classes by high-performance liquid chromatography and evaporative light- scattering mass detection. *J. Chromatogr. B Biomed. Appl.* **708**, 21–26

94. Puri, P., Baillie, R. A., Wiest, M. M., Mirshahi, F., Choudhury, J., Cheung, O., Sargeant, C., Contos, M. J., and Sanyal, A. J. (2007) A lipidomic analysis of nonalcoholic fatty liver disease. *Hepatology*. **46**, 1081–1090

95. Casanovas, A., Sprenger, R. R., Tarasov, K., Ruckerbauer, D. E., Hannibal-Bach, H. K., Zanghellini, J., Jensen, O. N., and Ejsing, C. S. (2015) Quantitative analysis of proteome and lipidome dynamics reveals functional regulation of global lipid metabolism. *Chem. Biol.* **22**, 412–425

96. Ejsing, C. S., Sampaio, J. L., Surendranath, V., Duchoslav, E., Ekroos, K., Klemm, R. W., Simons, K., and Shevchenko, A. (2009) Global analysis of the yeast lipidome by quantitative shotgun mass spectrometry. *Proc. Natl. Acad. Sci.* **106**, 2136–2141

97. Wheeldon, L. W., Schumert, Z., and Turner, D. A. (1965) Lipid composition of heart muscle homogenate. *J. Lipid Res.* **6**, 481–489

98. Morein, S., Andersson, A.-S., Rilfors, L., and Lindblom, G. (1996) Wild-type Escherichia coli cells regulate the membrane lipid composition in a “window” between gel and non-lamellar structures. *J. Biol. Chem.* **271**, 6801–6809

99. Horvath, S. E., and Daum, G. (2013) Lipids of mitochondria. *Prog. Lipid Res.* **52**, 590–614

100. Wanders, R. J. A., Ruiter, J. P. N., IJlst, L., Waterham, H. R., and Houten, S. M. (2010) The enzymology of mitochondrial fatty acid beta-oxidation and its application to follow-up analysis of positive neonatal screening results. *J. Inherit. Metab. Dis.* **33**, 479–494

101. Postle, A. D., Heeley, E. L., and Wilton, D. C. (2001) A comparison of the molecular species compositions

of mammalian lung surfactant phospholipids. *Comp. Biochem. Physiol. - A Mol. Integr. Physiol.* **129**, 65–73

102. Possmayer, F., Hall, S. B., Haller, T., Petersen, N. O., Zuo, Y. Y., Bernardino de la Serna, J., Postle, A. D., Veldhuizen, R. A. W., and Orgeig, S. (2010) Recent advances in alveolar biology: Some new looks at the alveolar interface. *Respir. Physiol. Neurobiol.* **173**, S55–S64

103. Gunasekara, L., Schürch, S., Schoel, W. M., Nag, K., Leonenko, Z., Haufs, M., and Amrein, M. (2005) Pulmonary surfactant function is abolished by an elevated proportion of cholesterol. *Biochim. Biophys. Acta - Mol. Cell Biol. Lipids*. **1737**, 27–35

104. Nemery, B., Verbeken, E. K., and Demedts, M. (2001) Giant Cell Interstitial Pneumonia (Hard Metal Lung Disease, Cobalt Lung). *Semin. Respir. Crit. Care Med.* **22**, 435–448

105. Johansson, A., Curstedt, T., and Camner, P. (1991) Lung lesions after combined inhalation of cobalt and nickel. *Environ. Res.* **54**, 24–38

106. Casarett-Bruce, M., Camner, P., and Curstedts, T. (1981) Changes in pulmonary lipid composition of rabbits exposed to nickel dust. *Environ. Res.* **26**, 353–362

107. Bal, W., Sokołowska, M., Kurowska, E., and Faller, P. (2013) Binding of transition metal ions to albumin: Sites, affinities and rates. *Biochim. Biophys. Acta - Gen. Subj.* **1830**, 5444–5455

108. Phillips, G. B., and Dodge, J. T. (1967) Composition of phospholipids and of phospholipid fatty acids in human red cells. *J. Lipid Res.* **8**, 667–675

109. Chabanel, A., Flamm, M., Sung, K. L., Lee, M. M., Schachter, D., and Chien, S. (1983) Influence of cholesterol content on red cell membrane viscoelasticity and fluidity. *Biophys. J.* **44**, 171–176

110. De Oliveira, S., and Saldanha, C. (2010) An overview about erythrocyte membrane. *Clin. Hemorheol. Microcirc.* **44**, 63–74

111. Zachowski, A. (1993) Phospholipids in animal eukaryotic membranes: transverse asymmetry and movement. *Biochem. J.* **294**, 1–14

112. Vest, R. S., Gonzales, L. J., Permann, S. A., Spencer, E., Hansen, L. D., Judd, A. M., and Bell, J. D. (2004) Divalent cations increase lipid order in erythrocytes and susceptibility to secretory phospholipase A2. *Biophys. J.* **86**, 2251–60

113. De Luca, G., Gugliotta, T., Parisi, G., Romano, P., Geraci, A., Romano, O., Scuteri, A., and Romano, L.

(2007) Effects of nickel on human and fish red blood cells. *Biosci. Rep.* **27**, 265–273

114. Nelson, G. J. (1967) Lipid composition of erythrocytes in various mammalian species. *Biochim. Biophys. Acta (BBA)/Lipids Lipid Metab.* **144**, 221–232

115. Schmitt, M., Gellert, G., Ludwig, J., and Lichtenberg-Fraté, H. (2004) Phenotypic yeast growth analysis for chronic toxicity testing. *Ecotoxicol. Environ. Saf.* **59**, 142–150

116. Pearce, D. A., and Sherman, F. (1999) Toxicity of copper, cobalt, and nickel salts is dependent on histidine metabolism in the yeast Saccharomyces cerevisiae. *J. Bacteriol.* **181**, 4774–4779

117. Yang, H.-C., and Pon, L. a (2003) Toxicity of metal ions used in dental alloys: a study in the yeast Saccharomyces cerevisiae. *Drug Chem. Toxicol.* **26**, 75–85

118. Lagunas, R., Investigaciones, I. De, Csic, B., Medicina, F. De, and Morcillo, A. (1986) Misconceptions About the Energy Metabolism of Saccharomyces cerevisiae. **2**, 221–228

119. Vasylkovska, R., Petriv, N., and Semchyshyn, H. (2015) Carbon sources for yeast growth as a precondition of hydrogen peroxide induced Hormetic phenotype. *Int. J. Microbiol.* **2015**, 1–8

120. Karathia, H., Vilaprinyo, E., Sorribas, A., and Alves, R. (2011) Saccharomyces cerevisiae as a model organism: A comparative study. *PLoS One*. **6**, 1–10

121. Bleackley, M. R., and MacGillivray, R. T. A. (2011) Transition metal homeostasis: From yeast to human disease. *BioMetals*. **24**, 785–809

122. Hosiner, D., Gerber, S., Lichtenberg-Fraté, H., Glaser, W., Schüller, C., and Klipp, E. (2014) Impact of acute metal stress in Saccharomyces cerevisiae. *PLoS One*. **9**, 1–14

123. Çakar, Z. P., Alkim, C., Turanli, B., Tokman, N., Akman, S., Sarikaya, M., Tamerler, C., Benbadis, L., and François, J. M. (2009) Isolation of cobalt hyper-resistant mutants of Saccharomyces cerevisiae by in vivo evolutionary engineering approach. *J. Biotechnol.* **143**, 130–138

124. Gharieb, M. M., and Gadd, G. M. (2004) Role of glutathione in detoxification of metal (loid) s by Saccharomyces cerevisiae. *Biometals*. **17**, 183–188

125. White, J., and Munns, D. J. (1951) Inhibitory effect of common elements towards yeast growth. *J. Inst. Brew.* **57**, 175–179

126. Ruotolo, R., Marchini, G., and Ottonello, S. (2008) Membrane transporters and protein traffic networks

differentially affecting metal tolerance: a genomic phenotyping study in yeast. *Genome Biol.* **9**, R67 1-19

127. Aoyama, I., Kudo, A., and Veliky, I. A. (1986) Effect of Cobalt-Magnesium Interaction on Growth of Saccharomyces Cereuisiae. *Toxic. Assess. An Int. Q. Vol.* **1**, 211–226

128. Schmidt, K., Wolfe, D. M., Stiller, B., and Pearce, D. A. (2009) Cd2+, Mn2+, Ni2+ and Se2+ toxicity to Saccharomyces cerevisiae lacking YPK9p the orthologue of human ATP13A2. *Biochem. Biophys. Res. Commun.* **383**, 198–202

129. Pimentel, C., Caetano, S. M., Menezes, R., Figueira, I., Santos, C. N., Ferreira, R. B., Santos, M. A. S., and Rodrigues-pousada, C. (2014) Yap1 mediates tolerance to cobalt toxicity in the yeast Saccharomyces cerevisiae. *BBA - Gen. Subj.* **1840**, 1977–1986

130. Broday, L., Cai, J., and Costa, M. (1999) Nickel enhances telomeric silencing in Saccharomyces cerevisiae. *Mutat. Res. - Genet. Toxicol. Environ. Mutagen.* **440**, 121–130

131. Conklin, D. S., Mcmaster, J. A., and Culbertson, M. R. (1992) COT1, a gene involved in cobalt accumulation in Saccharomyces cerevisiae. *Mol. Cell. Biol.* **12**, 3678–3688

132. M'Bemba-Meka, P., Lemieux, N., and Chakrabarti, S. K. (2005) Role of oxidative stress, mitochondrial membrane potential, and calcium homeostasis in nickel sulfate-induced human lymphocyte death in vitro. *Chem. Biol. Interact.* **156**, 69–80

133. Battaglia, V., Compagnone, A., Bandino, A., Bragadin, M., Rossi, C. A., Zanetti, F., Colombatto, S., Grillo, M. A., and Toninello, A. (2009) Cobalt induces oxidative stress in isolated liver mitochondria responsible for permeability transition and intrinsic apoptosis in hepatocyte primary cultures. *Int. J. Biochem. Cell Biol.* **41**, 586–594

134. Sousa, C. A., and Soares, E. V. (2014) Mitochondria are the main source and one of the targets of Pb (lead)-induced oxidative stress in the yeast Saccharomyces cerevisiae. *Appl. Microbiol. Biotechnol.* **98**, 5153–5160

135. Rama Rao, K. V., and Norenberg, M. D. (2004) Manganese induces the mitochondrial permeability transition in cultured astrocytes. *J. Biol. Chem.* **279**, 32333–32338

136. Ott, M., Gogvadze, V., Orrenius, S., and Zhivotovsky, B. (2007) Mitochondria, oxidative stress and cell death. *Apoptosis*. **12**, 913–922

137. Goldring, E. S., Grossman, L. I., Krupnick, D., Cryer, D. R., and Marmur, J. (1970) The petite mutation in

yeast. Loss of mitochondrial deoxyribonucleic acid during induction of petites with ethidium bromide. *J. Mol. Biol.* **52**, 323–335

138. Lindegren, C. C., Nagai, S., and Nagai, H. (1958) Induction of respiratory deficiency in yeast by manganese, copper, cobalt, and nickel. *Nature*. **182**, 446–448

139. Horn, P., and Wilkie, D. (1966) Selective advantage of the cytoplasmic respiratory mutant of Saccharomyces cerevisiæ in a cobalt medium. *Heredity (Edinb).* **21**, 625–635

140. Lindegren, C. C., and Miller, Paraskevi, M. B. (1969) Cobalt as a vital stain for yeast mitochondria in squash preparations. *Can. J. Genet. Cytol.* **11**, 987–992

141. Daum, G., Lees, N. D., Bard, M., and Dickson, R. (1998) Biochemistry, cell biology and molecular biology of lipids of Saccharomyces cerevisiae. *Yeast*. **14**, 1471–1510

142. Zinser, E., Sperka-Gottlieb, C. D. M., Fasch, E. V., Kohlwein, S. D., Paltauf, F., and Daum, G. (1991) Phospholipid synthesis and lipid composition of subcellular membranes in the unicellular eukaryote Saccharomyces cerevisiae. *J. Bacteriol.* **173**, 2026–2034

143. Chi, Z., and Arneborg, N. (1999) Relationship between lipid composition, frequency of ethanol-induced respiratory deficient mutants, and ethanol tolerance in Saccharomyces cerevisiae. *J. Appl. Microbiol.* **86**, 1047–1052

144. Rodriguez, R. J., Low, C., Bottema, C. D. K., and Parks, L. W. (1985) Multiple functions for sterols in Saccharomyces cerevisiae. *Biochim. Biophys. Acta (BBA)/Lipids Lipid Metab.* **837**, 336–343

145. Wilfling, F., Haas, J. T., Walther, T. C., and Jr, R. V. F. (2014) Lipid droplet biogenesis. *Curr. Opin. Cell Biol.* **29**, 39–45

146. Gleason, J. E., Corrigan, D. J., Cox, J. E., Reddi, A. R., McGinnis, L. A., and Culotta, V. C. (2011) Analysis of hypoxia and hypoxia-like states through metabolite profiling. *PLoS One*. 10.1371/journal.pone.0024741

147. Yang, J., and Black, J. (1994) Competitive binding of chromium, cobalt and nickel to serum proteins. *Biomaterials*. **15**, 262–268

148. Pande, A. H., Qin, S., and Tatulian, S. A. (2005) Membrane fluidity is a key modulator of membrane binding, insertion, and activity of 5-lipoxygenase. *Biophys. J.* **88**, 4084–94

149. Ames, B. N. (1966) Assay of inorganic phosphate, total phosphate and phosphatases. *Complex*

Carbohydrates. **8**, 115–118

150. Parasassi, T., Krasnowska, E. K., Bagatolli, L., and Gratton, E. (1998) Laurdan and prodan as polarity-sensitive fluorescent membrane probes. *J. Fluoresc.* **8**, 365–373

151. Origin Lab Corporation (2008) Origin Pro

152. Michel, N., Fabiano, A.-S., Polidori, A., Jack, R., and Pucci, B. (2006) Determination of phase transition temperatures of lipids by light scattering. *Chem. Phys. Lipids*. **139**, 11–19

153. Leroy, P., Tournassat, C., and Bizi, M. (2011) Influence of surface conductivity on the apparent zeta potential of TiO2 nanoparticles. *J. Colloid Interface Sci.* **356**, 442–453

154. Crommelin, D. J. A. (1984) Influence of lipid composition and ionic strength on the physical stability of liposomes. *J. Pharm. Sci.* **73**, 1559–1563

155. Bandrowski, J. F., and Benson, C. L. (1972) Investigation of the use of calcein in the ultramicro fluorometric determination of calcium in serum. *Clin. Chem.* **18**, 1411–1414

156. Düzgüneş, N. (2003) Fluorescence Assays for Liposome Fusion. *Methods Enzymol.* **372**, 260–274

157. Breuer, W., Epsztejn, S., Millgram, P., and Cabantchik, I. Z. (1995) Transport of iron and other transition metals into cells as revealed by a fluorescent probe. *Am. J. Physiol.* **268**, C1354–C1361

158. Scatchard, G. (1949) The attractions of proteins for small molecules and ions. *Ann. N. Y. Acad. Sci.* **51**, 660–672

159. Bordbar, A. K., Saboury, A. A., and Moosavi-Movahedi, A. A. (1996) The Shapes of Scatchard Plots for Systems with Two Sets of Binding Sites. *Biochem. Educ.* **24**, 172–175

160. Manzanares, D., Rodriguez-Capote, K., Liu, S., Haines, T., Ramos, Y., Zhao, L., Doherty-Kirby, A., Lajoie, G., and Possmayer, F. (2007) Modification of tryptophan and methionine residues is implicated in the oxidative inactivation of surfactant protein B. *Biochemistry*. **46**, 5604–5615

161. Shou-Hwa, Y., and Possmayer, F. (1988) Comparative studies on the biophysical activities of the low-molecular-weight hydrophobic proteins purified from bovine pulmonary surfactant. *Biochim. Biophys. Acta (BBA)/Lipids Lipid Metab.* **961**, 337–350

162. BLES Biochemicals Inc. (2012) BLES (bovine lipid extract surfactant) Product Monograph

163. Dodge, J. T., Mitchell, C., and Hanahan, D. J. (1963) The preparation and chemical characteristics of

hemoglobin-free ghosts of human erythrocytes. *Arch. Biochem. Biophys.* **100**, 119–130

164. Kamber, E., and Kopeikina-Tsiboukidou, L. (1986) Alterations in the activities of rabbit erythrocyte membrane-bound enzymes induced by cholesterol enrichment and depletion procedures. *Zeitschrift fur Naturforsch. - Sect. C J. Biosci.* **41**, 301–309

165. Churchward, M. A., Brandman, D. M., Rogasevskaia, T., and Coorssen, J. R. (2008) Copper (II) sulfate charring for high sensitivity on-plate fluorescent detection of lipids and sterols: quantitative analyses of the composition of functional secretory vesicles. *J. Chem. Biol.* **1**, 79–87

166. Skipski, V. P., Peterson, R. F., Sanders, J., and Barclay, M. (1963) Thin-layer chromatography of phospholipids using silica gel without calcium sulfate binder. *J. Lipid Res.* **4**, 227–228

167. Kellogg, E. W., and Fridovich, I. (1975) Superoxide, hydrogen peroxide, and singlet oxygen in lipid peroxidation by a xanthine oxidase system. *J. Biol. Chem.* **250**, 8812–8817

168. Oette, K. (1965) Identification of some lipid peroxides by thin-layer chromatography. *J. Lipid Res.* **6**, 449–454

169. Fuchs, B., Süß, R., Teuber, K., Eibisch, M., and Schiller, J. (2011) Lipid analysis by thin-layer chromatography-A review of the current state. *J. Chromatogr. A*. **1218**, 2754–2774

170. Lok, C. (1978) Versatile methods for the synthesis of mixed-acid 1, 2-diacylglycerols. *Chem. Phys. Lipids*. **22**, 323–337

171. Kokina, A., Kibilds, J., and Liepins, J. (2014) Adenine auxotrophy - be aware: Some effects of adenine auxotrophy in Saccharomyces cerevisiae strain W303-1A. *FEMS Yeast Res.* **14**, 697–707

172. Lunde, C. S., and Kubo, I. (2000) Effect of Polygodial on the Mitochondrial ATPase of Saccharomyces cerevisiae Effect of Polygodial on the Mitochondrial ATPase of Saccharomyces cerevisiae. *Antimicrob. Agents Chemother.* **44**, 1943–1953

173. Knorr, D., Shetty, K. J., and Kinsella, J. E. (1979) Enzymatic lysis of yeast cell walls. *Biotechnol. Bioeng.* **21**, 2011–2021

174. Smith, P. K., Krohn, R. I., Hermanson, G. T., Mallia, A. K., Gartner, F. H., Provenzano, M. D., Fujimoto, E. K., Goeke, N. M., Olson, B. J., and Klenk, D. C. (1985) Measurement of protein using bicinchoninic acid. *Anal. Biochem.* **150**, 76–85

175. Ferreira, C. M. H., Pinto, I. S. S., Soares, E. V., and Soares, H. M. V. M. (2015) (Un)suitability of the use of pH buffers in biological, biochemical and environmental studies and their interaction with metal ions – a review. *RSC Adv.* **5**, 30989–31003

176. Catanzaro, G., Rapino, C., Oddi, S., and Maccarrone, M. (2009) Anandamide increases swelling and reduces calcium sensitivity of mitochondria. *Biochem. Biophys. Res. Commun.* **388**, 439–442

177. Ricchelli, F., Dabbeni-Sala, F., Petronilli, V., Bernardi, P., Hopkins, B., and Bova, S. (2005) Species-specific modulation of the mitochondrial permeability transition by norbormide. *Biochim. Biophys. Acta - Bioenerg.* **1708**, 178–186

178. Ziolkowski, W., Vadhana, D. M. S., Kaczor, J. J., Olek, R. a, Flis, D. J., Halon, M., Wozniak, M., Fedeli, D., Carloni, M., Antosiewicz, J., and Gabbianelli, R. (2013) Exercise-induced heart mitochondrial cholesterol depletion influences the inhibition of mitochondrial swelling. *Exp. Physiol.* **10**, 23733522

179. Zinser, E., and Daum, G. (1995) Isolation and biochemical characterization of organelles from the yeast, Saccharomyces cerevisiae. *Yeast*. **11**, 493–536

180. Presley, A. D., Fuller, K. M., and Arriaga, E. a. (2003) MitoTracker Green labeling of mitochondrial proteins and their subsequent analysis by capillary electrophoresis with laser-induced fluorescence detection. *J. Chromatogr. B*. **793**, 141–150

181. Schindelin, J., Arganda-Carreras, I., Frise, E., Kaynig, V., Longair, M., Pietzsch, T., Preibisch, S., Rueden, C., Saalfeld, S., Schmid, B., Tinevez, J. Y., White, D. J., Hartenstein, V., Eliceiri, K., Tomancak, P., and Cardona, A. (2012) Fiji: An open-source platform for biological-image analysis. *Nat. Methods*. **9**, 676–682

182. Wojtala, A., Bonora, M., Malinska, D., Pinton, P., Duszynski, J., and Wieckowski, M. R. (2014) Methods to monitor ROS production by fluorescence microscopy and fluorometry. in *Methods in Enzymology*, 1st Ed., pp. 243–262, Elsevier Inc., **542**, 243–262

183. Ganesan, S., Shabits, B. N., and Zaremberg, V. (2015) Tracking diacylglycerol and phosphatidic acid pools in budding yeast. *Lipid Insights*. **2015**, 75–85

184. Folch, J., Lees, M., and Stanley, G. H. S. (1957) A simple method for the isolation and purification of total lipids from animal tissues. *J Biol Chem*. **226**, 497–509

185. Tornabene, T. G., Kates, M., Gelpi, E., and Oro, J. (1969) Occurrence of squalene, di- and tetra-

hydrolsqualenes, and vitamin MK8 in an extremely halophilic bacterium, Halobacterium cutirubrum. *J. Lipid Res.* **10**, 294–303

186. Choquet, C. G., Patel, G. B., Beveridge, T. J., and Sprott, G. D. (1992) Formation of unilamellar liposomes from total polar lipid extracts of methanogens. *Appl. Environ. Microbiol.* **58**, 2894–2900

187. Umbsaar, J., Kerek, E., and Prenner, E. J. (2018) Cobalt and nickel affect the fluidity of negatively-charged biomimetic membranes. *Chem. Phys. Lipids*. **210**, 28–37

188. Gruner, S. M., Cullis, P. R., Hope, M. J., and Tilcock, C. P. (1985) Lipid polymorphism: the molecular basis of nonbilayer phases. *Annu. Rev. Biophys. Biophys. Chem.* **14**, 211–238

189. van Blitterswijk, W. J., Hilkmann, H., and van der Meer, B. W. (1987) Quantitative contributions of cholesterol and the individual classes of phospholipids and their degree of fatty acyl (un)saturation to membrane fluidity measured by fluorescence polarization. *Biochemistry*. **26**, 1746–1756

190. Klasczyk, B., Knecht, V., Lipowsky, R., and Dimova, R. (2010) Interactions of alkali metal chlorides with phosphatidylcholine vesicles. *Langmuir*. **26**, 18951–18958

191. Stollery, J. G., and Vail, W. J. (1977) Interactions of divalent cations or basic proteins with phosphatidylethanolamine vesicles. *BBA - Biomembr.* **471**, 372–390

192. Mansour, H. M., and Zografi, G. (2007) The relationship between water vapor absorption and desorption by phospholipids and bilayer phase transitions. *J. Pharm. Sci.* **96**, 377–396

193. van Dijck, P. W. ., de Kruijff, B., Verkleij, A. ., van Deenen, L. L. ., and de Gier, J. (1978) Comparative studies on the effects of pH and Ca2+ on bilayers of various negatively charged phospholipids and their mixtures with phosphatidylcholine. *BBA - Biomembr.* **512**, 84–96

194. Lewis, R. N. A. H., and McElhaney, R. N. (2009) The physicochemical properties of cardiolipin bilayers and cardiolipin-containing lipid membranes. *BBA - Biomembr.* **1788**, 2069–2079

195. Sathappa, M., and Alder, N. N. (2016) The ionization properties of cardiolipin and its variants in model bilayers. *BBA - Biomembr.* **1858**, 1362–1372

196. Wadhwani, P., Epand, R. F., Heidenreich, N., Bürck, J., Ulrich, A. S., and Epand, R. M. (2012) Membrane-Active Peptides and the Clustering of Anionic Lipids. *Biophys. J.* **103**, 265–274

197. Lewis, R. N. A. H., Zweytick, D., Pabst, G., Lohner, K., and McElhaney, R. N. (2007) Calorimetric, x-ray

diffraction, and spectroscopic studies of the thermotropic phase behavior and organization of tetramyristoyl cardiolipin membranes. *Biophys. J.* **92**, 3166–3177

198. Paradies, G., Petrosillo, G., Paradies, V., and Ruggiero, F. M. (2009) Role of cardiolipin peroxidation and Ca2+ in mitochondrial dysfunction and disease. *Cell Calcium*. **45**, 643–650

199. Ren, M., Phoon, C. K. L., and Schlame, M. (2014) Metabolism and function of mitochondrial cardiolipin. *Prog. Lipid Res.* **55**, 1–16

200. Bangham, A. D., Morley, C. J., and Phillips, M. C. (1979) The physical properties of an effective lung surfactant. *Biochim. Biophys. Acta*

201. Morita, S., and Terada, T. (2015) Enzymatic measurement of phosphatidylglycerol and cardiolipin in cultured cells and mitochondria. *Sci. Rep.* **5**, 11737

202. Zhao, W., Róg, T., Gurtovenko, A. A., Vattulainen, I., and Karttunen, M. (2008) Role of phosphatidylglycerols in the stability of bacterial membranes. *Biochimie*. **90**, 930–938

203. Wydro, P., and Witkowska, K. (2009) The interactions between phosphatidylglycerol and phosphatidylethanolamines in model bacterial membranes. The effect of the acyl chain length and saturation. *Colloids Surfaces B Biointerfaces*. **72**, 32–39

204. Riske, K. A., Amaral, L. Q., and Lamy-Freund, M. T. (2001) Thermal transitions of DMPG bilayers in aqueous solution: SAXS structural studies. *Biochim. Biophys. Acta*. **1511**, 297–308

205. McLaughlin, A. C. (1982) Phosphorus-31 and carbon-13 nuclear magnetic resonance studies of divalent cation binding to phosphatidylserine membranes: use of cobalt as a paramagnetic probe. *Biochemistry*. **21**, 4879–4885

206. Tyurina, Y. Y., Shvedova, A. A., Kawai, K., Tyurin, V. A., Kommineni, C., Quinn, P. J., Schor, N. F., Fabisiak, J. P., and Kagan, V. E. (2000) Phospholipid signaling in apoptosis: peroxidation and externalization of phosphatidylserine. *Toxicology*. **148**, 93–101

207. Bevers, E. M., and Williamson, P. L. (2016) Getting to the outer leaflet: physiology of phosphatidylserine exposure at the plasma membrane. *Physiol. Rev.* **96**, 605–645

208. Nguyen, D. B., Wagner-britz, L., Maia, S., Steffen, P., Wagner, C., Kaestner, L., and Bernhardt, I. (2011) Regulation of phosphatidylserine exposure in red blood cells. *Cell. Physiol. Biochem.* **28**, 847–856

209. Mattai, J., Hauser, H., Demel, R. A., and Shipley, G. G. (1989) Interactions of metal ions with phosphatidylserine bilayer membranes: effect of hydrocarbon chain unsaturation. *Biochemistry*. **28**, 2322–2330

210. Sánchez, M. P., Aranda, F. J., and Gómez-Fernández, J. C. (1996) The interaction of α-tocopherol with phosphatidylserine vesicles and calcium. *Biochim. Biophys. Acta - Biomembr.* **1281**, 23–30

211. Hauser, H., and Shipley, G. G. (1983) Interactions of monovalent cations with phosphatidylserine bilayer membranes. *Biochemistry*. **22**, 2171–8

212. Delage, E., Puyaubert, J., Zachowski, A., and Ruelland, E. (2013) Signal transduction pathways involving phosphatidylinositol 4-phosphate and phosphatidylinositol 4,5-bisphosphate: Convergences and divergences among eukaryotic kingdoms. *Prog. Lipid Res.* **52**, 1–14

213. Kooijman, E. E., King, K. E., Gangoda, M., and Gericke, A. (2009) Ionization properties of phosphatidylinositol polyphosphates in mixed model membranes. *Biochemistry*. **48**, 9360–9371

214. van Paridon, P. A., de Kruijff, B., Ouwerkerk, R., and Wirtz, K. W. A. (1986) Polyphosphoinositides undergo charge neutralization in the physiological pH range: a 31P-NMR study. *Biochim. Biophys. Acta (BBA)/Lipids Lipid Metab.* **877**, 216–219

215. Bushby, R. J., Byard, S. J., Hansbro, P. M., and Reid, D. G. (1990) The conformational behaviour of phosphatidylinositol. *Biochim. Biophys. Acta*. **1044**, 231–236

216. Mühleisen, M., Probst, W., Hayashi, K., and Rahmann, H. (1983) Calcium binding to liposomes composed of negatively charged lipid moieties. *Jpn. J. Exp. Med.* **53**, 103–107

217. Slochower, D. R., Huwe, P. J., Radhakrishnan, R., and Janmey, P. A. (2013) Quantum and all-atom molecular dynamics simulations of protonation and divalent ion binding to phosphatidylinositol 4,5-bisphosphate (PIP2). *J. Phys. Chem. B*. **117**, 8322–8329

218. Tan, J., and Brill, J. A. (2014) Cinderella story: PI4P goes from precursor to key signaling molecule. *Crit. Rev. Biochem. Mol. Biol.* **49**, 33–58

219. Binder, H., and Zschörnig, O. (2002) The effect of metal cations on the phase behavior and hydration characteristics of phospholipid membranes. *Chem. Phys. Lipids*. **115**, 39–61

220. Papahadjopoulos, D., Poste, G., Schaeffer, B. E., and Vail, W. J. (1974) Membrane fusion and molecular

segregation in phospholipid vesicles. *BBA - Biomembr.* **352**, 10–28

221. Demel, R. A., Yin, C. C., Lin, B. Z., and Hauser, H. (1992) Monolayer characterstics and thermal behaviour of phosphatidic acids. *Chem. Phys. Lipids*. **60**, 209–223

222. Sánchez, M. P., Aranda, F. J., and Gómez-Fernández, J. C. (1996) The interaction of α-tocopherol with phosphatidylserine vesicles and calcium. *BBA - Biomembr.* **1281**, 23–30

223. Kwon, K. O., Kim, M. J., Abe, M., Ishinomori, T., and Ogino, K. (1994) Thermotropic Behavior of a Phospholipid Bilayer Interacting with Metal Ions. *Langmuir*. **10**, 1415–1420

224. Bers, D. M., Philipson, K. D., and Peskoff, A. (1985) Calcium at the surface of cardiac plasma membrane vesicles: Cation binding, surface charge screening, and Na-Ca exchange. *J. Membr. Biol.* **85**, 251–261

225. Asthagiri, D., Pratt, L. R., Paulaitis, M. E., and Rempe, S. B. (2004) Hydration structure and free energy of biomolecularly specific aqueous dications, including Zn2+ and first transition row metals. *J. Am. Chem. Soc.* **126**, 1285–1289

226. Persson, I. (2010) Hydrated metal ions in aqueous solution: How regular are their structures? *Pure Appl. Chem.* **82**, 1901–1917

227. Le, M. T., Gailer, J., and Prenner, E. J. (2009) Hg2+ and Cd2+ interact differently with biomimetic erythrocyte membranes. *BioMetals*. **22**, 261–274

228. Lewis, B. A., and Engelman, D. M. (1983) Lipid bilayer thickness varies linearly with acyl chain length in fluid phosphatidylcholine vesicles. *J. Mol. Biol.* **166**, 211–217

229. Lichtenberg, D., and Markello, T. (1984) Structural characteristics of phospholipid multilamellar liposomes. *J. Pharm. Sci.* **73**, 122–125

230. Gruber, H. J., and Schindler, H. (1994) External surface and lamellarity of lipid vesicles: a practice-oriented set of assay methods. *BBA - Biomembr.* **1189**, 212–224

231. Lohner, K., Latal, A., Degovics, G., and Garidel, P. (2001) Packing characteristics of a model system mimicking cytoplasmic bacterial membranes. *Chem. Phys. Lipids*. **111**, 177–192

232. Zhang, Y.-P., Lewis, R. N. A. H., and McElhaney, R. N. (1997) Calorimetric and spectroscopic studies of the thermotropic phase behavior of the n-saturated 1,2-diacylphosphatidylglycerols. *Biophys. J.* **72**, 779–793

233. Aranda, F. J., Bailey, A. L., Brown, M. F., Burger, K. N. J., Cullis, P. R., Delacroix, H., Epand, R. M.,

Gómez-Fernàndez, J. C., Gulik, A., Huang, L., Hui, S. W., Karlsson, O. P., Killian, J. A., de Kruijff, B., Gulik-Krxywicki, T., Kusters, R., Lewis, R. N. A. H., Lindblom, G., Luzzati, V., Mannock, D. A., Mariani, P., McElhaney, R. N., Parsegian, V. A., Rand, R. P., Rietveld, A. G., Sorgi, F. L., Thurmond, R. L., Vargas, R., Villalaín, J., Wieslander, A., Yeagle, P. L., and Zidovetzki, R. (1997) Lipid Polymorphism and Membrane Properties. in *Current Topics in Membranes*, 44th Ed. (Epand, R. M. ed), pp. 167–187, 209–227, Academic Press, San Diego

234. Elmore, D. E. (2006) Molecular dynamics simulation of a phosphatidylglycerol membrane. *FEBS Lett.* **580**, 144–148

235. Hassanin, M., Kerek, E., Chiu, M., Anikovskiy, M., and Prenner, E. J. (2016) Binding affinity of inorganic mercury and cadmium to biomimetic erythrocyte membranes. *J. Phys. Chem. B*. **120**, 12872–12882

236. Cong, X., Poyton, M. F., Baxter, A. J., Pullanchery, S., and Cremer, P. S. (2015) Unquenchable Surface Potential Dramatically Enhances Cu2+Binding to Phosphatidylserine Lipids. *J. Am. Chem. Soc.* **137**, 7785–7792

237. Kerek, E., Hassanin, M., and Prenner, E. J. (2018) Inorganic mercury and cadmium induce rigidity in eukaryotic lipid extracts while mercury also ruptures red blood cells. *Biochim. Biophys. Acta - Biomembr.* **1860**, 710–717

238. Kerek, E. (2016) *Interactions of Inorganic Mercury and Inorganic Cadmium with Biomimetic and Complex Biological Membranes and their Influence on Membrane Packing and Size*. Ph.D. thesis, University of Calgary

239. Macdermaid, C. M., Devane, R. H., Klein, M. L., and Fiorin, G. (2014) Dehydration of multilamellar fatty acid membranes: Towards a computational model of the stratum corneum. *J. Chem. Phys.* **141**, 1–9

240. Boggs, J. M. (1987) Lipid intermolecular hydrogen bonding: influence on structural organization and membrane function. *BBA - Rev. Biomembr.* **906**, 353–404

241. Martínez, M., and Mougan, I. (1998) Fatty acid composition of human brain phospholipids during normal development. *J. Neurochem.* **71**, 2528–2533

242. Chen, S. Y., and Cheng, K. H. (1996) Detection of membrane packing defects by time-resolved fluorescence depolarization. *Biophys. J.* **71**, 878–884

243. Engelmann, M. D., Bobier, R. T., Hiatt, T., and Cheng, I. F. (2003) Variability of the Fenton reaction characteristics of the EDTA, DTPA, and citrate complexes of iron. *BioMetals*. **16**, 519–527

244. Fu, F., Tang, B., Wang, Q., and Liu, J. (2010) Degradation of Ni-EDTA complex by Fenton reaction and ultrasonic treatment for the removal of Ni2+ions. *Environ. Chem. Lett.* **8**, 317–322

245. Parejo, I., Codina, C., Petrakis, C., and Kefalas, P. (2000) Evaluation of scavenging activity assessed by Co(II)/EDTA-induced luminol chemiluminescence and DPPH· (2,2-diphenyl-1-picrylhydrazyl) free radical assay. *J. Pharmacol. Toxicol. Methods*. **44**, 507–512

246. Shi, X., Dalal, N. S., and Kasprzak, K. S. (1992) Generation of free radicals from lipid hydroperoxides by Ni2+ in the presence of oligopeptides. *Arch. Biochem. Biophys.* **299**, 154–162

247. Frankel, E. N. (1984) Lipid oxidation: Mechanisms, products and biological significance. *J. Am. Oil Chem. Soc.* **61**, 1908–1917

248. Poyton, M. F., Sendecki, A. M., Cong, X., and Cremer, P. S. (2016) Cu2+Binds to phosphatidylethanolamine and increases oxidation in lipid membranes. *J. Am. Chem. Soc.* **138**, 1584–1590

249. Yin, H., and Zhu, M. (2012) Free radical oxidation of cardiolipin: Chemical mechanisms, detection and implication in apoptosis, mitochondrial dysfunction and human diseases. *Free Radic. Res.* **46**, 959–974

250. Veldhuizen, E. J. A., Batenburg, J. J., Van Golde, L. M. G., and Haagsman, H. P. (2000) The role of surfactant proteins in DPPC enrichment of surface films. *Biophys. J.* **79**, 3164–3171

251. Possmayer, F., Nag, K., Rodriguez, K., Qanbar, R., and Schürch, S. (2001) Surface activity in vitro: role of surfactant proteins. *Comp. Biochem. Physiol. A. Mol. Integr. Physiol.* **129**, 209–20

252. Pérez-Gil, J. (2008) Structure of pulmonary surfactant membranes and films: The role of proteins and lipid-protein interactions. *Biochim. Biophys. Acta - Biomembr.* **1778**, 1676–1695

253. Chang, R., Nir, S., and Poulain, F. R. (1998) Analysis of binding and membrane destabilization of phospholipid membranes by surfactant apoprotein B. *Biochim. Biophys. Acta - Biomembr.* **1371**, 254–264

254. Schulze, C., Schaefer, U. F., Ruge, C. A., Wohlleben, W., and Lehr, C. M. (2011) Interaction of metal oxide nanoparticles with lung surfactant protein A. *Eur. J. Pharm. Biopharm.* **77**, 376–383

255. Hallman, M., Feldman, B. H., Kirkpatrick, E., and Gluck, L. (1977) Absence of phosphatidylglycerol (PG) in respiratory distress syndrome in the newborn. Study of the minor surfactant phospholipids in newborns.

Pediatr. Res. **11**, 714–20

256. Hallman, M., and Gluck, L. (1976) Phosphatidylglycerol in lung surfactant. III. Possible modifier of surfactant function. *J. Lipid Res.* **17**, 257–262

257. Numata, M., Chu, H. W., Dakhama, A., and Voelker, D. R. (2010) Pulmonary surfactant phosphatidylglycerol inhibits respiratory syncytial virus-induced inflammation and infection. *Proc. Natl. Acad. Sci.* **107**, 320–325

258. Rae, T. (1978) The haemolytic action of particulate metals (Cd, Cr, Co, Fe, Mo, Ni, Ta, Ti, Zn, Co-Cr alloy). *J. Pathol.* **125**, 81–89

259. Ito, T., and Kon, H. (1987) The copper-induced deformability loss and echinocyte formation in human erythrocytes: An electron paramagnetic resonance study. *Toxicol. Appl. Pharmacol.* **88**, 242–254

260. Suwalsky, M., Villena, F., and Sotomayor, C. P. (2010) Mn2+ exerts stronger structural effects than the Mn-citrate complex on the human erythrocyte membrane and molecular models. *J. Inorg. Biochem.* **104**, 55–61

261. Beaven, G. H., Parmar, J., Nash, G. B., Bennett, B. M., and Gratzer, W. B. (1990) Effect of magnesium ions on red cell membrane properties. *J. Membr. Biol.* **118**, 251–7

262. Glaser, R. (1982) Echinocyte formation induced by potential changes of human red blood cells. *J. Membr. Biol.* **66**, 79–85

263. Sheetz, M. P., and Singer, S. J. (1974) Biological membranes as bilayer couples. A molecular mechanism of drug-erythrocyte interactions. *Proc. Natl. Acad. Sci.* **71**, 4457–4461

264. Bütikofer, P., Lin, Z. W., Chiu, D. T.-Y., Lubin, B., and Kuypers, F. A. (1990) Transbilayer distribution and mobility of phosphatidylinositol in human red blood cells. *J. Biol. Chem.* **265**, 16035–16038

265. Morris, S. J., Bradley, D., and Blumenthal, R. (1985) The use of cobalt ions as a collisional quencher to probe surface charge and stability of fluorescently labeled bilayer vesicles. *Biochim. Biophys. Acta*. **818**, 365–372

266. Nakada, S., Inoue, K., Nojima, S., and Imura, N. (1978) Change in permeability of liposomes caused by methyl- mercury and inorganic mercury. *Chem. Biol. Interact.* **22**, 15–23

267. Demel, R. A., Bruckdorfer, K. R., and Van Deenen, L. L. . (1972) The effect of sterol structure on the permeability of lipomes to glucose, glycerol, and Rb+. *Biochim Biophys Acta*

268. Allen, T. M., and Cleland, L. G. (1980) Serum-induced leakage of liposome contents. *Biochim. Biophys. Acta - Biomembr.* **597**, 418–426

269. Yokouchi, Y., Tsunoda, T., Imura, T., Yamauchi, H., Yokoyama, S., Sakai, H., and Abe, M. (2001) Effect of adsorption of bovine serum albumin on liposomal membrane characteristics. *Colloids Surfaces B Biointerfaces*. **20**, 95–103

270. Ramsay, L. M., and Gadd, G. M. (1997) Mutants of Saccharomyces cerevisiae defective in vacuolar function confirm a role for the vacuole in toxic metal ion detoxification. *FEMS Microbiol. Lett.* **152**, 293–298

271. He, L., Poblenz, A. T., Medrano, C. J., and Fox, D. A. (2000) Lead and calcium produce rod photoreceptor cell apoptosis by opening the mitochondrial permeability transition pore. *J. Biol. Chem.* **275**, 12175–12184

272. Bragadin, M., Toninello, A., Mancon, M., and Manente, S. (2007) The interactions of cobalt(II) with mitochondria from rat liver. *J. Biol. Inorg. Chem.* **12**, 631–635

273. Wang, Y. F., Shyu, H. W., Chang, Y. C., Tseng, W. C., Huang, Y. L., Lin, K. H., Chou, M. C., Liu, H. L., and Chen, C. Y. (2012) Nickel (II)-induced cytotoxicity and apoptosis in human proximal tubule cells through a ROS- and mitochondria-mediated pathway. *Toxicol. Appl. Pharmacol.* **259**, 177–186

274. Fulda, S., Galluzzi, L., and Kroemer, G. (2010) Evasion of cell death is a hallmark of human cancers and a major cause of treatment failure. *Nat. Rev. Drug Discov.* **9**, 447–464

275. Jung, D. W., Bradshaw, P. C., and Pfeiffer, D. R. (1997) Properties of a cyclosporin-insensitive permeability transition pore in yeast mitochondria. *J. Biol. Chem.* **272**, 21104–21112

276. Guthrie, C., and Fink, G. (2002) *Methods in Enzymology: Guide to Yeast Genetics and Molecular Biology Part A*, Academic Press

277. Borklu-Yucel, E., Eraslan, S., and Ulgen, K. O. (2015) Transcriptional remodeling in response to transfer upon carbon-limited or metformin-supplemented media in S. cerevisiae and its effect on chronological life span. *Appl. Microbiol. Biotechnol.* **99**, 6775–6789

278. Corbacho, I., Teixidó, F., Velázquez, R., Hernández, L. M., and Olivero, I. (2011) Standard YPD, even supplemented with extra nutrients, does not always compensate growth defects of Saccharomyces cerevisiae auxotrophic strains. *Antonie van Leeuwenhoek, Int. J. Gen. Mol. Microbiol.* **99**, 591–600

279. Gonzalez-Gil, G., Jansen, S., Zandvoort, M. H., and Van Leeuwen, H. P. (2003) Effect of yeast extract on speciation and bioavailability of nickel and cobalt in anaerobic bioreactors. *Biotechnol. Bioeng.* **82**, 134–142

280. Nyberg, S. M. H. T., Cefola, M., and Sabine, D. (1959) Chelation of cobalt, nickel and copper with glutamic acid. *Arch. Biochem. Biophys.* **85**, 82–88

281. Albers, E., Larsson, C., Liden, G., Niklasson, C., and Gustafsson, L. (1996) Influence of the Nitrogen Source on Saccharomyces cerevisiae Anaerobic Growth and Product Formation. *Appl. Environ. Microbiol.* **62**, 3187–3195

282. Lemire, J., Milandu, Y., Auger, C., Bignucolo, A., Appanna, V. P., and Appanna, V. D. (2010) Histidine is a source of the antioxidant, α-ketoglutarate, in Pseudomonas fluorescens challenged by oxidative stress. *FEMS Microbiol. Lett.* **309**, 170–177

283. Hamada, H., Toshimitsu, N., Kojima, M., and Morita, T. (1985) Effects of methanol and magnesium chloride on the induction of respiration-deficient mutants in yeast by metal ions. *Chem. Pharm. Bull.* **33**, 1571–1575

284. Egilsson, V., Evans, I. H., and Wilkie, D. (1979) Toxic and mutagenic effects of carcinogens on the mitochondria of Saccharomyces cerevisiae. *Mol. Gen. Genet.* **174**, 39–46

285. Okamoto, K., and Shaw, J. M. (2005) Mitochondrial morphology and dynamics in yeast and multicellular eukaryotes. *Annu. Rev. Genet.* **39**, 503–536

286. Cottet-Rousselle, C., Ronot, X., Leverve, X., and Mayol, J. F. (2011) Cytometric assessment of mitochondria using fluorescent probes. *Cytom. Part A*. **79 A**, 405–425

287. Rajakumar, S., Bhanupriya, N., Ravi, C., and Nachiappan, V. (2016) Endoplasmic reticulum stress and calcium imbalance are involved in cadmium-induced lipid aberrancy in Saccharomyces cerevisiae. *Cell Stress Chaperones*. **21**, 895–906

288. Xu, S., Pi, H., Chen, Y., Zhang, N., Guo, P., Lu, Y., He, M., Xie, J., Zhong, M., Zhang, Y., Yu, Z., and Zhou, Z. (2013) Cadmium induced Drp1-dependent mitochondrial fragmentation by disturbing calcium homeostasis in its hepatotoxicity. *Cell Death Dis.* **4**, 1–10

289. Pendergrass, W., Wolf, N., and Pool, M. (2004) Efficacy of MitoTracker Green™ and CMXRosamine to measure changes in mitochondrial membrane potentials in living cells and tissues. *Cytom. Part A*. **61**, 162–9

290. Keij, J. F., Bell-Prince, C., and Steinkamp, J. A. (2000) Staining of mitochondrial membranes with 10-nonyl acridine orange MitoFluor Green, and MitoTracker Green is affected by mitochondrial membrane potential altering drugs. *Cytometry*. **39**, 203–210

291. Westermann, B., and Neupert, W. (2000) Mitochondria-targeted green fluorescent proteins: Convenient tools for the study of organelle biogenesis in Saccharomyces cerevisiae. *Yeast*. **16**, 1421–1427

292. Molecular Probes (2005) MitoSOX Red mitochondrial superoxide indicator for live-cell imaging

293. Zielonka, J., and Kalyanaraman, B. (2010) Hydroethidine- and MitoSOX-derived red fluorescence is not a reliable indicator of intracellular superoxide formation: Another inconvenient truth. *Free Radic. Biol. Med.* **48**, 983–1001

294. Kowaltowski, A. J., and Vercesi, A. E. (1999) Mitochondrial damage induced by conditions of oxidative stress. *Free Radic. Biol. Med.* **26**, 463–471

295. Mykytczuk, N. C. S., Trevors, J. T., Ferroni, G. D., and Leduc, L. G. (2011) Cytoplasmic membrane response to copper and nickel in Acidithiobacillus ferrooxidans. *Microbiol. Res.* **166**, 186–206

296. Steels, E. L., Learmonth, R. P., and Watson, K. (1994) Stress tolerance and membrane lipid unsaturation in Saccharomyces cerevisiae grown aerobically or anaerobically. *Microbiology*. **140**, 569–76

297. Hostetler, K. Y., Galesloot, J. M., Boer, P., and Van den Bosch, H. (1975) Further studies on the formation of cardiolipin and phosphatidylglycerol in rat liver mitochondria - effect of divalent cations and the fatty acid composition of CDP-diglyceride. *Biochim. Biophys. Acta*. **380**, 382–389

298. Tamai, K. T., and Greenberg, M. L. (1990) Biochemical characterization and regulation of cardiolipin synthase in Saccharomyces cerevisiae. *Biochim. Biophys. Acta (BBA)/Lipids Lipid Metab.* **1046**, 214–222

299. Czabany, T., Athenstaedt, K., and Daum, G. (2007) Synthesis, storage and degradation of neutral lipids in yeast. *Biochim. Biophys. Acta - Mol. Cell Biol. Lipids*. **1771**, 299–309

300. Xie, S., Naslavsky, N., and Caplan, S. (2015) Diacylglycerol kinases in membrane trafficking. *Cell. Logist.* **5**, 1–9

301. Eichmann, T. O., and Lass, A. (2015) DAG tales: The multiple faces of diacylglycerol - Stereochemistry, metabolism, and signaling. *Cell. Mol. Life Sci.* **72**, 3931–3952

302. Narváez-Rivas, M., Vicario, I. M., Constante, E. G., and León-Camacho, M. (2007) Changes in the

concentrations of free fatty acid, monoacylglycerol, and diacylglycerol in the subcutaneous fat of Iberian ham during the dry-curing process. *J. Agric. Food Chem.* **55**, 10953–10961

303. Domart, M. C., Hobday, T. M. C., Peddie, C. J., Chung, G. H. C., Wang, A., Yeh, K., Jethwa, N., Zhang, Q., Wakelam, M. J. O., Woscholski, R., Byrne, R. D., Collinson, L. M., Poccia, D. L., and Larijani, B. (2012) Acute manipulation of diacylglycerol reveals roles in nuclear envelope assembly & endoplasmic reticulum morphology. *PLoS One*. **7**, e51150

304. Veiga, M. P., Arrondo, J. L. R., Goñi, F. M., and Alonso, A. (1999) Ceramides in phospholipid membranes: effects on bilayer stability and transition to nonlamellar phases. *Biophys. J.* **76**, 342–350

305. Sorger, D., and Daum, G. (2002) Synthesis of triacylglycerols by the acyl-coenzyme A: diacyl-glycerol acyltransferase Dga1p in lipid particles of the yeast Saccharomyces cerevisiae. *J. Bacteriol.* **184**, 519–524

306. Rajakumari, S., Grillitsch, K., and Daum, G. (2008) Synthesis and turnover of non-polar lipids in yeast. *Prog. Lipid Res.* **47**, 157–171

307. Wagner, A., and Daum, G. (2005) Formation and mobilization of neutral lipids in the yeast Saccharomyces cerevisiae. *Biochem. Soc. Trans.* **33**, 1174–1177

308. Klug, L., and Daum, G. (2014) Yeast lipid metabolism at a glance. *FEMS Yeast Res.* **14**, 369–388

309. Han, G. S., Wu, W. I., and Carman, G. M. (2006) The Saccharomyces cerevisiae lipin homolog is a Mg2+-dependent phosphatidate phosphatase enzyme. *J. Biol. Chem.* **281**, 9210–9218

310. Hosaka, K., and Yamashita, S. (1984) Regulatory role of phosphatidate phosphatase in triacylglycerol synthesis of Saccharomyces cerevisiae. *Biochim. Biophys. Acta*. **796**, 110–117

311. Czabany, T., Wagner, A., Zweytick, D., Lohner, K., Leitner, E., Ingolic, E., and Daum, G. (2008) Structural and biochemical properties of lipid particles from the yeast Saccharomyces cerevisiae. *J. Biol. Chem.* **283**, 17065–17074

312. Athenstaedt, K., and Daum, G. (2003) YMR313c/TGL3 encodes a novel triacylglycerol lipase located in lipid particles of Saccharomyces cerevisiae. *J. Biol. Chem.* **278**, 23317–23323

313. Athenstaedt, K., and Daum, G. (2005) Tgl4p and Tgl5p, two triacylglycerol lipases of the yeast Saccharomyces cerevisiae are localized to lipid particles. *J. Biol. Chem.* **280**, 37301–37309

314. Abelson, P. H., and Aldous, E. (1950) Ion antagonisms in microorganisms; interference of normal

magnesium metabolism by nickel, cobalt, cadmium, zinc, and manganese. *J. Bacteriol.* **60**, 401–413

315. Fishelson, Z., and Müller-Eberhard, H. J. (1982) C3 convertase of human complement : enhanced formation and stability of the enzyme generated with nickel instead of magnesium. *J. Immunol.* **129**, 2603–2607

316. Brzozowski, A. M., Derewenda, U., Derewenda, Z. S., Dodson, G. G., Lawson, D. M., Turkenburg, J. P., Bjorkling, F., Huge-Jensen, B., Patkar, S. A., and Thim, L. (1991) A model for interfacial activation in lipases from the structure of a fungal lipase-inhibitor complex. *Nature*. **351**, 491–494

317. Kurat, C. F., Wolinski, H., Petschnigg, J., Kaluarachchi, S., Andrews, B., Natter, K., and Kohlwein, S. D. (2009) Cdk1/Cdc28-dependent activation of the major triacylglycerol lipase Tgl4 in yeast links lipolysis to cell-cycle progression. *Mol. Cell*. **33**, 53–63

318. Li, Y., Zong, W. X., and Ding, W. X. (2017) Recycling the danger via lipid droplet biogenesis after autophagy. *Autophagy*. **13**, 1995–1997

319. Li, Z., Berk, M., McIntyre, T. M., Gores, G. J., and Feldstein, A. E. (2008) The lysosomal-mitochondrial axis in free fatty acid-induced hepatic lipotoxicity. *Hepatology*. **47**, 1495–1503

320. Feldstein, A. E., Werneburg, N. W., Canbay, A., Guicciardi, M. E., Bronk, S. F., Rydzewski, R., Burgart, L. J., and Gores, G. J. (2004) Free fatty acids promote hepatic lipotoxicity by stimulating TNF-α expression via a lysosomal pathway. *Hepatology*. **40**, 185–194

321. Alvarez-Vasquez, F., Riezman, H., Hannun, Y. A., and Voit, E. O. (2011) Mathematical modeling and validation of the ergosterol pathway in saccharomyces cerevisiae. *PLoS One*. **6**, 1–17

322. Rajakumar, S., Ravi, C., and Nachiappan, V. (2016) Defect of zinc transporter ZRT1 ameliorates cadmium induced lipid accumulation in Saccharomyces cerevisiae. *Metallomics*. **8**, 453–460

323. Choudhary, V., Golani, G., Joshi, A. S., Cottier, S., Schneiter, R., Prinz, W. A., and Kozlov, M. M. (2018) Architecture of lipid droplets in endoplasmic reticulum is determined by phospholipid intrinsic curvature. *Curr. Biol.* **28**, 915–926

324. Ouahoud, S., Fiet, M. D., Martínez-Montañés, F., Ejsing, C. S., Kuss, O., Roden, M., and Markgraf, D. F. (2018) Lipid droplet consumption is functionally coupled to vacuole homeostasis independent of lipophagy. *J. Cell Sci.* **131**, 1–15

325. Park, J. S., Thorsness, M. K., Policastro, R., McGoldrick, L. L., Hollingsworth, N. M., Thorsness, P. E., and

Neiman, A. M. (2016) Yeast Vps13 promotes mitochondrial function and is localized at membrane contact sites. *Mol. Biol. Cell*. **27**, 2435–2449

326. Helle, S. C. J., Kanfer, G., Kolar, K., Lang, A., Michel, A. H., and Kornmann, B. (2013) Organization and function of membrane contact sites. *Biochim. Biophys. Acta - Mol. Cell Res.* **1833**, 2526–2541

327. Simbeni, R., Pon, L., Zinser, E., Paltauf, F., and Daum, G. (1991) Mitochondrial membrane contact sites of yeast: Characterization of lipid components and possible involvement in intramitochondrial translocation of phospholipids. *J. Biol. Chem.* **266**, 10047–10049

328. Kannan, M., Lahiri, S., Liu, L.-K., Choudhary, V., and Prinz, W. A. (2017) Phosphatidylserine synthesis at membrane contact sites promotes its transport out of the ER. *J. Lipid Res.* **58**, 553–562

329. Lentz, B. R. (1989) Membrane “fluidity” as detected by diphenylhexatriene probes. *Chem. Phys. Lipids*. **50**, 171–190

330. Ranquet, C., Ollagnier-de-Choudens, S., Loiseau, L., Barras, F., and Fontecave, M. (2007) Cobalt stress in Escherichia coli: The effect on the iron-sulfur proteins. *J. Biol. Chem.* **282**, 30442–30451

331. Chen, H., and Costa, M. (2009) Iron- and 2-oxoglutarate-dependent Dioxygenases: An emerging group of molecular targets for nickel toxicity and carcinogenicity. *BioMetals*. **22**, 191–196

332. Cheng, H. T., and London, E. (2011) Preparation and properties of asymmetric large unilamellar vesicles: Interleaflet coupling in asymmetric vesicles is dependent on temperature but not curvature. *Biophys. J.* **100**, 2671–2678

333. Jin, T., Pennefather, P., and Lee, P. I. (1996) Lipobeads: A hydrogel anchored lipid vesicle system. *FEBS Lett.* **397**, 70–74

334. Ng, C. C., Cheng, Y. L., and Pennefather, P. S. (2001) One-step synthesis of a fluorescent phospholipid-hydrogel conjugate for driving self-assembly of supported lipid membranes. *Macromolecules*. **34**, 5759–5765

335. Garidel, P., and Blume, A. (1999) Interaction of alkaline earth cations with the negatively charged phospholipid 1,2-dimyristoyl-sn-glycero-3-phosphoglycerol: a differential scanning and isothermal titration calorimetric study. *Langmuir*. **15**, 5526–5534

336. Alonso, C., Alig, T., Yoon, J., Bringezu, F., Warriner, H., and Zasadzinski, J. A. (2004) More than a

monolayer: relating lung surfactant structure and mechanics to composition. *Biophys J*. **87**, 4188–4202

337. Daear, W., Mahadeo, M., and Prenner, E. J. (2017) Applications of Brewster angle microscopy from biological materials to biological systems. *Biochim. Biophys. Acta - Biomembr.* **1859**, 1749–1766

338. Scansetti, G., Maina, G., Botta, G. C., Bambace, P., and Spinelli, P. (1998) Exposure to cobalt and nickel in the hard-metal production industry. *Int. Arch. Occup. Environ. Health*. **71**, 60–63

339. Kaiser, C. A., Chen, E. J., and Losko, S. (2002) Subcellular fractionation of secretory organelles. *Methods Enzymol.* **351**, 325–338

340. Agrawal, B., Czymmek, K. J., Sparks, D. L., and Bais, H. P. (2013) Transient influx of nickel in root mitochondria modulates organic acid and reactive oxygen species production in nickel hyperaccumulator alyssum murale. *J. Biol. Chem.* **288**, 7351–7362

341. Kooijman, E. E., and Burger, K. N. J. (2009) Biophysics and function of phosphatidic acid: A molecular perspective. *Biochim. Biophys. Acta - Mol. Cell Biol. Lipids*. **1791**, 881–888

342. Yadav, S., Scherer, T. M., Shire, S. J., and Kalonia, D. S. (2011) Use of dynamic light scattering to determine second virial coefficient in a semidilute concentration regime. *Anal. Biochem.* **411**, 292–296

343. Dacaranhe, C. D., and Terao, J. (2001) A unique antioxidant activity of phosphatidylserine on iron-induced lipid peroxidation of phospholipid bilayers. *Lipids*. **36**, 1105–1110

344. Recknagel, R. O., and Glende, E. A. J. (1984) Spectrophotometric detection of lipid conjugated dienes. in *Methods in Enzymology*, pp. 331–337, Academic Press, Inc

345. Buege, J. A., and Aust, Steven, D. (1978) Microsomal lipid peroxidation. in *Methods in Enzymology*, pp. 302–310, Academic Press, Inc, **52**, 302–310

346. Wójtowicz, H., Bielecki, M., Wojaczyński, J., Olczak, M., Smalley, J. W., and Olczak, T. (2013) The Porphyromonas gingivalis HmuY haemophore binds gallium(iii), zinc(ii), cobalt(iii), manganese(iii), nickel(ii), and copper(ii) protoporphyrin IX but in a manner different to iron(iii) protoporphyrin IX. *Metallomics*. **5**, 343–351

347. Ricchelli, F. (1995) Photophysical properties of porphyrins in biological membranes. *J. Photochem. Photobiol. B Biol.* **29**, 109–118

Appendix A

1.1 Interaction of Co^{2+} and Ni^{2+} with Laurdan

The potential direct interaction of Co^{2+} and Ni^{2+} with Laurdan was measured by injecting metal into a sample of 9:1 (*v/v*) isopropanol/buffer containing 1 µM Prodan, a structural analogue of Laurdan without the acyl chain (150). The final metal to Prodan ratio was 1000:1.

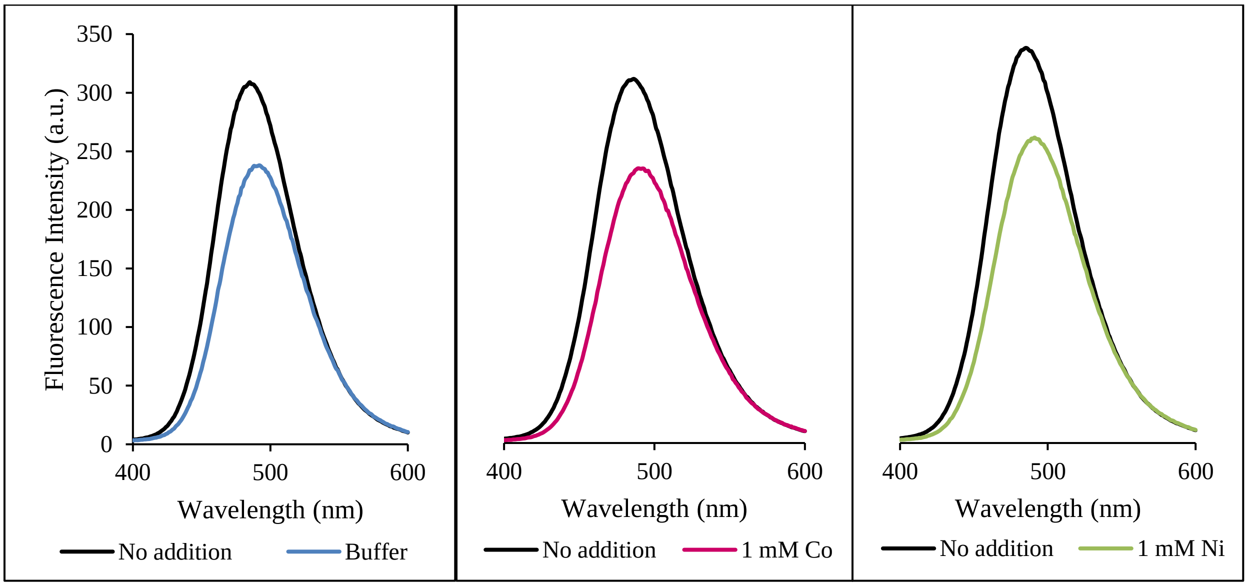

Figure A-1. Fluorescence emission spectra of 1 µM Prodan in 7:1 isopropanol/buffer initially, and following the addition of: buffer, 1 mM Co^{2+}, 1 mM Ni^{2+}.

Neither Co^{2+} nor Ni^{2+} quenched free Prodan significantly upon immediate addition or over time. However, both metals were able to quench Laurdan in the membrane, suggesting that the membrane acts as a scaffold for interaction.

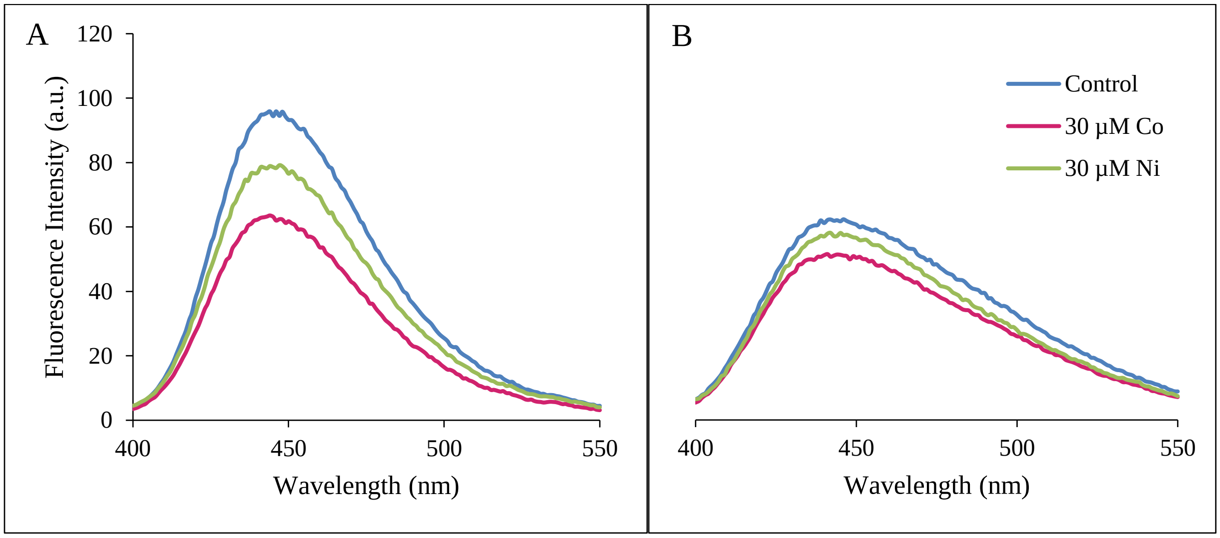

Figure A-2. Fluorescence spectra of Laurdan in DMPA at (A) 40°C and (B) 50°C with buffer, 30 µM Co, or 30 µM Ni.

The quenching interaction did not result in peak shifts, so the GP ratio is still valid.

1.2 DLS count rate melting curves

To verify that the Laurdan quenching interaction was not affecting the results obtained, the T_m's of DMPG (not shown) and DMPA were also measured using DLS count rate (152). Other lipid systems were tested but the transitions were too broad and poorly-resolved to determine accurate T_m's.

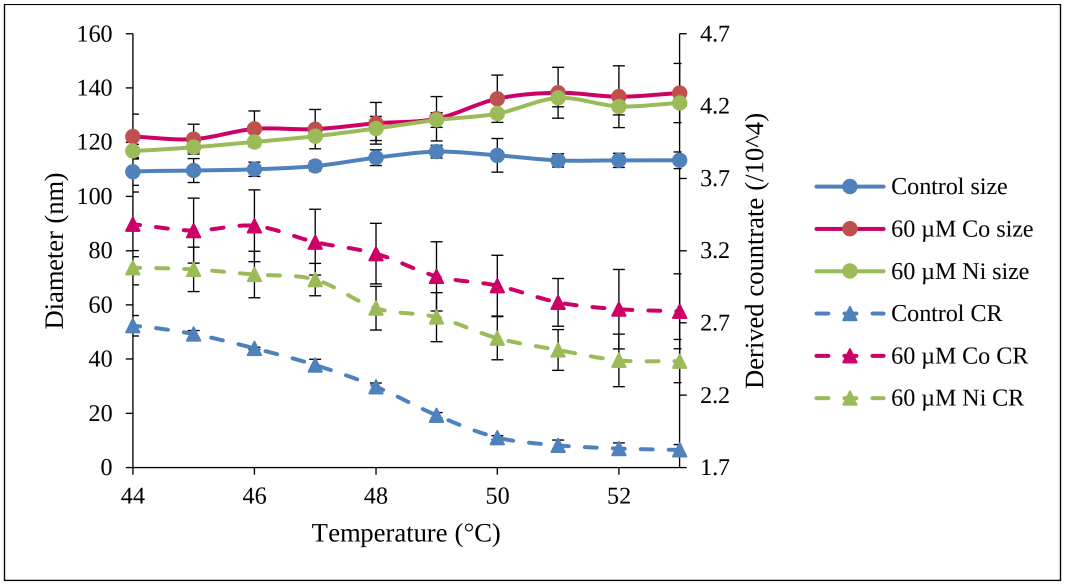

Figure A-3. DLS count rate (CR) melting curves (right axis) and size profiles (left axis) of 0.3 mM DMPA liposomes with 60 µM Co^{2+} or Ni^{2+}.

Table A-1. Comparison of T_m's of DMPA derived from Laurdan GP and DLS melting curves.

System	Laurdan T_m	DLS T_m	Percent Error
DMPA	47.5	47.9	0.9
DMPA + 60 µM Co	48.6	48.9	0.6
DMPA + 60 µM Ni	48.3	48.7	0.8

The T_m's derived from Laurdan and DLS were found to have errors of 0.5–2.0%, suggesting that the techniques were in good agreement. Thus, the Laurdan quenching does not appear to affect the results.

1.3 Verifying the T_m of POPA

The T_m of POPA was found to be 20.5°C, which was unexpectedly low compared to the T_m of 28°C listed on the Avanti Polar Lipids website. Thus, the melting of POPA was also tested in 20 mM phosphate, 100 mM NaCl pH 7.4 buffer to confirm that the Hepes was not having an effect. The curves are shown in Figure :

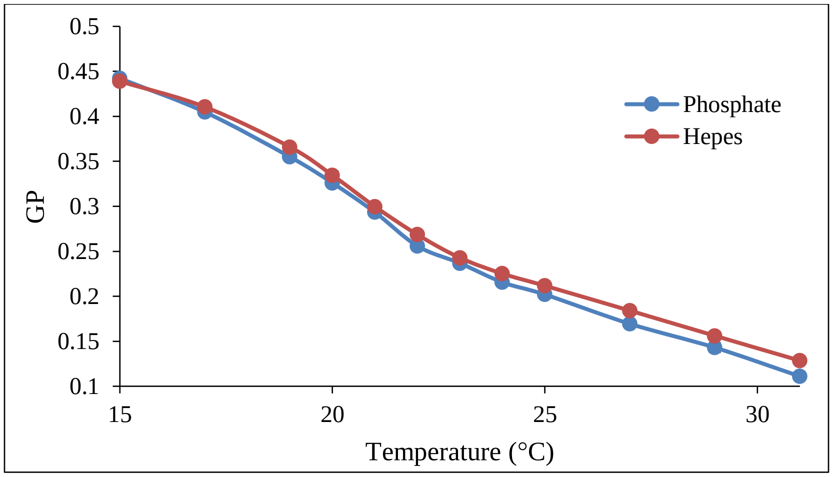

Figure A-4. Laurdan GP melting curves of 0.3 mM POPA liposomes in 100 mM NaCl with 20 mM Phosphate or 20 mM Hepes pH 7.4.

The melting of POPA was found to be essentially unchanged in phosphate buffer, thus it did not appear to be a buffer effect. It may be that POPA is very condition-sensitive, as the ionization changes within a physiological pH range (341), and head group charge would affect how well the membrane packs together.

1.4 Quenching of Calcein by Co^{2+} and Ni^{2+}

The quenching of Calcein was used to detect Co^{2+} and Ni^{2+} in solution. The characteristics of quenching are summarized in Figure :

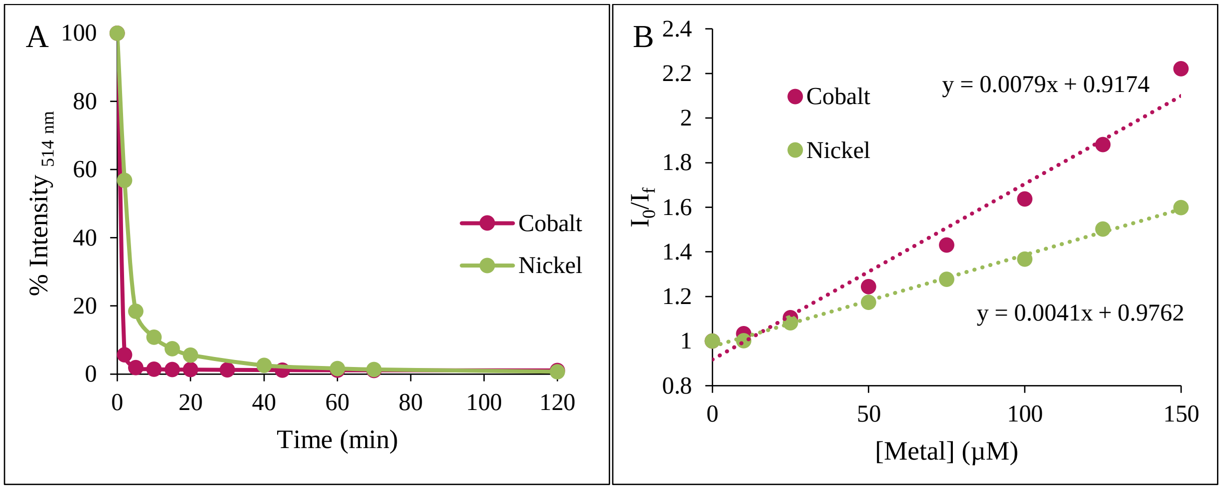

Figure A-5. (A) % Intensity remaining of 0.3 µM Calcein in the presence of 3 µM Co^{2+} or Ni^{2+} over time. (B) Stern-Volmer plot for quenching of 0.3 µM Calcein by Co^{2+} or Ni^{2+} after 1 hr equilibration.

The quenching of Calcein was time-dependent for Ni^{2+}, in that it took about 1 hr to fully equilibrate, while Co^{2+} quenched almost immediately (Figure A). Co^{2+} was also a more potent quencher, as shown by the steeper slope in the Stern-Volmer plot (Figure B).

1.4.1 Standard curves

Standard curves for detection of Co^{2+} and Ni^{2+} in the nanomolar range were made using Calcein quenching:

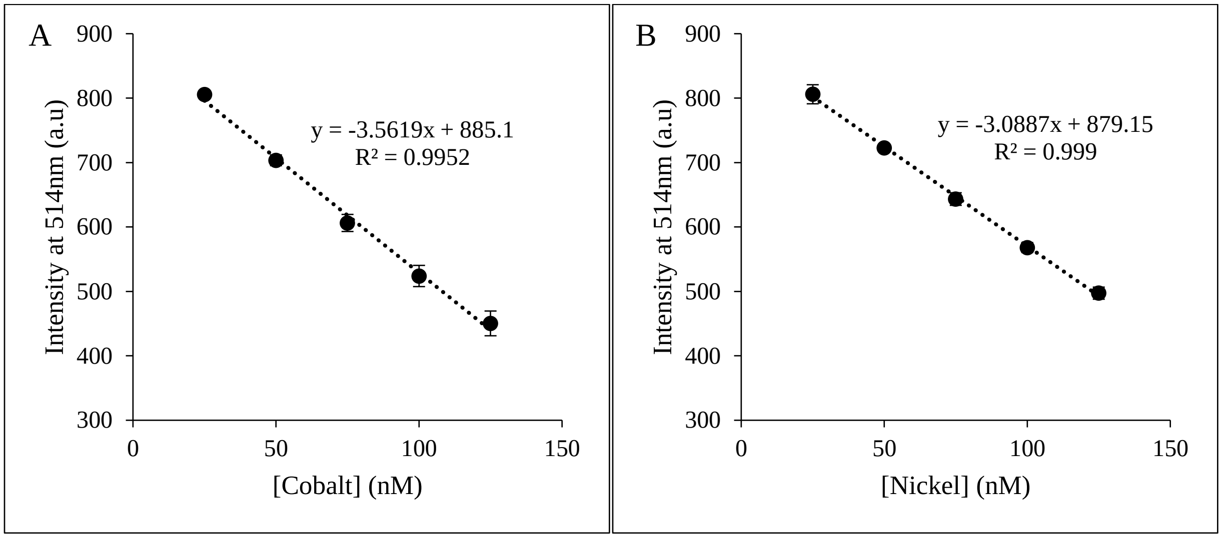

Figure A-6. Standard curves for fluorescence quenching of 0.3 µM Calcein by (A) Co^{2+} or (B) Ni^{2+} after 1 hr incubation in the dark at room temperature.

1.5 MLV centrifugation and binding assay

1.5.1 Preliminary screening

A preliminary screen for the binding of Co^{2+} and Ni^{2+} to various membranes were tested to determine if the method would work, if there was any difference between PO and DM forms, and if there was any difference with incubation temperature. This preliminary screen was performed before further optimization of the assay, thus the MLV samples were "unwashed" and likely contained sonication-derived vesicles which did not spin down. The results are summarized in Figure :

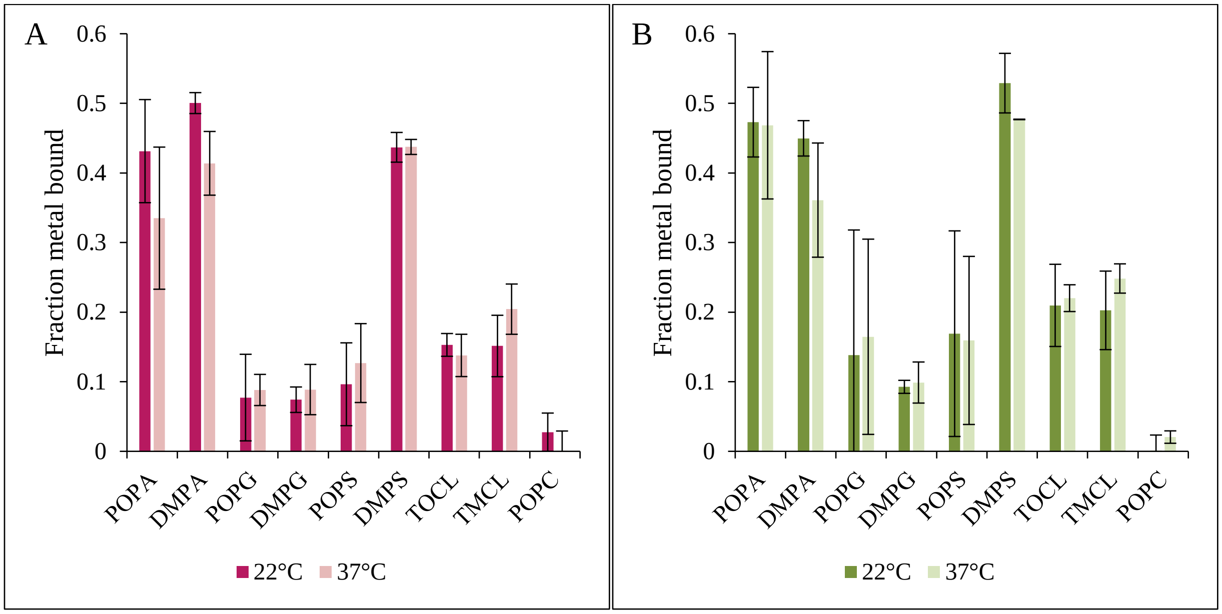

Figure A-7. Preliminary screen of binding of 50 µM (A) Co^{2+} or (B) Ni^{2+} to 50 µM MLVs in 20 mM Hepes 100 mM NaCl pH 7.4 buffer determined by Calcein quenching of the supernatant.

The preliminary screen suggested that the assay could work, and the results were sensible in that no more than half of the lipid was bound at a 1:1 metal/lipid ratio, and no binding was found with POPC. Co^{2+} and Ni^{2+} showed very similar binding patterns. The only case in which acyl chains made a large difference was between POPS and DMPS, as a much greater fraction of Co^{2+} and Ni^{2+} could bind DMPS. There was not a clear temperature-dependence in binding, but it is quite likely that the equilibrium at 37°C was altered upon handling at room temperature after incubation. The apparent association followed the order of: PA > ~PS > CL > PG, which was mostly consistent with the effects observed in Laurdan GP.

1.5.2 Accessible lipid in MLVs calculation

The approximate accessible lipid available in MLVs was determined by measuring the sizes with DLS and assuming 4 bilayer structures (229, 230). The radii of the internal bilayer structures were assigned as 80%, 50%, and 30% of the external bilayer size, and the surface areas (SA) of the outer and inner leaflets of each bilayer were calculated using the surface area for a sphere ($4\pi r^2$) and a bilayer thickness of 5.4 nm (228).

Table A-2. Calculated parameters for MLV structures to estimate fraction accessible lipid. A, B, C refers to the internal bilayer structures O = outer leaflet, I = inner leaflet.

Parameter	POPA	POPS	POPG
MLV $_{radius}$ (nm)	419	335	184
A $_{radius}$ (nm) (MLV $_{radius}$*0.8)	335.2	268	147.2
B $_{radius}$ (nm) (MLV $_{radius}$*0.5)	209.5	167.5	92
C $_{radius}$ (nm) (MLV $_{radius}$*0.3)	125.7	100.5	55.2
MLV layer SA_O (nm^2)	2206165	1410261	425447
MLV layer SA_I (nm^2)	2093900	1320796	376969
A layer SA_O (nm^2)	1411945	902567	272286
A layer SA_I (nm^2)	831289	831289	233797
B layer SA_O (nm^2)	551541	352565	106361
B layer SA_I (nm^2)	496142	308566	82856
C layer SA_O (nm^2)	198555	126923	38290
C layer SA_I (nm^2)	165901	101110	24773
Fraction accessible (MLV SA_O/sum SA)	0.2773	0.2634	0.2726

1.5.3 MLV size changes with metal addition

The effect of metal addition on the MLV structure was monitored by DLS, which is summarized in Figure :

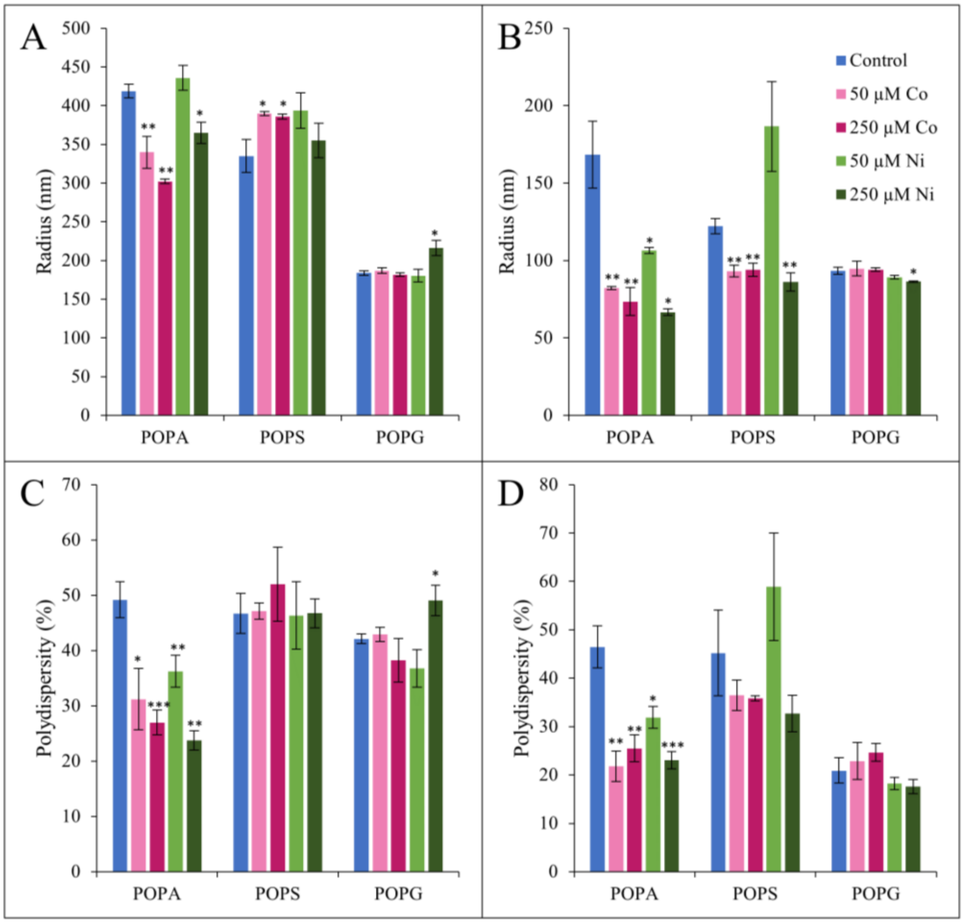

Figure A-8. Radii (nm) (A,B) and polydispersity (C,D) of MLV samples (A,C) and supernatants after incubation (B,D) as measured by DLS.

In general, the addition of Co^{2+} or Ni^{2+} caused the structures in both the MLV pellet and the supernatants to become smaller in size on average. This was not necessarily expected from the finding that both metals cause swelling and aggregation in LUVs of PA and PS. It is possible that in the presence of metal there is an “optimal size” somewhere between LUV and MLV. This is especially reflected in the PA data, in which the metals also caused significant decreases in the polydispersity of both the MLVs and supernatants. This suggests that there is a narrowing of the size distribution peak. In terms of the relevance for the assay, metal-induced changes in the structure of MLVs may affect their ability to pellet.

1.5.4 Pelleting efficiency estimates from DLS count rate

The count rate in DLS is a measure of how many scattered photons are reaching the detector. It can be used as a very rough indicator of concentration, but it is affected by shape and size (342). The count rates are shown in Figure :

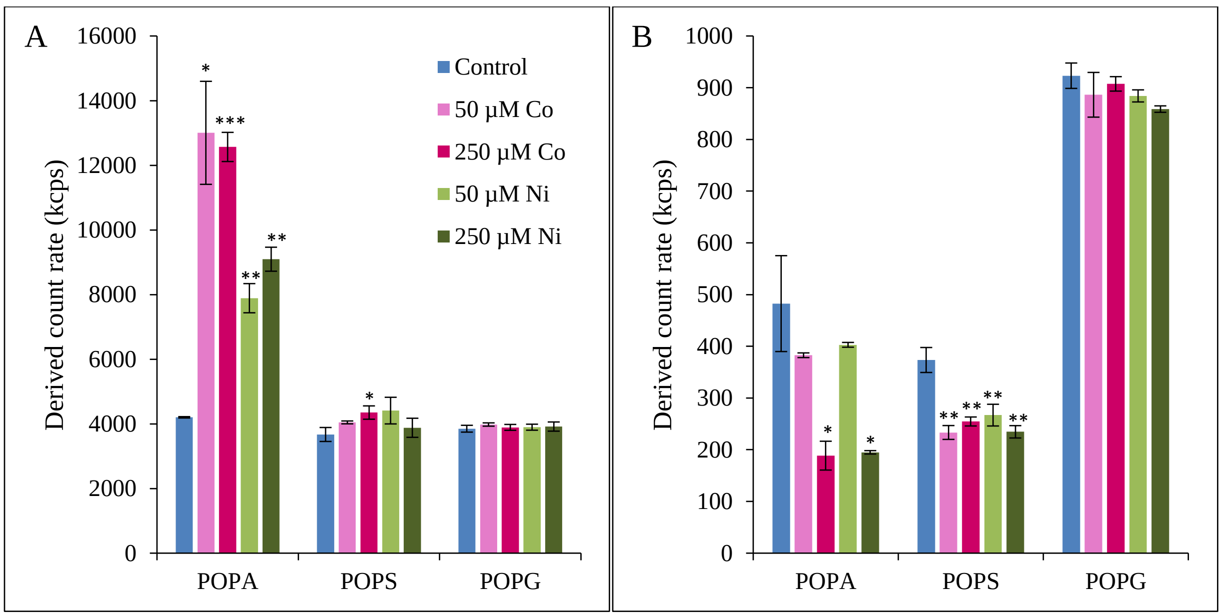

Figure A-9. Derived count rate (kcps) of (A) MLVs and (B) supernatants after incubation.

The count rate data for POPA shows a massive increase upon metal addition. As Co^{2+} and Ni^{2+} were not found to increase the sizes of POPA MLVs (Figure), this likely indicates that the metals increase the pelleting efficiency. This correlates with a decreased count rate in the supernatant. The pelleting efficiency of POPS appears to be slightly affected, but the metals do not affect POPG, which would be expected based on the absence of size changes observed in LUVs (Section 3.7.2). It appears that POPG is inherently worse at pelleting than POPA and

POPS, as the count rate of the supernatant is higher (Figure B), which is likely due to the smaller MLV sizes (Figure A).

While interesting, these findings highlight many of the complications in this assay for comparative analysis; thus it was not pursued for further characterization of interactions beyond POPA, POPS, and POPG.

Appendix B

2.1 Sizes of complex membranes with Co^{2+} and Ni^{2+} addition

The sizes of complex liposomes incubated with Co^{2+} and Ni^{2+} are shown in Figure :

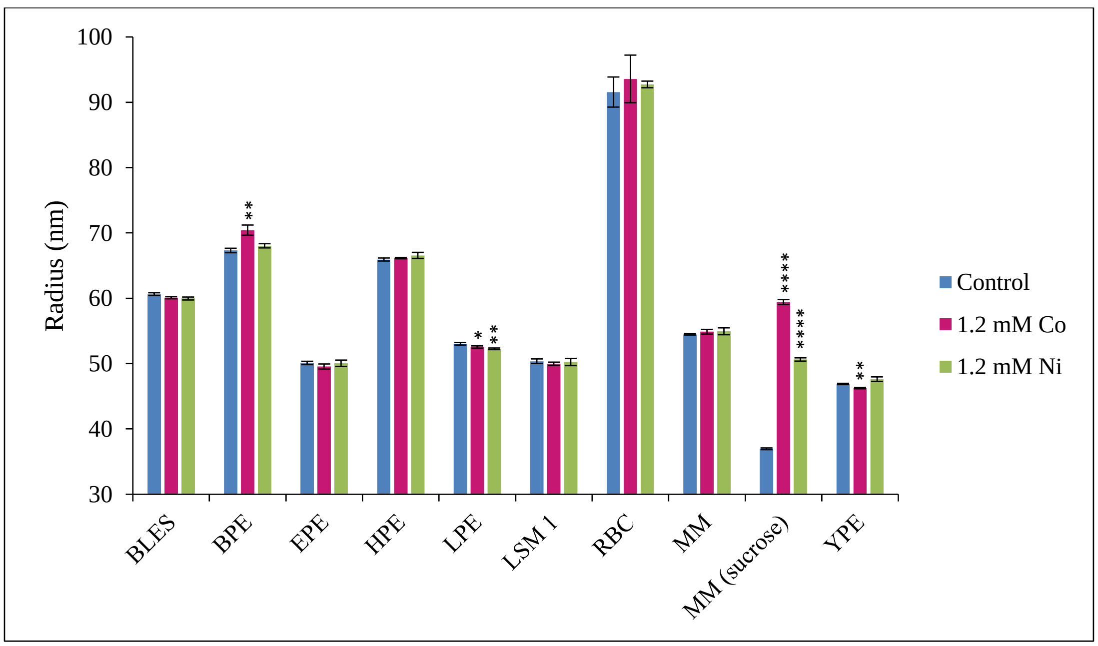

Figure B-1. Radii (nm) of complex liposomes in 20 mM Hepes, 100 mM NaCl pH 7.4 with 1.2 mM Co^{2+} or Ni^{2+}. BLES = bovine lipid extract surfactant, BPE = brain polar extract, EPE = E. coli polar extract, HPE = heart polar extract, LPE = liver polar extract, LSM = lung surfactant model 1, RBC = red blood cell extract, MM = mitochondrial mimic, YPE = yeast polar extract. The MM was also resuspended in 250 mM sucrose 10 mM Hepes pH 7.2.

Surprisingly, Co^{2+} and Ni^{2+} essentially did not affect the sizes of complex membranes containing minor amounts of negatively-charged lipid. This is in contrast to heavy metals Cd^{2+} and Pb^{2+} which caused swelling and aggregation (90, 237). The only notable size change occurred in the MM when in an NaCl-free buffer, likely due to absence of charge-screening.

2.2 Preliminary lipid peroxidation experiments

An initial test for lipid oxidation was performed with DOPE (not shown), and Yeast polar extract (Avanti Polar Lipids, Alabaster, AL):

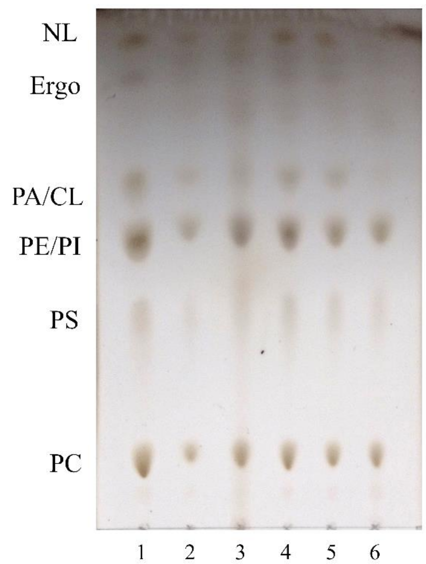

Figure B-2. Polar lipid TLC of oxidized Yeast polar extract (Avanti Polar Lipids) under various oxidizing conditions for 18 hrs. 1) = unoxidized YPE, 2) = Control, 3) = $FeCl_2$, 4) = $CoCl_2$, 5) = $NiCl_2$, 6) = $FeCl_2$ (1 hr).

Only Fe^{2+} was able to catalyze oxidation of YPE and DOPE, but the extent of oxidation was quite low, likely a result of the lack of polyunsaturation (96). A KI/starch spray for detection of lipid peroxides was tested with the 24-hr oxidized HPE:

Figure B-3. Polar lipid TLC of oxidized Heart polar extract (Avanti Polar Lipids) under various conditions for 24-hrs, visualized with 1:4 (v/v) 4% KI/1% acetic acid and then 2% starch. 1) = Control, 2) = $FeCl_2$, 3) = $CoCl_2$, 4) = $NiCl_2$, 5) = Fe/Co, 6) = Fe/Ni, 7) = Co/Ni, 8) = Fe/Co/Ni.

The peroxide stain indicated that only the Fe/Co/Ni treatment contained peroxides after 24 hrs, and that these highly-polar products remain at the origin. The reason that only the triple metal mixture contained peroxides may be because the reaction is slower and some of the peroxides have not yet been oxidized to further polar products (247). The intense band below the solvent front was consistently observed when using this stain and may indicate peroxides present in one of the solvents.

A preliminary test with a 1:1 POPC/POPA mixture to determine if negatively-charged lipids are selectively-depleted yielded the following results:

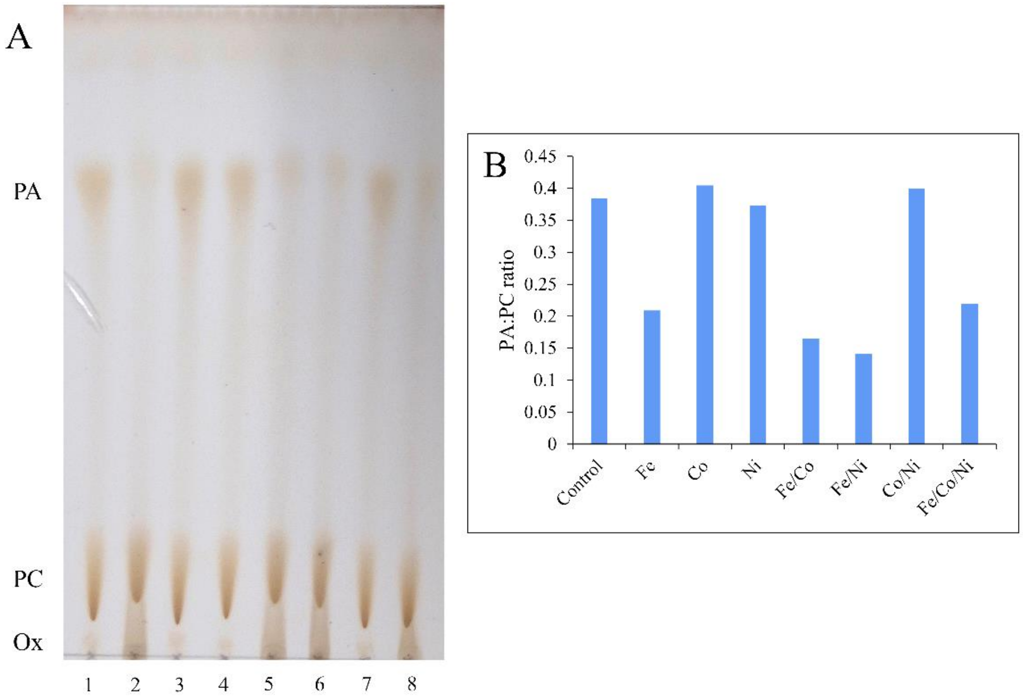

Figure B-4. (A) TLC of Fenton-oxidized 1:1 POPC/POPA MLVs under varying conditions of metal catalyst. (B) Ratio of PA to PC spots on TLC plate. 1) = Control, 2) = $FeCl_2$, 3) = $CoCl_2$, 4) = $NiCl_2$, 5) = Fe/Co, 6) = Fe/Ni, 7) = Co/Ni, 8) = Fe/Co/Ni.

The oxidation of PO- type lipids was not very efficient, and Co^{2+} and Ni^{2+} were unable to catalyze the reaction (Figure). However, the results do suggest that PA is decreased relative to PC in any of the Fe^{2+}-containing treatments. Alike to Co^{2+} and Ni^{2+}, Fe^{2+} has been previously-found to bind negatively-charged lipids (343). This supports the idea that the localization of redox-active metals to negatively-charged lipids results in selective depletion. Non-redox-active metals may exert a similar effect simply by clustering these lipids for Fe^{2+} to catalyze the reaction (80).

2.3 Effects of GSH on lipid interactions of $HgCl_2$ and $CdCl_2$

The effects of GSH on Co^{2+} and Ni^{2+} interactions in model systems were compared to $HgCl_2$ and $CdCl_2$ to determine if the interactions were stronger with heavy metals and dependent on speciation. A summary of the results is shown in Figure :

2.3.1 Laurdan GP of various PS mixtures

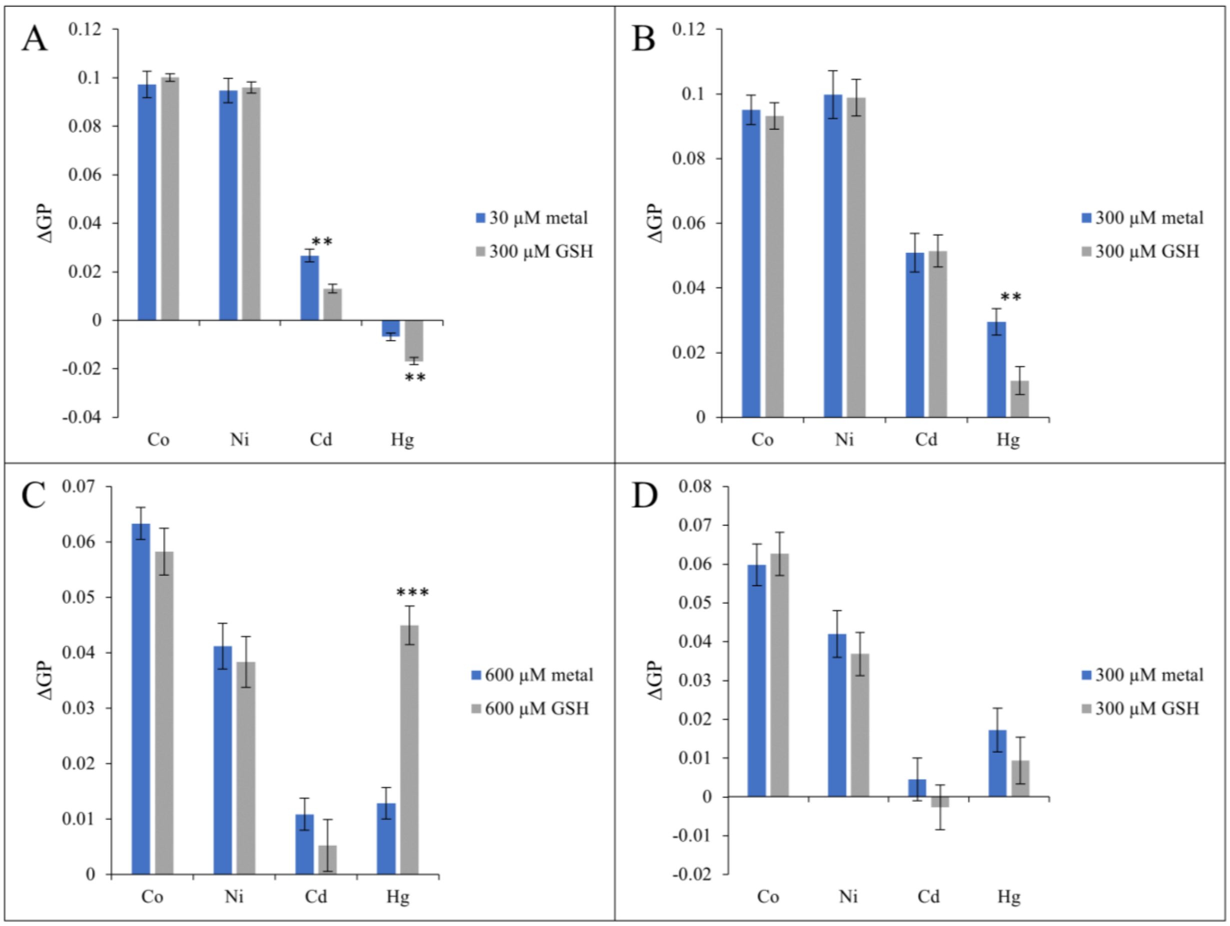

Figure B-5. Change in GP at 40°C in 0.3 mM liposomes in the presence of $CoCl_2$, $NiCl_2$, $CdCl_2$, or $HgCl_2$ with or without GSH present. (A) POPS, (B) 50:50 POPC/POPS, (C) 85:15 POPC/POPS, (D) 45:40:15 POPC/Chol/POPS.

While Co^{2+} and Ni^{2+} binding was unaffected in any system, GSH was able to affect $CdCl_2$ and $HgCl_2$ interactions. GSH slightly decreased the effect of $Cd^{2+}/CdCl^{+}$ on POPS, suggesting that GSH may out-compete the membrane for Cd species. On the other hand, GSH lead to a slightly enhanced fluidizing effect of $HgCl_2$, suggesting that the Hg-GSH complex may carry a positive charge which allows it to bind POPS. $HgCl_2$ otherwise does not target POPS due to speciation into primarily $HgCl_3^-$ and $HgCl_4^{2-}$ (32, 85). In the 50:50 POPC/POPS system, the effects with $HgCl_2$ were different than expected, in that GSH caused a slight decrease in effects. A control test with POPC showed that Hg-GSH had no effect. The most striking results came from the 85:15 POPC/POPS system, as $HgCl_2$ in the presence of GSH at a 1:1 ratio resulted in an increased rigidifying effect similar to that of Ni^{2+}. This, in combination with the results from other systems, suggests that GSH does affect the speciation of $HgCl_2$ and allows it to target negatively-charged lipids. However, it appears to depend strongly on the composition and packing of the membrane, as the addition of Chol eliminated this effect.

2.3.2 Conductivity of metals with GSH present

To confirm that speciation changes may be occurring, the conductivity of metal solutions with and without GSH were tested with 1:1 metal/GSH in duplicate.

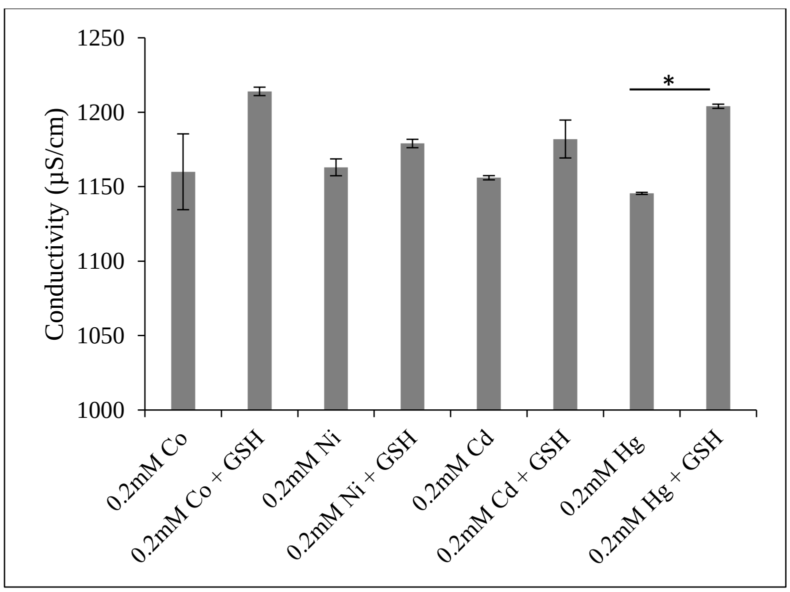

Figure B-6. Conductivity of 0.2 mM metal solutions with and without 0.2 mM GSH in 10 mM NaCl pH 7.4.

The conductivity of the Hg/GSH solution significantly changes compared to $HgCl_2$ alone, suggesting again that the speciation of $HgCl_2$ is affected by the presence of GSH. It would be of further interest to characterize the lipid-GSH-Hg interactions occurring, yet this was beyond the scope of this thesis.

Appendix C

3.1 Metal-media Interactions

The potential interactions of $CoCl_2$, $NiCl_2$, $MnCl_2$, and $Pb(NO_3)_2$ with various types of yeast media were tested by monitoring OD_{600} over time.

3.1.1 OD_{600} over time

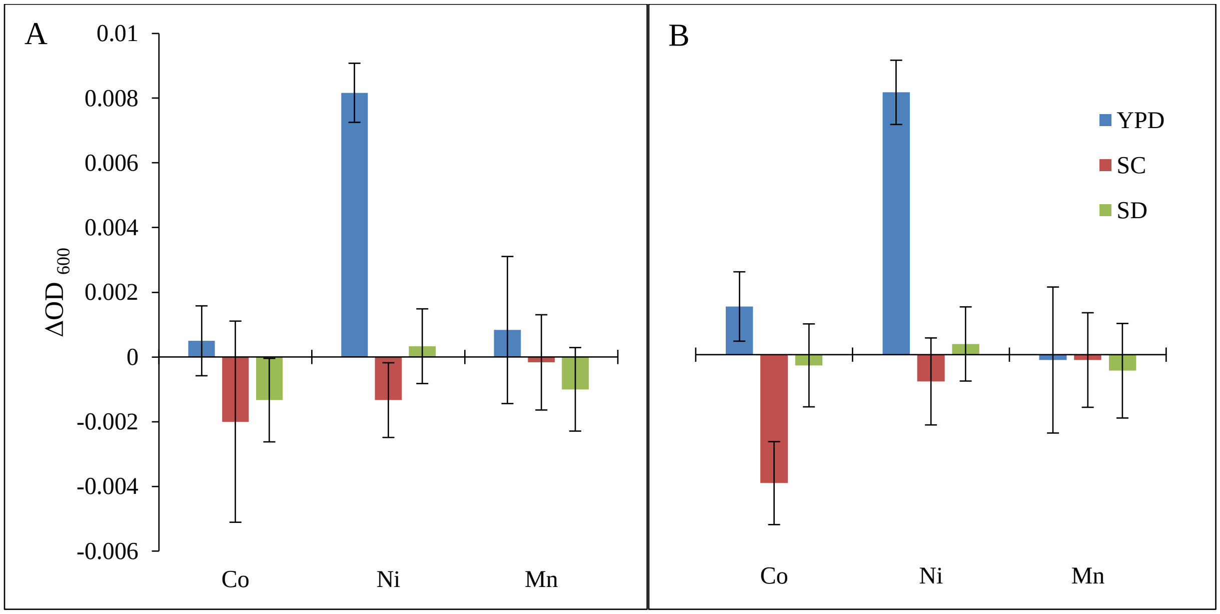

Figure C-1. OD_{600} of yeast media with 5 mM metal at (A) 0 hrs and (B) 1 hr.

Upon incubation with complex (YPD) and synthetic defined (SC/SD) media, Co^{2+}, Ni^{2+}, and Mn^{2+} did not lead to precipitation of media components. Ni^{2+} caused a slight increase in OD (<0.01), but this did not change over 1 hr (Figure B) and can thus be easily corrected for. On the other hand, 5 mM Pb^{2+} caused massive precipitation, so the changes caused by 0.5 mM Pb^{2+} instead were monitored over time:

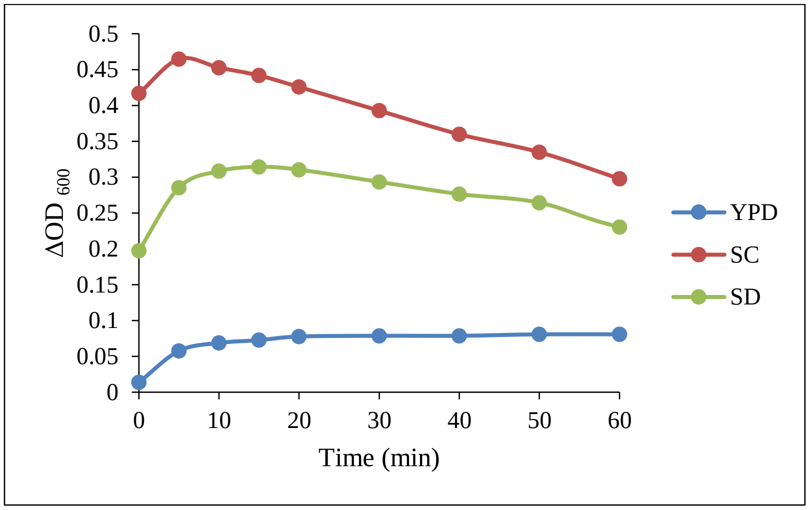

Figure C-2. Change in OD_{600} caused by $Pb(NO)_3$ in various yeast media over 1 hr with agitation.

Unexpectedly, YPD appeared to be the least-precipitated media by Pb^{2+} and did not change substantially over 1 hr. The synthetic defined media were highly precipitated and showed a settling effect over time suggesting that components are removed from solution. Defined media was the preferred choice for toxicity testing, so the fraction of free metal was then considered.

3.1.2 Calcein metal quenching to determine fraction bound to media

All four metals were able to be detected by Calcein quenching and standard curves were made as in Section 2.4.3, though it was more sensitive for Co^{2+} and Ni^{2+}. 0.5 mM metal were incubated with SD media for 1 hr and then centrifuged at 15,000 g for 15 min before assaying the supernatant for remaining metal. The values were corrected for a metal-free media blank and are shown in Figure :

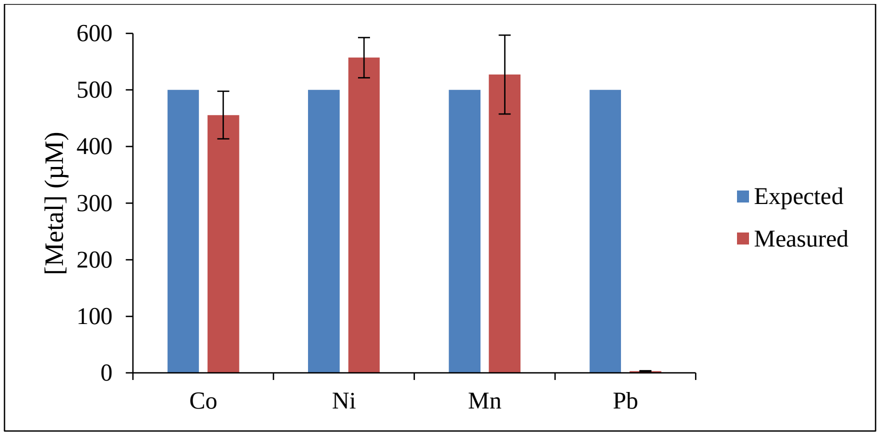

Figure C-3. Expected and measured metal concentrations in supernatants of SD media incubated at 30°C for 15 min, as determined by Calcein quenching.

The free Pb^{2+} concentration in SD media was essentially zero, while the Co^{2+}, Ni^{2+}, and Mn^{2+} concentrations were as expected. An Ames assay (149) on supernatant and pellet fractions of Pb^{2+}-treated media showed that phosphate was being pelleted by Pb^{2+}, which cannot be excluded from the growth medium. Pb^{2+} was thus not used in further growth experiments, as it may interfere with OD_{600} measurements and cause inhibitory effects simply by media depletion.

3.2 *S. cerevisiae* cell morphology

The morphology of treated yeast cells was occasionally monitored, and generally found to be similar to the control. A representative image is shown in Figure :

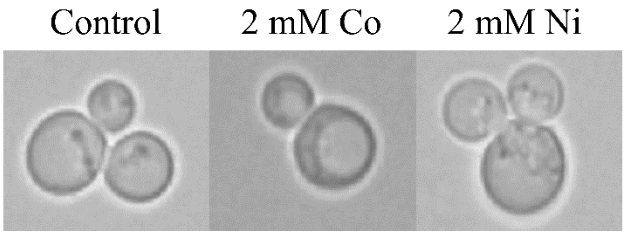

Figure C-4. BY4741 after 26 hrs in SC media at 1000x magnification.

Upon treatment with Co^{2+}, most cells showed a large, well-defined internal compartment which may be a swollen vacuole. The Ni^{2+}-treated cells contained similar features to control cells, but some were slightly shriveled.

3.3 Yeast growth curves with Mn^{2+}

Growth experiments were also performed with Mn^{2+} to determine if there was specificity or unique interaction among several similar transition metals. The results for SCglu, SC, and YPD are shown in Figure :

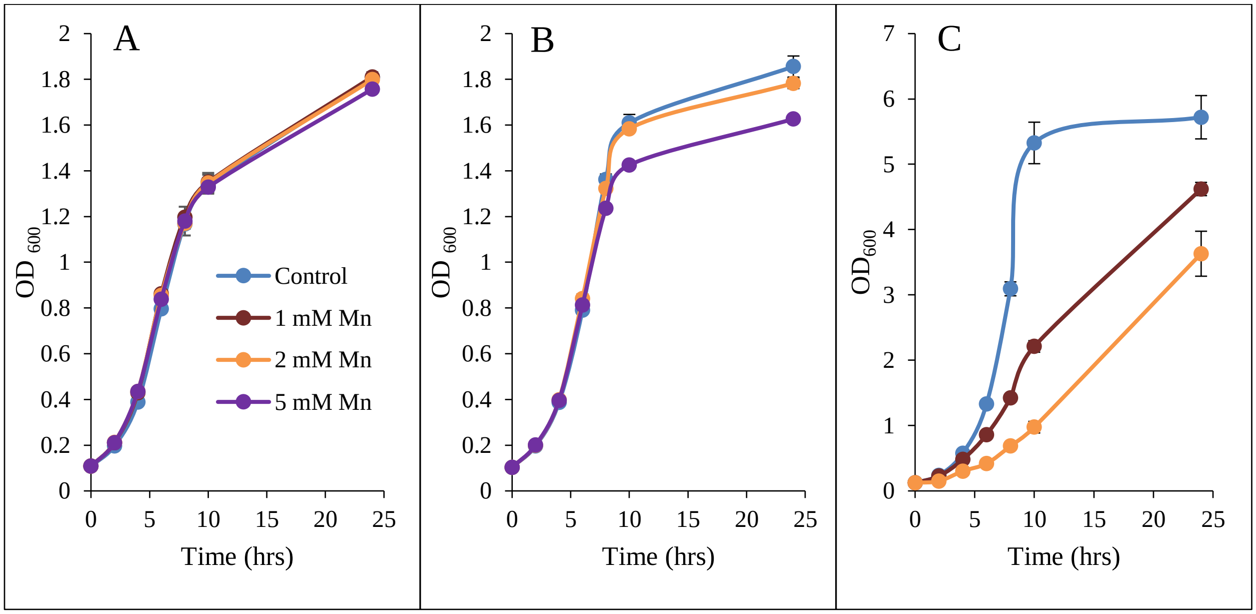

Figure C-5. Growth curves of BY4741 in (A) SCglu, (B) SC, and (C) YPD in the presence of various concentrations of Mn^{2+}.

Alike to Co^{2+} and Ni^{2+}, Mn^{2+} was unable to have an effect on growth when glutamate is used as a nitrogen source. Again, similar reasons may be contributing as presented in Section 5.1.1. Mn^{2+} was much less potent than Co^{2+} and Ni^{2+} in SC media, as only at 5 mM could it cause a slight decrease in stationary phase OD. In contrast, Mn^{2+} had greater effects than Co^{2+} and Ni^{2+} in YPD, suggesting that its interaction with media components, and thus bioavailability, is different. The results suggested that Co^{2+}, Ni^{2+}, and Mn^{2+} all had different levels of interaction with cells and possibly by different pathways. For the interest of time, Mn^{2+} was not pursued further.

3.4 TLC of Avanti yeast extracts

The commercially-available yeast extracts from Avanti Polar Lipids were also run on TLC to see if the composition extracted in this thesis was similar.

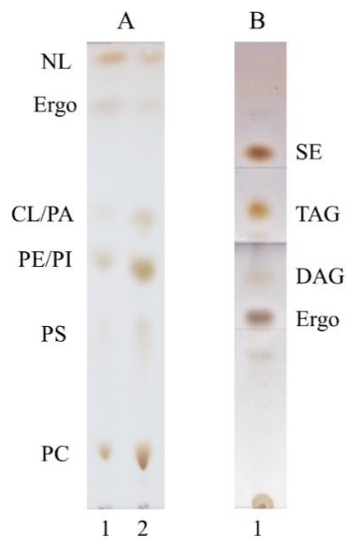

Figure C-6. (A) Polar lipid TLC and (B) Neutral lipid TLC of Avanti lipid extracts: 1) = Total yeast extract (YTE), 2) = Polar yeast extract (YPE).

The Avanti YTE and YPE were found to not differ greatly in composition, with the only major difference being the relative enrichment of Ergo/NL (Figure). This is in contrast to the experimental extracts made in this thesis, as my YPE was devoid of Ergo/NL. The neutral lipids found in the Avanti YTE show a similar distribution to the control in this thesis, as TAG is much more enriched than DAG. However, the large unidentified spot observed in the experimental extracts was not present in the Avanti YTE. It is possible that this spot represents non-lipid contaminants.

3.5 Absorbance spectra of neutral lipid extracts

It was observed that the acetone-soluble lipid extracts from metal-treated yeast were pigmented compared to the control, so the absorbance spectra of these samples were measured:

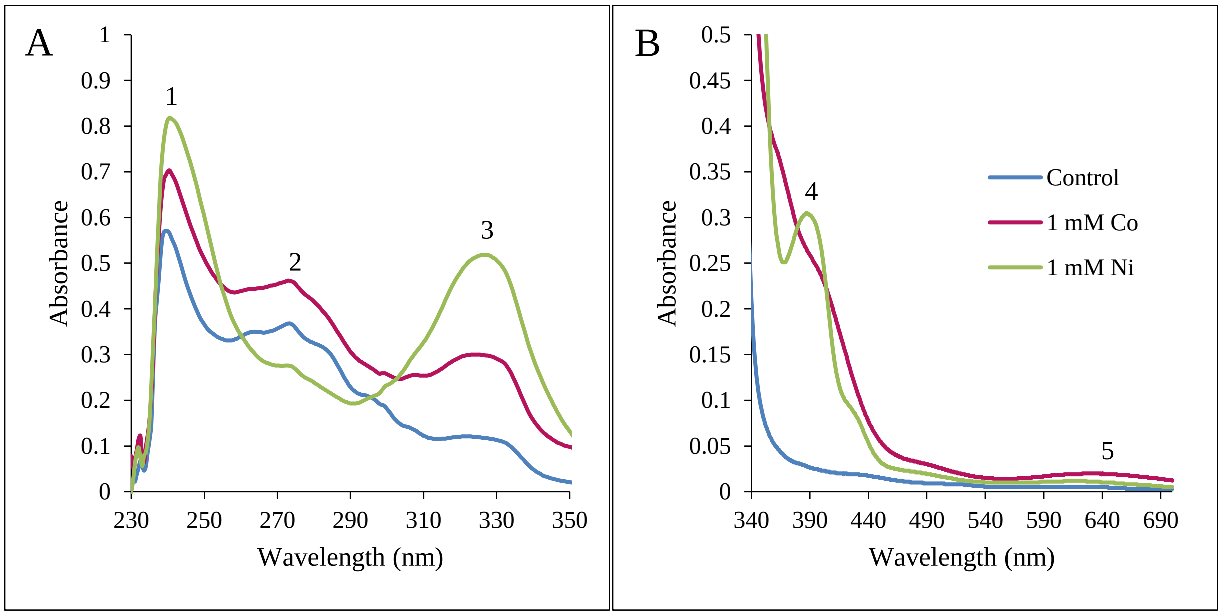

Figure C-7. Absorbance spectra of (A) 0.2 mg/mL and (B) 1 mg/mL neutral lipid extracts from BY4741 dissolved in 7:3 chloroform/methanol.

The spectra of control and metal-treated extracts were very different, but most of the absorbance occurred in the UV range. The various peaks observed are shown in Table C-1:

Table C-1. Wavelength of peaks 1–5 observed in the absorbance spectra of neutral lipid extracts in 7:3 chloroform/methanol.

Peak	Control	1 mM Co	1 mM Ni	Possible Identity
1	240	240	241	Peroxidised lipid? (344, 345)
2	273	273	273	Protein
3	322	324	327	?
4	N/A	385/404	387	Porphyrins (346)
5	N/A	640	N/A	?

All extracts appeared to have some protein contamination around 280 nm (Peak 2) which may represent the unknown spot in TLC. The main difference in pigment must therefore come from the peak and shoulder around 390 nm in the visible region. The identities of the peaks have not been characterized but can be speculated. Peak 4 observed clearly in the Ni^{2+}-treated extract is consistent with the Soret peak previously reported for Ni^{2+}-protoporphyrin IX, occurring at 384 nm (346). Thus, it is possible that this peak represents an accumulation of Ni^{2+}-substituted porphyrin. The Co^{2+}-protoporphyrin IX has been shown to have Soret peaks at 417 and 388 nm, which is not clearly observed here, but may be indicated in the two shoulders from 350–450 nm. Protoporphyrin is expected to be lipid-soluble, so it could theoretically be co-extracted (347) and may be responsible for pigmentation.

The identities of Peaks 1 and 3 are a bit more elusive, as they are also present in the control, suggesting that they are naturally present. It has been previously shown that lipid peroxides absorb at 233 nm (167, 344, 345), so this is a potential explanation for Peak 1. This would also be consistent with the idea that Co^{2+} and Ni^{2+} induce oxidative stress, though the absorbance in the control is fairly high as well. To determine whether or not this may represent lipid peroxides, the neutral lipid TLC plate was sprayed with 1:4 (*v/v*) 4% KI/ 1% acetic acid and 2% starch (167, 168). The extracts did not stain blue/brown, so there are likely no lipid peroxides present. There is no obvious hypothesis for Peak 3, but this may represent a lipid-soluble aromatic compound.

Appendix D

4.1 Publications

Umbsaar, J., Kerek, E., and Prenner, E. J. (2018) Cobalt and nickel affect the fluidity of negatively-charged biomimetic membranes. *Chem. Phys. Lipids*. **210**, 28–37

4.2 Posters and Presentations

Jenelle Umbsaar, Robyn Mundle, and Elmar J Prenner. (2017). Nickel and Cobalt Affect the Fluidity of Biomimetic Membranes. 1st Biological Sciences Graduate Symposium. Calgary, AB, Canada. February 17, 2017.

Jenelle Umbsaar and Elmar J Prenner. (2017). The Effects of Cobalt and Nickel on Biomimetic Membranes. Institute of Environmental Science and Research (ESR) Seminar Session. Christchurch, New Zealand. May 2, 2017.

Weiam Daear, Jenelle Umbsaar, and Elmar J Prenner. (2018). Study of the Interactions of Polymeric Nanoparticles with Model Lung Surfactant. 101st Canadian Chemistry Conference and Exhibition. May 29, 2018.

Jenelle Umbsaar, Robyn Mundle, and Elmar J Prenner. (2018). The Interactions of Lead, Nickel, and Cobalt with Simple and Complex Model Membranes. 101st Canadian Chemistry Conference and Exhibition. May 29, 2018.

Copyright Clearance Center RightsLink®

Home | Create Account | Help

Title: Cobalt and nickel affect the fluidity of negatively-charged biomimetic membranes

Author: Jenelle Umbsaar, Evan Kerek, Elmar J. Prenner

Publication: Chemistry and Physics of Lipids

Publisher: Elsevier

Date: January 2018

© 2017 Elsevier B.V. All rights reserved.

LOGIN

If you're a copyright.com user, you can login to RightsLink using your copyright.com credentials.

Already **a RightsLink user** or want to learn more?

Please note that, as the author of this Elsevier article, you retain the right to include it in a thesis or dissertation, provided it is not published commercially. Permission is not required, but please ensure that you reference the journal as the original source. For more information on this and on your other retained rights, please visit: https://www.elsevier.com/about/our-business/policies/copyright#Author-rights

BACK | CLOSE WINDOW

Copyright © 2018 Copyright Clearance Center, Inc. All Rights Reserved. Privacy statement. Terms and Conditions.
Comments? We would like to hear from you. E-mail us at customercare@copyright.com